

**DESIGN, MICRO-MANUFACTURING, AND
CHARACTERIZATION OF A NEW FAST PARALLEL-
PROCESSING FOURIER TRANSFORM INTERFEROMETER
(FTIR) WITH SINGLE NON-PERIODIC
PULSE CAPABILITY**

SASCHA PIERRE HEUSSLER

NATIONAL UNIVERSITY OF SINGAPORE

2010

**DESIGN, MICRO-MANUFACTURING, AND
CHARACTERIZATION OF A NEW FAST PARALLEL-
PROCESSING FOURIER TRANSFORM INTERFEROMETER
(FTIR) WITH SINGLE NON-PERIODIC
PULSE CAPABILITY**

SASCHA PIERRE HEUSSLER
(Dipl. Ing.(FH), Zweibruecken, Germany)

A THESIS SUBMITTED

FOR THE DEGREE OF DOCTOR OF PHILOSOPHY

DEPARTMENT OF MECHANICAL ENGINEERING

NATIONAL UNIVERSITY OF SINGAPORE

2010

To my grandfather

Adolf Schäfer

ACKNOWLEDGEMENTS

This work was performed at Singapore Synchrotron Light Source (SSLS) under NUS Core Support C-380-003-003-001, A*STAR/MOE RP 3979908M and A*STAR 12 105 0038 grants.

Foremost, I would like to express my sincere gratitude to Prof. Herbert Oskar Moser for his heartfelt support throughout the years. The study accomplishments would not have been possible without his expertise, coaching, and guidance. Alongside Prof. Herbert Oskar Moser, my special thanks go to Prof Quan C and Prof Tay Cho Jui for their continuous support within the project and specifically during the regular project reviews.

As a key contributor in the field of spectroscopy, I would like to thank Dr. Mohammed Bahou for his hands-on experimental support and the fruitful discussions. In the field of micro-fabrication, I am grateful for Dr. Jian giving me the opportunity to utilize the SSLS LiMiNT facility.

I would like thank Mr Tan Choon Huat of AML, Dr. Liu Kui of SIMTech, Eric Tang Xiaosong and Dr. Raman Akkipeddi of IMRE for their straight forward and practical support in various machining processes.

Many thanks to Dr. Herman Bergmann and Dr. Andreas Fechtenkoetter of BASF for their help with the molecular weight measurements of PMMA samples.

I would like to thank Dr. Yang Ping for the XDD measurements.

For their patience and help throughout the dissertation, I am thanking my colleagues particularly S. M. Kalaiselvi, Miao Hua, Shahrain bin Mahmood, and Vo Trong Nghia.

The continuous support of my family has been the foundation of my work. My mother Dorothea, and my sister Christina, my father Hans and his wife Ingrid have always been there for me when I needed them the most.

A special thanks to Silke Neumann for her continuous motivation and encouragement. Last but not least this work would have not been possible without the support and the patience of my friends. I would like to thank all my friends back home and in Singapore accompanying me through the 'highs' but even more importantly helping me through the 'lows'. My personal "DANKE" goes to: Manuel Dasch, Oliver Wilhelmi, Marcus Kuhnert, Heiko Pohland, Neeraj Gupta, Namunu Chintaka, Thomas Berner, Hermann Bergmann, MC, 'The Newton Hawker Philosophenrunde' (Denis Mecklenburg and Joerg Kuehn) as well as many others.

My final thanks goes to Joerg Kuehn. It has been a pleasure and a great journey. I am deeply happy and thankful for your support.

Thank you very much.

CONTENTS

| | |
|---|------------|
| Acknowledgements | i |
| Publications | vi |
| Summary | vii |
| List of Tables | ix |
| List of Figures | x |
| | |
| 1 Introduction | 1 |
| 1.1 Background of the project | 1 |
| 1.2 Motivation and objectives (scope of work) | 4 |
| 1.3 Outline and organization of the thesis | 6 |
| | |
| 2 Theory of Fourier Transform Spectroscopy | 7 |
| 2.1 Introduction | 7 |
| 2.1.1 Electromagnetic radiation | 7 |
| 2.1.2 Measuring light | 8 |
| 2.2 Theory of Fourier Transform Spectroscopy | 10 |
| 2.2.1 Advantages of Fourier transform spectroscopy | 11 |
| 2.2.2 Interferogram and spectrum | 12 |
| 2.2.3 Symmetric and asymmetric interferograms | 14 |
| 2.2.4 The complex Fourier transform | 16 |
| 2.2.5 Instrumental line shape function, apodization, and resolution | 18 |
| 2.2.5.1 Truncation and instrumental line shape function | 18 |
| 2.2.5.2 Apodization | 19 |
| 2.2.5.3 Resolution | 21 |
| 2.2.6 Sampling | 23 |
| 2.2.7 Field of view | 25 |
| 2.2.7.1 Interferogram and spectrum of extended sources | 27 |
| 2.2.8 Noise | 29 |
| 2.2.8.1 Additive noise | 29 |
| 2.2.8.2 Multiplicative noise | 30 |
| 2.2.8.3 Signal-to-Noise ratio | 31 |
| 2.3 Summary | 33 |

| | |
|--|-----------|
| 3 The Concept of the Fast Parallel Processing Fourier Transform Spectrometer (FPP FTS) | 34 |
| 3.1 Introduction | 34 |
| 3.2 Miniature spectrometers | 34 |
| 3.3 The Fast Parallel Processing Fourier Transform Spectrometer (FPPFTS) | 38 |
| 3.3.1 Design considerations | 40 |
| 3.3.1.1 Spectra of interest | 40 |
| 3.3.1.2 The Micro Mirror Array (MMA) | 42 |
| 3.3.1.2.1 The single cell design | 43 |
| Design A: Even number of rectangular mirror surfaces | 46 |
| Design B: Odd number of rectangular mirror surfaces of width w_F and w_B | 50 |
| Design C: Odd number of rectangular mirror surfaces of width w and center mirror of double width | 51 |
| 3.3.1.3 Resolution, sampling, and number of MMA cells | 54 |
| 3.3.1.4 Detector acceptance angle | 57 |
| 3.3.1.5 Long wavelength limitation | 63 |
| 3.3.1.6 Angle of incidence | 64 |
| 3.3.1.6.1 Shadowing | 64 |
| 3.3.1.7 Extended sources | 66 |
| 3.3.1.7.1 Spatial coherence | 67 |
| 3.3.1.8 Spatial filtering and spectrometer throughput | 70 |
| 3.3.1.9 Reflection of metals | 73 |
| 3.3.1.9.1 Estimation of required layer thickness | 76 |
| 3.3.1.9.2 Influence of surface roughness on reflection | 77 |
| 3.4 Summary | 79 |
| | |
| 4 Fabrication | 80 |
| 4.1 Introduction | 80 |
| 4.2 MMA design parameters | 80 |
| 4.3 3D micro-fabrication technologies – A review | 83 |
| 4.4 3D micro-fabrication using Synchrotron radiation | 87 |
| 4.4.1 3D X-ray lithography (3D XRL) | 88 |
| 4.4.2 Moving mask exposure station for 3D X-ray lithography | 90 |
| 4.4.3 X-ray masks for 3D X-ray lithography | 92 |
| 4.4.4 3D Structuring of poly-methylmethacrylate (PMMA) | 99 |
| 4.4.4.1 The resist-developer-system | 101 |
| 4.4.4.2 Resist-developer characterization | 104 |
| 4.5 Reflection layer coating | 120 |

| | |
|---|------------|
| 4.6 Summary | 123 |
| 5 Spectral Characterization | 125 |
| 5.1 Introduction | 125 |
| 5.2 Experimental setup at SSLs' IFS 125 HR spectrometer | 125 |
| 5.3 Spectral response of single MMA cells | 130 |
| 5.4 Spectral characterization of 10 x 10 MMA cell spectrometer | 133 |
| 5.4.1 Data processing | 133 |
| 5.4.2 Frequency calibration | 139 |
| 5.4.3 Spatial source 'non'-uniformity and its compensation | 141 |
| 5.4.4 Noise | 147 |
| 5.4.4.1 Infrared camera noise | 148 |
| 5.4.4.2 Background noise | 150 |
| 5.4.4.3 Temporal source fluctuation | 151 |
| 5.4.4.4 Noise in spectra | 153 |
| The influence of apodization | 153 |
| Data averaging | 154 |
| Pixel binning | 157 |
| 5.5 Single pulse spectra | 158 |
| 5.6 Time-resolved spectroscopy | 161 |
| 5.7 Summary | 164 |
| 6 Summary and Conclusion | 165 |
| Bibliography | 167 |
| Appendix | 186 |
| Appendix 1: Cosine transforms | 186 |
| Appendix 2: Effect of truncation of the interferogram | 187 |
| Appendix 3: Fraunhofer diffraction of identical similarly oriented apertures | 188 |
| Appendix 4: Optical path difference for tilted detector plane | 191 |
| Appendix 5: The LiMiNT facility at the Singapore Synchrotron Light Source | 193 |
| Appendix 6: The gold stencil mask fabrication process | 199 |
| Appendix 7: The characterization of surface roughness and surface waviness of etched mirror surfaces | 201 |
| Appendix 8: The Bruker IFS 125 HR FTIR at SSLs ISMI beamline | 204 |

PUBLICATIONS

S. P. Heussler, H. O. Moser, C. G. Quan, C. J. Tay, K. D. Moeller, M. Bahou, and L. K. Jian.
Deep X-Ray Lithography in the Fabrication Process of a 3D Diffractive Optical Element. AIP Conf. Proc. Volume 879, pp. 1503-1506, DOI:10.1063/1.2436350 (2007)

S.P. Heussler, H.O. Moser, C.G. Quan, C.J. Tay, K.D. Moeller, M. Bahou, and L.K. Jian.
Fabrication of high aspect-ratio diffractive optical elements by deep X-ray lithography.
The Asia-Pacific Conference of Transducers and Micro-Nano Technology APCOT, 25-28 June, Singapore (2006).

H.O. Moser, L.K. Jian, H.S. Chen, M. Bahou, S.M.P. Kalaiselvi, S. Virasawmy, S.M. Maniam, X.X. Cheng, S.P. Heussler, Shahrain bin Mahmood, B.-I. Wu. *All-metal self-supported THz metamaterial – the meta-foil.* Optics Express 17 (26), 2009.

H. O. Moser, J. A. Kong, L. K. Jian, H. S. Chen, G. Liu, M. Bahou, S. M. P. Kalaiselvi, S. M. Maniam, X. X. Cheng, B. I. Wu, P. D. Gu, A. Chen, S. P. Heussler, Shahrain bin Mahmood, and L. Wen. *Free-standing THz electromagnetic metamaterials.* Opt. Express 16, 13773(2008).

F. Giro, K. Bedner, C. Dhum, J. E. Hoffmann, S. P. Heussler, L. Jian, U. Kirsch, H. O. Moser, M. Saumer. *Pulsed electrodeposition of high aspect-ratio NiFe assemblies and its influence on spatial alloy composition.* Microsyst Technol 14:1111–1115(2008).

SUMMARY

Fourier transform spectroscopy is known as a powerful tool for measuring weak radiation with high resolution. Commonly, Fourier transform spectrometers use highly precise scanning mirror mechanisms to obtain spectral information resulting in large scale and high cost spectrometers. Miniaturization of spectrometers may overcome the cost and size limitation of the instrument at the expense of resolution. Such miniature, lower resolution spectrometers however allow a wide range of attractive applications in science and industries.

This work includes the theoretical analysis, the design, construction, and experimental characterization of a new type of spectrometer dubbed the Fast Parallel Processing Fourier Transform Spectrometer (FPP FTS) as invented by Moser and Moeller 15 years ago (Moser and Moeller, 1994).

We achieved the experimental proof of concept by measuring spectra in the mid-infrared and demonstrated the capability of the FPP FTS to detect spectra of single short pulses provided sufficient signal-to-noise ratios are generated by the source and the detector. We have shown that the multiplex advantage applies in the mid-infrared spectral range. Furthermore, we expect a throughput advantage as well as wider spectral working bands when compared to its competitor the grating spectrographs, since the FTS is not limited by small entrance apertures and does not require cut-off filters to reject higher diffraction orders.

The core of the spectrometer is formed by a micro mirror array (MMA). To fabricate the MMA, we developed a micro manufacturing process on the basis of X-ray lithography using the novel concept of multiple moving masks. The influence of exposure and development parameters on the inclination and surface roughness of the

mirror facets were thoroughly investigated. Numerous other features of the fabrication process were also studied in detail. We have shown its capability to deliver 3D monolithic MMA's in PMMA for a prototype mid-infrared FPP FTS. The analytical treatment of the FPP FTS on the basis of Kirchhoff's diffraction theory lead to excellent agreement with experimental results.

LIST OF TABLES

| | | |
|-------------|--|-----|
| Table 2-1: | Apodization functions and the resultant full-width-at-half-maximum (FWHM) values as a function of the maximum optical path difference δ_{\max} , percentage increase in FWHM and the maximum sidelobe height. Functions are taken from references (Chamberlain 1979, Bell, 1972, Happ and Genzel, 1961). | 21 |
| Table 3-1: | Infrared Classification | 41 |
| Table 3-2: | Simulated cell designs and parameters | 46 |
| Table 4-1: | MMA design parameters | 81 |
| Table 4-2: | Sample spectrometer layouts | 82 |
| Table 4-3: | Properties of mask materials (references are Touloukian and Ho, 1979 and DuPont.com for Kapton® data). | 94 |
| Table 4-4: | Parameters influencing the dissolution rate of PMMA in X-ray lithography as reported by the respective references. | 100 |
| Table 4-5: | Molecular weight distribution of PMMA used for the experiments. The weight distributions were obtained via Gel Permeation Chromatography (GPC) in tetrahydrofuran (THF) solution. | 103 |
| Table 4-6: | GG developer and GG rinse formulation used in experiments (after Ghica and Glashauser, 1983). | 104 |
| Table 4-7: | Development parameters after Eq. (4-3) for Degussa and CQ PMMA at different GG developer temperatures and starting ring currents. Minimum dose corresponds to an exposure dose at which etching of PMMA is observed. Parameters K and α are found by least square fit of the dissolution rate according to Eq. (4-3) for dose regime from 0 – 4 kJ/cm ³ and 4 – 8 kJ/cm ³ . | 110 |
| Table 4-8: | Statistics of mirror inclination angle for Degussa and CQ PMMA down to an etch depth of 140 μ m. The mirror inclination is measured with respect to the top micro-mirror surfaces as illustrated in the red hatched surfaces in Figure 4-13 (b). | 116 |
| Table 4-9: | Reflection layer thickness and surface roughness obtained by high resolution x-ray specular reflectometry at grazing incidence angle at SSLS XDD beamline at X-ray energy of 8.048 keV. All layers were coated on a 2 mm Degussa PMMA sheet by magnetron sputtering (NSP 12-1 NTI) at a pressure below 5 E-06 bar. (Remark ^: The roughness of Cr layer varies around 1.2 nm). | 122 |
| Table 5-1: | Increase in signal-to-noise-ratio (SNR) for selected apodization functions. | 156 |
| Table A5-1: | Characteristic Helios 2 and LiMiNT beamline parameters. | 197 |
| Table A5-2: | Process equipment LiMiNT facility / SSLS | 198 |
| Table A6-1: | Process flow for Au stencil mask fabrication. | 200 |
| Table A8-1: | Specifications of SSLS' IFS 125 HR spectrometer (IFS125, 2006). | 208 |

LIST OF FIGURES

| | | |
|-------------|--|----|
| Figure 2-1: | Transverse electromagnetic wave. \vec{E} depicts the electric and \vec{H} the magnetic wave vector, λ , τ , and \vec{k} represent the wavelength, the temporal period, and the wave vector, respectively. | 8 |
| Figure 2-2: | Simplified wave dividing principles: Plane waves of wavelength λ and amplitude A_0 (its magnitude is illustrated by the width of the lines) impinge on the beam splitter and are split into two beams by (a) an amplitude splitter, and (b) by a wavefront splitter. | 11 |
| Figure 2-3: | Schematic illustration of the interference function $I(\delta)$ as recorded by the detector, the interferogram $f(\delta)$, both as a function of optical path difference δ (a), and (b) the acquired spectrum $B(\sigma)$ as a function of wavenumber σ . | 14 |
| Figure 2-4: | Effect of finite extent of the interferogram on the spectral line shape. (a) Interferogram of finite (black solid line), and of infinite (dashed line) extent. The thick solid line indicates the truncation of the cosine function at δ_{\max} . (b) Resulting spectra of truncated interferogram (solid black) and of infinite interferogram (solid blue). | 19 |
| Figure 2-5: | Simplified diagram of Michelson interferometer with an extended source in the focal point of the collimating optics. Ψ denotes the angle a ray makes with the optical axis when emitted off the center of the source and d the distance between both reflecting mirrors. | 26 |
| Figure 2-6: | Effect of extended source on interferogram $f(\delta, \Omega)$ (a) and spectrum (b) in comparison to interferogram of a point source $f(\delta)$. Both examples are given for truncated interferometric data. The source extension results in a recovered spectrum of increased spectral width centered at a wavenumber $\sigma_0 \left(1 - \frac{\Omega}{4\pi}\right)$ and amplitude $\frac{\pi}{\sigma_0 \Omega}$. | 29 |
| Figure 3-1: | (a) Schematics of Fast-Parallel-Processing Fourier Transform Spectrometer (FPP-FTS). Source radiation is collimated and directed to the Micro Mirror Array (MMA). Upon reflection from the (here) 3 x 3 cell MMA, the collimated beam is split into 3 x 3 sub-beams, each of which is modulated in amplitude with respect to its individual optical path difference introduced by the front and back facet mirrors. Subsequently, these sub-beams are focused onto the plane of a 3 x 3 array detector, positioned at a distance from the MMA. Each detector cell measures one single intensity point of the interferogram. From the position of the spot on the detector its optical path difference is known. Both, the intensity and the respective optical path difference constitute the interferogram. Subsequent Fourier transformation yields the spectrum. (b) Schematic of the wave front division and | 39 |

- diffraction at a single MMA cell, P is the grating constant, h the grating depth, λ the wavelength of the incident light, α the diffraction angle and φ the phase difference due to the optical path difference of rays reflected by the front and by the back facet mirrors.
- Figure 3-2: Simulation schematic. The reflection grating is simulated as a transmission grating which is placed in the ξ - η -plane. The grating consists of surfaces either introducing a 0 (whitish areas) or a φ phase shift (grayish areas). The arrangement of the phase-steps depends on the individual cell design. Here, a rectangular grating design is exemplarily shown. P_s and P_i are the position of the source- and the image-point, respectively. Z denotes the optical axis and n the grating normal. 43
- Figure 3-3: (a) MMA cell formed by binary grating of depth h , lamellar width w and grating cell length l . Inset of (a) Denomination of angles: \vec{k} is the plane wave normal, γ the angle between \vec{k} and its projection in ξz plane, Φ the angle between \vec{k} projection in the ξz plane and the ξ axis. (b) Converted phase map. 44
- Figure 3-4: Cell Design A: Fraunhofer diffraction pattern in x direction for a ratio of $w/\lambda = 5$ and phase shifts φ of λ , $1/4\lambda$, $1/2\lambda$, and $3/4\lambda$ for (a) $N_{MS}=2$, (b) $N_{MS}=4$, (c) $N_{MS}=8$, and (d) $N_{MS}=12$ mirrors per cell. (e) Fraunhofer diffraction pattern in x direction for $N_{MS}=12$ mirrors and a ratio $w/\lambda=10$. (f) Fraunhofer diffraction pattern in y direction 49
- Figure 3-5: Cell Design B: Fraunhofer diffraction pattern in x direction for a ratio of $w_F/\lambda = 5$ of the front facets mirrors, $w_B/\lambda=(w_F/\lambda)(N_{MS}+1)/(N_{MS}-1)$ for the back facet mirrors, and phase shifts φ of λ , $1/4\lambda$, and $1/2\lambda$ for (a) $N_{MS}=3$, and (b) for $N_{MS}=5$ (solid) and $N_{MS}=11$ (dashed) mirrors per cell. 51
- Figure 3-6: Cell Design C: Fraunhofer diffraction pattern in x direction for a ratio of $w/\lambda = 5$ of the front and back facet mirrors, center mirror is of double width, phase shifts φ are λ , $1/4\lambda$, and $1/2\lambda$ for $N_{MS}=7$ (solid), and $N_{MS}=11$ (dashed) mirrors per cell. 52
- Figure 3-7: Number of MMA cells as a function of high frequency cutoff at spectral resolution \mathfrak{R}_{ILS} (no apodization) after Shannon (Shannon, 1949). (a) for band limited signals with $\sigma_{min} = 0$ cm^{-1} at \mathfrak{R}_{ILS} of 25 cm^{-1} (black), 10 cm^{-1} (red), 4 cm^{-1} (green), and 2 cm^{-1} (blue). (b) for band limited signals with σ_{min} is 0 cm^{-1} (black), $1/2 \sigma_{max}$ (red), $3/4 \sigma_{max}$ (green), and $4/5 \sigma_{max}$ (blue) at a spectral resolution of $\mathfrak{R}_{ILS} = 4 \text{ cm}^{-1}$. 55
- Figure 3-8: Modulation amplitudes as function of detector acceptance angles for cells of $P/\lambda=10$. (a) Modulation amplitudes as a function of phase shift φ and detector acceptance angle for cell design A and 12 mirror surfaces. (b) Comparison of cell designs A, B, and C. 58

| | | |
|--------------|---|----|
| Figure 3-9: | Modulation amplitude as a function of diffraction angle α and ratio P/λ for design A and $N=12$. | 59 |
| Figure 3-10: | Concept of detector acceptance angle for maximum modulation amplitude for a spectrometer with a spectral working band ranging from λ_{\min} the shortest to λ_{\max} the longest wavelength component. Radiation transmitted or reflected from the grating cell is diffracted into angles off the optical axis. The diffraction angles are wavelength dependent and the acceptance angle of the detector needs to be chosen to transmit zeroth order (indicated by the whitish area at the screen) whereas higher diffraction orders are permitted (greyish hatched area) from reaching the detector plane. M denotes the diffraction order, Ψ_A , α_{ap} and α_d the detector acceptance angle, the aperture angle, and the diffraction angle of the first diffraction order, respectively. | 60 |
| Figure 3-11: | (a) Normalized spectra for low modulation amplitude (top), and high modulation amplitude (middle) at a random noise of 10 % the maximum signal amplitude, in comparison to noise-free spectra (bottom). (b) Quality ratio Q_h/Q_l as a function of noise level. | 62 |
| Figure 3-12: | Effect of shadowing. (a) Schematic: For plane wave incidence, the front facet mirrors cast a shadow on the back facet mirrors (hatched surfaces). Denomination of angles: \vec{k} is the plane wave normal, Y the angle between \vec{k} and its projection in xz plane, Φ the angle between \vec{k} projection in the xz plane and the x axis. (b) Amplitude modulation as a function of phase shift ϕ for plane wave incident under an angle Y with $\Phi=\pi/2$ (black), and angle Φ with $Y=0$ (red). | 66 |
| Figure 3-13: | Diffraction patterns from two narrow slits at distance a , originating from the central part of the source (solid curve) and from the edge of the source at height $D_s/2$ (dashed curve). D_s denotes the source width, a slit spacing, r and L the distance from source to diffraction screen and from diffraction screen to the detector plane, respectively. The slit distance a is such that the two patterns are in antiphase. This occurs for $a = \lambda r/D_s$, after reference (Veen and Pfeiffer, 2004). | 68 |
| Figure 3-14: | Influence of an extended source on the diffraction pattern of a cell. D_s , and D_c denote the source and collimated beam diameter. | 69 |
| Figure 3-15: | Schematic of spatial filtering. | 71 |
| Figure 3-16: | (a) Calculated reflectivity of metals at perpendicular incidence. (optical constants taken from references (Palik, 1998 and Ordal et al., 1982). (b) Calculated reflectivity of gold for perpendicularly R_{\perp} and parallel R_{\parallel} polarized light for a wavelength of 10 μm . | 74 |
| Figure 3-17: | Calculated thin film reflectivity of gold at perpendicular incidence (optical constants taken from reference (Palik, 1998)). | 77 |

| | | |
|--------------|---|----|
| Figure 3-18: | Reduction of specular reflectivity as a function of mean-square surface roughness after (Bennett and Porteus, 1961), (Bennett and Bennett, 1967), and (Porteus, 1963) for various wavelengths from 0.5 to 10 μm . | 78 |
| Figure 4-1: | Moving mask technique for synchrotron X-ray lithography using two masks and step motion to move one mask with respect to the other. The cumulative dose describes the dose transmitted through the mask system on the photosensitive resist surface (here PMMA). | 89 |
| Figure 4-2: | Moving mask exposure station (MMES) at LiMiNT beamline in SSLs. MMES is comprised of sliding plate, a mask holder plate, micrometer screws, a linear micro-translation stage, and substrate table. Mask 1 (compare Figure) is fixed onto a standard mask holder ring (NIST ring) and mounted onto the mask holder plate (top). Below the mask holder plate (see side view in bottom drawing), a substrate table holds the sample during exposure. The substrate table is fixed onto a linear micro-translation stage allowing its translation with respect to mask 1. The gap between mask 1 and sample surface is adjusted by three micrometer screws. The gap between Mask 1 and resist surface is adjusted to a minimum and is typically within 1 mm. The MMES is fixed via a sliding plate to a holder plate and subsequently to the X-ray scanner table. The sliding plate allows easy mounting and removal from the holder plate. Alignment of masks is done prior to exposure under standard microscopes. | 91 |
| Figure 4-3: | Absorption coefficient as a function of photon energy of mask membrane and absorber materials used for x-ray masks. Data plot produced with XOP 2.11 software (Rio and Dejus, 2006). | 93 |
| Figure 4-4: | Preliminary results of PMMA etching using (a) graphite based mask membrane (scale bar 200 μm) and (b) stencil mask . | 96 |
| Figure 4-5: | Gold stencil mask for X-ray lithography. (a) Schematic of the mask, the gold membrane is held by silicon frame. Gold thickness of the mask is 15 μm . (b) Image of backside of gold stencil mask held by silicon frame. The size of the window is 12 x 12 mm^2 . (c) SEM image of mask (scale bar 100 μm). | 97 |
| Figure 4-6: | (a) Schematic experimental setup to measure the temperature development during X-ray exposure at SSLs LiMiNT facility. One of the two J-type thermocouples (TC1) was attached to the gold absorber layer held by a 500 μm thick Si frame and was shielded from the radiation during the exposure while the second thermocouple (TC2) was attached to the top PMMA surface and was directly exposed to the X-ray beam. (b) Temperature development during exposure as a function of time for five sequential experiments (inset A to E in the figure). For all experiments the same dose is | 98 |

| | | |
|--------------|--|-----|
| | deposited but the vertical scan length is reduced. A: 125-700 s, beam current 225 mA, vertical scan distance ± 45 mm. B: 800-1300 s, beam current 220 mA, vertical scan distance ± 25 mm. C: 1600-1900 s, beam current 210 mA, vertical scan distance ± 15 mm. D: 2000-2250 s, beam current 210 mA, vertical scan distance ± 5 mm. E: 2250-2600 s, beam current 210 mA, vertical scan distance ± 2.5 mm. | |
| Figure 4-7: | Experiment setup for step etching in PMMA. (a) Experiment schematic. Using the MMES, the PMMA sheets are moved step-wise behind a 15 μm thick absorber etch. The exposure dose increment for each step is kept constant. (b) SEM image of steps etched into PMMA. Here: Degussa Plexiglas with a stepping depth of approx 1 μm is shown. The scale bar is 500 μm . | 105 |
| Figure 4-8: | Experimental results for etching of Degussa PMMA sheet at a synchrotron beam current of 195 mA, a development cycle of 30 minutes, and a solution temperature of 30 $^{\circ}\text{C}$. | 106 |
| Figure 4-9: | (a) Influence of dose rate on the development rate R for Degussa PMMA sheets. Samples were exposed at different ring currents whereas exposure and development conditions were kept constant. (b) Average ring currents and dose rates as a function of exposure dose. Average values are given to attribute for the accumulated exposure dose of successive exposures. | 108 |
| Figure 4-10: | Development rate for Degussa and CQ PMMA for GG developer solutions at a temperature of 18 and 30 $^{\circ}\text{C}$. All samples were exposed at an average dose rate of 300 mW/cm^2 and a starting ring current of 315 mA. | 111 |
| Figure 4-11: | Surface roughness of etched CQ and Degussa PMMA micro-mirrors. Both samples were exposed and developed under the same conditions. (a) Surface roughness (root-mean-square-average) as a function of etch depth, and (b) as a function of exposure dose. (c) Surface waviness (root-mean-square-average) as a function of etch depth, and (d) as a function of exposure dose. | 112 |
| Figure 4-12: | Surface structure of etched Degussa PMMA at an etch depth of 72.3 μm via Atomic Force Microscope (AFM) measurement. | 113 |
| Figure 4-13: | (a) SEM image of 3 x 3 3D MMA cells. Scale bar is 500 μm . In the sequence from 1 to 9 each cell is deeper than its predecessor. (b) Profiler measurement of cells 4-9 as shown in (a). Cell depths vary by 4 μm in vertical direction (4-5-6, 7-8-9) while, in horizontal direction (4-7, 5-8, 6-9) by 40 μm . From this data plot micro-mirror inclination angles were computed parallel (vertical direction in b) and perpendicular (horizontal direction in b) to the long side of the rectangular micro-mirrors. | 114 |

| | | |
|--------------|--|-----|
| Figure 4-14: | (a) Mirror inclination of etched micro-mirrors as a function of etch depth when referenced to the top mirror surface (red hatched surfaces in Figure (b)). \parallel and \perp denote the inclination angle parallel and perpendicular to the grating grooves, respectively. (b) Corresponding average surface waviness as a function of etch depth. | 115 |
| Figure 4-15: | (a) Etch depth 'h' (in CQ PMMA) as a function of MMA cell number 'N' (black dotted) for a linear increment of exposure dose (inset). The red, horizontal drop lines indicate the etch depth of each cell. The variation of the density of these lines highlights the non-uniform etch depth difference as a function of MMA cell. (b) Corresponding etch depth difference ' Δh ' ($\Delta h = h_N - h_{N-1}$) as a function of MMA cell number 'N' and exposure dose. | 117 |
| Figure 4-16: | Influence of resist contrast on structure fidelity. (a, b) Reference structure and its measured structure width of the Au absorber structure. (c, d) S-test-structure etched $29.9 \pm 0.1 \mu\text{m}$ into CQ PMMA (high molecular weight). (e, f) S-test-structure etched $30.1 \pm 0.1 \mu\text{m}$ into Degussa PMMA (low molecular weight). | 119 |
| Figure 4-17: | Reflectivity of sputtered Cr and Au reflection layers for various thicknesses on PMMA basis (2 mm thick Degussa PMMA sheets). | 121 |
| Figure 4-18: | Reflectivity curve measured by high resolution x-ray specular reflectometry at grazing incidence angle versus angle 2θ and its simulated curve fit for a 2mm PMMA sheet coated with $31 \pm 1 \text{ nm}$ Cr and $8.5 \pm 0.4 \text{ nm}$ Au reflection layer. | 122 |
| Figure 5-1: | Top view IFS 125 HR in standard operation mode A. Definitions: A: Sources, B: Spherical mirror, D: Input apertures (field stop), E: Collimating parabolic mirror, F ₁₋₄ : Folding mirrors, G: Beam splitter, H: Scanner with movable corner-cube mirror, I: Fixed corner-cube mirror, J: Focusing parabolic mirror, K: Toroidal mirror, L: Collimating parabolic mirror, M: Focusing parabolic mirror, N: Detector position (MCT), X: Sample position for transmission measurements. | 127 |
| Figure 5-2: | Top view IFS 125 HR spectrometer in operation mode B: Definitions: A: Sources, B: Spherical mirror, D: Input apertures (field stop), E: Collimating parabolic mirror, F ₁₋₅ : Folding mirrors, J: Focusing parabolic mirror, K: Toroidal mirror, L: Collimating parabolic mirror, M: Focusing parabolic mirror, R: MMA / plane mirror, S: Circular/ rectangular aperture, T: Collimating parabolic mirror, U: Germanium lens system, V: Micro-bolometer array detector, X: Sample position for transmission measurements. | 129 |

| | | |
|--------------|--|-----|
| Figure 5-3: | Image of the detector compartment of IFS 125 interferometer in optical setup B for the spectrometric validation of the FPP FTIR working principle. F ₅ : Folding mirror, L: Collimating parabolic mirror, M: Focusing parabolic mirror, R: MMA / plane mirror, S: Circular/ rectangular aperture, T: Collimating parabolic mirror, U: Germanium lens system, V: Micro-bolometer array detector. | 129 |
| Figure 5-4: | Intensity modulation of a single MMA cell at an incidence angle of 46 degrees with respect to the grating normal as a function of wavenumber for two detector aperture openings. The MMA cell (Design A) examined has a grating depth of 8.2 μm and a period of 200 μm. The inset shows the infrared images (in the spectral range of 625 – 1350 cm ⁻¹) of the two cases, aperture accepting zero and higher order diffracted light (top, right) for an aperture diameter of Ø = 5.2 mm and aperture accepting zero diffraction order (in the spectral range of 625 – 1350 cm ⁻¹) only (bottom, right) corresponding to an aperture diameter of Ø = 1.0mm. | 131 |
| Figure 5-5: | Data processing flowchart to acquire spectra | 135 |
| Figure 5-6: | Intensity distribution and spatial interference function after reflection from the MMA (placed at position R in Fig. 5-2). The white boxes indicate the imaging area of the individual MMA cells. Here each MMA cell is imaged onto 4 x 3 pixels | 136 |
| Figure 5-7: | Intensity readout for a single infrared image taken with the detector. | 137 |
| Figure 5-8: | Interference function and resulting Interferogram after digital band-pass filtering. | 138 |
| Figure 5-9: | Comparison of source spectra recorded with the Bruker HR 125 spectrometer (red line) at a resolution of 4 cm ⁻¹ and the FPP FTS (black lines) at resolutions of 100 and 26 cm ⁻¹ . The narrower spectral band-pass shown by the FPP FTS is due to the fact that in the current experimental set-up, the useful spectral range of the FPP FT spectrometer is limited at low frequency at 600 cm ⁻¹ by the transmission characteristics of the Germanium lens and at high frequency (1400 cm ⁻¹) by the filter characteristics of the microbolometer detector window. All spectra were taken with triangular apodization. | 139 |
| Figure 5-10: | Reference transmission spectra of two narrow band-pass filters (BP10 and BP8) taken with the Bruker IFS 66 FTIR at a resolution of 4 and 26 cm ⁻¹ , respectively. The peak positions at a resolution of 4 cm ⁻¹ / 26 cm ⁻¹ were found at 958 cm ⁻¹ / 958 cm ⁻¹ , and at 1245 cm ⁻¹ / 1248 cm ⁻¹ for the BP10 and the BP8 transmission filter, respectively. | 140 |
| Figure 5-11: | Comparison of normalized band pass filter (BP10 and BP8) spectra taken with IFS 66 at 4 cm ⁻¹ (dashed) and 26 cm ⁻¹ resolution and FPP FTS (solid) for two narrow band pass filters centered at 958 cm ⁻¹ (red curves) and 1046 cm ⁻¹ (blue curves) after frequency calibration procedure. | 141 |

| | | |
|--------------|---|-----|
| Figure 5-12: | Intensity distribution of IFS 125 HR globar source obtained with plain mirror at the position of the MMA. The white boxes indicate the imaging area of the individual MMA cells. Here each MMA cell is imaged onto 4 x 3 pixels. | 142 |
| Figure 5-13: | Interference function and source compensation | 143 |
| Figure 5-14: | Power spectra taken with the FPP FTIR prototype. Curves are shifted with respect to each other for better viewing. $B(\sigma)_{10}$ (dashed red line), $B(\sigma)_1$ (solid blue line), and $B(\sigma)_{1/210}$ (solid black line) denote the power spectra arising from the source non-uniformity only, the uncompensated, and the compensated source spectra taken with the MMA, respectively. | 144 |
| Figure 5-15: | Power and transmission spectra of compensated (black) and uncompensated (blue) source uniformity taken with the FPP FTIR in comparison to the reference spectra (red) taken with the Bruker IFS spectrometers at a resolution of 26 cm^{-1} . Transmission spectra of BP8 and BP10 were normalized to the reference spectra for better comparison. | 146 |
| Figure 5-16: | (a) Grey level intensity output of 384 x 288 pixel infrared camera (Thermoteknix Miricle 100K) at $24.1 \pm 0.1 \text{ }^\circ\text{C}$ and (b) its standard deviation for 100 consecutive images | 149 |
| Figure 5-17: | (a) Intensity of 54 x 40 pixel in the center of the array for a constant temperature of $24.1 \pm 0.1 \text{ }^\circ\text{C}$ (top) and pixel dark current (bottom). (b) Standard deviation as a function of detected intensity as measured from the dark current (7160 grey levels), the $24.1 \pm 0.1 \text{ }^\circ\text{C}$ background (7893 grey levels), and the globar source at various entrance aperture settings (> 8100 grey levels). | 149 |
| Figure 5-18: | Mean background radiation of the instrument (a) and the standard deviation (b) of 100 consecutive measurements as a function of pixel number in the center of the detector array. | 150 |
| Figure 5-19: | Interference function of the background as a function of cell position (a) and its resulting power spectrum (b). | 151 |
| Figure 5-20: | Mean source radiation of the globar at a 2 mm entrance aperture (a), and the standard deviation (b) of 250 consecutive measurements as a function of pixel number in the center of the array detector. | 152 |
| Figure 5-21: | (a) Power spectra of globar source for various apodization functions, and the corresponding spectral signal-to-noise-ratio (SNR) as computed from the standard deviation of 500 spectra (b). Both figures use the same color coding. | 154 |
| Figure 5-22: | (a) Signal-to-noise-ratios (SNR) as a function of added spectra and apodization function. The apodization functions and their color coding in sequence from lowest to highest SNR performance are: Rectangular (green), cosine (magenta), Happ-Genzel (blue), cosine square (cyan), triangular (black), and Gauss (red). (b) Normalized transmission spectra of narrow band pass filter (BP10) for rectangular (green), and triangular (black) apodization function in comparison to reference spectra (red) taken with | 155 |

| | | |
|--------------|--|-----|
| | the IFS66 spectrometer. All spectra are shifted with respect to each other for better viewing. | |
| Figure 5-23: | Influence of pixel binning on Signal-to-noise-ratio (SNR) for triangular apodization. (a) SNR for triangular apodization as function of added spectra and number of pixel utilized for pixel binning. (b) Factorial increase of SNR for pixel binning of 4 and 12 pixels per cell. | 158 |
| Figure 5-24: | (a) Spectra of pulsed global source taken with the FPP FTS at a nominal resolution of 100 cm^{-1} . Pulse length and standard deviation (bracketed) are shown alongside the graph. (b) Normalized integral energy as a function of pulse length. | 160 |
| Figure 5-25: | (a) Close-up on pulsed global spectra taken with the FPP FTIR at a nominal resolution of 100 cm^{-1} . (b) Signal-to-noise-ratio (SNR) as a function of pulse length and number of pixels for pixel binning. | 161 |
| Figure 5-26: | (a) In-situ spectra of global source heating taken at a resolution of 100 cm^{-1} . (b) Chronologic development of spectral power, SNR and global's temperature, respectively. | 162 |
| Figure 5-27: | (a) In-situ spectra of first 30 seconds of global heating taken at a time and spectral resolution of 2.4 s and 100 cm^{-1} , respectively. (b) Chronologic increase in spectral power in terms of % maximum power at 920 and 1260 cm^{-1} . | 163 |
| Figure A3-1: | Simulation schematic for rectangular cell design of an even number of mirror surfaces. The mirror width of the front facets is denoted by w_F , the width of the back facets by w_B , the length by l , the distance between front and back facet by c , and the phase step due to the height difference h between front and back facet mirrors is ϕ . | 188 |
| Figure A4-1: | (a) Definition of grating cell orientation. The cell depth is h , lamellar width w and grating cell length l . Inset of (b): Denomination of angles: \vec{k} is the plane wave normal, Y the angle between \vec{k} and its projection in xz plane, Φ the angle between \vec{k} projection in the xz plane and the x axis. (b) Schematic (yz plane) indicating detector plane tilt β . h denotes the cell depth, DP the detector plane, Y , FF, and BF, the angle of incidence, the front and back facet reflecting surfaces, respectively. | 191 |
| Figure A5-1: | LiMiNT beamline at SSSL (Wilhelmi, 2004). | 194 |
| Figure A5-2: | LiMiNT beamline at SSSL. Radiation emitted from the storage ring is collimated by an aperture. Two Beryllium windows (BeW1 and BeW2) divide the beamline into three vacuum sections. The size of the second aperture at the first Beryllium window determines the acceptance angle of horizontal radiation of 10 mrad. | 194 |
| Figure A5-3: | Spectral power distribution of the LiMiNT beamline for a Helios 2 current of 500 mA. Simulation was performed with XOP 2.11 software (Rio and Apte, 2006). | 196 |

-
- Figure A8-1: View of IFS 125 HR FTIR as installed at ISMI beamline of SSLS. Definitions: A: ISMI beamline pipes, B: Input port for IR produced by Helios 2, C: Source compartment, D: Interferometer compartment, E: Scanner compartment, F: Sub-chambers for beam switching and sample compartment, G: Gas cell, H: Detector compartment. 205
- Figure A8-2: IFS 125 HR in standard operation mode A. Definitions: A: Sources, B: Spherical mirror, C: ISMI beamline input port, D: Input apertures (field stop), E: Collimating parabolic mirror, F₁₋₄: Folding mirrors, G: Beam splitter, H: Scanner with movable retroreflecting mirror, I: Fixed retroreflecting mirror, J: Focusing parabolic mirror, K: Toroidal mirror, L: Collimating parabolic mirror, M: Focusing parabolic mirror, N: Detector position (MCT), O: Focusing parabolic mirror, P: Detector position (Bolometer). 207
- Figure A8-3: Normalized spectrum of globar source as taken with IFS 125 HR FTIR at a resolution of 4 cm⁻¹. The spectrum was recorded in ambient atmosphere with KBr beam splitter and MCT detector. 208

1 INTRODUCTION

1.1 Background of the project

Since the development of the first interferometer by Michelson in 1880, spectral analysis has evolved to an established technique to measure electromagnetic emission or absorption radiation. The infrared portion of the electromagnetic spectrum is thereby of particular interest. Absorption or emission radiation of molecular oscillations and bending vibrations in the fingerprint region enables qualitative and quantitative substance identification. Spectrally, the fingerprint region corresponds to the infrared radiation band from 7-20 μm wavelength.

Beyond the scope of qualitative and quantitative analysis, the study of chemical and physical reactions while they occur opens another dimension in the understanding of the progression of reactions. Depending on the nature of these reactions, the time-scale varies from split seconds to days. Transient chemical and physical processes such as explosions or plasmas occur in the sub-100 ms time frame (Smith, 2002). Such phenomena require time-resolved spectral measurement techniques capable of detecting absorption and emission radiation at a speed one order of magnitude faster as the event itself.

Over the past years various approaches to resolve time-dependent spectra have been developed. Among these, laser based approaches possess the highest time resolution but are limited to a narrow spectral bands. With the fast development of infrared (IR) focal plane array (FPA) detectors, various new approaches of time-resolved spectroscopy have become feasible, such as the so-called spectrographs. These spectrographs remove the exit slit of dispersive spectrometers and record the dispersed IR radiation using an IR FPA detector. Contrary to these spectrographs

which make use of the dispersion of the radiation into its spectral components, Fourier transform (FT) spectrometers make use of the amplitude modulation of interfering radiation beams. Fourier transform spectrometers thereby feature specific advantages over dispersive devices which persist in time-resolved spectroscopy. These advantages known as the Fellgett, Jacquinot, and Connes advantage allow Fourier transform spectrometers to record spectra of weak radiation sources at a higher signal-to-noise ratio compared to dispersive spectrometers. Even today, most FT spectrometers follow the basic concept of the Michelson interferometer. In order to detect at ever higher rates, time-resolved FT approaches mainly focused on the steady increment of the detection speed by improving the scanning speed of the movable mirror device. Such advancements of Michelson interferometer include rapid scanning techniques, ultra rapid scanning techniques as well as step scanning techniques. Although these are established techniques to record reactions of repeatable phenomena at a time scale below micro-seconds, these techniques do not allow the study of transient phenomena. Moreover, the use of scanning mirrors to obtain spectral data requires highly accurate and precise mirror control, which makes these devices expensive and prone to vibration, and restricts their use to stable and controlled environments.

To avoid such difficulties, stationary FT interferometers do not utilize scanning mirrors. Similar to the approach of the spectrograph, such stationary FT spectrometers record the spectrum in space and not in the time domain by using an array detector instead of a single detector element. These stationary spectrometers are characterized by their compactness, simplicity and sturdy setup.

However, these devices use an amplitude-beam-splitter to separate the incident radiation at a semitransparent plate into at least two coherent beams. As a

consequence, these spectrometers are limited by the transmission or rather the spectral absorption characteristics of the amplitude-beam-splitter and the recording of spectra beyond the absorption band of the beam-splitter requires the exchange of the beam-splitter. Moreover, amplitude-beam-splitters inherently reflect 50% of the source radiation back to the source without making use of it.

On the contrary, FT interferometers following the wave-front-dividing-principle such as the lamellar grating interferometer invented by Strong and Vanasse in 1960 (Strong and Vanasse, 1960) offer the distinct advantage to work more efficiently over a broad spectral band. Thus, the combination of a static device with the wave-front-dividing principle as proposed by Moser and Moeller (Moser and Moeller, 1994) offers the opportunity to disrupt current technology. The device is dubbed the ‘Fast-Parallel-Processing-Fourier-transform Spectrometer’ or FPP-FTS. Using micro-fabrication technologies to fabricate the core-body of the spectrometer, this new type spectrometer can be fabricated at comparably small dimensions, while its static layout makes it sturdy and enables the study of transient phenomena over a broad spectral range.

1.2 Motivation and objectives (scope of work)

The aims of this study were to develop, build, and prove the concept of the Fast-Parallel-Processing Fourier-transform spectrometer (FPP FTS) as proposed by Moser and Moeller (Moser and Moeller 1994). The stationary lamellar grating interferometer should enable the spectral analysis of infrared absorption or emission radiation, specifically the analysis of the fingerprint region of molecules in which the known advantages of FT spectroscopy fully exert. Moreover, the capability of the device to disrupt current technology in terms of its capability to detect the spectral information of a single pulse of electromagnetic radiation, moreover its capability to resolve spectral data in-situ shall be demonstrated.

The study thereby focused on three major aspects:

1) System development:

Based on fundamental theories of optics and FT spectroscopy, principle design parameters of the FPP FTS are developed and evaluated. An optical prototype system, consisting of an illumination source, a micro-mirror-array (MMA) as the core of stationary lamellar grating, an infrared array detector, collimating, focusing, and spatial filtering optics is proposed.

2) Manufacturing:

On the basis of the design parameters, this section comprises a review of micro fabrication techniques capable to fabricate prototype MMAs. The investigation includes techniques such as micro machining based on silicon technology, laser ablation techniques, precision engineering techniques, as well as lithographical processes. On the background of this investigation, a novel process to manufacture monolithic MMAs via 3D X-ray lithography is developed and a prototype MMA is manufactured. In this core discipline, the study does not claim

to have investigated all possible manufacturing techniques. The proposed manufacturing process allows highly precise 3D structuring and in combination with other micro-fabrication and precision engineering techniques it may be further extended to enable 3D manufacturing from the sub-micron to millimeter-scale.

3) Validation:

The final part of the study concentrated on the experimental validation of the FPP FTS principle. This included the interferometric and spectral analysis of a prototype spectrometer for continuous and pulsed input radiation as well as a validation of its capability to resolve spectra in-situ. The performance of the prototype in terms of resolution and signal-to-noise ratio is studied experimentally and methods to improve both are discussed.

The FPP FTS may be particularly useful to measure time resolved spectra of transient emission sources such as explosions, flames, electrical discharges, plasma processes, and lightning. Moreover, it may find applications in spectroscopic scanning of chemicals, flowing toxic or flammable gases, and the like. Such processes are of high significance in monitoring and diagnosing internal combustion, jet engines, fires, environmental pollution, waste treatment, toxic gas hazards, chemical reactions, explosives safety and security, warfare, civil defence, and homeland security. The sturdy and compact design of the interferometer through the absence of moving parts may be of particular interest for satellite or missile applications and may enable its implementation in harsh environments such as space, while its reflection optics replacing the commonly used transmission optics allows efficient wave splitting in a wide spectral working band.

1.3 Outline and organization of the thesis

The thesis is split into three main parts following the aims of the work presented earlier. After an introduction of the fundamental theories of FT spectroscopy (Chapter 2), the first of the three (Chapter 3) reviews state-of-the-art miniature spectrometers and introduces the FPP FTS principle in detail. Furthermore, design parameters of the MMA forming the core of the spectrometer, and the optical layout are elaborated.

The second main part of the thesis (Chapter 4) is dedicated solely to the fabrication of the MMA. The chapter first reviews 3D micro-fabrication methods and presents the development of a novel 3D micro-fabrication technology via X-ray lithography. In the process, 3D micro structures are produced by independently moving at least two X-mask during exposure thereby creating a multitude of dose grey levels which, when developed, form 3D micro-structures required for the MMA.

Chapter 5 presents the third main body of the thesis. It focuses on the spectral characterization of the FPP FTS prototype. Experimental setups and the retrieval of the spectral data from the raw detected signal are presented. Spectra of a number of transmission filters were measured and compared to transmission spectra taken with the Bruker IFS spectrometers. Calibrations procedures for the FPP FTS are developed and the capability of the device to measure the spectra of a single pulse of light are shown. The capability of the spectrometer to resolve spectra in-situ is shown for the heating of the globar source.

Finally, Chapter 6 summarizes the main findings and concludes the thesis.

2 THEORY OF FOURIER TRANSFORM SPECTROSCOPY

2.1 Introduction

The aim of chapter 2 is to provide an overview of the theoretical background applied in this work in particular, the most prominent theories in Fourier transform spectroscopy (FTS). The basic Fourier transformation integrals are introduced and the computation of the spectrum from the recorded interferogram in FTS is shown. Characteristic properties of FTS are discussed. Most of the material is stated without proof as it is part of the open literature and would exceed the scope of the work. All presented theoretical concepts related to optics, Fourier transform spectroscopy and diffraction theories heavily rely on references (Bell, 1972, Saptari, 2004, Hecht, 2002, Goodman, 1996, Born, 1997, Strong 1958, and Chamberlain, 1979).

2.1.1 Electromagnetic radiation

Based on Maxwell's theory of electromagnetism (Maxwell, 1865) and Hertz' experimental demonstration (Hertz, 1887), light is described as a transverse electromagnetic wave formed by an electric field \vec{E} and a magnetic field \vec{H} that oscillate perpendicularly to each other and to its direction of propagation (Figure 2-1). Electromagnetic waves combine and form wave packets transporting momentum and energy and its direction is denoted by the Poynting vector \vec{S} . Schematically, in a right handed system formed by the perpendicularly oriented vectors of the electric field \vec{E} , the magnetic field \vec{H} , and the wave vector \vec{k} , the Poynting vector points in the direction of the flux of energy and is given by the cross product of the electric and magnetic field vectors $\vec{S} = \vec{E} \times \vec{H}$. The spatial period of a wave is referred to as

wavelength λ (observed as spatial oscillation period at a given time) or its inverse, the wavenumber σ . The temporal period τ is the time a wave of length λ takes to pass a stationary object (observed as temporal oscillation period at a given location). Commonly, the terms temporal frequency ν , or angular temporal frequency $\omega=2\pi\nu$ are used instead.

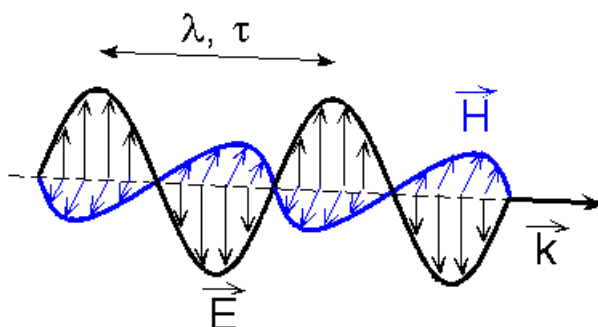


Figure 2-1: Transverse electromagnetic wave. \vec{E} depicts the electric and \vec{H} the magnetic wave vector, λ , τ , and \vec{k} represent the wavelength, the temporal period, and the wave vector, respectively.

The spectrum of electromagnetic radiation extends from gamma rays with wavelengths in the range of 10^{-13} meters to radio waves with hundreds of meters wavelengths.

2.1.2 Measuring light

In the infrared and visible spectral range, radiation is commonly analyzed by absorbing its flux of energy, either by generating a temperature increase as in the case of far infrared radiation or by generating electric charges which are measured as a current. From the absorbed flux under known conditions, one can infer the fields involved.

Strong describes the flux or flow of energy of electromagnetic radiation as the time average value of the Poynting vector (Strong, 1958, pp 47-48):

$$B = (\vec{E} \times \vec{H})_{avg} \quad (2-1)$$

In an isotropic medium of refractive index n and with the dielectric permittivity ϵ_0 of free space Eq. (2-1) becomes:

$$B = \frac{1}{2} c \epsilon_0 n E^2 \quad (2-2)$$

whereby c denominates the vacuum velocity of light and E the magnitude of the electric field vector. Thus, the flux of energy is proportional to the square of the electric field vector E . In units Eq. (2-2) describes the electromagnetic flux per area in units of Watt/m². It is referred to as *irradiance*, *flux density* or *illumination*. One refers to *intensity* as the flux per solid angle in units of Watt/steradian.

2.2 Theory of Fourier transform spectroscopy

In Fourier transform spectroscopy (FTS), the spectrum of a source is obtained via the measurement of the electromagnetic flux of interfering beams as the optical path difference between the beams is varied. The device to produce and to record the flux of the interfering beams is called an interferometer. In an interferometer, electromagnetic radiation from a source is collimated and is divided into at least two coherent beams by a beam splitter. The divided beams travel optical paths of different lengths and recombine on their way towards the detector, whereby the interferometer records the forming radiation flux with respect to the optical path difference introduced.

Commonly these interferometers are classified into amplitude splitting and wavefront splitting interferometers. Contrary to amplitude splitting interferometers dividing the magnitude of the amplitude of the electromagnetic wave into two equal halves by a semitransparent plate, wavefront splitting interferometers split electromagnetic wave into small wave fronts without altering its amplitude (Figure 2-2). Representatives of both types are the Michelson and Lamellar Grating Interferometer. Although both interferometers showed their potential in a number of applications only the Michelson interferometer found its application beyond the research laboratories - a fact which bases mainly on the easier manufacturing of the interferometer. Nevertheless, the relations stated below work for wave front dividing as well for amplitude splitting interferometers.

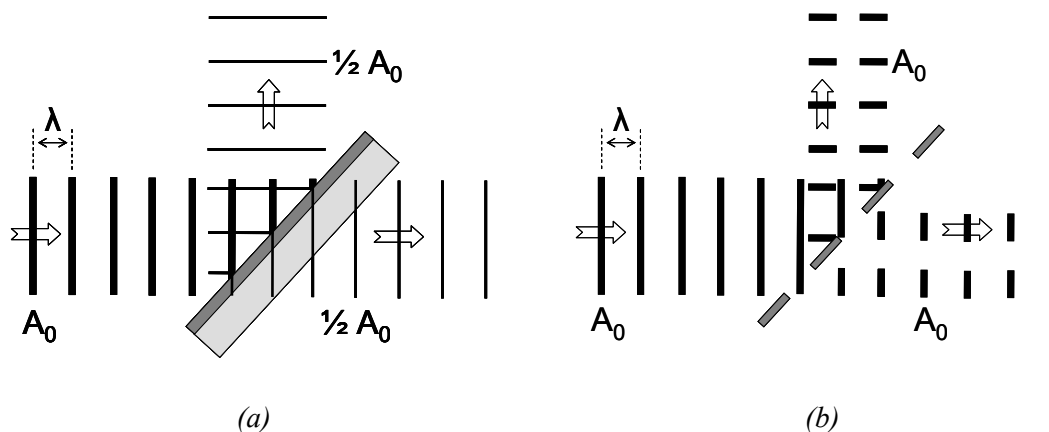


Figure 2-2: Simplified wave dividing principles: Plane waves of wavelength λ and amplitude A_0 (its magnitude is illustrated by the width of the lines) impinge on the beam splitter and are split into two beams by (a) an amplitude splitter, and (b) by a wavefront splitter.

2.2.1 Advantages of Fourier transform spectroscopy

When Fourier transform spectrometers (FTS) are compared with spectrometers that use dispersive or diffracting elements such as prism or grating spectrometers, the FTS offer two main advantages in particular in the infrared part of the electromagnetic spectrum. These advantages are known as the Fellgett and Jacquinot advantage. Both base on the ability of the FTS to obtain higher signal powers.

The Jacquinot advantage thereby claims that for two spectrometers of the same resolving power (see 2.2.5.3), the FTS can accept sources at a larger field of view (see 2.2.7) compared to the grating spectrometers, thus resulting in a so-called ‘throughput’ or ‘étendue’ advantage of the FTS (Bell, 1972, p. 21).

The second advantage, the so-called Fellgett advantage states that for the same resolving power and the same integration time for the three types of spectrometers, the FTS posses a multiplex advantage, which, similar to the Jacquinot advantage, results in a higher signal-to-noise-ratio (SNR) compared to the dispersive or diffracting spectrometers. This multiplex advantage thereby bases on the fact the FTS registers the integral intensities of all spectral elements M at every time instance an

interferogram data point is taken while the dispersive or the diffracting spectrometer integrates the spectral elements sequentially. If the noise is random and independent of the signal strength, this leads to an improvement of the SNR of FTS over dispersing or diffracting spectrometers by a factor of \sqrt{M} (Bell, 1972, p. 24).

A third, commonly mentioned advantage is the so-called Connes-advantage (Connes, 1966) which states, that by using a laser beam as an internal reference signal when recording the interferogram data, the FTS obtains a higher peak position accuracy compared to the scanning accuracy of the dispersive spectrometer.

All of these advantages have led to the supremacy of FTS over dispersive and diffracting spectrometers in particular in the infrared part of the electromagnetic spectrum in which the radiation power is low and the noise is additive (see 2.2.8).

2.2.2 Interferogram and spectrum

When a beam of radiation emitted from a source of spectral band ($\sigma \geq 0$) is divided into two coherent beams by a beam splitter, and each travelling a distance of z and $z+\delta$, respectively, recombine again, the resulting electric field is given by:

$$E_R(z, \delta) = \int_0^{\infty} T_1(\sigma) E(\sigma) e^{i(2\pi\sigma z - \omega t)} d\sigma + \int_0^{\infty} T_2(\sigma) E(\sigma) e^{i(2\pi\sigma(z+\delta) - \omega t)} d\sigma \quad (2-3)$$

$$E_R(z, \delta) = e^{-i\omega t} \int_0^{\infty} E(\sigma) e^{i(2\pi\sigma z)} (T_1(\sigma) + T_2(\sigma) e^{i2\pi\sigma\delta}) d\sigma \quad (2-4)$$

whereby $T_1(\sigma)$ and $T_2(\sigma)$ describes the wavenumber-dependent transmission characteristics for of each of the beams, i.e., T is a scalar function between zero and one describing the ratio of transmitted and incident flux. As explained in 2.1.2, the flux density of the radiation measured with an interferometer in vacuum is given by:

$$I(z, \delta) = \frac{1}{2} c \varepsilon_0 E_R(z, \delta) E_R^*(z, \delta)$$

Using

$$\left(\int f(x) dx \right)^* = \int f(x)^* dx$$

where * denotes the complex conjugate, it follows that the dependence of the travelled distance z on the resulting flux density denoted by $I(z, \delta)$ drops (Eq. (2-5)).

$$I(z, \delta) = \frac{1}{2} c \varepsilon_0 \int_0^{\infty} \left[(T_1(\sigma)^2 + T_2(\sigma)^2) E(\sigma)^2 + T_1(\sigma) T_2(\sigma) E(\sigma)^2 (e^{i2\pi\sigma\delta} + e^{-i2\pi\sigma\delta}) \right] d\sigma \quad (2-5)$$

We therefore rewrite the flux density only as a function of path difference δ according to:

$$I(\delta) = \frac{1}{2} c \varepsilon_0 \int_0^{\infty} \left[(T_1(\sigma)^2 + T_2(\sigma)^2) E(\sigma)^2 + T_1(\sigma) T_2(\sigma) E(\sigma)^2 2 \cos(2\pi\sigma\delta) \right] d\sigma \quad (2-6)$$

where we made use of the trigonometric conversion of the exponential function in Eq. (2-5). The flux density is made up of a constant and a modulated part of which the modulation frequency depends on the *optical path difference* δ , the *wavenumber* σ and their amplitudes, and last but not least on the transmission characteristics of the superimposed beams. Eq. (2-6) is called the *interference function*, its modulated part is called the *interferogram* $f(\delta)$.

In a perfectly working interferometer, $T_1(\sigma)$ and $T_2(\sigma)$ are equal for both split beams, and independent of the wavenumber. Thus, $T_x(\sigma)$ reduces to T . Such interferometers produce symmetric interferograms whereby the axis of symmetry is the zero optical path difference ($\delta=0$). Upon separation of modulated signal from un-modulated signal Eq. (2-6) yields:

$$f(\delta) = \frac{1}{T^2} \left(I(\delta) - \frac{1}{2} I(0) \right) = 2 \int_0^{\infty} [B(\sigma) \cos(2\pi\sigma\delta)] d\sigma \quad (2-7)$$

where $I(0)$ expresses the contributions of the un-modulated part of the interference function at zero optical path difference. Eq. (2-7) describes the cosine transform relationship between the interferogram and the spectrum $B(\sigma)$. The spectrum, as the quantity in demand is obtained via the inverse transforms:

$$B(\sigma) = 2 \int_0^{\infty} f(\delta) \cos(2\pi\sigma\delta) d\delta \quad (2-8)$$

Figure 2-3 shows the procedure to obtain the spectrum schematically.

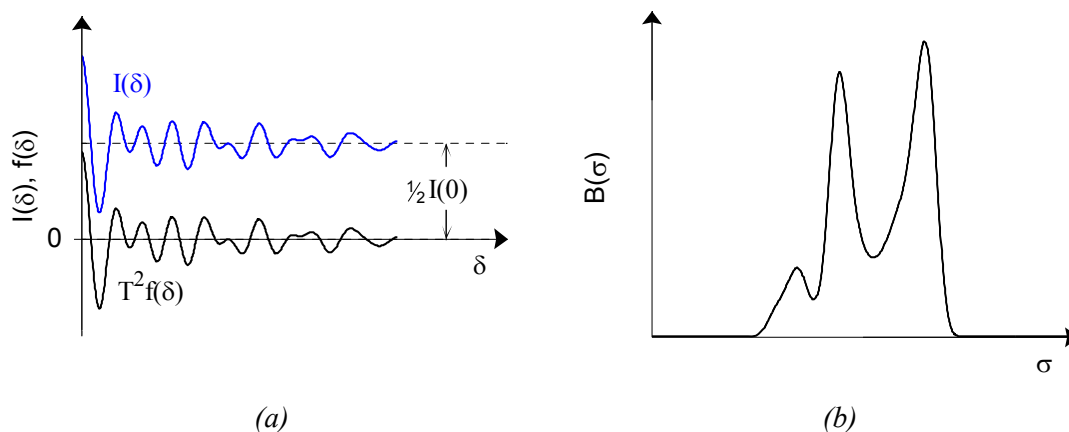


Figure 2-3: Schematic illustration of the interference function $I(\delta)$ as recorded by the detector, the interferogram $f(\delta)$, both as a function of optical path difference δ (a), and (b) the acquired spectrum $B(\sigma)$ as a function of wavenumber σ .

2.2.3 Symmetric and asymmetric interferograms

In symmetric interferometry, all waves of wavenumber σ are superimposed constructively at zero optical path difference ($\delta=0$), meaning reflection and transmission coefficients $T(\sigma)$ are the same for all waves travelling through the interferometer. The interferogram is symmetric to the intensity axis at zero optical path difference ($\delta=0$). In the particular case, it is sufficient to record the interferogram

only for positive optical path differences and to recover the spectrum via its cosine Fourier transforms.

On the other hand, asymmetric interferograms are not symmetric to the zero optical path difference and practically most interferometers do not produce perfectly symmetric interferograms. Asymmetries in the interferogram acquisition may arise because of:

- The split beams of the interferometer traverse through media of different transmission/reflection characteristics,
- misalignment of the interferometer, or
- the actual zero optical path difference point is not recorded.

For single side recorded interferograms ($\delta > 0$), asymmetry in the interferogram introduces a wavenumber-dependent phase error in the observed interferogram (Chamberlain, 1979, p. 163). These phase error may be corrected following Gibbs treatment (Gibbs, 1965) for symmetrical but displaced interferograms or via a general treatment by Forman et al. (Forman, 1966). Alternatively, the phase error may be corrected by recording two-sided interferograms and using the complex Fourier transform (Chamberlain, 1979, p. 175).

Moreover, asymmetric interferometry is a technique that is deliberately used to measure transmission characteristics, refractive indices, and extinction coefficients (Bell, 1972, Chamberlain, 1979).

2.2.4 The complex Fourier transform

The customary formulas of the complex Fourier transformation are:

$$B(\sigma) = \int_{-\infty}^{\infty} f(\delta) e^{-i2\pi\delta\sigma} d\delta \quad (2-9)$$

$$f(\delta) = \int_{-\infty}^{\infty} B(\sigma) e^{i2\pi\delta\sigma} d\sigma \quad (2-10)$$

For a given $B(\sigma)$, $f(\delta)$ is uniquely determined given the following conditions for validity of the Fourier transforms fulfilled (Bell, 1972):

- $B(\sigma)$ is everywhere finite; discontinuities are finite in size and number.
- The derivatives of $B(\sigma)$ and $f(\delta)$ must exist except at a finite number of points, and then, the left and right derivatives must exist.
- $\int_{-\infty}^{\infty} |B(\sigma)| d\sigma < \infty$, $B(\sigma)$ is absolutely integrable.

The use of complex Fourier transform on a recorded interferogram yields a complex term $\hat{B}(\sigma)$, its modulus is the spectrum $B(\sigma)$.

$$\int_{-\infty}^{\infty} f(\delta) e^{-2\pi\delta\sigma} d\delta = \hat{B}(\sigma) \quad (2-11)$$

$$\hat{B}(\sigma) = B(\sigma) e^{i\phi(\sigma)} = \text{Re}\left\{\hat{B}(\sigma)\right\} - i \text{Im}\left\{\hat{B}(\sigma)\right\} \quad (2-12)$$

$$B(\sigma) = \sqrt{\left(\text{Re}\left\{\hat{B}(\sigma)\right\}\right)^2 + \left(\text{Im}\left\{\hat{B}(\sigma)\right\}\right)^2} \quad (2-13)$$

$\phi(\sigma)$ is the phase angle for each of the frequency components of $B(\sigma)$. It is computed by:

$$\phi(\sigma) = \tan^{-1} \left(\frac{\text{Im}\{\hat{B}(\sigma)\}}{\text{Re}\{\hat{B}(\sigma)\}} \right) \quad (2-14)$$

Physically, the interferogram is the superposition of cosinusoidal waves, each corresponding to a particular wavenumber. The complex phase component describes the phase delay of each wavenumber component.

For symmetric interferometers, all cosinusoidal waves add constructively at $\delta = 0$ and the phase delay $\phi(\sigma) = 0$. For this particular case the interferogram is symmetric. Its complex and cosine Fourier transform yield the same result (Appendix 1).

Thus, the phase delay $\phi(\sigma)$ can be interpreted as an indicator for the symmetry or asymmetry of the recorded interferogram. The complex Fourier transform provides a tool to quantify the phase delay. It has to be noted, however, that for the retrieval of the spectrum via complex FT positive and negative interferogram data (two sided interferograms) must be recorded.

Throughout the thesis, the mathematical operations stated in Eq. (2-9) and (2-10) are referred to as inverse Fourier transformation denoted by $FT^{-1}\{\}$ and Fourier transformation denoted by $FT\{\}$, respectively.

2.2.5 Instrumental line shape function, apodization, and resolution

2.2.5.1 Truncation and instrumental line shape function

The basic Fourier transform integrals, Eq. (2-9) and Eq. (2-10) have infinite limits for the optical path difference. However, working interferometers cannot obtain infinite interferograms and place a physical limitation to the maximum obtainable optical path difference δ_{\max} . The effect of cutting the interferogram to a finite extent is known as *truncation*.

If the infinite limits of the integral in Eq. (2-9) are substituted by either extending from $-\delta_{\max}$ to $+\delta_{\max}$ for a double-sided interferogram, or from 0 to δ_{\max} for a single-sided interferogram, the retrieval of the spectrum of a monochromatic line σ_0 via complex Fourier transform effectively yields a spectrum according to (Appendix 2):

$$B(\sigma) \approx 2\delta_{\max} B(\sigma_0) \frac{\sin[2\pi(\sigma_0 - \sigma)\delta_{\max}]}{2\pi(\sigma_0 - \sigma)\delta_{\max}} \quad (2-15)$$

Eq. (2-15) is referred to as *instrumental line shape function (ILS)*. It may be rewritten in the form of a *sinc*(ζ) function, where $\zeta = 2\pi(\sigma_0 - \sigma)\delta_{\max}$. Figure 2-4 schematically compares the spectrum of an infinite extended interferogram and the spectrum of a truncated interferogram.

The effect of the *truncation* of the interferograms on the recovery of the spectrum via the Fourier transform is twofold:

- The spectrum of a monochromatic line broadens, and
- secondary maxima appear on either side of the main peak.

At the secondary maxima, referred to as *sidelobes*, the retrieved spectrum falls to a minimum of 21% below the zero level of power spectrum. The negative flux of

energies at the sidelobes is physically impossible and is purely an outcome of the Fourier transformation over a limited extent of the interferogram. A mathematical modification of the interferogram, allows the correction for the erroneous sidelobes. The mathematical correction operation is known as *apodization*.

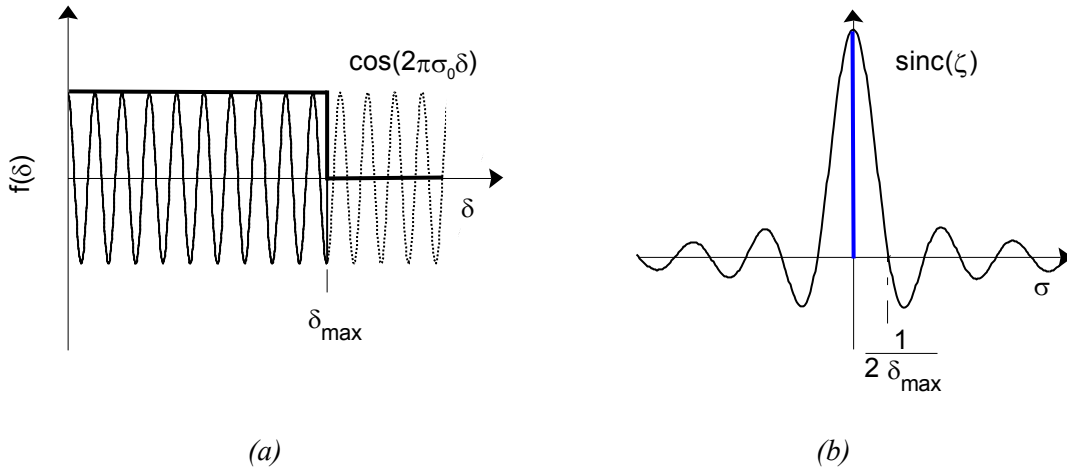


Figure 2-4: Effect of finite extent of the interferogram on the spectral line shape. (a) Interferogram of finite (black solid line), and of infinite (dashed line) extent. The thick solid line indicates the truncation of the cosine function at δ_{\max} . (b) Resulting spectra of truncated interferogram (solid black) and of infinite interferogram (solid blue).

2.2.5.2 Apodization

The main purpose of apodization is to reduce the influence of the erroneous sidelobes produced by the Fourier transform of an interferogram of finite extent. This is done by multiplying the interferogram by a weighing function $A(\delta)$. Various weighing functions are proposed (Chamberlain, 1979, Bell, 1972). Here, a list of weighing functions is given and their influence on the resulting line shape function is shown.

In general, one may write the interferogram function according to:

$$f_{apod}(\delta) = A(\delta)f(\delta) \tag{2-16}$$

Using the convolution theorem stated by Bracewell (Bracewell, 2000, p. 115), the spectrum is given by the convolution of the Fourier transform of the apodization function and the Fourier transform of the interferogram:

$$B_{apod}(\sigma) = FT^{-1}\{A(\delta)\} \circ FT^{-1}\{f(\delta)\}, \quad (2-17)$$

$$B_{apod}(\sigma) = FT^{-1}\{A(\delta)\} \circ B(\sigma), \quad (2-18)$$

where the convolution operation and the inverse Fourier transformation are denoted by \circ and $FT^{-1}\{ \}$, respectively.

Table 2-1 lists common apodization functions and their effect on the full-width-at-half-maximum value, together with the maximum sidelobe height. The data was simulated according to the apodization functions given in the table. According to Table 2-1, a rectangular windowing function results in the smallest FWHM value. The rectangular window complies with the truncation introduced earlier. However, the spurious sidelobes are at maximum among all apodization functions. Triangular and Happ and Genzel (Happ and Genzel, 1961) apodization functions significantly decrease the sidelobe effect at the expense of a widening of the peak width. These results have also been confirmed experimentally by Rabolt and Bellar (Rabolt and Bellar, 1981).

Table 2-1: Apodization functions and the resultant full-width-at-half-maximum (FWHM) values as a function of the maximum optical path difference δ_{\max} , percentage increase in FWHM and the maximum sidelobe height. Functions are taken from references (Chamberlain 1979, Bell, 1972, Happ and Genzel, 1961).

| Apodization function | $A(\delta)$ | Full width half maximum (FWHM) | Increase FWHM [%] | Max. side-lobe [%] |
|--------------------------|--|--------------------------------|-------------------|--------------------|
| Rectangular (truncation) | $rect\left(\frac{\delta}{2\delta_{\max}}\right) = \begin{cases} 0, & \left \frac{\delta}{2\delta_{\max}}\right > 0.5 \\ 0.5, & \left \frac{\delta}{2\delta_{\max}}\right = 0.5 \\ 1, & \left \frac{\delta}{2\delta_{\max}}\right < 0.5 \end{cases}$ | $0.6/\delta_{\max}$ | - | 21 |
| Cosine | $\cos\left(\frac{\pi\delta}{2\delta_{\max}}\right)$ | $0.82/\delta_{\max}$ | 36 | 7 |
| Triangular | $\left[1 - \left \frac{\delta}{\delta_{\max}}\right \right]$ | $0.88/\delta_{\max}$ | 47 | 5 |
| Happ-Genzel | $\left[0.54 + 0.46 \cos\left(\frac{\pi\delta}{\delta_{\max}}\right)\right]$ | $0.91/\delta_{\max}$ | 51 | 1 |
| Gauss | $\exp\left(\frac{-\pi\delta^2}{\delta_{\max}^2}\right)$ | $0.96/\delta_{\max}$ | 60 | 0 |
| Cosine square | $\left[\cos\left(\frac{\pi\delta}{2\delta_{\max}}\right)\right]^2$ | $1/\delta_{\max}$ | 67 | 2 |

2.2.5.3 Resolution

The amount of detail seen in an experimental spectrum is limited. As previously described, these limitations are inevitably given by the truncation of the interferogram. The result is a broadening of spectral lines which we expressed in the *instrument line shape function* derived for monochromatic radiation. The *spectral resolution* \mathfrak{R} is a measure of the ability of a spectrometer to qualitatively distinguish two spectral peaks in close proximity. The *Rayleigh criterion* states that two spectral lines are resolved if the position of the minimum of the first peak falls on the maximum of second peak. Thus, the spectral resolution depends on the apodization

function used. If the criterion is applied to the ILS function and to triangular apodization, the resolution is given by:

$$\mathfrak{R}_{ILS} = \frac{1}{2\delta_{\max}} \quad (2-19)$$

$$\mathfrak{R}_{apod} = \frac{1}{\delta_{\max}} \quad (2-20)$$

Both, criteria coincide in the fact, that the resolution of a spectrometer is inversely proportional to the optical path difference. Note that high resolution is denoted by a small wavenumber value, and low resolution is denoted by a large wavenumber value.

In terms of wavelength the theoretical resolution is given by:

$$\mathfrak{R}_{ILS,\lambda} = \frac{\lambda^2}{2\delta_{\max}} \quad (2-21)$$

Another commonly used figure is the *spectral resolving power* R which is given by:

$$R = \frac{\sigma_{\max}}{\mathfrak{R}}, \quad (2-22)$$

where \mathfrak{R} is the *spectral resolution* either the 'apodized' or the ILS value and σ_{\max} is the maximum wavenumber or shortest wavelength resolved in the spectrum. Contrary to the spectral resolution, the high resolution devices are represented by large numbers of *spectral resolving power*.

2.2.6 Sampling

In general, the interferogram introduced earlier is shown as a continuous intensity signal with respect to the optical path difference δ . However, it is in fact possible to recover a continuous signal from sampled, discrete set of values. It is common practice for analog to digital data conversion. The *shah function* W introduced by Bracewell (Bracewell, 2000, p. 83) is a commonly used function symbolizing the digitization of analog data. The character W is used here to picture the comb properties of the *shah function*. It is mathematically defined as a summation of shifted *Dirac delta function*:

$$W\left(\frac{x}{b}\right) = b \sum_{n=-\infty}^{\infty} D(x - nb) \quad (2-23)$$

where $D(x - nb)$ is a *Dirac delta function* defined according to (Bracewell, 2000, p. 83)

$$D(x) = 0 \text{ for } x \neq 0,$$

$$\text{and } \int_{-\infty}^{\infty} D(x) dx = 1.$$

n and b in Eq. (2-23) denotes an integer and the spacing between two adjacent sample points, respectively.

The sampled interferogram $f_s(\delta)$ may be written as the multiplication of the *shah function* with the continuous interferogram $f(\delta)$:

$$f_s(\delta) = W\left(\frac{\delta}{b}\right) f(\delta), \quad (2-24)$$

of which the inverse Fourier transform $FT^{-1}\{ \}$ yields the spectrum $B_s(\sigma)$ of the sampled interferogram.

$$FT^{-1}\{f_s(\delta)\} \equiv B_s(\sigma) = FT^{-1}\left\{W\left(\frac{\delta}{b}\right)f(\delta)\right\}, \quad (2-25)$$

Again, the FT of the product of two functions is the convolution of the independent FT of each of the two functions. The FT of a shah function is itself a shah function (Chamberlain, 1979, p. 52) and the FT of the interferogram is the spectrum. It follows that the “sampled” spectrum $B_s(\sigma)$ is a convolution of a shah function with the real spectrum and is thus:

$$B_s(\sigma) = \sum_{n=-\infty}^{\infty} B\left(\sigma - \frac{n}{b}\right), \quad (2-26)$$

That is, the “sampled” spectrum computes the contour of the spectrum repeatedly at an interval n/b . Alike any computed spectra, the computation of “sampled” spectra results in negative and positive frequency components which are not only symmetric about the origin but also about $\pm n/b$.

Given, the interval spacing $1/b$ is wider than the spectral band of physical spectrum, no overlapping of sampled spectra occurs. If the reverse is true, positive and negative frequency components of the “sampled” spectra overlap and a false spectrum is computed. The effect is known as *aliasing*. To avoid *aliasing* the spectra must be bandwidth-limited and the interferogram sampled at a particular sample spacing b . It must be chosen small enough so that the maximum frequency σ_{\max} of the spectrum does not overlap with the imaged negative spectrum (Bell, 1972, p. 75):

$$b \leq \frac{1}{2\sigma_{\max}} \quad (2-27)$$

The above minimum sampling interval for band-limited signals was first mentioned by Nyquist and is named the *Nyquist rate* (Nyquist, 1928). For the particular case for which the minimum frequency is $\sigma_{\min} \geq 0$ and the condition $n(\sigma_{\max} - \sigma_{\min}) = \sigma_{\max}$, for n being an integer, is met, the sampling interval is given by:

$$b \leq \frac{1}{2(\sigma_{\max} - \sigma_{\min})} \quad (2-28)$$

The number of sample points N is given by:

$$N = 2(\sigma_{\max} - \sigma_{\min})\delta_{\max} \quad (2-29)$$

Shannon introduced the above *sampling theorem* to communication theory (Shannon, 1949). He remarked that the total number of sampling points N does not need to be equally spaced, a point which is of particular importance for the development of the FPP FTS.

2.2.7 Field of view

In practice, light sources used in interferometer applications do have a finite extent. The finite extent of sources unavoidably results in light rays traveling under different angles through the interferometer. The effect persists with collimating optics at the entrance of the interferometer (Figure 2-5). The angle ψ , a ray makes with the optical axis of the interferometer determines the optical path difference of split rays.

We compare the phase shift introduced by a beam splitter for rays at parallel incidence with rays which are incident at an angle of ψ . The angles in both cases are measured with respect to the surface normal of the beam splitter.

It follows that the optical path difference for a ray at an incidence angle of ψ is given by $\delta_{\psi} = 2d \cos(\psi)$ while for a ray at parallel incidence it is given by $\delta = 2d$. The difference in phase of both rays arriving at the detector is:

$$\varphi_{\parallel} - \varphi_{\psi} = 2\pi\sigma\delta(1 - \cos(\psi)) \quad (2-30)$$

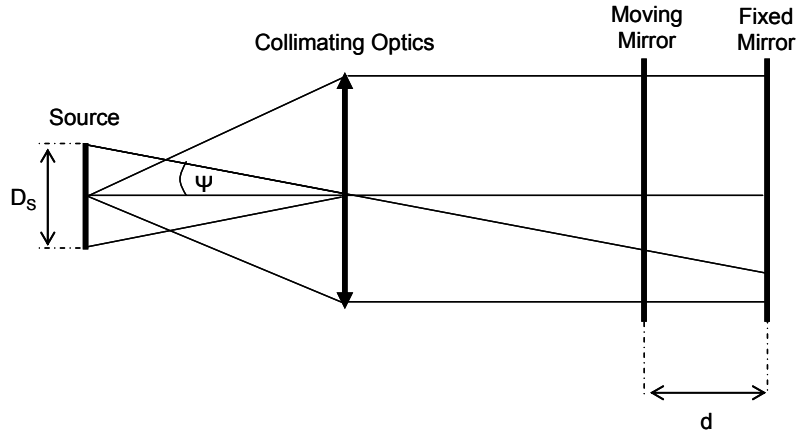


Figure 2-5: Simplified diagram of Michelson interferometer with an extended source in the focal point of the collimating optics. ψ denotes the angle a ray makes with the optical axis when emitted off the center of the source and d the distance between both reflecting mirrors.

To avoid the superposition of rays being π out of phase, it follows for the critical phase difference:

$$2\pi\sigma\delta(1 - \cos(\psi_c)) = \pi \quad (2-31)$$

A source with a circular area subtends a solid angle given by $\Omega = 2\pi(1 - \cos(\psi))$.

Thus, Eq. (2-31) may be rewritten in terms of the critical solid angle Ω_c .

$$\Omega_c = \frac{\pi}{\sigma\delta} \quad (2-32)$$

The critical solid angle is inversely proportional to the wavenumber and the optical path difference. It places in practice a physical limitation to the maximum obtainable optical path difference set by the maximum wavenumber in the spectrum and thus the resolution of the interferometer. Eq. (2-32) can be expressed in terms of *maximum resolving power* limited by the critical angle, where the proportionality sign allows for the factorial influence of the apodization function used (Eq. (2-33)).

$$R \propto \frac{\pi}{\Omega_c} \quad (2-33)$$

In an interferometer, apertures physically limit the solid angle. It is common practice in high resolution interferometers to reduce solid angle in order to resolve the interferogram modulation at large optical path differences.

2.2.7.1 Interferogram and spectrum of extended sources

The interferogram produced by an extended source is given by integrating over the solid angle Ω subtended by the source.

$$f(\delta, \Omega) = \int_0^{\infty} B(\sigma) \left(\int_0^{\Omega} \cos(2\pi\sigma\delta \cos(\psi)) d\Omega \right) d\sigma \quad (2-34)$$

For a the solid angle of a circular apertures Eq. (2-34) results in

$$f(\delta, \Omega) = \int_0^{\infty} B(\sigma) \left(\int_0^{\Omega} \cos(2\pi\sigma\delta - \sigma\delta\Omega) d\Omega \right) d\sigma \quad (2-35)$$

Integration over some maximum solid angle the above equation yields the *interferogram of a source of finite extent*.

$$f(\delta, \Omega) = \int_0^{\infty} B(\sigma) \frac{\sin(\frac{1}{2}\Omega\sigma\delta)}{(\frac{1}{2}\Omega\sigma\delta)} \cos(2\pi\sigma\delta - \frac{1}{2}\Omega\sigma\delta) d\sigma \quad (2-36)$$

To demonstrate the effect of extended source, the spectrum for a monochromatic source of wavenumber σ_0 is computed according to:

$$B(\sigma_0, \Omega) = \int_{-\infty}^{\infty} f(\delta, \Omega) e^{-i2\pi\sigma\delta} d\delta = \int_{-\infty}^{\infty} \frac{\sin(\frac{1}{2}\Omega\sigma_0\delta)}{(\frac{1}{2}\Omega\sigma_0\delta)} \cos(2\pi\sigma_0\delta - \frac{1}{2}\Omega\sigma_0\delta) e^{-i2\pi\sigma\delta} d\delta \quad (2-37)$$

Using Euler's formula and trigonometric identities Eq. (2-37) is converted into:

$$B(\sigma_0, \Omega) = \frac{1}{2} \int_{-\infty}^{\infty} \frac{\sin(\frac{1}{2}\Omega\sigma_0\delta)}{(\frac{1}{2}\Omega\sigma_0\delta)} e^{i2\pi\sigma_0\delta(1-\frac{\Omega}{4\pi})} e^{-i2\pi\sigma\delta} d\delta, \quad (2-38)$$

whereby in deriving Eq. (2-38) contributions of negative wavenumbers have been dropped.

Careful examination of Eq. (2-38) shows that the spectrum is given by the multiplication of a *sinc-function* with an exponential function. Using the convolution theorem (Bracewell, 2000, p. 115) one may conveniently interpret Eq. (2-38) as the convolution of a rectangular function $rect\left(\frac{2\pi\sigma}{\sigma_0\Omega}\right)$ with a delta Dirac pulse $D(x)$ at $\sigma_0\left(1 - \frac{\Omega}{4\pi}\right)$.

$$B(\sigma_0, \Omega) = \frac{1}{2} \left[FT^{-1} \left\{ \frac{\sin\left(\frac{1}{2}\Omega\sigma_0\delta\right)}{\left(\frac{1}{2}\Omega\sigma_0\delta\right)} \right\} \circ FT^{-1} \left\{ e^{i2\pi\sigma_0\delta\left(1 - \frac{\Omega}{4\pi}\right)} \right\} \right] \quad (2-39)$$

$$B(\sigma_0, \Omega) = \frac{1}{2} \left[\left(\frac{2\pi}{\sigma_0\Omega} \right) rect\left(\frac{2\pi\sigma}{\sigma_0\Omega}\right) \circ D\left(\sigma - \sigma_0\left(1 - \frac{\Omega}{4\pi}\right)\right) \right] \quad (2-40)$$

The recovered spectrum of extended monochromatic source is of rectangular shape shifted to a lower wavenumber. The component $\sigma_0\left(1 - \frac{\Omega}{4\pi}\right)$ in the exponential function of Eq. (2-38) may be referred to the medium wavenumber in the spectrum.

The outcome on the spectrum of extended sources in FTS is twofold (Bell, 1972, p. 141):

- the computed spectrum is shifted to lower wave numbers,
- and a wavenumber spread is introduced.

Figure 2-6 illustrates the effect of the extended source by comparing the interferogram and spectrum of monochromatic radiation emitted from a point source with that emitted from an extended source. Note that in both cases, the acquired spectral data bases on truncated interferograms.

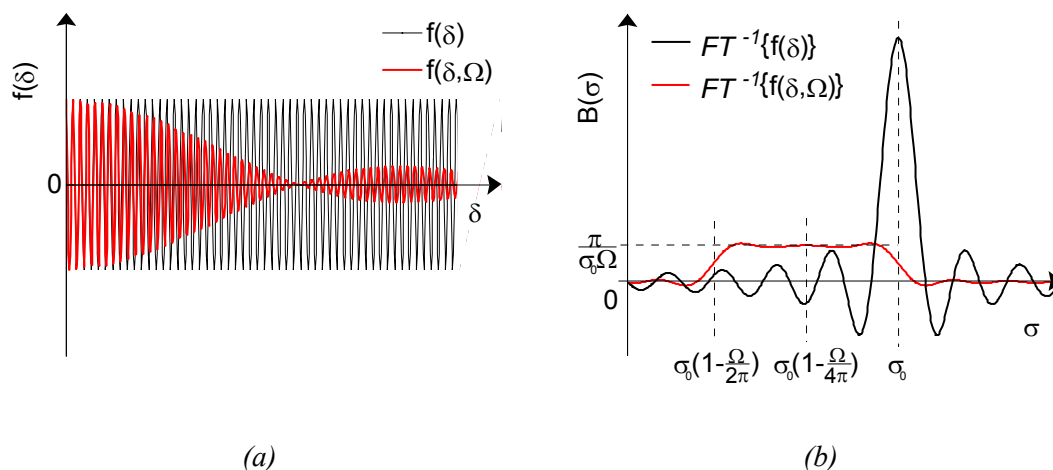


Figure 2-6: Effect of extended source on interferogram $f(\delta, \Omega)$ (a) and spectrum (b) in comparison to interferogram of a point source $f(\delta)$. Both examples are given for truncated interferometric data. The source extension results in a recovered spectrum of increased spectral width centered at a wavenumber $\sigma_0 \left(1 - \frac{\Omega}{4\pi}\right)$ and amplitude $\frac{\pi}{\sigma_0 \Omega}$.

2.2.8 Noise

The study of noise in FTS is difficult as a broad range of noise sources in the operation of the interferometer exist. Such noise sources include the instrument itself which may generate noise in the signal through vibration, misalignment or sampling errors, the detector may generate noise in its read out circuitry or the source may produce fluctuating output.

Chamberlain (Chamberlain, 1979, p. 263) differentiates mainly two types of noise, namely *additive* and *multiplicative noise*.

2.2.8.1 Additive noise

Additive noise is generated in the interferometer from sources such as background radiation entering the interferometer together with signal and from noise generated in the recording electronics. It contributes to the noise by adding to the “noise-free” interferometric signal. *Additive noise* is dominating at photon energies in the infrared

part of electromagnetic spectrum, where the photon energies are in the range of eV to meV and thus in the same order of magnitude as thermal energies kT (k is Boltzmann's constant and T the temperature in K). The thermally generated noise is also called *Johnson* or *Thermal noise*. Infrared detectors, such as bolometers, operate in the range of Johnson noise (Hudson, 1969, p. 311). Chamberlain (Chamberlain, 1979, p. 263) states that *Johnson noise* is the dominating noise characteristics for most infrared detectors even if the detectors are cooled to cryogenic temperatures. *Additive noise* is independent of the signal power received by the detector and accounts for the multiplex advantage of FTS compared with grating spectrometers stated in section 2.2.1.

2.2.8.2 Multiplicative noise

Multiplicative noise is associated with the radiation. Multiplicative noise may be subdivided in *photon* and *signal noise*. *Photon noise* (also *shot noise*) arises from the random arrival of photons at the detector. It is related to the random nature of spontaneous emission processes in thermal sources and tends to dominate in the optical part of the spectrum. One refers to *Signal noise* if the output of the source or in the transmission medium fluctuates. Increasing the signal strength increases the noise level, there is no net gain, and multiplexing techniques are in this type of noise regime disadvantageous.

2.2.8.3 Signal-to-Noise ratio

The Signal-to-Noise ratio (SNR) compares the mean radiation power and the mean background noise power.

$$SNR = \frac{Signal_{received}}{Noise} \quad (2-41)$$

Due to the multiplexing ability of the FTS, the signal strength depends on the spectral components and its powers, and thus the SNR in FTS is dependent on the spectral power of the resolved spectral components and on the width of the detected spectrum.

The noise level in the spectrometer may be estimated by analyzing standard deviations of multiple measurements taken under same experimental conditions.

One other simple way to quantify the background noise of a spectrometer is to measure e.g. the transmission spectra of a sample or the background twice at different instants (T_1 and T_2) and to compute the spectral noise and its root-mean-square value according to Eq. (2-42) and (2-43) (Saptari, 2004).

$$N(\sigma) = 1 - \frac{T_1(\sigma)}{T_2(\sigma)} \quad (2-42)$$

$$N_{rms} = \sqrt{\frac{1}{n} \sum_{i=1}^n [N(\sigma_i)]^2} \quad (2-43)$$

where n denotes the number of spectral elements in the spectral range of interest. The SNR is then computed by:

$$SNR = \frac{1}{N_{rms}} \quad (2-44)$$

The determination of SNR is useful to conclude whether a spectral feature is real or not. Smith (Smith, 1996, p. 8) recommends that the intensity of spectral features must be at least 3 times the intensity of the background noise.

In order to cope with signals embedded into noise of equal or higher power the SNR must be increased. In principle this can be accomplished by

- a) increasing the signal strength, by improving the throughput of the spectrometer (for additive noise),
- b) increasing the sensitivity of the detector, or
- c) Time-averaging.

All of the above points help to improve the SNR of which the time-averaging is likely to be the easiest method. When the signal is time-averaged, the measurement is repeated many times and added up. Given the signal is stable over the time-averaging interval the signal accumulates whereas the random noise will cancel out and increase at a lower rate. As a result the SNR grows following square root function. It is commonly applied when the experimentalist has to deal with low signals. The time-averaging increases the SNR at the expense of detection speed and thus time-resolution.

2.3 Summary

Chapter two introduced the fundamental theoretical background upon which the development of the spectrometer rests. We briefly discussed electromagnetic radiation and presented how it is analyzed by a Fourier transform spectrometer in theory. Advantages of FTS over dispersive or diffracting spectrometers were treated, basic mathematical formulation briefly derived, and presented the elementary mathematical formulation of the Fourier transformation. With the concept of truncation we showed how Fourier transformation can be utilized for physically measurable quantities of finite extent. Moreover, we introduced the idea of apodization which beyond the scope of truncating the interferogram to its finite extent alters the spectral result, alters interferometric data to yield more realistic spectra. We defined the resolution of the spectrometer as the ability to differentiate two adjacent spectral lines by the *Rayleigh criterion* and introduced the concept of sampling of band-limited signals at minimum sampling interval as discovered by *Shannon* and *Nyquist*, respectively. We showed the influence of extended sources on the interferometric data and the resulting spectrum and revealed that it places a limitation of the maximum resolution. Finally, we defined two types of noises, namely *additive* and *multiplicative* noise mentioned the concept of signal-to-noise ratio and introduced common methods to improve it.

3 THE CONCEPT OF THE FAST PARALLEL PROCESSING FOURIER TRANSFORM SPECTROMETER (FPP FTS)

3.1 Introduction

This chapter first reviews developments in the field of miniature spectrometers. State-of-the-art micro-sized spectrometers are examined and the concept of the Fast Parallel Processing Fourier-transform Spectrometer (FPP FTS) is introduced.

The main part of the chapter establishes a link between the theories introduced in chapter two and design parameters of the FPP-FTS. In the interest of a potentially wide variety of applications of the FPP-FTS concept, the parameters are developed independent of possible spectral working bands. However, the infrared spectral band, particularly the finger print region, serves as an example working band. The attractiveness of the spectral band is emphasized and design and fabrication parameters are developed.

3.2 Miniature spectrometers

Miniaturization of instruments, sensors, and actuators offers an attractive potential for science and industries. Smaller size enables faster and cheaper devices, moreover, besides the economic interest, the small size allows for a wide range of new applications not possible with macro-scale instruments. With the advancements of micro-fabrication techniques a multitude of new devices evolve, and among these, miniature spectrometers.

In the visible and near infrared part of the electromagnetic spectrum, a plethora of miniature spectrometers were developed. A great part of these devices make use of gratings (Avrutsky, 2006, Yee, 1997, Smith 2009, Mohr 1991, Crocombe, June 2008)

or band-pass filter systems (Crocombe, May 2008, Wang, 2007, Smith, 2009) to acquire spectral information. Fourier-transform spectrometers (FTS) using MEMS (microelectromechanical systems) motion devices to scan spectral bands as in the case of Fabry- Perot (Correia, 1999, Kung, 2000, Crocombe, June 2008), Michelson- type (Ataman, 2009, Crocombe, January 2008, Crocombe, June 2008, Yu, 2006, Collins, 1999), and Lamellar grating spectrometers (Manzardo et al., 2004, Ataman, 2006, Ataman and Urey, 2009, Yu et al. 2008) also contribute a large number of publications and push into commercial market. Static FT spectrometers following the Michelson (Ivanov, 2000 and Zhan, 2002) or lamellar grating setup (Chau, 2008) were reported. The technology platform for most of these small size devices is known as MEMS and MOEMS (micro-opto-electromechanical systems) but also other technologies like the LIGA process infrastructure have shown its capability to produce compact so-called slab waveguide spectrometers (Mohr 1991, Crocombe, June 2008). For the detection of signals in the visible as well as the short wavelength near infrared spectral band shot-noise prevails and grating- or filter- based devices dominate in the spectral band. Most of the reported miniature spectrometers operate at a low-to-moderate resolution (2-10 nm) and are specifically tailored to their application.

On the contrary, detection of signals in the spectral band ranging from near infrared to far infrared is restricted by the detector noise. Going from the short wavelength to longer wavelengths, from visible to the infrared, the photon energy of the electromagnetic radiation reduces and detection of low energy photons becomes crucial. The detector noise continuously becomes the limiting factor, and light throughput the decisive parameter for spectrometers. Miniaturization is then counterbalanced by the light throughput of the spectrometer. In this spectral band, FT

interferometers, known for their throughput advantage compared with dispersive devices dominate. The small-size of MEMS devices is then less capable to produce high throughput spectrometers. However, MEMS scanning Michelson interferometers (Crocombe, January and June 2008, Schildkraut et al., 2004), were reported. The time-resolution of these devices is limited by their time consuming scanning mechanisms. Moreover, the scanning mechanism is susceptible to mirror deformations, wobbling, and vibration. Static setups, replacing the scanning mechanism by tilted or stepped mirrors overcome the time consuming scanning and allow time-resolved spectroscopy.

Junttila et al. (Junttila, 1991) analyzed the performance of stationary FTS setups such as stationary Michelson, Mach-Zehnder, triangle interferometer, and a double mirror interferometer. The group concluded that stationary FTS present low-resolution but mechanical stable, compact, and low-cost instruments capable to measure wideband spectra or temporally changing radiation sources.

Recently, a French group of researchers (Brachet et al., 2008 and Hebert et al., 2008) demonstrated, to our knowledge, the first static high-resolution Michelson-type spectrometer operating in two narrow spectral infrared bands, namely the B1 band (9.35-9.71 μm) and in the B2 band (4.59-4.67 μm). Both bands are required to study the atmospheric pollution by measuring ozone and carbon monoxide concentrations. Their spectrometer bases on a static Michelson setup in which reference and moving mirror are replaced by two crossed stepped mirrors. The overlapping images of the two mirrors form a chessboard-like image of which each of the square cells corresponds to a specific optical path difference and thus interferogram point. A focal plane array detector reads the intensity of each cell.

The technique, however, has one major drawback inherent to all Michelson-type spectrometers: Amplitude beam splitters reflect 50% of the source radiation back to the source. Thus, half of radiation is lost in the system without making use of it in the interferometer.

Grating spectrographs (Kruzelecky et al., 2004, Elmore et al., 2002, Pelletier et al., 2005, Pellerin et al., Vol. 58 (6 and 7), 2004, and Pellerin and Pelletier, 2005) remove the exit slit, and replace the single detector element with a detector array. These static spectrometers also allow time-resolved spectroscopy but overlapping diffraction orders and the lower detected signal due to the dispersion of light into its spectral components limit their spectral working band.

3.3 The Fast Parallel Processing Fourier Transform Spectrometer (FPP FTS)

The thesis examines a new type of Fourier-transform spectrometer, dubbed the fast parallel-processing Fourier-transform spectrometer (FPP-FTS). The FPP-FTS is neither limited by a time consuming scanning mechanism nor is it conceptually limited to a narrow spectral working band. It was invented by Moser and Moeller in 1994 (Moser and Moeller, 1994). On the basis of its predecessors, the lamellar grating interferometer invented by Strong and Vanasse in 1960 (Strong and Vanasse, 1960), the spectrometer combines the high modulation efficiency (the unique advantage of the lamellar grating Fourier-transform interferometer) with a static multilevel mirror array. Comparing the FPP-FTS concept with static spectrometers working in the infrared such as grating spectrographs, static Michelson-type FTS, or filter spectrometers, we expect a throughput and multiplex advantage (common to infrared FTS) resulting in a superior performance over a wider spectral working band. The spectrometer possesses the inherent advantage of no moving parts and offers the capability to detect at highest detection speeds.

In 1995, Moeller proposed a number of possible spectrometer layouts (Moeller, 1995). However, this thesis concentrates on the setup as proposed in the patent of 1994 as it is expected to deliver the most compact spectrometer design.

The heart of the FPP-FTS is formed by an array of binary grating cells called the micro mirror array (MMA) (Heussler et al., 2007). Each of its binary grating cells is producing a different optical path between waves reflected at the top or bottom surface of the grating (Figure 3-1a). When a wave is reflected at such an array, each array cell produces an interferogram point with its specific optical path difference or

phase difference (Figure 3-1b). An array detector records the zeroth diffraction order intensity of each cell in the Fraunhofer field.

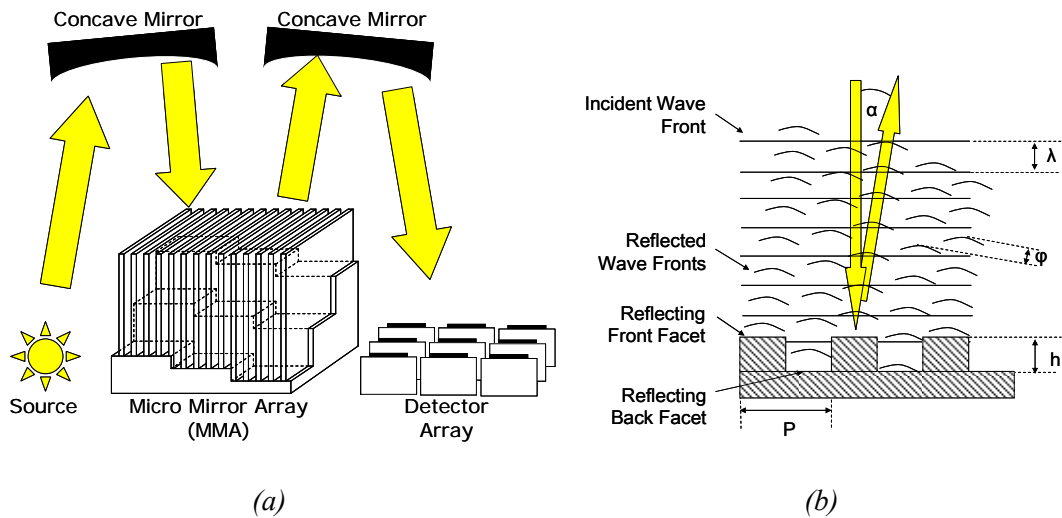


Figure 3-1: (a) Schematics of Fast-Parallel-Processing Fourier Transform Spectrometer (FPP-FTS). Source radiation is collimated and directed to the Micro Mirror Array (MMA). Upon reflection from the (here) 3×3 cell MMA, the collimated beam is split into 3×3 sub-beams, each of which is modulated in amplitude with respect to its individual optical path difference introduced by the front and back facet mirrors. Subsequently, these sub-beams are focused onto the plane of a 3×3 array detector, positioned at a distance from the MMA. Each detector cell measures one single intensity point of the interferogram. From the position of the spot on the detector its optical path difference is known. Both, the intensity and the respective optical path difference constitute the interferogram. Subsequent Fourier transformation yields the spectrum. (b) Schematic of the wave front division and diffraction at a single MMA cell, P is the grating constant, h the grating depth, λ the wavelength of the incident light, α the diffraction angle and ϕ the phase difference due to the optical path difference of rays reflected by the front and by the back facet mirrors.

3.3.1 Design considerations

3.3.1.1 Spectra of interest

The nature of radiation interacting with matter strongly depends on the photon energy of the radiation. Different parts of the electromagnetic spectrum trigger very different effects. In the visible part of the spectrum e.g. photons have energies high enough to cause electron transitions in atoms and the spectral analysis permits information of the atoms involved. When infrared radiation interacts with matter, vibrations and rotations of molecular dipoles are excited. These so-called vibration and rotation modes are either specific for the whole molecule or for smaller molecular groups. The spectral analysis of radiation either emitted or absorbed by molecules permits their identification. This offers a huge potential for the study of virtually any samples such as liquids, solutions, pastes, powders, films, gases and surfaces and makes infrared spectroscopy one of the most important analytical techniques (Stuart, 2004, p. 1).

The infrared is commonly divided into three parts: the near- (NIR), mid- (MIR), and far- (FIR) infrared spectral bands. These bands and their main characteristics are listed in Table 3-1. Within the infrared, the fingerprint region ($1500\text{-}400\text{ cm}^{-1}$) is thereby of particular interest for substance identification. In the spectral region, radiation interacts with matter and excites bending and skeletal vibrations in the molecule. These vibrations produce a molecule specific spectral fingerprint. The comparison of these fingerprint spectra with reference spectra of authentic substances allows the identification of the substance (Guenzler and Gremlich, 2002, p. 176).

Table 3-1: Infrared Classification

| NIR 13,000-4000 cm ⁻¹ 0.76-2.5 μm | MIR 4000-400 cm ⁻¹ 2.5-25 μm | FIR 400-10 cm ⁻¹ 25-1000 μm |
|--|---|--|
| <ul style="list-style-type: none"> • Overtones and combination bands of fundamental stretching bands occurring in the MIR region (Chalmers and Griffiths, 2002, p. 196), typically overtones of X-H vibrations (Stuart, 2004) • Spectral features tend to be: <ul style="list-style-type: none"> ○ broad ○ overlapped ○ weak compared with their fundamental vibrations in the MIR (Stuart, 2004, Bhargava and Levin, 2005) <ul style="list-style-type: none"> → less useful for qualitative analysis. • Functional groups can be assigned to NIR position of the spectral features (Bhargava and Levin 2005). <ul style="list-style-type: none"> → exploited for quantitative analysis (Stuart, 2004) | <ul style="list-style-type: none"> • Fundamental vibration bands → strong absorption (Bhargava and Levin, 2005). • Four regions <ul style="list-style-type: none"> ○ X-H stretching (4000-2500/cm) ○ triple-bond region (2500-2000/cm) ○ double-bond region (2000-1500/cm) ○ fingerprint region (1500-400/cm) • Each of the bands (4000-1500/cm) can be assigned to particular deformation of the molecule, movement of a group of atoms, or bending or stretching of particular bond. • Fingerprint region (1500-400/cm) bending and skeletal vibrations unique for the respective molecule. <ul style="list-style-type: none"> → qualitative analysis. | <ul style="list-style-type: none"> • Vibration bands of molecules containing <ul style="list-style-type: none"> ○ heavy atoms ○ molecular skeleton vibrations ○ molecular torsions ○ crystal lattice vibrations. • Provides information about: <ul style="list-style-type: none"> ○ Molecules containing halogen atoms. ○ Organo-metallic compounds ○ Inorganic compounds |

3.3.1.2 The Micro Mirror Array (MMA)

The MMA can be seen as a spatial arrangement of mirror surfaces. Regionally, these mirror surfaces form binary reflection gratings which are referred to as cells. Globally, the cells constitute the MMA. Here, the response of single cells to spatially coherent radiation (single point source) in the far Fraunhofer field is studied. Three mirror designs and their spectral performance are simulated. The simulation is equally valid for the response of an array of single cells forming the MMA. Optical filtering to read the individual intensities of the cells is introduced in later chapters.

The study in this part of the thesis is restricted to scalar diffraction theory. Limitations of the theory for conducting gratings are discussed in references (Gremaux and Gallagher, 1993, and Wirgin, 1973). Wirgin proved the validity of scalar diffraction theory to predict correct results for the perfectly conducting lamellar gratings if the period of the grating is larger than 10 times the longest wavelength of the probing light (Wirgin, 1973). Within this restriction the spectral performance of mirror designs are evaluated. The effects of violating the restriction are not studied in the thesis. Born's treatment of scalar diffraction is taken as reference material throughout this part of the thesis (Born and Wolf, 1997, p. 425-446).

3.3.1.2.1 The single cell design

Following an approach by Gremaux and Gallagher (Gremaux and Gallagher, 1993), single MMA cells are modeled as transmission gratings consisting of spatially arranged areas of 0 and φ phase steps (see Figure 3-2).

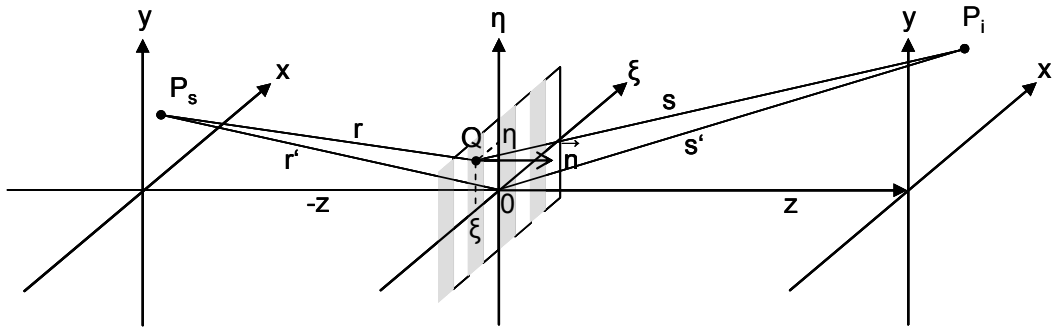


Figure 3-2: Simulation schematic. The reflection grating is simulated as a transmission grating which is placed in the ξ - η -plane. The grating consists of surfaces either introducing a 0 (whitish areas) or a φ phase shift (grayish areas). The arrangement of the phase-steps depends on the individual cell design. Here, a rectangular grating design is exemplarily shown. P_s and P_i are the position of the source- and the image-point, respectively. Z denotes the optical axis and n the grating normal.

The phase steps are given by the optical path difference (δ) between front and back facet reflections multiplied by the propagation number k ($k = 2\pi/\lambda$). Thus, the depth h of the cell, the angle of incidence, and the wavelength λ determines the phase steps φ . Considering Figure 3-3 (a), the phase step is:

$$\varphi(\xi, \eta) = \frac{4\pi h(\xi, \eta)}{\lambda \cos Y \sin \Phi} \quad (3-1)$$

where Φ and Y are the angles included between the projection of the wave vector \vec{k} of the incident wave onto the ξ - z -plane and the ξ -axis, and between the projection of the wave vector \vec{k} of the incident wave onto the ξ - z -plane and the wave vector itself, respectively (inset Figure 3-3 (a)).

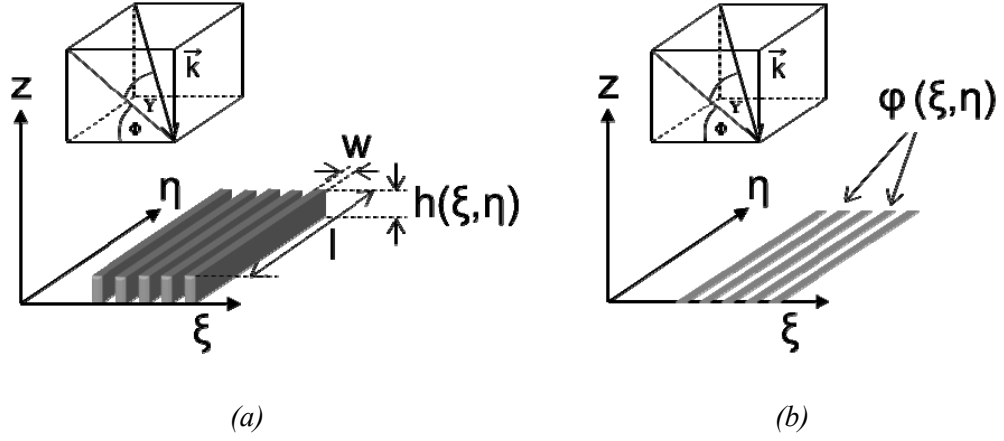


Figure 3-3: (a) MMA cell formed by binary grating of depth h , lamellar width w and grating cell length l . Inset of (a) Denomination of angles: \vec{k} is the plane wave normal, Y the angle between \vec{k} and its projection in ξz plane, Φ the angle between \vec{k} projection in the ξz plane and the ξ axis. (b) Converted phase map.

First, we restrict the incoming radiation to plane waves at perpendicular incidence ($\Phi = \pi/2$ and $Y = 0$). A factor of 2 attributes for twice the optical path for reflected radiation. Figure 3-3 (b) indicates the resulting 0 and φ phase step elements with the white and grayish hatched areas, respectively.

Using the Fresnel-Kirchhoff diffraction integral, Fraunhofer approximation, and the obtained phase map, the complex wave amplitude in a plane parallel to the diffraction screen at a distance z_i is given by (Born and Wolf, 1997):

$$U(P_i) = K \iint e^{-ikf(\xi, \eta)} e^{-i\varphi(\xi, \eta)} d\xi d\eta, \quad (3-2)$$

with
$$K = \frac{-iE}{\lambda} \frac{1}{r' s'} e^{ikr'} e^{iks'} \cos \chi,$$

and
$$f(\xi, \eta) = \left(\frac{x_i}{s'} + \frac{x_s}{r'} \right) \xi + \left(\frac{y_i}{s'} + \frac{y_s}{r'} \right) \eta \quad (3-3)$$

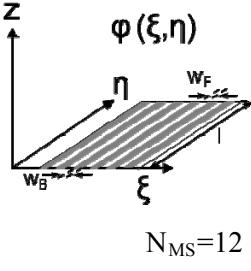
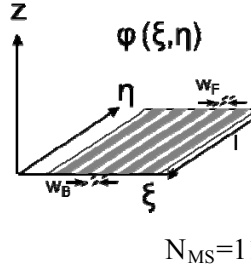
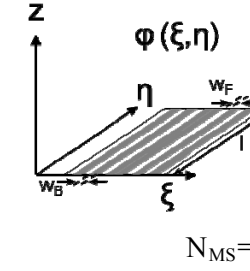
where r' and s' denote the distances from the source point to the origin of the diffraction screen in the ξ - η -plane and from to origin to the image point, respectively (see Figure 3-2). λ is the wavelength, k the propagation number, and χ describes the

angle between a line connecting source and image point and the normal \vec{n} of the diffraction screen. E is the amplitude of the electric field vector of the emitted wave.

Two types of cell designs are studied, namely rectangular mirror surface designs with an even or an odd number N_{MS} of mirror surfaces per cell. A circular cell design as proposed by Möller (Möller, 1991) is not considered, because of its restrictions to near perpendicular incidence – an effect which is studied in greater detail in section 3.3.1.6.1 Shadowing.

All designs are made of a number of N_{MS} mirror surfaces forming alternating front and back facet surfaces. For an even number of N_{MS} , both front and back facet surfaces are of width 'w' and length 'l'. The rectangular design with an odd number of surfaces is further distinguished into two designs: (1) alternating front and back facet surfaces of which the width of the back facet surfaces is wider than the front facet surfaces to compensate the surface area, and (2) alternating front and back facet surfaces of which the surface of the center facet is of twice the width. Both are of length 'l'. The period P of a perfectly reflecting grating is assumed to be at least 10 times the largest wavelength λ_{\max} of the recorded spectrum (compare (Wirgin, 1973)). Accordingly, single mirror elements have a minimum ratio of $w/\lambda=5$. Table 3-2 lists the cell designs and its parameters studied.

Table 3-2: Simulated cell designs and parameters

| Cell Type | Rectangular | | |
|--|--|---|--|
| | A | B | C |
| Cell Design |  $N_{MS}=12$ |  $N_{MS}=11$ |  $N_{MS}=11$ |
| Comments | Even number of mirror surfaces of width w ($w_F = w_B$) and length l . | Odd number of mirror surfaces of width w_F and w_B and length l . | Odd number of mirror surfaces of width w ($w_F = w_B$) and length l . center mirror is of width $2w$ |
| Number of mirror surfaces ' N_{MS} ' | Even number of mirror surfaces $N_{MS} = 2, 4, 8, 12$ | Odd number of mirror surfaces $N_{MS} = 3, 7, 11$ | |
| Ratio x ' w/λ ' | 5, 10 | $w_F/\lambda = 5$ $w_B/\lambda = (N+1)/(N-1)$ | 5 |
| Ratio y ' l/λ ' | 50, 100 | | |

Design A: Even number of rectangular mirror surfaces

The structure having an even number of N_{MS} alternating rectangular mirror surfaces of depth h is commonly referred to as binary grating and is frequently used in industry and research as diffraction gratings. However, for the interferometric use of the binary grating the depth h is variable. Its contribution onto the intensity field forming in the far Fraunhofer field is derived (see Appendix 3).

Accordingly, the coherent superposition of an even number of N_{MS} mirror surfaces may be expressed mathematically as:

$$B(P_i) \propto KK^* (2wl)^2 \left(\frac{\sin\left(k\left(\frac{x_i + x_s}{s' + r'}\right)\frac{w}{2}\right)}{k\left(\frac{x_i + x_s}{s' + r'}\right)\frac{w}{2}} \right)^2 \left(\frac{\sin\left(k\left(\frac{y_i + y_s}{s' + r'}\right)\frac{l}{2}\right)}{k\left(\frac{y_i + y_s}{s' + r'}\right)\frac{l}{2}} \right)^2 \left(\frac{\sin\left(kw\frac{N_{MS}}{2}\left(\frac{x_i + x_s}{s' + r'}\right)\right)}{\sin\left(kw\left(\frac{x_i + x_s}{s' + r'}\right)\right)} \right)^2 \times \left(\cos\left(\frac{kw\left(\frac{x_i + x_s}{s' + r'}\right) + \varphi}{2}\right) \right)^2, \quad (3-4)$$

where * denotes the complex conjugate.

Assuming plane waves incident onto the cell (far source point on the optical axis), one may rewrite the Cartesian coordinates in form of diffraction angles α and β in x and y direction, respectively.

$$B(P_i) = KK^* (2wl)^2 \left(\frac{\sin\left(k\frac{w}{2}\sin\alpha\right)}{k\frac{w}{2}\sin\alpha} \right)^2 \left(\frac{\sin\left(k\frac{l}{2}\sin\beta\right)}{k\frac{l}{2}\sin\beta} \right)^2 \left(\frac{\sin\left(kw\frac{N_{MS}}{2}\sin\alpha\right)}{\sin(kw\sin\alpha)} \right)^2 \times \left(\cos\left(\frac{kw\sin\alpha + \varphi}{2}\right) \right)^2 \quad (3-5)$$

Thus, the intensity pattern of is made up of three main contributions:

$$1) B_{1x} = \left(\frac{\sin\left(k\frac{w}{2}\sin\alpha\right)}{k\frac{w}{2}\sin\alpha} \right)^2 \text{ and } B_{1y} = \left(\frac{\sin\left(k\frac{l}{2}\sin\beta\right)}{k\frac{l}{2}\sin\beta} \right)^2, \text{ the } \text{sinc}^2 \text{ functions, describing the}$$

diffraction pattern of a single slit or mirror surface of width w and length l . It has maximum value for the zeroth diffraction order and minima for even diffraction orders.

$$2) B_{2x} = \left(\frac{\sin\left(kw\frac{N}{2}\sin\alpha\right)}{\sin(kw\sin\alpha)} \right)^2, \text{ describing the contribution of all } N \text{ illuminated mirror}$$

surfaces. It has maxima for all diffraction orders.

$$3) B_{3x} = \left(\cos\left(\frac{kw\sin\alpha + \varphi}{2}\right) \right)^2, \text{ the } \cos^2 \text{ function, taking the contribution of the phase shift between front and back facet mirrors into account.}$$

While the terms B_1 and B_2 describe the diffraction properties, both governed by the ratio of mirror width w or length l and the probing wavelength λ , the term B_3

represents the interferometric properties of the cell. Varying the depth of the grating introduces a path difference between rays reflected from front or back facet mirrors and subsequently alters the intensity pattern. Figure 3-4 (a)-(d) shows the forming intensity distribution of cells of $N= 2, 4, 8,$ and 12 surfaces for $\varphi=2\pi, 3/2\pi, \pi,$ and $\pi/2$ phase steps. For phase shifts $\varphi=M2\pi$, where M is an integer, light reflected from the cell interferes constructively and most of the flux is concentrated in the zero diffraction order, whereas for $\varphi=(2M+1)\pi$ light interferes destructively and is distributed into an angle off the center, usually called 1st diffraction order. These are the two extreme conditions. Other phase shifts distribute the light accordingly between the diffraction orders.

Diffraction and aperture angles for all diffraction orders are determined by B_2 . The diffraction angle α of the M^{th} diffraction order is defined by:

$$\frac{2w}{\lambda} \sin(\alpha) = M \text{ for } M = 0, \pm 1, \pm 2, \dots$$

from
$$\sin(\alpha) = M \frac{\lambda}{P}, \tag{3-6}$$

with
$$P = 2w.$$

P is the period. As a result, the propagation direction of the M^{th} diffraction order is inversely proportional to the ratio P/λ .

The aperture angle for the diffraction orders α_{ap} is given by:

$$\sin(\alpha_{ap}) = \frac{\lambda}{N_{MS} \frac{P}{2}}, \tag{3-7}$$

The aperture angle is inversely proportional to the number of surfaces, an effect which is demonstrated in Figure 3-4 (a)-(d) for a ratio of $w/\lambda = 5$. A higher number of diffracting surfaces per cell concentrates radiation into smaller aperture angles.

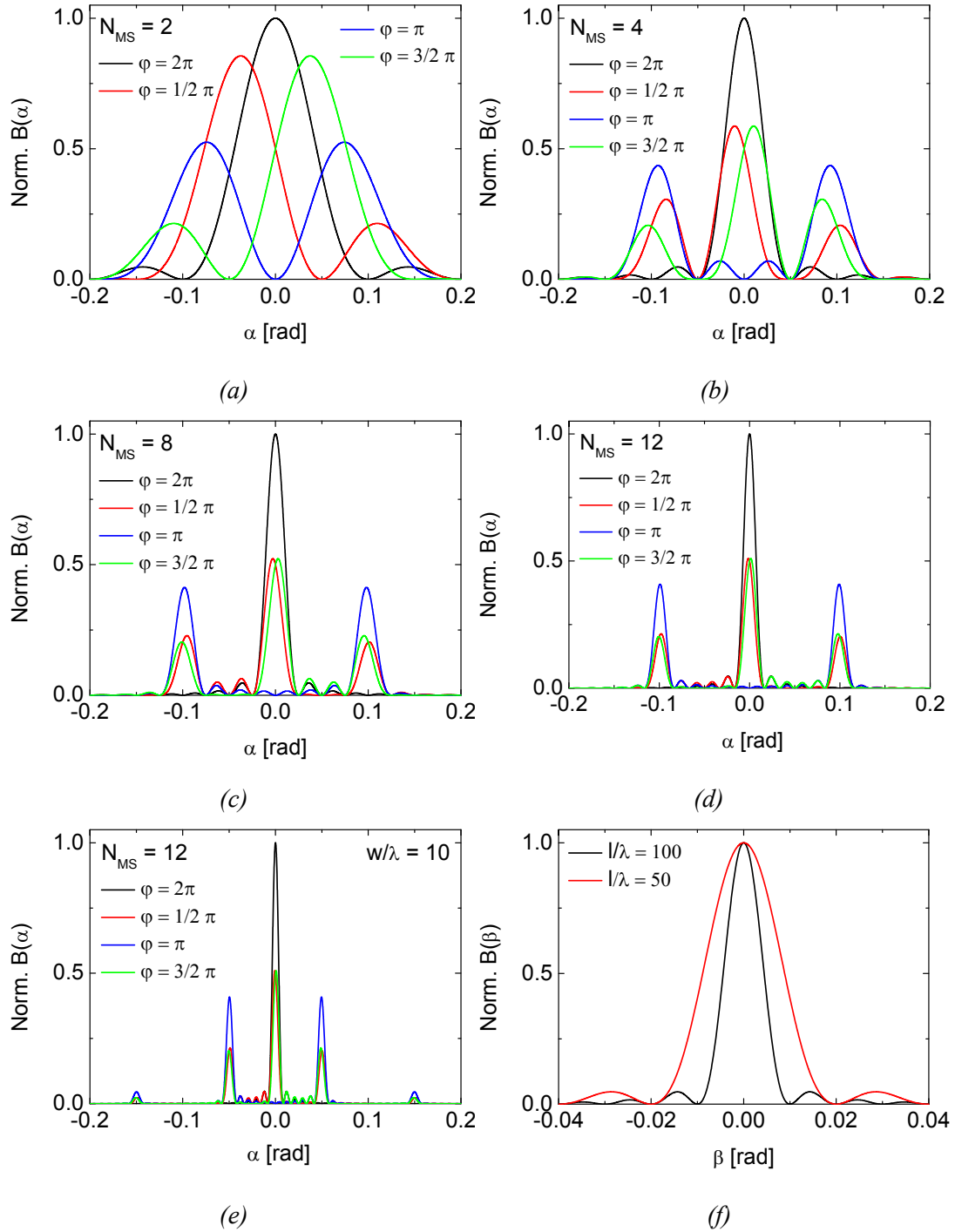


Figure 3-4: Cell Design A: Fraunhofer diffraction pattern in x direction for a ratio of $w/\lambda = 5$ and phase shifts φ of λ , $1/4\lambda$, $1/2\lambda$, and $3/4\lambda$ for (a) $N_{MS}=2$, (b) $N_{MS}=4$, (c) $N_{MS}=8$, and (d) $N_{MS}=12$ mirrors per cell. (e) Fraunhofer diffraction pattern in x direction for $N_{MS}=12$ mirrors and a ratio $w/\lambda=10$. (f) Fraunhofer diffraction pattern in y direction.

Comparing Figure 3-4 (d) and Figure 3-4 (e) demonstrates the influence of a ratio w/λ on the diffraction pattern. Increasing the ratio w/λ , results in smaller diffraction and aperture angles.

Figure 3-4 (f) shows diffraction pattern in the orthogonal y-direction in which in principle no diffraction is desirable. For a factor of ten higher ratio l/λ of 50 the aperture angle in y direction is ten times smaller than its orthogonal counterpart.

Design B: Odd number of rectangular mirror surfaces of width w_F and w_B

For an odd number of mirror surfaces per cell of length l and width w_F and w_B for front and back mirrors, the intensity distribution is given by:

$$\begin{aligned}
 B(P_i) \propto & KK^* l^2 \left(\frac{\sin\left(k\left(\frac{y_i+y_s}{s'+r'}\right)\frac{l}{2}\right)}{k\left(\frac{y_i+y_s}{s'+r'}\right)\frac{l}{2}} \right)^2 \left[\left(w_F \right)^2 \left(\frac{\sin\left(k\left(\frac{x_i+x_s}{s'+r'}\right)\frac{w_F}{2}\right)}{k\left(\frac{x_i+x_s}{s'+r'}\right)\frac{w_F}{2}} \right)^2 \left(\frac{\sin\left(k\frac{P}{2}\left(\frac{x_i+x_s}{s'+r'}\right)\left(\frac{N_{MS}+1}{2}\right)\right)}{\sin\left(k\frac{P}{2}\left(\frac{x_i+x_s}{s'+r'}\right)\right)} \right)^2 \right. \\
 & + \left. \left(w_B \right)^2 \left(\frac{\sin\left(k\left(\frac{x_i+x_s}{s'+r'}\right)\frac{w_B}{2}\right)}{k\left(\frac{x_i+x_s}{s'+r'}\right)\frac{w_B}{2}} \right)^2 \left(\frac{\sin\left(k\frac{P}{2}\left(\frac{x_i+x_s}{s'+r'}\right)\left(\frac{N_{MS}-1}{2}\right)\right)}{\sin\left(k\frac{P}{2}\left(\frac{x_i+x_s}{s'+r'}\right)\right)} \right)^2 \right. \\
 & \left. + 2w_F w_B \frac{\sin\left(k\left(\frac{x_i+x_s}{s'+r'}\right)\frac{w_F}{2}\right)}{k\left(\frac{x_i+x_s}{s'+r'}\right)\frac{w_F}{2}} \frac{\sin\left(k\frac{P}{2}\left(\frac{x_i+x_s}{s'+r'}\right)\left(\frac{N_{MS}+1}{2}\right)\right)}{\sin\left(k\frac{P}{2}\left(\frac{x_i+x_s}{s'+r'}\right)\right)} \frac{\sin\left(k\left(\frac{x_i+x_s}{s'+r'}\right)\frac{w_B}{2}\right)}{k\left(\frac{x_i+x_s}{s'+r'}\right)\frac{w_B}{2}} \frac{\sin\left(k\frac{P}{2}\left(\frac{x_i+x_s}{s'+r'}\right)\left(\frac{N_{MS}-1}{2}\right)\right)}{\sin\left(k\frac{P}{2}\left(\frac{x_i+x_s}{s'+r'}\right)\right)} \cos(\varphi) \right] \quad (3-8)
 \end{aligned}$$

where P is the period ($P = w_F + w_B$), N_{MS} a odd number of mirror surfaces, φ the phase shift attached to the back facet mirrors, K , and its complex conjugate K^* are given by (3-8). The number of front and back facet mirrors is $(N_{MS}+1)/2$ and $(N_{MS}-1)/2$, respectively. To compensate the surface area of an imbalanced number of front and back facet mirrors, the width of the back facets w_B mirrors is given by:

$$\frac{w_B}{\lambda} = \left(\frac{N_{MS} + 1}{N_{MS} - 1} \right) \frac{w_F}{\lambda} \quad (3-9)$$

Figure 3-5 (a) and (b) shows the resulting diffraction pattern for $N_{MS} = 3, 5,$ and $11,$ at a ratio w_F/λ of 5. Similar to the cell design with an even number of mirror surfaces,

the intensity pattern is modulated as a function of phase shift φ . M^{th} order diffraction angle and aperture angle are given by (3-6), and (3-7), where the period P is given by the sum of w_F and w_B .

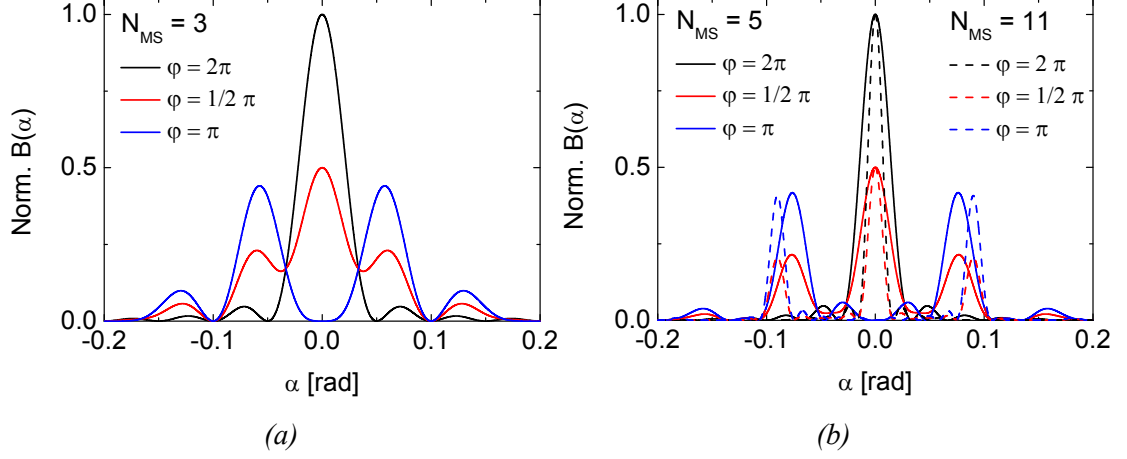


Figure 3-5: Cell Design B: Fraunhofer diffraction pattern in x direction for a ratio of $w_F/\lambda = 5$ of the front facets mirrors, $w_B/\lambda = (w_F/\lambda) (N_{MS} + 1)/(N_{MS} - 1)$ for the back facet mirrors, and phase shifts φ of λ , $1/4\lambda$, and $1/2\lambda$ for (a) $N_{MS}=3$, and (b) for $N_{MS} = 5$ (solid) and $N_{MS} = 11$ (dashed) mirrors per cell.

Design C: Odd number of rectangular mirror surfaces of width w and center mirror of double width

For the design with alternating front and back facet surfaces of which the center surface of the cell is of twice the width, the intensity distribution is given by:

$$\begin{aligned}
 B(P_i) \propto & KK^* l^2 \left(\frac{\sin\left(k\left(\frac{y_i + y_s}{s' + r'}\right)\frac{l}{2}\right)}{k\left(\frac{y_i + y_s}{s' + r'}\right)\frac{l}{2}} \right)^2 (2w)^2 \left(\frac{\sin\left(k\left(\frac{x_i + x_s}{s' + r'}\right)\frac{w}{2}\right)}{k\left(\frac{x_i + x_s}{s' + r'}\right)\frac{w}{2}} \right)^2 \left(\frac{\sin\left(kw\left(\frac{x_i + x_s}{s' + r'}\right)\left(\frac{N_{MS} + 1}{4}\right)\right)}{\sin\left(kw\left(\frac{x_i + x_s}{s' + r'}\right)\right)} \right)^2 \\
 & \times \left[\cos\left(kw\left(\frac{x_i + x_s}{s' + r'}\right)\left(\frac{N_{MS} + 3}{4}\right)\right)^2 + \cos\left(kw\left(\frac{x_i + x_s}{s' + r'}\right)\left(\frac{N_{MS} - 1}{4}\right)\right)^2 \right. \\
 & \left. + \cos\left(kw\left(\frac{x_i + x_s}{s' + r'}\right)\left(\frac{N_{MS} + 3}{4}\right)\right) \cos\left(kw\left(\frac{x_i + x_s}{s' + r'}\right)\left(\frac{N_{MS} - 1}{4}\right)\right) \cos(\varphi) \right] \quad (3-10)
 \end{aligned}$$

for $N_{MS} = 3, 5, 11, 15, \dots$

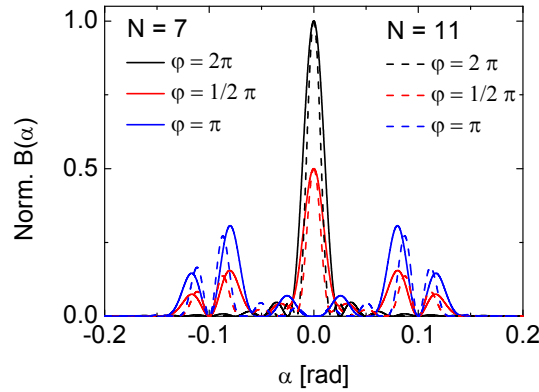


Figure 3-6: Cell Design C: Fraunhofer diffraction pattern in x direction for a ratio of $w/\lambda = 5$ of the front and back facet mirrors, center mirror is of double width, phase shifts ϕ are λ , $\frac{1}{4}\lambda$, and $\frac{1}{2}\lambda$ for $N_{MS}=7$ (solid), and $N_{MS}=11$ (dashed) mirrors per cell.

Figure 3-6 demonstrates the resulting intensity pattern for $N_{MS} = 7$ and $N_{MS} = 11$ mirror surfaces. The ratio w/λ is kept at 5 for comparison. For both designs, the intensity is modulated as a function of the phase shift ϕ which was attached to the center mirror of width $2w$ and alternating attached to adjacent mirror surfaces. Contrary to the other cell designs, the 1st diffraction order is spread into two peaks of lower intensity of which the valley separating them is given by the angle $\sin(\alpha) = \lambda/(2w)$.

The aperture angle is:

$$\sin(\alpha_{ap}) = \frac{\lambda}{(N_{MS} + 1)w} \quad (3-11)$$

In summary, all cell designs modulate their intensity pattern as a function of the phase shift. In case of constructively interfering rays reflected from front and back facet mirrors the intensity is concentrated in the zero diffraction order, whereas in the case of destructive interference it is redistributed to higher diffraction orders.

The odd number cell designs offer the advantage that the zeroth diffraction order is modulated on the optical axis whereas for the even number cell design, the center

intensity is diffracted into angles depending on the optical path difference. This is shown explicitly in Figure 3-4 (a), and (b) for $N_{MS}=2$ and $N_{MS}=4$ mirror surfaces with a phase shift of $\frac{1}{2} \pi$. For larger numbers of reflecting surface per cell the effect is negligible. The results and derived responses obtained for the cell designs are in agreement with theoretical studies by Moeller (Möller, 1991). Furthermore, these findings agree well with the theoretical and experimental studies by Yin (Yin, 2000). Yin et al. investigated the wave-front dividing principle for a scanning lamellar grating interferometer of different numbers of lamellae in a Mach-Zehnder interferometer setup. They demonstrate using a He-Ne laser light source that the diffraction pattern in the Fraunhofer field agreed well with the predictions provided by the scalar diffraction theory.

3.3.1.3 Resolution, sampling, and number of MMA cells

As introduced in chapter two of the thesis, the resolution of an FTS, together with the largest wavenumber in the spectrum to be detected, specifies the sampling interval and the necessary number of interferogram data points one has to acquire. For the FPP FTS, this relationship sets a minimum number of MMA cells.

Accordingly, the number of interferogram data points N is equivalent to the number of MMA cells. With reference to sections 2.2.5 and 2.2.6 of the thesis, N is given by:

$$N \geq \frac{\sigma_{\max}}{\mathfrak{R}_{ILS}}, \quad (3-12)$$

for spectra limited to a maximum wavenumber σ_{\max} ($\sigma_{\min} = 0$).

Limiting the spectral working band on both ends of the spectrum, high and low wavenumber end ($\sigma_{\min} - \sigma_{\max}$), under the condition of $\sigma_{\max} = n(\sigma_{\max} - \sigma_{\min})$ for integers of n , the number of sample points is reduced to:

$$N \geq \frac{\sigma_{\max} - \sigma_{\min}}{\mathfrak{R}_{ILS}} \quad (3-13)$$

Figure 3-7 exemplarily shows the number of MMA cells as a function of highest wavenumber. High resolution and large wavenumbers necessitates large number of MMA cells. The reduction of necessary number of cells if the system is limited to narrow bands is shown in Figure 3-7 (b) for a resolution of 4 cm^{-1} .

In the interferometer operation, the signal obtained (the interferogram) is the spectral flux as a function of the optical path difference introduced. Thus, the sampling interval b sets the increment of the optical path difference δ (OPD) from one to the next cell. For the MMA cells, this boils down to the cell depth increment Δh from cell to cell which depends on the highest wavenumber component of the spectrum and the angle of incidence (compare Eq. (2-27) and (3-1), respectively).

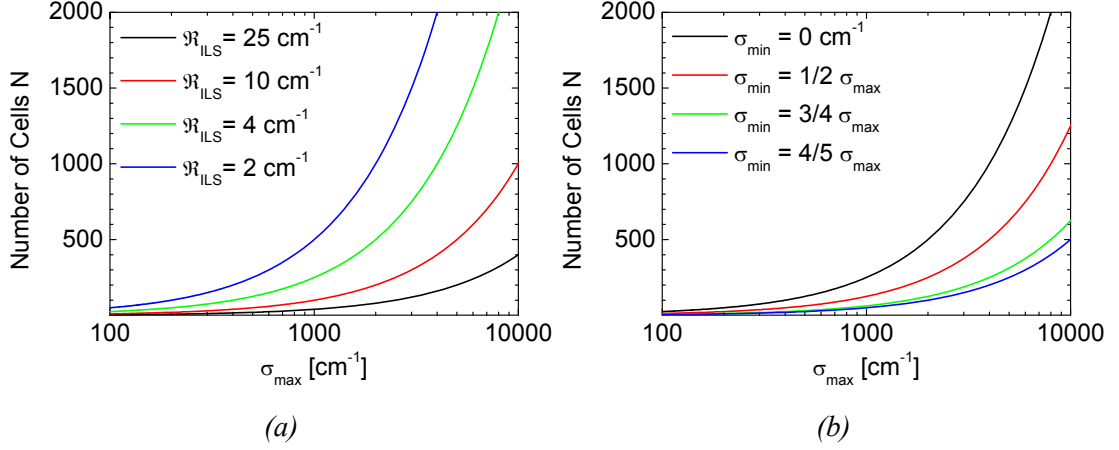


Figure 3-7: Number of MMA cells as a function of high frequency cutoff at spectral resolution \mathfrak{R}_{ILS} (no apodization) after Shannon (Shannon, 1949). (a) for band limited signals with $\sigma_{min} = 0 \text{ cm}^{-1}$ at \mathfrak{R}_{ILS} of 25 cm^{-1} (black), 10 cm^{-1} (red), 4 cm^{-1} (green), and 2 cm^{-1} (blue). (b) for band limited signals with σ_{min} is 0 cm^{-1} (black), $1/2 \sigma_{max}$ (red), $3/4 \sigma_{max}$ (green), and $4/5 \sigma_{max}$ (blue) at a spectral resolution of $\mathfrak{R}_{ILS} = 4 \text{ cm}^{-1}$.

Moreover, it is dependent on the orientation of the detector plane to the MMA normal (compare Appendix 4). For parallel MMA and detector plane as illustrated in Figure 3-2, it follows:

$$h_{Cell N} = \frac{\delta_{Cell N} \cos(Y) \sin(\Phi)}{2}, \quad (3-14)$$

$$\Delta h \leq \frac{\cos(Y) \sin(\Phi)}{4\sigma_{max}}, \quad (3-15)$$

$$h_{max} = \frac{\cos(Y) \sin(\Phi)}{4\mathfrak{R}_{ILS}}. \quad (3-16)$$

Remarks:

The resolution of the FTS is inversely proportional to the maximum optical path difference the device can measure (chapter 2.2.5) and depends, in practice, on the particular application of the spectrometer. As an example, we list recommendations of a number of applications found in the literature. For analysis of liquid condensed phase samples, special cases of solid samples such as crystalline materials and most of

low molecular weight solid samples, Nishikida et al. (Nishikida et al., 1995, p 11) recommend 2 cm^{-1} resolution. For the analysis of most polymers and plastics they recommend 4 or 8 cm^{-1} and $1-2\text{ cm}^{-1}$ for quantitative analysis of gaseous samples. Similarly, Smith (Smith, 1996, p. 37) recommends a resolution of $4-8\text{ cm}^{-1}$ for solid and liquid samples, and higher than 4 cm^{-1} resolution for the analysis of gases. Crocombe mentions that for the majority of industrial applications a resolution of 8 cm^{-1} is sufficient (Crocombe, January 2008).

One final point to address is the sampling interval b , which is of particular importance for the feasibility of the MMA manufacturing. As already stated in *Shannon's Sampling theorem*, the sample points are not necessarily required to be equidistant. The topic of non-uniform sampling is content of a plethora of publications in the field of signal processing and a detailed discussion of the problem is out of the scope of the thesis. The interested reader is referred here to (Beutler, 1966, Marvasi, 2001, Gröchenig, 1993, Boumenir, 1999, Meynart, 1992, Stoica and Sandgren, 2006, Sarkissian and Bowman, 2003, Tian, 2005, Jerri, 1977). According to Jerri (Jerri, 1977) who restates earlier work by Beutler (Beutler, 1961), the sampling points need not to be periodic and may vary by over 20 percent from the periodic signal points given by the *Nyquist criterion* without sacrificing capability of restoring the signal. Furthermore, Beutler (Beutler, 1966) states that error free recovery is feasible for irregularly spaced sampling points provided that the average sampling rate exceeds the *Nyquist* rate. The sampling positions, however, need to be precisely known.

3.3.1.4 Detector acceptance angle

In the previous section, the diffraction pattern for single wavelengths has been considered. It was shown that for constructive interference, the light is concentrated in the center of the diffraction pattern (called zeroth diffraction order), and that for destructive interference in the zeroth order most of the incident light is diffracted into angles off the center (M^{th} diffraction orders – see Eq. (3-6)). Zeroth and 1st diffraction orders are modulated π out of phase, meaning the 1st diffraction order carries maximum radiant flux when the zeroth diffraction order carries no flux and vice versa. Furthermore, it was shown that the zeroth diffraction order carries most of the radiant flux and that the propagation direction of the zeroth diffraction order is wavelength independent. Both are of particular interest for the interferometric use of the lamellar grating cells. Recall, that one needs to record the modulation of the radiant flux as a function of path difference or phase shift in an interferogram. High amplitude of the modulated radiant flux is desirable to obtain sufficient signal-to-noise ratios. To gain maximum amplitude modulation in the zeroth diffraction order, one must prevent higher order diffracted radiation from reaching the detector. In a noise-free system, the detector acceptance angle determines physically the modulation amplitude. Acceptance angles permitting the zeroth and first order diffracted light, result in a high intensity being transmitted to the detector at a low modulation amplitude as shown for the case of an acceptance angle of 0.15 radians for a cell of *design A* with a number of 12 mirror surfaces (Figure 3-8). Reducing the detector acceptance angle allows higher modulation amplitudes in the zeroth diffraction order. Figure 3-8 (b) compares the modulation amplitude for the three cell designs with respect to detector acceptance angle and a ratio of $w/\lambda=5$.

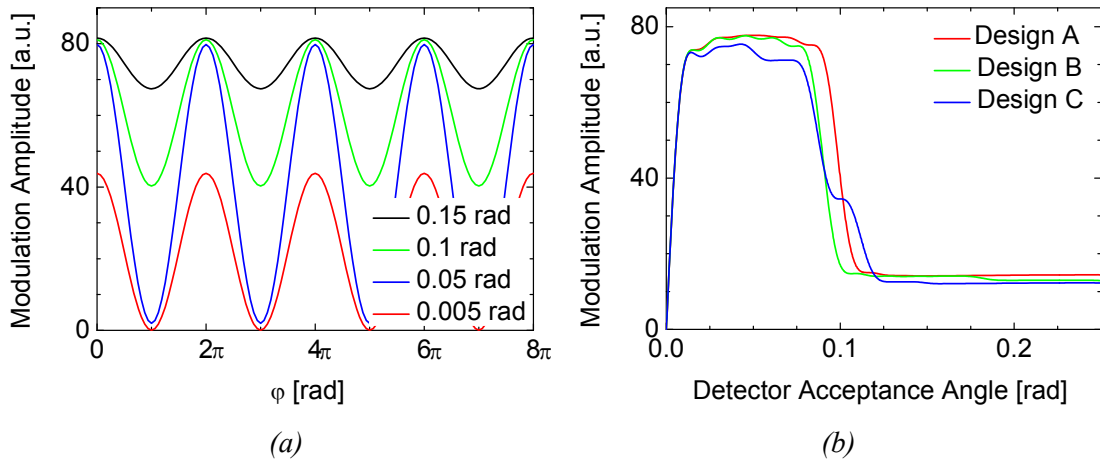


Figure 3-8: Modulation amplitudes as function of detector acceptance angles for cells of $P/\lambda=10$. (a) Modulation amplitudes as a function of phase shift φ and detector acceptance angle for cell design A and 12 mirror surfaces. (b) Comparison of cell designs A, B, and C.

The Figure shows that cell *design A* allows the highest modulation amplitude to an acceptance angle of 0.1 radians. A fact which is not surprising, as the cell design is made of alternating front and back facet mirrors of the same rectangular surface (w/l). In turn, both odd designs have either one or more mirrors of a bigger surface, and thus diffract to smaller angles. The amplitude modulation drops for detector acceptance angles bigger than the diffraction angle of the 1st diffraction order. We have seen that the diffraction angle of higher orders is inversely proportional to the ratio of the period P and wavelength λ (Eq. (3-6)).

For incident light containing many wavelengths, the ratio P/λ and thus the angles of higher diffraction orders differ. Larger ratios diffract higher orders to smaller angles and reduce the amplitude modulation at smaller detector acceptance angles, an effect which is shown exemplary in Figure 3-9. For a ratio P/λ of 30, the amplitude modulation reduces at smaller angles compared to a ratio of 10. The acceptance angle of the detector and the period of the grating should be chosen to allow highest amplitude modulation in spectral band to be observed.

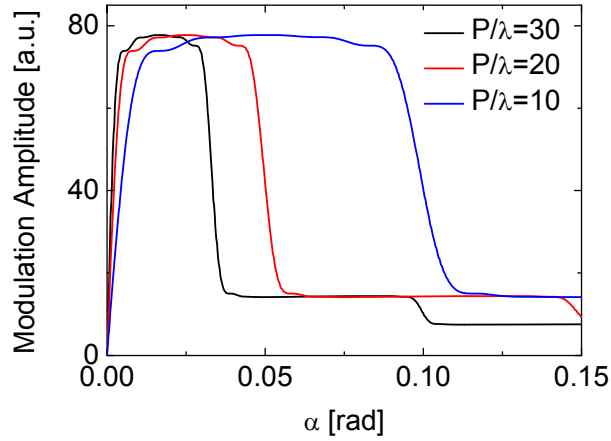


Figure 3-9: Modulation amplitude as a function of diffraction angle α and ratio P/λ for design A and $N=12$.

Two angles determine the choice of the detector acceptance angle:

- 1) the aperture angle of the zeroth diffraction order of the longest wavelength,
and
- 2) the diffraction angle of the 1st diffraction order of the shortest wavelength.

Highest modulation amplitude in a spectral band (λ_{\min} , λ_{\max}) is given if the conditions for the detector acceptance angle Ψ_A

$$\Psi_A = (\alpha_{ap})_{\lambda_{\max}}, \text{ and}$$

$$\sin(\alpha_{ap})_{\lambda_{\max}} < \sin(\alpha_d)_{\lambda_{\min}} - \sin(\alpha_{ap})_{\lambda_{\min}} \quad (3-17)$$

are met. The subscript d denotes the diffraction angle of the 1st diffraction order, and ap the aperture angle. Figure 3-10 shows the concept schematically, whereby the greyish hatched area demonstrates the diffraction angles which need to be prevented from entering the detector.

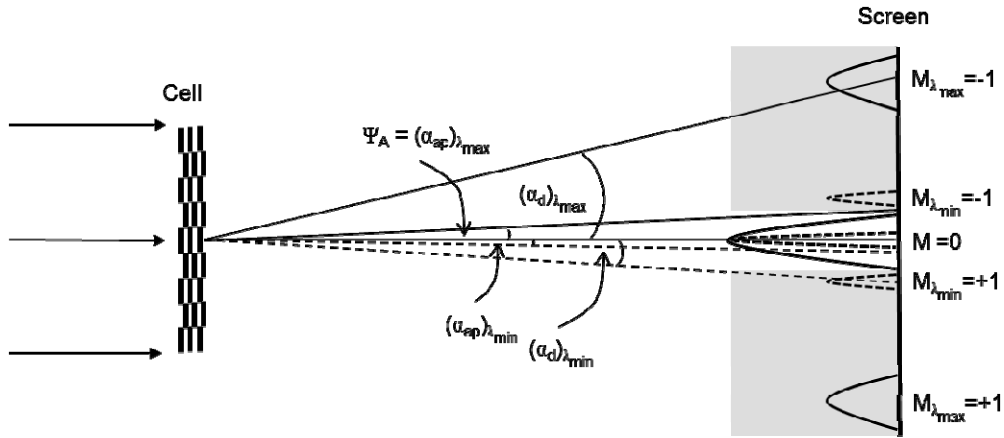


Figure 3-10: Concept of detector acceptance angle for maximum modulation amplitude for a spectrometer with a spectral working band ranging from λ_{min} , the shortest to λ_{max} , the longest wavelength component. Radiation transmitted or reflected from the grating cell is diffracted into angles off the optical axis. The diffraction angles are wavelength dependent and the acceptance angle of the detector needs to be chosen to transmit zeroth order (indicated by the whitish area at the screen) whereas higher diffraction orders are permitted (greyish hatched area) from reaching the detector plane. M denotes the diffraction order, Ψ_A , α_{ap} , and α_d the detector acceptance angle, the aperture angle, and the diffraction angle of the first diffraction order, respectively.

These conditions necessitate a number N_{MS} of mirror surfaces per cell:

$$\frac{N_{MS}}{2} - 1 > \frac{\lambda_{max}}{\lambda_{min}}, \text{ for design A, B} \quad (3-18)$$

$$\frac{N_{MS} - 3}{2} > \frac{\lambda_{max}}{\lambda_{min}}, \text{ for design C.} \quad (3-19)$$

With our earlier assumption of a minimum ratio $P/\lambda=10$ according to Wirgin's work (Wirgin, 1973), the shortest wavelength modulated at maximum amplitude is:

$$\lambda_{min} = \frac{P}{10 \left(\frac{N_{MS}}{2} - 1 \right)}, \text{ for design A, B,} \quad (3-20)$$

and

$$\lambda_{min} = \frac{P}{10 \left(\frac{N_{MS} - 3}{2} \right)}, \text{ for design C.} \quad (3-21)$$

At shorter wavelength the efficiency of modulation drops off. Larger numbers of mirrors per cell allow broader spectral working bands of the interferometer.

For a circular or square aperture limiting the detector acceptance angle, the length 'l' of the lamellae must satisfy the condition:

$$\sin(\beta_{ap})_{\lambda_{\max}} < \sin(\alpha_d)_{\lambda_{\min}} - \sin(\alpha_{ap})_{\lambda_{\min}} \quad (3-22)$$

$$\frac{\lambda_{\max}}{l} < \frac{\lambda_{\min}}{P} \left(1 - \frac{2}{N_{MS}} \right), \text{ for } N_{MS} > 2. \quad (3-23)$$

The benefit of a high amplitude modulation is demonstrated in Figure 3-11 (a). The figure compares the spectra of high and low amplitude modulation in combination with random noise. The bottom spectrum in Figure 3-11 (a) shows the normalized, noise-free spectrum for a single wavelength of $\lambda = 6 \mu\text{m}$ ($P/\lambda=26.6$) at an exemplary resolution, while the middle and the top curves show the spectrum in the case of a random noise of 10 % of the maximum intensity amplitude and an acceptance angle of 0.01 radians and 0.1 radians (Figure 3-11(a)), respectively. In both cases, the peak of a 6 μm wavelength spectral line (1667 cm^{-1}) is resolved. However, ghost peaks appearing in the spectrum of the low modulated signal, may distort nearby spectral information. In order to compare the quality of spectra, Bell (Bell, 1972, p. 7-8) describes a Quality Factor Q :

$$Q = MF \frac{B_{av}}{B_{rms}} \quad (3-24)$$

$$MF = \frac{\sigma_{\max} - \sigma_{\min}}{\Re} \quad (3-25)$$

where MF is the number of spectral elements in the spectral working bandwidth of the spectrometer, \Re the spectral resolution, B_{av} and B_{rms} the average signal level and the

average noise level, respectively. MF is also called the *multiplex factor* (Bell, 1972). Without specifying MF , Figure 3-11 (b) plots the averaged ratio of high modulated signal (0.01 radians acceptance angle) Q_h and low modulated signal (0.1 radians acceptance angle) Q_l with respect to various noise amplitudes. Accordingly, a high modulated signal allows a 6 times higher noise suppression in the spectrum at a random noise level of 1% the maximum amplitude, and at a noise level of 20% a 20 times higher noise suppression.

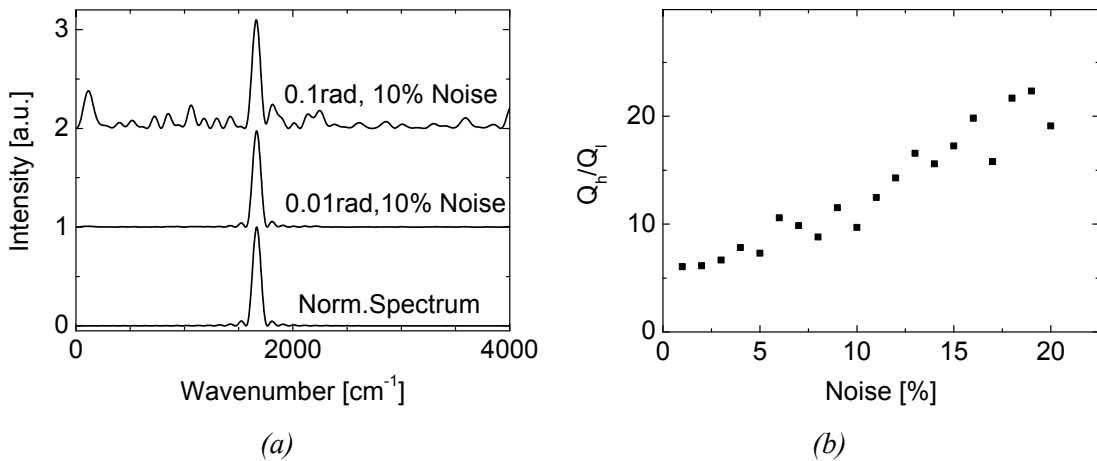


Figure 3-11: (a) Normalized spectra for low modulation amplitude (top), and high modulation amplitude (middle) at a random noise of 10 % the maximum signal amplitude, in comparison to noise-free spectra (bottom). (b) Quality ratio Q_h/Q_l as a function of noise level.

3.3.1.5 Long wavelength limitation

So far we have shown that the sampling interval of the interferogram and with it the minimum height stepping of the recessed micro mirror surfaces place a limitation to the maximum wave number the FTS can resolve. The restriction is imposed by the *Nyquist criterion* and relies purely on signal processing.

Furthermore, we have shown the influence of the detector acceptance angle on the amplitude modulation and derived critical design parameters. We have shown in Eq. (3-17) that the detector acceptance angle should be chosen smaller than the angle of the first diffraction order of the longest wavelength in the spectrum implying that large 1st order diffraction angles of long wavelengths are beneficial. However, on the long wavelength end of the spectrum to be resolved by the spectrometer, at small wave numbers, a physical limitation is placed on the lamellar grating spectrometers. Here, the prediction of the cosine modulation as a function of the optical path difference and wavenumber as the basis of the Fourier transform (Eq. 2-8) fails to predict the physics. The effect is known to lamellar grating interferometers as the *cavity effect* or *long wavelength limit*.

In the following the long wavelength limit will be briefly argued. The limit was studied in a number of references (Richards, 1964, Wirgin, 1973, Bell, 1972, and Gremaux and Gallagher, 1993) and thus not further theoretically investigated within the framework of this thesis. To avoid the cavity effect, we followed Wirgin's (Wirgin, 1973) thorough theoretical investigation for lamellar grating interferometers. A description of the effect in terms of waveguide theory can be found in reference (Bell, 1972). In its physical essence, the cavity effects stems from the polarization and damping effects of the electromagnetic radiation as it travels between the lamellae walls on its way towards and away from the back facet mirrors. The degree of which

depends on the conductivity of the lamellae walls, the depth of the lamellar grating, and the ratio of grating period and wavelength P/λ . For low ratios of grating period and wavelength the effect increases. As the electromagnetic wave passes along the lamellae sidewall, its electric field in the plane of the wall is attenuated. The damping of the electromagnetic wave distorts the cosine modulation in the interferogram and consequently results in false spectral information. In the work we have assumed $\lambda < w$ and treated problem as propagation in free space. For the hypothesis of perfectly conducting lamellae walls, Wirgin's study has shown that this assumption is justified for ratios of wavelength and grating period P/λ in excess of 10 (Wirgin, 1973).

3.3.1.6 Angle of incidence

One of the advantages of the FPP FTS concept is: The system spectral transmission band can be tailored and is less limited by the filter characteristics of the filter material of an amplitude beam splitter. However, this concept necessitates reflection optics. Its spectral performance is dependent on the optics and its illumination angles. In the following the effect of illuminating the MMA under an angle is studied.

3.3.1.6.1 Shadowing

If we assume ideally parallel rays are incident along the grooves of the MMA under an angle of $-\pi/2 < Y < \pi/2$ and $\Phi = \pi$ (Figure 3-3) all MMA mirror surfaces are uniformly illuminated and the interferometer generates the highest amplitude modulations. On the contrary, if the incident rays are inclined and no longer parallel to the grating grooves shadowing sets in. In this case, the front facet mirrors cast a shadow on the back facet mirror and reduce the net surface area illuminated and

reflected of the back facet mirrors. The 'loss' of mirror surface area for reflection from the back facet mirrors effectively reduces the modulation amplitude and limits the maximum high aspect ratio (h/w) of the MMA and subsequently the resolution of the interferometer. Figure 3-12 demonstrates the effect of shadowing for an exemplary inclination angle Φ of 85° ($\gamma = 0^\circ$) and an arbitrary wavelength. With increasing phase shift or equally spoken with increasing cell depth, the effective surface area illuminated and contributing to the reflection of back facet mirrors reduces linearly. The ratio of surface area of front to back facet mirrors (A_B/A_F) drops from 1 for equally illuminated surface area to 0, and the amplitude modulation reduces to a constant value. The constant value does not contain interferometric information and thus limits the maximum depth of the MMA. The effect is the same for all single cell designs, whereby design B balances the effect of shadowing by wider back facet surfaces and thus holds a slight advantage over the other designs - an advantage which only holds for a low number of mirror surfaces per cell.

In either case of illumination, it has to be pointed out, that ideally plane waves are merely a theoretical construct which hold for infinitely small source points. The physical size of real light sources implicates shadowing and thus it will remain present in the lamellar grating interferometer.

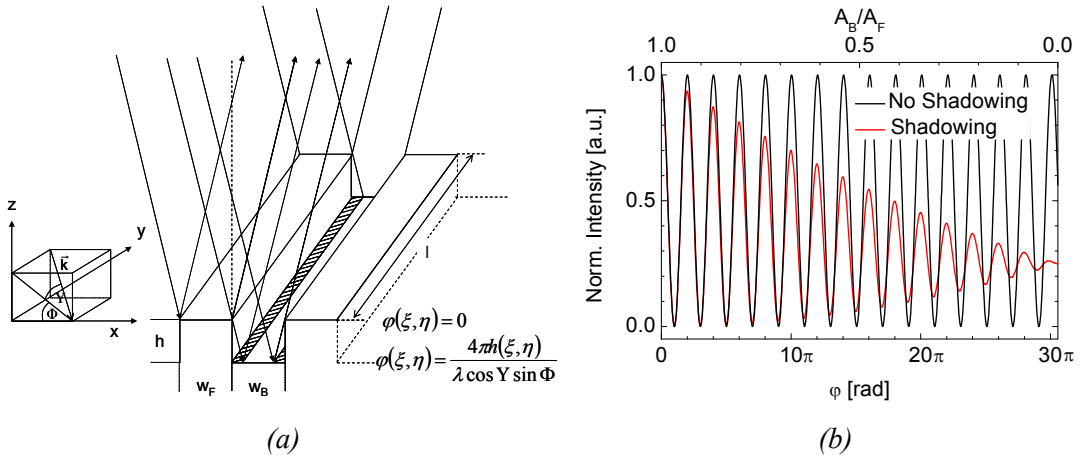


Figure 3-12: Effect of shadowing. (a) Schematic: For plane wave incidence, the front facet mirrors cast a shadow on the back facet mirrors (hatched surfaces). Denomination of angles: \vec{k} is the plane wave normal, Y the angle between \vec{k} and its projection in xz plane, Φ the angle between \vec{k} projection in the xz plane and the x axis. (b) Amplitude modulation as a function of phase shift ϕ for plane wave incident under an angle Y with $\Phi = \pi/2$ (black), and angle Φ with $Y = 0$ (red).

3.3.1.7 Extended sources

In section 2.2.7, we discussed the effect of extended sources on the computed spectrum. It was shown that the critical solid angle, places a physical limitation to the maximum obtainable optical path difference set by the maximum wavenumber in the spectrum and thus the resolution of the interferometer (see Eq. 2-32).

Combining Eq.(2-31) and (2-19), the critical solid angle, or the critical acceptance angle Ψ_c for a given resolution and highest wavenumber of the spectral band targeted is estimated:

$$\cos(\Psi_c) = 1 - \frac{\mathfrak{R}_{ILS}}{\sigma_{\max}}. \quad (3-26)$$

It determines the maximum acceptance angle under which rays can travel through the spectrometer and thus the acceptable size (D_s) of a source far away from the diffracting screen (Fraunhofer Field). Additional optical elements such as collimators can be added to optimize the system without altering the performance.

3.3.1.7.1 Spatial coherence

Dealing with extended sources instead of point sources unavoidably opens the discussion of *spatial coherence*. A source is said to be spatially coherent across its lateral dimensions when its emitted wave forms an interference pattern after transmission through an aperture containing two slits. The setup is known as Young's double slit experiment. In the experiment, the degree of spatial coherence is quantified by the contrast of the interference pattern formed in the Fraunhofer field.

One can refer to an extended source as a multitude of laterally displaced, infinitely small point sources. Each of these infinitesimal small source points located on the source plane parallel to the slit screen form identical interference patterns emerging under different diffraction angles. The forming interference patterns of individual source points on the detector plane are intensity modulations of high contrast, referred to as fringes. The superposition of the interference patterns of all individual source points results in a loss of the visibility of the fringes or contrast. An infinitesimal small source point located on the optical axis produces fringes at diffraction angles $\alpha = m\lambda/a$ with $m = 0; \pm 1; \pm 2; \dots$ for maxima, and $m = \pm \frac{1}{2}; \pm \frac{3}{2}; \pm \frac{5}{2}$ for minima (small angle approximation). On the contrary, fringes produced from light emanating from an infinitesimal small source point on the edge of the source at $D_s/2$ are shifted by an amount of $m\lambda/a + D_s/(2r)$, where the letter r denotes the distance between source and diffraction screen (see Figure 3-13).

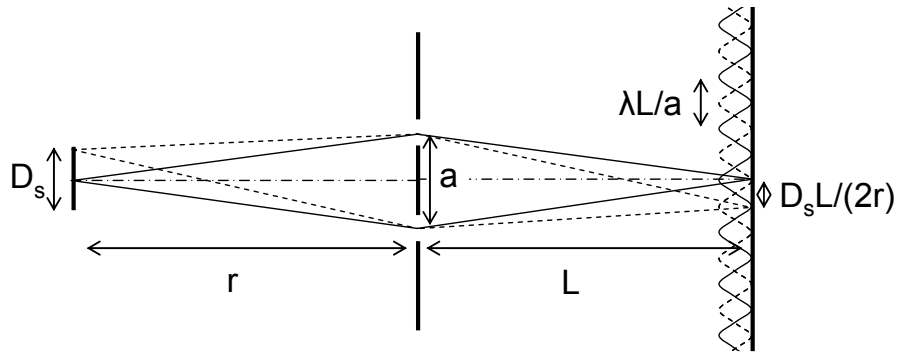


Figure 3-13: Diffraction patterns from two narrow slits at distance a , originating from the central part of the source (solid curve) and from the edge of the source at height $D_s/2$ (dashed curve). D_s denotes the source width, a slit spacing, r and L the distance from source to diffraction screen and from diffraction screen to the detector plane, respectively. The slit distance a is such that the two patterns are in antiphase. This occurs for $a = \lambda r/D_s$. after reference (Veen and Pfeiffer, 2004).

Given a slit spacing of $a = \lambda r/D_s$, minima from the edge source point overlap with maxima from the point source on the optical axis and the visibility of the fringe pattern vanishes. This distance is defined as the spatial coherence length

$$l_c = \frac{\lambda r}{D_s}. \quad (3-27)$$

As all elementary areas of the extended source radiate wavefronts whose amplitude and phase rapidly fluctuate in time, the interference pattern can be found by (incoherent) summation of intensities contributed by each of the area elements over the entire source area, whereby the intensity of each contribution element is weighted according to the intensity profile of the source (Veen and Pfeiffer, 2004).

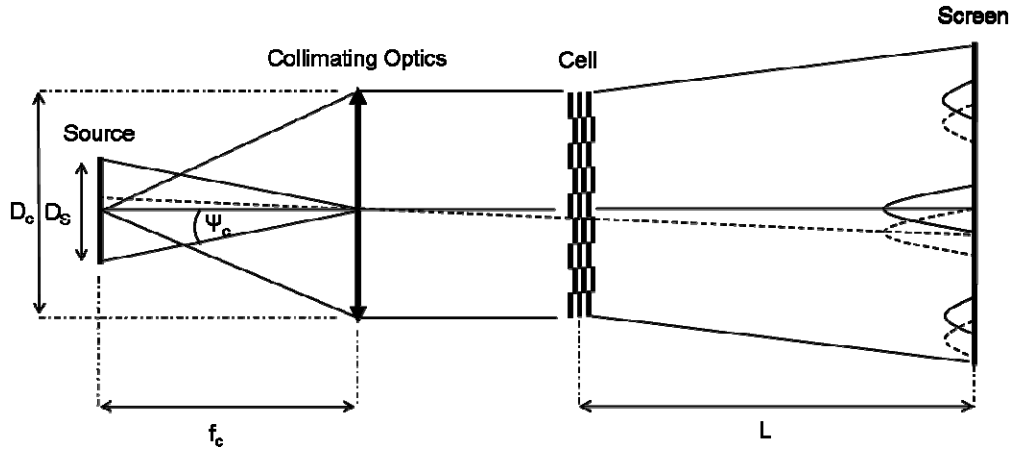


Figure 3-14: Influence of an extended source on the diffraction pattern of a cell. D_s , and D_c denote the source and collimated beam diameter.

Applying the considerations of Young's experiment to the MMA design, the maximum acceptance angle is calculated. Figure 3-14 demonstrates the effect of extended source size on the diffraction pattern generated. Radiation emanating from source points off the optical axis produces the same intensity pattern propagating under an angle with respect to the optical axis (see dashed line Figure 3-14). For a spatial coherence length l_c of $P/2$, the 1st diffraction order of a source point on the optical axis overlaps with the zeroth diffraction order of an off axis source point at $\pm D_s/2$. This marks the maximum acceptance angle in terms of spatial coherence.

$$\tan(\Psi_c) \leq \frac{\lambda}{P}. \quad (3-28)$$

Subsequently, the source acceptance angle and thus the acceptable source size for a given collimator focus length are either limited by Eq. (3-26) or Eq. (3-28) whichever is smaller. Both cases depend on the highest frequency component in the spectra to be examined.

$$\cos(\Psi_c) = \min \left[\left(\frac{(P\sigma_{\max})^2}{\sqrt{1 + (P\sigma_{\max})^2}} \right), \left(1 - \frac{\mathfrak{R}_{ILS}}{\sigma_{\max}} \right) \right] \quad (3-29)$$

3.3.1.8 Spatial filtering and spectrometer throughput

For the filtering of the single cells intensities arranged in the MMA, we propose a system consisting of a focusing lens and an aperture. The lens is placed perpendicular to the optical axis at a distance greater than its focal length downstream the MMA, depending on the magnification or demagnification required for the imaging. A lens in the imaging condition such as $2f$ to $2f$ offers the advantage to separate the single cells intensities spatially. The aperture is positioned in the focal plane of the lens as shown in Figure 3-15; the detector is placed in the image plane. In paraxial approximation, a converging lens on the optical axis introduces a phase shift to the incoming wave front as described in reference (Goodman, 1996).

$$U(l) = U(Pi) e^{-i \frac{k}{2f} (x^2 + y^2)} \quad (3-30)$$

$U(l)$ describes the phase change in the wave field just behind the lens surface. f symbolizes the focal length of the lens. Thus, in the focal plane of the lens the spherical phase curvature of the diffraction screen cancels with the phase curvature introduced by the lens (compare Eq. (3-3)), leaving a Fourier transform relationship for the complex amplitude. Placing a spatial filter in the focal plane is a way of filtering out higher diffraction orders. Rays parallel to the optical axis of a focusing lens converge to a point on the optical axis at the focal length of the lens, while rays travelling at an angle with respect to the optical axis are brought to a focal point on the focal plane off the optical axis. Thus, an aperture centered on the optical axis transmits all zero order diffracted light and blocks higher order diffracted light. The diameter of the aperture is given by the acceptance angle Ψ_A . The acceptance angle depends on the cell design, the number mirror surfaces per cell, and the highest frequency component in the spectrum. For the MMA as well as in the case of single

cells, the acceptance angle Ψ_A is identical to the detector acceptance as introduced in section 3.3.1.4. It follows:

$$\sin(\Psi_A) < \frac{1}{P\sigma_{\max}} \left(1 - \frac{2}{N_{MS}} \right), \quad (3-31)$$

for $N_{MS} > 2$.

For a rectangular cell design as introduced earlier, the acceptance angle can be split up into its two perpendicularly oriented components:

- a) The acceptance angle transverse to the lamellae walls determined by Eq. (3-29) (Figure 3-15), and
- b) alongside the lamellae walls, the acceptance angle is limited by the condition stated in Eq. (3-32). Alongside the lamellae walls it is specified according to the critical acceptance angle of the spectrometer (compare Eq. (3-26)).

$$\cos(\Psi_A) < \left(1 - \frac{\mathfrak{R}_{ILS}}{\sigma_{\max}} \right) \quad (3-32)$$

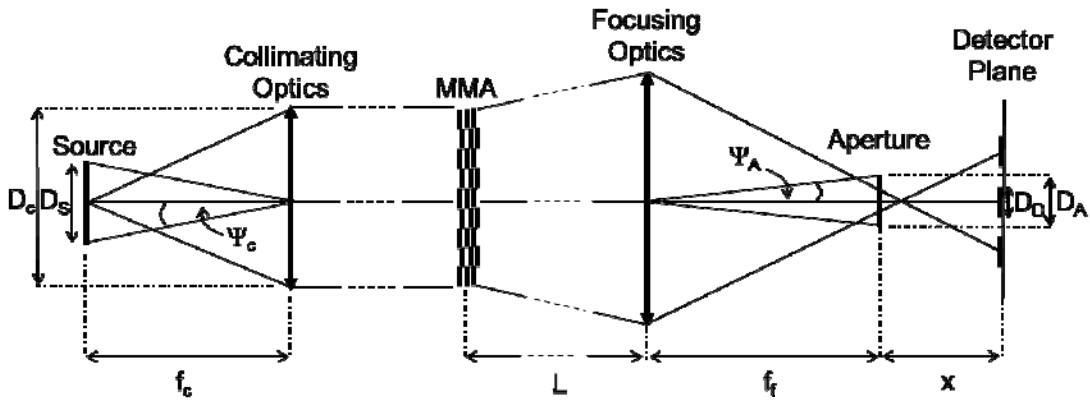


Figure 3-15: Schematic of spatial filtering. Radiation emitted from the source of diameter D_s is collimated by a collimator-optics of diameter D_c and focal length f_c and directed towards the MMA. Upon transmission or reflection from the MMA the diverging beams are focused by a focusing optics of focal length f_f onto an aperture of either a diameter D_A for circular apertures or of width D_A for rectangular apertures. After transmission through the aperture the MMA is imaged onto the detector plane a distance x from the aperture. D_D denotes the diameter or pixel width, Ψ_c and Ψ_A the critical and the detector acceptance angle, respectively. The broken lines indicate that the drawing is not in scale.

The use of apertures to filter effectively reduces the spectral flux passing through the optical system. A bundle of rays transmitted through the spectrometer may either be defined by the acceptance angle of the source or the acceptance angle of the detector whichever is smaller. The capacity of the spectrometer to collect and transmit spectral power is known as the spectrometers *throughput* or *étendue* \dot{E} and is quantified by:

$$\dot{E} = \Omega_c A_S = \Omega_D A_D, \quad (3-33)$$

where Ω_c and Ω_D denote the solid angles of the collimator and condenser, A_S and A_D the surface areas of the source and the detector area, respectively.

Thus, discussing *throughput*, the influence of the aperture size has to be mentioned. It can be easily shown that for a rectangular cell design, rectangular apertures permit higher *throughput* compared with circular apertures when the radius or the width of the aperture is chosen to pass zeroth diffraction orders only. For any possible acceptance angle either limited through the constraints for high resolution and/or the size of the source, the rectangular area, and thus the *throughput* is a minimum of 27 % higher. As an example, the gain in *throughput* for a medium resolution spectrometer of 10 cm^{-1} and a highest frequency component of 2000 cm^{-1} is a factor of 5 using rectangular aperture.

3.3.1.9 Reflection of metals

Fresnel first derived reflection and refraction formulas for homogeneous, isotropic and nonconductive materials.

In metals, however, free electrons in the metallic lattice give rise to conduction, and simultaneously account for the high reflectivity of electromagnetic radiation (Born and Wolf, 1997, p. 615ff.). Conduction, in turn, is inevitably accompanied by the appearance of Joule loss whereby electromagnetic energy is dissipated into heat. As a result the electromagnetic radiation is attenuated in conducting materials. To account for the attenuation losses, the index of refraction may be written as a complex quantity \hat{n} in conducting materials, which is wavelength dependent. It is given by:

$$\hat{n} = n + i\kappa, \quad (3-34)$$

where κ is called the attenuation coefficient.

Fresnel's reflection and refraction formulas are then rewritten in terms of a complex refraction index \hat{n} . A thorough derivation of the reflection formulas of metals is given in reference (Born and Wolf, 1997, p. 629). Here, only the required formulas are stated.

For the electric wave vector perpendicularly (TE wave) and parallel (TM wave) oriented to the plane of incidence, the reflectivity is given by (Born and Wolf, 1997, p. 628):

$$R_{\perp} = \frac{(n_1 \cos(\theta) - u)^2 + v^2}{(n_1 \cos(\theta) + u)^2 + v^2}, \text{ and} \quad (3-35)$$

$$R_{\parallel} = \frac{\left[(n_2^2 - \kappa_2^2) \cos(\theta) - n_1 u \right]^2 + [2n_2 \kappa_2 \cos(\theta) - n_1 v]^2}{\left[(n_2^2 - \kappa_2^2) \cos(\theta) + n_1 u \right]^2 + [2n_2 \kappa_2 \cos(\theta) + n_1 v]^2}, \quad (3-36)$$

with

$$2u^2 = n_2^2 - \kappa_2^2 - n_1^2 \sin^2(\theta) + \sqrt{[n_2^2 - \kappa_2^2 - n_1^2 \sin^2(\theta)]^2 + 4n_2^2 \kappa_2^2}, \text{ and} \quad (3-37)$$

$$2v^2 = -[n_2^2 - \kappa_2^2 - n_1^2 \sin^2(\theta)] + \sqrt{[n_2^2 - \kappa_2^2 - n_1^2 \sin^2(\theta)]^2 + 4n_2^2 \kappa_2^2}. \quad (3-38)$$

n_1 is the refractive index of the homogeneous material (e.g. vacuum) from which the electromagnetic wave is incident onto the metal surface under an angle θ (with respect to the surface normal), and n_2 and κ_2 denominate the real and imaginary part of the complex refractive index of the metal, respectively. Thus, the reflection of electromagnetic radiation is dependent on the wavelength, the angle of incidence θ and its polarization.

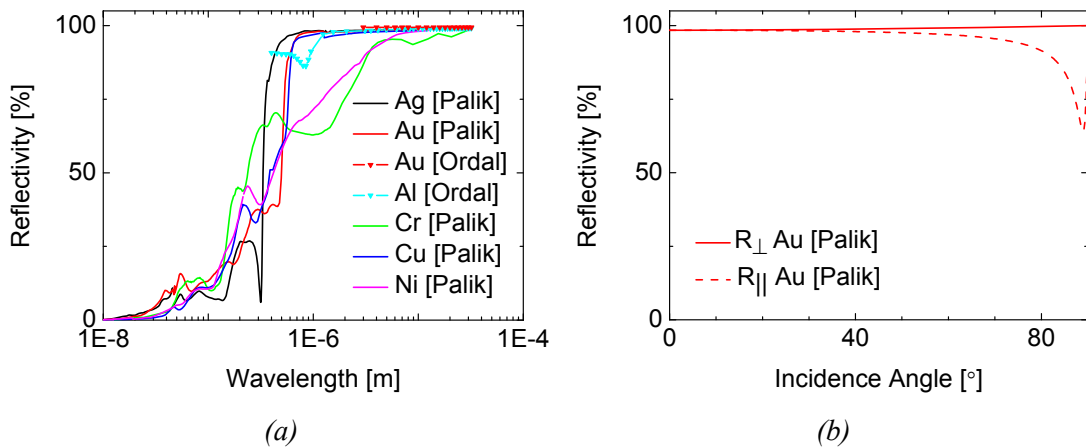


Figure 3-16: (a) Calculated reflectivity of metals at perpendicular incidence. (optical constants taken from references (Palik, 1998 and Ordal et al., 1982)). (b) Calculated reflectivity of gold for perpendicular R_{\perp} and parallel R_{\parallel} polarized light for a wavelength of $10 \mu\text{m}$.

Figure 3-16 (a) shows the calculated reflectivity of metals commonly used in the field of micro engineering as a function of wavelength at perpendicular incidence. For the calculation, the optical constants published by Palik (Palik, 1998) and Ordal et al. (Ordal et al., 1982) were used. As it can be seen in the figure, the reflectivity of metals is wavelength dependent. In the ultra violet part of the spectrum, aluminium shows the highest reflectivity, whereas in the visible silver reflects the best. In the

regime ranging from near infrared to the far infrared, metals such as aluminium, copper, gold, and silver have the highest reflectivity. Thus, depending on the spectral working range of the FPP FTS, a suitable metal for the reflection surface may be selected.

Silver and gold feature the highest reflectivity throughout the entire infrared, whereby gold surfaces are of particular interest. Unlike silver which tarnishes and therefore requires a protection layer, gold is inert and is commonly used as reflective metal coating.

The effect of incidence angle on reflectivity of gold is demonstrated in Figure 3-16 (b) at a wavelength of 10 μm . The figure shows that the reflection of parallel polarized light reduces continuously as the incidence angle increases until the pseudo-Brewster-angle and increases afterwards again. The reflection for perpendicular polarized light in turn increases with increasing incidence angle. For small incidence angles, both polarization directions are evenly reflected and thus the effect of polarization through the reflection from gold surfaces may be neglected for the design of the FPP FTS.

3.3.1.9.1 Estimation of required layer thickness

To estimate the required reflection layer thickness, we follow Born (Born and Wolf, 1997, p. 628ff.). The reflectivity of a conductor of thickness t between two dielectric media of refractive index n_1 and n_3 is calculated by:

$$R = \frac{R_{1,2}^2 e^{2v\eta} + R_{2,3}^2 e^{-2v\eta} + 2R_{1,2}R_{2,3} \cos(\phi_{2,3} - \phi_{1,2} + 2u\eta)}{e^{2v\eta} + R_{1,2}^2 R_{2,3}^2 e^{-2v\eta} + 2R_{1,2}R_{2,3} \cos(\phi_{1,2} + \phi_{2,3} + 2u\eta)} \quad (3-39)$$

with

$$\eta = \frac{2\pi}{\lambda_0} t, \quad (3-40)$$

$$R_{1,2}^2 = \frac{(n_1 \cos(\theta_1) - u)^2 + v^2}{(n_1 \cos(\theta_1) + u)^2 + v^2}, \quad \tan(\phi_{1,2}) = \frac{2vn_1 \cos(\theta_1)}{u^2 + v^2 - n_1^2 \cos^2(\theta_1)}, \quad (3-41)$$

$$R_{2,3}^2 = \frac{(n_3 \cos(\theta_3) - u)^2 + v^2}{(n_3 \cos(\theta_3) + u)^2 + v^2}, \quad \tan(\phi_{2,3}) = \frac{2vn_3 \cos(\theta_3)}{u^2 + v^2 - n_3^2 \cos^2(\theta_3)}, \quad (3-42)$$

and

$$n_3 \sin(\theta_3) = n_1 \sin(\theta_1). \quad (3-43)$$

$R_{1,2}^2$ and $R_{2,3}^2$ is the reflectivity for perpendicularly polarized light at the interface between the dielectric medium (1) and the conductor (2), and between the conductor (2) and the dielectric medium (3) behind the conductor, respectively. $\phi_{1,2}$ and $\phi_{2,3}$ are the phase shifts introduced at the respective interfaces. To estimate the required layer thickness at perpendicular incidence, Eq. (3-39)–(3-43) are sufficient. Figure 3-17 shows the reflectivity with respect to the wavelength for metal foils ranging from 20 nm to 100 nm thickness. Accordingly, in the infrared gold reaches 95 % reflectivity at thicknesses beyond 40 nm. Thus, reflection layers for operation of the FPP FTS in the infrared part of electromagnetic spectrum require at least 40 nm thicknesses to preserve the high reflectivity of gold.

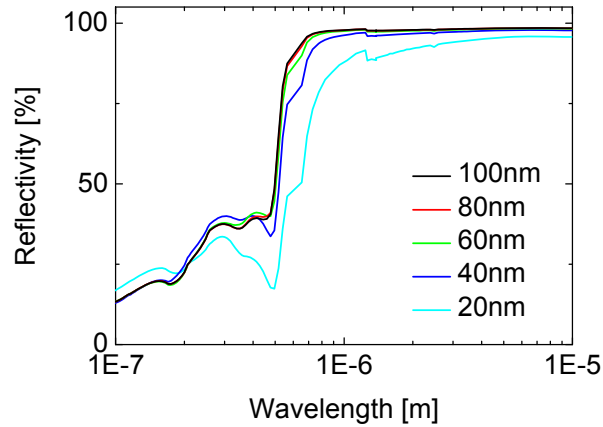


Figure 3-17: Calculated thin film reflectivity of gold at perpendicular incidence (optical constants taken from reference (Palik, 1998)).

3.3.1.9.2 Influence of surface roughness on reflection

The previously introduced formulas assume ideal, perfectly smooth mirror surfaces. However, real surfaces possess surface irregularities departing from the ideally smooth case. This departure is quantified as surface roughness. Its influence on the specular reflectance, when the heights of the surface irregularities are small compared to the wavelength, is discussed in references (Bennett and Porteus, 1961), (Bennett and Bennett, 1967), and (Porteus, 1963). For normally incident light and a Gaussian distribution of roughness values, the observed reflectance in specular direction R is given by

$$\frac{R}{R_0} = e^{-(4\pi r_{rms}/\lambda)^2} + \left[1 - e^{-(4\pi r_{rms}/\lambda)^2}\right] \left[1 - e^{-2(\pi r_{rms} \alpha/m\lambda)^2}\right] \quad (3-44)$$

where R_0 is the reflectance of a perfectly smooth surface of the same material as introduced in the previous chapter, r_{rms} is the roughness (root mean square value), λ the wavelength, m the root mean square slope of the irregularities, and α the half acceptance angle of the measuring instrument. The first term of Eq. (3-44) considers the coherent reflectance and the second term accounts for the incoherent, diffuse

reflectance. Comparing both terms, the second term is strongly wavelength dependent (λ^{-4}) and for small surface roughness and comparable large wavelengths, specular reflection dominates. Figure 3-18 depicts the influence of the root-mean-square roughness on the specular reflection for different wavelengths. The relative reflectance R/R_0 is in the form of a Gaussian which approaches zero for $r_{rms}/\lambda \approx 1/5$. Greater than 67 % relative reflection is given for ratios of $r_{rms}/\lambda \leq 1/20$ and serves in the work as reference value.

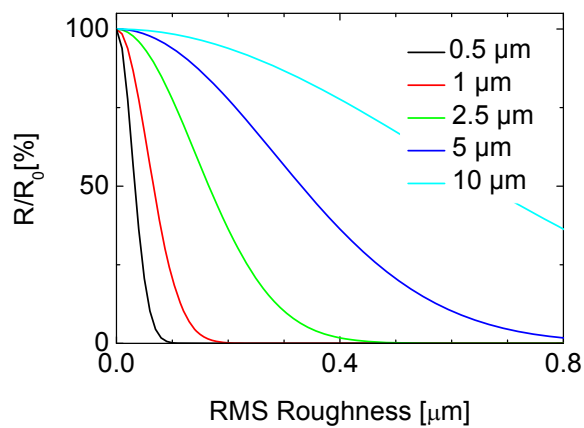


Figure 3-18: Reduction of specular reflectivity as a function of mean-square surface roughness after (Bennett and Porteus, 1961), (Bennett and Bennett, 1967), and (Porteus, 1963) for various wavelengths from 0.5 to 10 μm .

3.4 Summary

After a review of state-of-the-art miniature spectrometers, chapter three examined the principle of the FPP FTS in theory. The concept of the spectrometer was introduced and important spectrometer parameters elaborated. The MMA forming the core of the spectrometer was discussed in detail. We studied different rectangular MMA cell designs and demonstrated the intensity modulation of the zeroth diffraction order as a function of path difference needed for its interferometric use. On the basis of *Nyquist criterion* and *Shannon's Sampling theorem*, we derived the minimum stepping height of the back facet micro mirrors and number of MMA cells required to obtain spectra for a given spectral band and resolution. Furthermore, the influence of the detector acceptance angle on the modulation of the amplitude in the zeroth diffraction order was studied. Parameter dependencies such as the influence of cell number, ratio of grating period and wavelength, aperture as well as detector acceptance angle on the amplitude modulation were elaborated. We demonstrated the importance of high amplitude modulation in the presence of noise for the retrieval of spectra. The effect of shadowing through inclined off-axis illumination was shown to present a resolution limitation and thus requires illuminations inline with the lamellae walls. Critical acceptance angles for extended sources together with a spatial filtering technique to read the single MMA cells intensities with a detector were worked out. We showed that for rectangular MMA cells a rectangular spatial filter allows highest throughput. The concept of the long wavelength limit of lamellar grating interferometers was introduced, and the reflection of metals was studied in detail.

4 FABRICATION

4.1 Introduction

This chapter focuses on the fabrication of the micro mirror array (MMA). Based on the spectrometer specifications worked out in chapter three, this chapter first summarizes the parameters determining the MMA design and discusses key-manufacturing issues for MMA's tailored to work in the visible or infrared spectral bands. Subsequently, state-of-the-art fabrication technology capable to produce three dimensional MMA is reviewed. A potential fabrication process that is based on a novel kind of 3D X-ray lithography is proposed and its feasibility investigated. Process architecture ranging from the development of an exposure station enabling 3D x-ray lithography to the fabrication of novel X-ray stencil masks and finally the 3D micromanufacturing of stepped MMA micro-mirror surfaces is demonstrated.

4.2 MMA design parameters

The targeted resolution (\mathfrak{R}_{ILS}) and the spectral working band $\Delta\sigma$ ($\sigma_{\max}-\sigma_{\min}$) are the two spectrometer parameters primarily determining the design of the MMA. Provided both parameters are given, Table 4-1 lists functions specifying MMA design parameters.

According to these MMA design parameters, Table 4-2 specifies example MMA parameters for a spectrometer working in the visible or infrared spectral bands at exemplary resolutions. The case study in the visible spectral band, focuses on comparable specifications of reported miniature spectrometers (section 3.2). Most of these work at a wavelength resolution in the range of 2-10 nm. The example in the

near infrared band focuses on the telecommunication band which is of high interest in high-speed internet connections.

Table 4-1: MMA design parameters

| | |
|---|---|
| MMA design parameter | \mathfrak{R}_{ILS} : Resolution [1/cm]; σ_{\max} and σ_{\min} : Highest and lowest frequency component in the spectrum [cm^{-1}]; $\Delta\sigma = (\sigma_{\max} - \sigma_{\min})$: Spectral working band [cm^{-1}]; |
| Number of MMA cells N_{Cell} | $N_{Cell} \geq \frac{\Delta\sigma}{\mathfrak{R}_{ILS}}$, for $\Delta\sigma = \frac{\sigma_{\max}}{n}$, $n = 1, 2, 3, \dots$ |
| Maximum optical path difference δ_{\max} | $\delta_{\max} = \frac{1}{2\mathfrak{R}_{ILS}}$ |
| Sampling b | $b \leq \frac{1}{2\Delta\sigma}$, for $\Delta\sigma = \frac{\sigma_{\max}}{n}$, $n = 1, 2, 3, \dots$ |
| Minimum micro-mirror period P_{\min} | $P_{\min} = \frac{10}{\sigma_{\min}}$ |
| Minimum Number of micro mirrors per cell N_{MS} | $N_{MS} > 2 \left(\frac{\sigma_{\max}}{\sigma_{\min}} + 1 \right)$ |
| Micro mirror length l (circular/ square aperture limiting detector acceptance angle) | $l > \left(1 - \frac{2}{N_M} \right) \frac{\sigma_{\max}}{\sigma_{\min}}$, for $N_L > 2$. |
| Mirror inclination ν | $\nu < \tan^{-1} \left(\frac{1}{4\sigma_{\max} l} \right)$ |
| Surface roughness reflection layer r_{rms} | $r_{rms} \leq \frac{1}{20\sigma_{\max}}$ |
| Critical acceptance angle ψ_c | $\psi_c < \min \left[\cos^{-1} \left(\sqrt{\frac{(P\sigma_{\max})^2}{1 + (P\sigma_{\max})^2}} \right), \cos^{-1} \left(1 - \frac{\mathfrak{R}_{ILS}}{\sigma_{\max}} \right) \right]$ |

Large data transmission rates in fiber optic connections require wavelength multiplexing and de-multiplexing techniques capable to work at fastest rates. The use of the FPP FT interferometer as a wavelength de-multiplexer presents a potential application in the near infrared. The mid- and far-infrared examples focus on fingerprint region and substance identification applications at moderate resolution.

Table 4-2: Sample spectrometer layouts

| MMA parameter | Visible | NIR | MIR | MIR | FIR |
|--|-----------------|----------------|----------------------|----------------------|------------|
| | | Telecom. band: | Finger-print-region: | Finger-print-region: | |
| $\lambda_{\min} - \lambda_{\max}$ [μm] | 0.38 - 0.75 | 1.4 - 1.65 | 6 - 25 | 6 - 16 | 25 - 100 |
| $\sigma_{\max} - \sigma_{\min}$ [cm^{-1}] | 26,316 - 13,333 | 7,143 - 6,061 | 1,667 - 400 | 1,667 - 625 | 400 - 100 |
| $\mathfrak{R}_{ILS,\lambda}$ [nm] | 5 | 1 | | | |
| \mathfrak{R}_{ILS} [cm^{-1}] | 90 | 4 | 4 | 25 | 4 |
| N_{Cell} | 148 | 300 | 418 | 68 | 75 |
| δ_{max} [μm] | 56 | 1,250 | 1,250 | 200 | 1,250 |
| b [μm] | 0.38 | 4.2 | 3 | 3 | 12.5 |
| P_{min} [μm] | 7.5 | 16.5 | 250 | 160 | 1,000 |
| N_{MS} | 6 | 5 | 11 | 8 | 11 |
| l [μm] | 52 | 33 | 1,274 | 568 | 4,889 |
| v [mrad] | 1.8 | 10 | 1.2 | 2.64 | 1.3 |
| Ψ_c [mrad] | 51 | 34 | 24 | 37 | 25 |
| r_{rms} [μm] | 0.02 | 0.07 | 0.3 | 0.3 | 1.25 |

As expected, the visible spectral band imposes stringent requirements on surface roughness, parallelism, and stepping of the MMA mirror surfaces. An MMA operating in the visible demands a 20 nm surface roughness and back facet mirror stepping of 190 nm (remember twice the optical path at reflection for perpendicular incidence). Spectrometers working in the longer wavelength regime, moreover in narrow spectral band such as the presented telecommunication band, require a surface roughness of 70 nm and for perpendicularly incident radiation a back facet mirror stepping of 2.1 μm , instead. The mirror size is 33 times 8.25 μm^2 . In comparison, broader working bands such as the complete finger-print region necessitate a mirror stepping of 1.5 μm , and, given a square or circular aperture is used, mirror surfaces of 125 times 1,250 μm^2 . Lower resolution and narrower working band allow cell number, mirror size and mirror number reduction as shown for the 25 cm^{-1} resolution

MIR spectrometer. Surface roughness requirements reduce to 300 nm and 1.25 μm in the MIR and FIR spectral range, respectively.

With respect of the above examples, the following sections of the chapter discuss state-of-the-art manufacturing techniques capable to produce three-dimensional MMA structures.

4.3 3D micro-fabrication technologies – A review

The MMA structure is a complex three-dimensional (3D) shape. The stepped back facet mirrors form an element with hundreds depth levels and mirror surfaces at the micrometer scale. Such fine structures naturally calls for micro-fabrication techniques based on lithography. In a standard lithography process, a two-dimensional mask pattern is projected onto a photosensitive polymer matrix and its pattern is transferred into the thickness of the polymer. These so-called quasi-3D structures permit the precise manufacturing of the fine micro-scale structures but not the fabrication of multilevel surfaces.

To overcome the limitation various methods are reported in the literature. Among them, multilevel photoresist layers which consecutively structure negative tone photoresist layer by layer (Jian et al., 2001 and Mata et al., 2006) as well as alternating processes using lithography to pattern a layer and subsequent DRIE etching to transfer the pattern into the depth were reported to produce multilevel shapes such as diffractive optical elements (Taghizadeh et al., 1997). Both methods, however, are limited to a relatively small number of surface levels. Taghizadeh et al. e.g. fabricated a maximum of 8 levels. Moreover, multiple exposure steps require accurate mask alignments making this technique cumbersome for hundreds of depth levels.

Grey-tone lithography enhances standard two-dimensional lithography and permits multilevel three-dimensional structuring with a single exposure. In grey-tone lithography, the mask consists of a two-dimensional geometry containing variable optical transmission zones. When these types of masks are used in a lithographic step, the transmission zones modulate the light intensity and form dose grey-levels in exposed photoresist thus generating a three-dimensional photoresist shape. To form the transmission zones several approaches are reported in literature. Oppliger et al. (Oppliger et al., 1994) report two types of grey-tone mask approaches, namely pulse-width-, and pulse-density-modulation. In both cases, dots of a size below the resolution limit of the exposure tool are arranged in the transparent part of the chromium mask (two-dimensional geometry) and reduce the transmitted intensity. Using an e-beam mask writing system, they produced an 8 level grey-tone chromium mask which they used with a g-line stepper (436 nm wavelength) to shape a 2 μm thick positive resist. Subsequently, the resist profile was transferred 1:1 into the substrate by plasma etching techniques. Kalus et al. (Kalus et al., 1998) reported a 5 nm peak-to-valley resist roughness at a 6.9 μm high prism-like structure using a 15 level pulse-width-modulated grey-tone mask exposed with g-line exposure tool. Yao et al. (Yao et al., 2001, and Gao et al., 2002) generated a grey-tone mask for g-line exposure by varying the dot size and dot position and produced 4 μm deep and 38 μm wide spherical micro-lenses in a lens array.

Despite its wide range of applications, the grey-tone technique using UV exposure stations is limited to shallow etch depth and low aspect-ratios. In contrast, synchrotron X-ray lithography is known as a lithographic tool providing the capability to produce high aspect ratio micro-structures (Becker, 1986). Thus, Cabrini et al. (Cabrini et al., 2000) combined X-ray lithography with the grey-tone X-ray mask. They produced a 4

level grey-tone mask by varying the gold absorber thickness. The varying gold absorber thickness in turn necessitates multilevel structuring and multiple electro-deposition steps to produce the gold absorber layers of required thicknesses, making the technique tedious and finally impractical for hundreds of depth steps as required for the MMA structure. To overcome these difficulties Kudryashov (Kudryashov and Lee, 2001) proposed and tested grey-tone mask for X-ray lithography which base on the grey-tone mask presented for UV lithography. Because of the short X-ray wavelengths and thus the required small dot size, the author proposes to increase the gap between mask and resist thereby making use of shadow blurring. This technique, however, requires resist reflowing at 190 °C after development to produce 20 height steps in 1.75 μm thick resist making it difficult to adapt in case of real 3D-shaped structures. Inclined absorber structures forming a grey- tone X-ray masks and slanted surface profiles in the resists were reported by Mekar (Mekar et al., 2007). Also inclined X-ray exposures to fabricate tetrahedral three-facet micro mirrors with surface roughness (rms) below the 10 nm level were reported by Oh et al. (Oh et al., 2001).

A different method to produce 3D geometries utilizing the properties of synchrotron X-rays was presented by Nishi et al. in 1999 (Nishi et al., 1999, Katoh et al., 2000, and Katoh et al., 2001). The Japanese group used an 80 μm diameter pinhole mask to form an X-ray pencil beam which irradiated a substrate under an angle while it was rotated on a stage. The intense beam allows the three dimensional micromachining of cone, trapezoidal, and helical structures. With the presented setup they etched PTFE at an etching rate of 100 μm per minute and were able to achieve a 110 nm surface roughness at the bottom of structure. In 2000, Tabata et al. (You et al., 2000) proposed a moving mask technique capable to produce precise 3D shapes. Unlike

other grey-tone techniques, the moving mask technology forms a locally variable dose profile by moving the mask with respect to the substrate. In 2006, Fukuda et al. (Fukuda, 2006) showed the capability of the technique to produce blazed diffraction gratings. Using a binary mask scanned across the resist surface they were able to form blazed mirror surfaces of 9.4 nm surface roughness. On the basis of their experiments they estimated a etch depth control at a precision of 18 nm. Moreover, using bias dosages they were able to avoid non-linear resist sensitivities resulting in linear dose-etching rate dependence and reduced surface roughness. Provided sharper absorber edges the authors expect further surface roughness improvement. On the basis of the moving mask technique, Kato et al. (Kato et al., 2005) presented a *plane-pattern to cross section transfer* (PCT) technique. The X-ray mask used for the technique is made of a pattern with changing line-width such as triangular shapes. When these types of masks are scanned or dragged along the resist surface during exposure, a grey-tone dose is generated and slanted surface profile in the resist is formed after resist development.

Other techniques such as laser ablation have also shown their potential for micro-fabrication (Gower, 2000). Mode-locked, high peak power, pico- and femto- second pulsed laser sources enable non-thermal ablation thereby reducing debris and heat damage during the machining process (Keller, 2003). Combining these laser sources with mask projection or mask dragging techniques (Gower, 2000, Harvey and Rumsby, 1997, and Rizvi and Apte, 2002) allows 3D surface machining. However, the reported surface roughness of etched PMMA polymer surfaces is one order of magnitude worse compared with the X-ray lithographic technique. Heng et al. (Heng et al., 2006) reported a surface roughness in the micrometer scale for the etching of PMMA with an Excimer laser and Neiss et al. (Neiss et al., 2008) ablated a sol-gel to

form a 3 level diffractive optical element with a surface roughness of 200 nm at the 3rd level (1.457 μm depth).

Micromachining using proton or electron beams are further tools allowing 3D machining (Kalus et al., 1998, and Teo et al., 2004). Both beams can vary the exposure dose locally but are confined to relative small exposure areas due to their small beam diameter. Kalus et al. e.g. report an e-beam machined 3D step pattern (depth of 100 nm) with a surface roughness in the range of 40 nm.

4.4 3D micro-fabrication using Synchrotron radiation

In respect of the review in section 4.3, a feasible 3D manufacturing process combines synchrotron X-ray lithography with grey-level exposures as presented by the Japanese research group (You et al., 2000, and Fukuda et al., 2006). Merging moving mask technology with the properties of short wavelength and small divergence angle of X-ray radiation produced by synchrotron sources is expected to allow 3D micromachining of high-aspect-ratio (HAR) multilevel diffractive optical elements. We enhance the moving mask technique reported by making use of two masks which we move against each other during X-ray exposure. The forming dose grey-levels allow shaping of complex, monolithic MMA structures in positive tone PMMA resist. To our knowledge the technique is novel. Contrary to the Japanese group who fabricated continuous, slanted mirror surfaces in a shallow etching depth (maximum etching depth is 1 μm) our interest is to fabricate equally stepped staircase micro-mirrors of low surface roughness into depths of hundreds of micrometers (compare the maximum depth h_{max} requirement in Eq. 3-16).

The fabrication of MMA structures for interferometry consists of a multitude of required fabrication process steps, including X-ray mask fabrication, 3D X-ray

lithography, and coating of reflection layers. The following section first introduces the 3D X-ray lithography process as it outlines the key-manufacturing technology. Subsequent sections introduce the developed exposure station and preliminary results using graphite and gold stencil mask membranes. A novel fabrication technology to produce X-ray stencil masks and 3D micromanufacturing of stepped MMA surfaces is demonstrated. Most experiments were carried out at the *Lithography for Micro- and Nano- Technology* (LiMiNT) facility of the *Singapore Synchrotron Light Source* (SSLS). The facility and its infrastructure are presented in Appendix 5.

4.4.1 3D X-ray lithography (3D XRL)

Besides synchrotron X-ray radiation (see Appendix 5 introducing the infrastructure of the LiMiNT facility), the fabrication of fine staircase micro-mirrors requires two X-ray masks which are movable against each other (mask 1 and 2 in Figure 4-1) and a photosensitive resist such as poly-methylmethacrylate (PMMA, $[C_5H_8O_2]_n$). PMMA is a positive-tone resist of moderate sensitivity and high contrast (Pantenburg et al., 1998), and is one of the most commonly used resists in X-ray lithography. During X-ray exposure, masks and resist are in close proximity to allow for the highest pattern transfer accuracy. Mask 2 is fixed to the resist surface whereas either mask 1 is moved with respect to the mask-2-resist-stack or vice versa. Figure 4-1 untangles the stack for easier viewing. In a first exposure step, X-ray radiation passing through the penetrable parts of mask 1 deliver a confined but uniform dose profile to mask 2. The absorber structure of mask 2 further confines the radiation transmitted to the resist. After exposure, mask 1 e.g. is shifted laterally by a defined step and the exposure is repeated. The resulting dose profile (cumulative dose) transmitted to the resist after 4 exposure steps is shown schematically in the Figure. In a resist development step,

irradiated parts become soluble in a developer solution at a development rate which is dependent on the dose profile received and finally stepped PMMA surfaces remain.

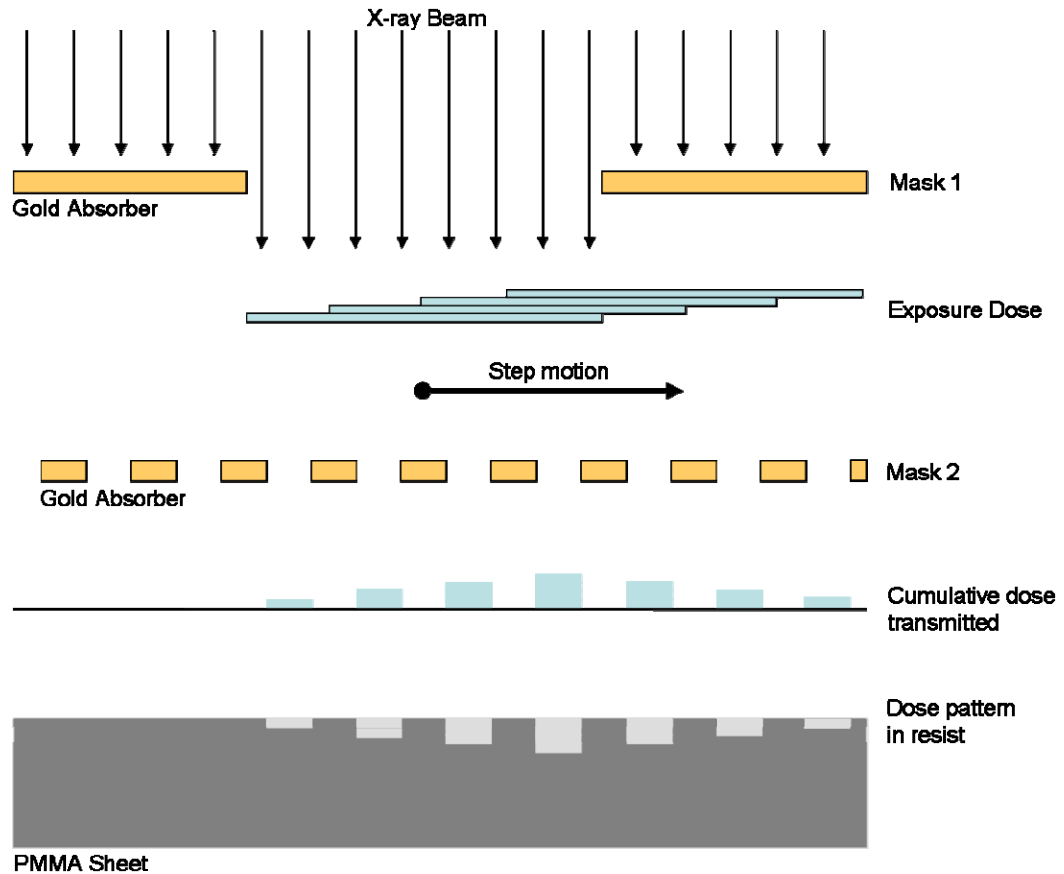


Figure 4-1: Moving mask technique for synchrotron X-ray lithography using two masks and step motion to move one mask with respect to the other. The cumulative dose describes the dose transmitted through the mask system on the photosensitive resist surface (here PMMA).

4.4.2 Moving mask exposure station for 3D X-ray lithography

The moving mask technology requires a controlled motion of mask with respect to substrate during exposure. The motion of the X-ray mask during exposure, however, is not supported by most of the X-ray exposure stations such as the Oxford Instruments X-ray scanner of the LiMiNT facility at the Singapore Synchrotron Light Source. Typically, mask and substrate are brought in close contact, aligned, and fixed firmly prior to the exposure. During exposure any kind of mask movement must be prevented to allow good pattern transfer from mask to substrate in a standard X-ray lithography process. Therefore, SSSL's X-ray scanner was retrofitted with a moving mask exposure station (MMES). Figure 4-2 shows the MMES developed for the experiments at SSSL X-ray scanner. The MMES is mainly comprised of a sliding plate, a mask holder plate, micrometer screws, a linear micro-translation stage, and a substrate table. All components are mounted to the sliding plate, allowing easy mounting of the MMES onto a holder plate, and then to the X-ray scanner table. One of the masks (here named mask 1 in agreement with Figure 4-1) is fixed onto a standard NIST ring commonly used to hold 4 inch X-ray mask for X-ray lithography and fixed by mounting clamps onto the mask holder plate. Below the mask holder plate (Figure 4-2 (b)) a substrate table holds either just the sample or sample and the second mask during exposure. The substrate table in turn is fixed onto a linear micro-translation stage (PI M-112.1VG) with a travel range of 25 mm at a design resolution of 4.8 nm. The gap between mask 1 and sample surface is adjusted by 3 micrometer screws and alignment of masks with respect to the motion of the translations stage is done prior to exposure under standard microscope.

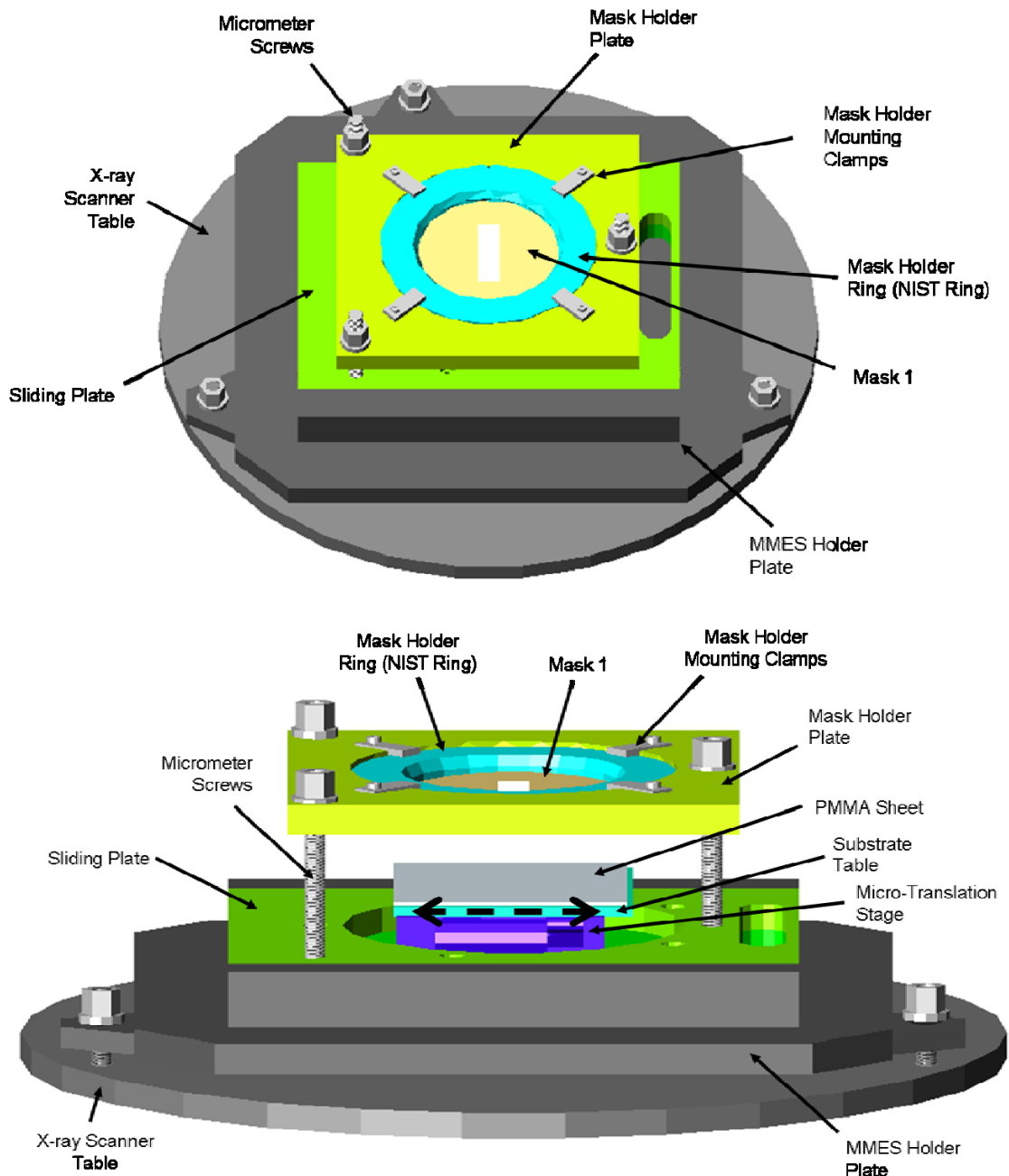


Figure 4-2: Moving mask exposure station (MMES) at LiMiNT beamline in SSLs. MMES is comprised of sliding plate, a mask holder plate, micrometer screws, a linear micro-translation stage, and substrate table. Mask 1 (compare Figure 4-1) is fixed onto a standard mask holder ring (NIST ring) and mounted onto the mask holder plate (top). Below the mask holder plate (see side view in bottom drawing), a substrate table holds the sample during exposure. The substrate table is fixed onto a linear micro-translation stage allowing its translation with respect to mask 1. The gap between mask 1 and sample surface is adjusted by three micrometer screws. The gap between Mask 1 and resist surface is adjusted to a minimum and is typically within 1 mm. The MMES is fixed via a sliding plate to a holder plate and subsequently to the X-ray scanner table. The sliding plate allows easy mounting and removal from the holder plate. Alignment of masks is done prior to exposure under standard microscopes.

4.4.3 X-ray masks for 3D X-ray lithography

X-ray proximity lithography is a 1:1 shadow printing technique requiring a mask pattern which is replicated into a photosensitive resist. This mask pattern is formed by an absorber structure which prevents X-ray radiation from penetration. Typically, X-ray mask consist of an absorber structure and a membrane holding it. In X-ray lithography, a distinct contrast between the absorption and transmission for X-rays in the absorber and mask membrane is required. This so-called *mask contrast* is the ratio of the dose received at the top of the resist parts being exposed to radiation (dose after transmission through mask membrane) and the dose received at the top surface of the resist behind the absorber structure (dose after transmission through mask absorber and membrane). It depends on the particular source spectrum reaching the mask, absorber as well as membrane materials and their thicknesses, and last but not least on the sensitivity of the resist. The mask contrast required for PMMA exposures e.g. is determined by a maximum tolerable dose the resist can receive at the top surface in the un-shadowed resist areas and the lowest dose it requires to initiate the etching in a developer solution. For PMMA these doses are 20 kJ/cm^3 and 100 J/cm^3 , respectively. PMMA resist areas receiving doses in excess of 20 kJ/cm^3 begin to foam and are destroyed. The low end dose value of 100 J/cm^3 is dependent on the developer conditions and is given here indicatively as reported by Pantenburg (Pantenburg et al., 1998). Both values together set the mask contrast required for PMMA exposures to 200.

To obtain the mask contrast, absorber structures are made of materials of high absorption coefficients, whereas materials of low absorption coefficient are useful for the mask membranes. A multitude of materials, material combinations, and fabrication processes are reported in literature (Tolfree, 1998, Cabrini et al., 2005,

Sheats and Smith, 1998, p. 417, Coane and Friedrich, 1996, Li, 2004, van Kan et al., 2007, Yue et al., 2008, Sheu et al., 1998, Shan et al. 2003, Shew et al., 1998, Divan et al., 2002, Chou et al., 1985, Voigt et al. 2008, Wang et al. 2004, Desta et al., 2003, Achenbach, 2004, Kim and Choi, 2005, and Stadler et al., 1997).

Besides the above criteria for mask contrast, the choice further depends on the application, required pattern transfer accuracy and depth, side-wall surface roughness, lifetime, and cost of the mask. Moreover, heat generation and transport due to the absorption of the synchrotron beam energy in mask and resist are known to cause mask membrane and subsequently dimensional distortions (Neumann et al., 1997, Feiertag et al. 1995, Manohara et al., 1996) and must be considered for X-ray masks. Neumann et al. (Neumann et al., 1997) recommend membrane materials with high thermal conductivity to reduce temperature gradients on the mask during irradiation. Figure 4-3 compares the absorption coefficients of commonly used materials in X-ray lithography and lists additional material properties.

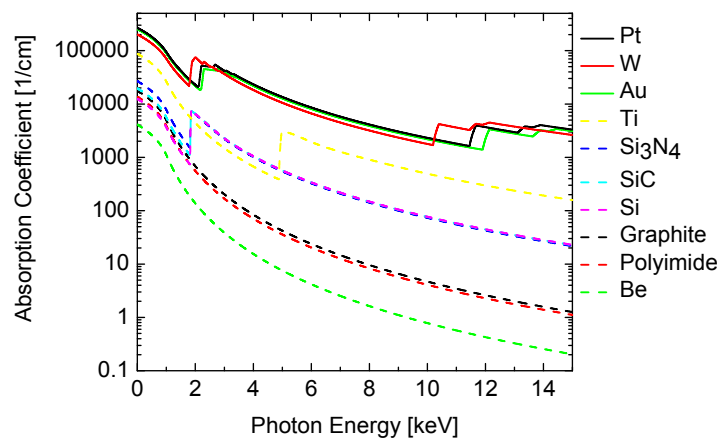


Figure 4-3: Absorption coefficient as a function of photon energy of mask membrane and absorber materials used for x-ray masks. Data plot produced with XOP 2.11 software (Rio and Dejus, 2006).

Table 4-3: Properties of mask materials (references are Touloukian and Ho, 1979 and DuPont.com for Kapton® data).

| Material | thermal expansion coefficient [10^{-6} K^{-1}] | thermal conductivity [$\text{Wcm}^{-1}\text{K}^{-1}$] |
|---|--|---|
| Au | 14.2 | 3.15 |
| Pt | 8.8 | 0.714 |
| W | 4.5 | 1.78 |
| Be | 11.3 | 2.0 |
| Graphite (Poco grade DFP 3-2 / Erodex UK) | 7.1 | 0.25-4.7 |
| Si | 2.6 | 1.48 |
| SiC | 3.3 | 1.35 - 4.9 |
| Si ₃ N ₄ | 3.3 | 0.05 - 0.185 |
| Ti | 8.6 | 0.219 |
| Polyimide (Kapton® HN / Du Pont) | 20 | 0.0012 |
| PMMA | 61 | 0.00192 |

Mask membrane materials with low absorption coefficients are beryllium, graphite, silicon, or thin foils, e.g. titanium, Si₃N₄, SiC, and polyimide. Beryllium features the highest transparency throughout the X-ray spectrum and good thermal conductivity, but its particles or powders which may be generated when the material is scratched are toxic. Furthermore, the material is environmental unfriendly, and expensive. On the other hand, graphite mask membranes offer a cheap alternative but their porosity and inhomogeneous structure causes X-ray scattering and limits the performance of these masks. Thin foil membranes are inherently fragile, prone to stress, and mostly restricted to small area membranes. Polymer based thin foils such as Polyimide (Kapton®) masks are reported as cheap masks providing large surface areas (Stadler et al., 1997), but dimensional variation and limited radiation resistance when exposed to X-ray radiation are key issues. Another type of mask reported is stencil masks. These masks combine the function of membrane and absorber into a single (singly-connected) structured foil. Mekarū et al. (Mekarū et al., 2008) reported stainless steel

and silicon-micro-machined X-ray masks of 100 and 200 μm thickness with smallest feature size of 40 and 20 μm , respectively.

SSLS is currently pursuing two X-ray mask processes, based on graphite and Kapton® mask membranes. In both cases electroplated gold is used as absorber material. Both masks are primarily used for X-ray lithography with chemically amplified photoresists such as negative tone SU-8 photoresist. The chemical amplification of SU-8 resists allow low exposure doses in the range of 20 J/cm^2 , whereas positive tone resists such as poly-methylmetacrylate (PMMA) demand 200 times higher exposure dosages. This high exposure dosages of PMMA resists and thus long exposure times for the processing of PMMA resists, in turn necessitate thermally stable and radiation resistant mask membrane materials.

Preliminary results using graphite mask membranes (200 μm thickness) to etch a test structure into 2 mm thick PMMA resist sheets (CQ-PMMA) are shown in Figure 4-4 (a). As seen in the figure, the inhomogeneous structure of graphite leads to surface roughness greater than 1 μm (rms) of etched PMMA, discarding graphite based membrane for the moving mask technology. On the other hand, the fabrication of Kapton® based masks is difficult due to the low adhesion of metal layers on its surface. Moreover, the low thermal conductivity of Kapton® is expected to result in temperature accumulation and membrane buckling when the mask is exposed to synchrotron radiation for a long time.

To overcome the disadvantages of Kapton® and graphite membranes, a gold stencil mask held by a silicon frame was developed. Using gold instead of silicon as stencil mask material (compare Mekaru et al., 2008), permit the rigorous reduction of the membrane thickness. Such stencil masks feature a number of advantages:

- 1) Reduced number of materials (Si and Au), thus reducing thermal stress issues stemming from different thermal expansion coefficients of mask materials.
- 2) No absorption of membrane material, thus no radiation loss in membrane, high radiation throughput, and reduced exposure times.
- 3) Permit through-the-mask alignment.

To compare the surface roughness produced with graphite based membranes as shown in Figure 4-4 (a), Figure 4-4 (b) demonstrates the surface roughness of etched PMMA produced with a gold stencil mask.

Note that all absorber structures must be connected to the main frame layer forming a continuous pattern. Mask designs such as annuli are not possible.

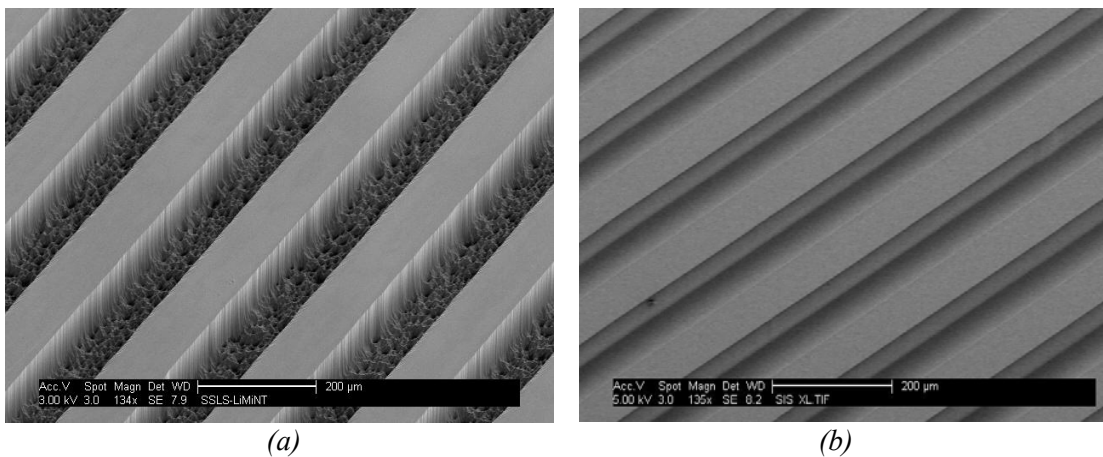


Figure 4-4: Preliminary results of PMMA etching using (a) graphite based mask membrane (scale bar 200 μm) and (b) stencil mask .

The developed process to fabricate gold stencil mask is presented in Appendix 6 and was conducted in collaboration with the *Institute of Materials Research and Engineering* (IMRE) as the process requires *deep reactive ion etching* technique (DRIE). On the basis of double-side-polished silicon wafer, the main process steps include the structuring of the front side via UV lithography and subsequent gold electroplating, the structuring of the backside via UV lithography and subsequent

etching of silicon frame to form a freely-suspended gold membrane. Figure 4-5 presents the gold stencil mask developed for the PMMA etching.

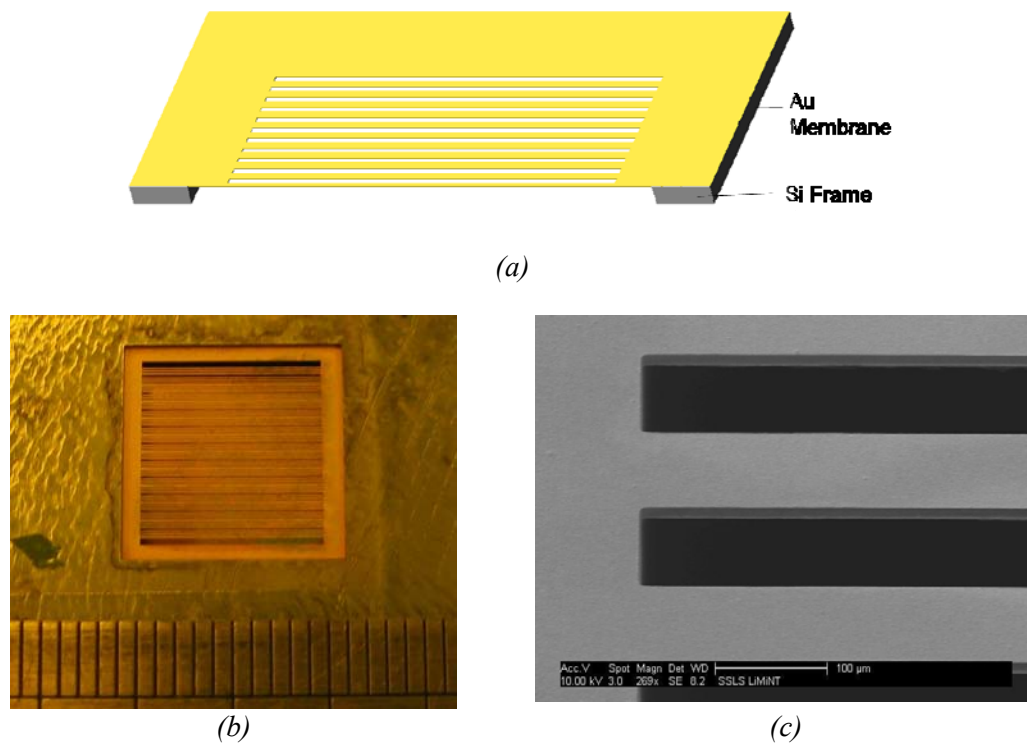


Figure 4-5: Gold stencil mask for X-ray lithography. (a) Schematic of the mask, the gold membrane is held by silicon frame. Gold thickness of the mask is 15 μm . (b) Image of backside of gold stencil mask held by silicon frame. The size of the window is 12 x 12 mm^2 . (c) SEM image of mask (scale bar 100 μm).

To test the stencil mask, first the temperature development during the X-ray exposure was measured. Figure 4-6 (a) depicts the schematic of the experimental setup. Two J-type thermocouples were used for the measurements of which one was attached to the absorber layer while the other was attached to the PMMA sheet directly exposed to the X-ray radiation. The stencil mask in the experiments shielded 50 % of the PMMA surface while the rest was exposed to the X-ray beam. During X-ray exposure, the stack of stencil mask and PMMA sheet is scanned vertically through X-ray beam of a 92 x 8.4 mm^2 footprint produced by Helios 2 light source (see Appendix 5) while the temperature is recorded as a function of time (Figure 4-6 b). The scanner speed is

maintained at 40 mm/s throughout. Five experiments (A-E) were run sequentially of which the dose deposited in each of the experimental runs is the same but at reduced vertical scanning distances. For a vertical scanning distance of ± 45 mm (A), both thermocouples record a nearly identical temperature. It rises by approximately 1°C from 21°C at the beginning of the exposure and increases steadily to 23°C and drops within 200 s to 22°C after the exposure stopped. The temperature increment of 1°C during exposure for both PMMA and gold absorber is maintained until the vertical scanner distance is reduced to ± 5 mm at which both mask and PMMA are continuously exposed to the X-ray beam.

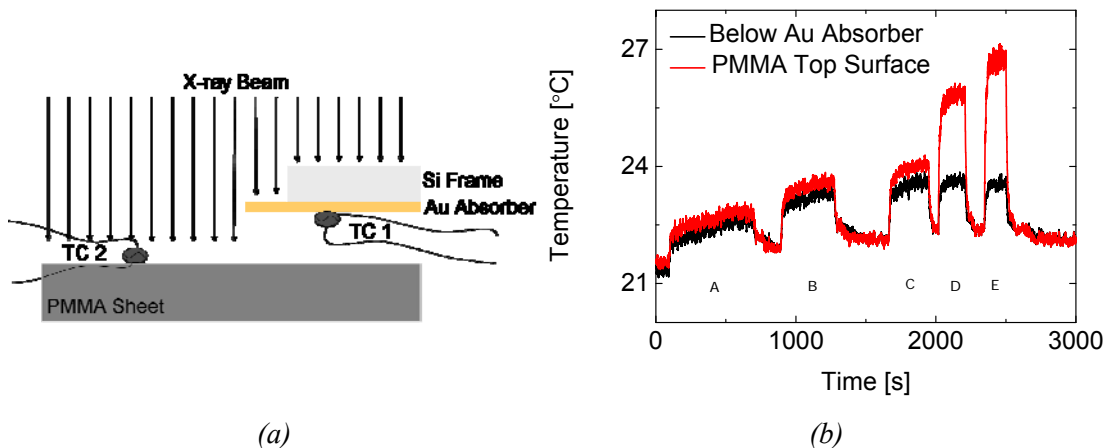


Figure 4-6: (a) Schematic experimental setup to measure the temperature development during X-ray exposure at SSLS LiMiNT facility. One of the two J-type thermocouples (TC1) was attached to the gold absorber layer held by a $500\ \mu\text{m}$ thick Si frame and was shielded from the radiation during the exposure while the second thermocouple (TC2) was attached to the top PMMA surface and was directly exposed to the X-ray beam. (b) Temperature development during exposure as a function of time for five sequential experiments (inset A to E in the figure). For all experiments the same dose is deposited but the vertical scan length is reduced. A: 125-700 s, beam current 225 mA, vertical scan distance ± 45 mm. B: 800-1300 s, beam current 220 mA, vertical scan distance ± 25 mm. C: 1600-1900 s, beam current 210 mA, vertical scan distance ± 15 mm. D: 2000-2250 s, beam current 210 mA, vertical scan distance ± 5 mm. E: 2250-2600 s, beam current 210 mA, vertical scan distance ± 2.5 mm.

In this regime (D and E), the low thermal conductivity of PMMA (Table 4-3) results in a temperature rise of $3\text{-}4^\circ\text{C}$ on the PMMA top surface, while the temperature of the gold absorber of the stencil mask is maintained at $+1^\circ\text{C}$.

The low rise in the stencil mask temperature during exposure results in a negligibly small volume expansion of gold of 0.043 % indicating a very good temperature stability of the stencil mask.

Note that from the temperature reading of the thermocouple at the resist surface it is not possible to conclude the PMMA temperature as the thermocouple measures its own heating in the radiation beam. Its measurement merely serves as a comparison.

4.4.4 3D Structuring of poly-methylmethacrylate (PMMA)

When PMMA is irradiated with X-ray radiation a number of reaction mechanism in the polymeric matrix occur. Main-chain scission reaction (decreasing the molecular weight), recombination reactions of long chained fragments, branching and crosslinking reactions (resulting in an increase of molar mass at high doses) are observed. The mechanism and rate depend on the chemical structure of the PMMA, the energy of the radiation and environmental influences such as the presence of reactive atmosphere, additives, temperature etc (Schmalz et al., Part I, 1996). The degradation of the molar mass of PMMA is thereby the predominant reaction caused by X-ray radiation (Schmalz et al., Part III, 1996).

Thus, polymer areas which are not shielded by the absorber structure during irradiation are reduced in molecular weight. In a subsequent development step, these low molecular weight areas are selectively dissolved in a developer solution. A detailed study of the reaction mechanism involved during irradiation and development of PMMA can be found in references (Schmalz et al., Part I-III, 1996, and Wollersheim et al., 1995). The rate at which the irradiated PMMA is dissolved in the developer solution depends on a number of parameters listed in Table 4-4.

Table 4-4: Parameters influencing the dissolution rate of PMMA in X-ray lithography as reported by the respective references.

| Parameter | References |
|---|--|
| Type of PMMA <ul style="list-style-type: none"> • crosslinked or non-crosslinked, sheets, cast PMMA • spin coated | (Pantenburg et al., 1998, Meyer et al., 1999, Liu et al., 1998, and De Carlo et al., 1998) (Mappes et al., 2007) |
| initial molecular weight | (Fujimura et a., 2001, Mappes et al., 2007, and Pantenburg et al., 1998) |
| exposure dose | (Pantenburg et al., 1998, Tan et al., 1998, Zanghellini et al., 1997, El-Kholi et al., 1994, and Fujimura et a., 2001) |
| chain-scission yield | (Pantenburg et al., 1998, and Tan et al., 1998) |
| developer type | (De Carlo et al., 1998, and Malek and Yajamanyam, 2000) |
| developer temperature | (Pantenburg et al., 1998, Liu et al., 1998, Tan et al., 1998, De Carlo et al., 1998, Divan et al., 2002, and Malek and Yajamanyam, 2000) |
| type of development <ul style="list-style-type: none"> • dip- • ultrasonic- • mega-sonic- supported • bath stirring | (Zanghellini et al., 1997, and Malek and Yajamanyam, 2000) (Meyer et al., 2002, El-Kholi et al., 1994, and Malek and Yajamanyam, 2000) (Liu et al., 1998 and Malek and Yajamanyam, 2000) |
| pre and post exposure treatment (thermal annealing) | (Divan et al., 2002, and Malek and Yajamanyam, 2000) |
| time delay between exposure and development | (Meyer et al., 2002) |
| aspect ratio of microstructures | (Zanghellini et al., 1997, El-Kholi et al., 1994, and Meyer et al., 1999) |
| synchrotron source, dose rate | (Tan et al., 1998, and De Carlo et al., 1998) |

A detailed study of the influence of these parameters on the dissolution rate is out of the scope of this work. Only a very limited number of experiments have been carried out to characterize the performance of the resist-developer-system in respect of 3D structuring. A thorough study of this field has to be undertaken in future studies.

4.4.4.1 The resist-developer-system

The performance of resist for micro-fabrication is strongly influenced by the interaction of resist and developer and must be carefully chosen to the specific requirement. Quantitatively, the system of resist and developer is characterized by (Achenbach et al., 2000, Greeneich, 1975, and Brewer, 1980):

- 1) Sensitivity of the resist to incident radiation. Typically given by the dose required per unit area to expose the resist pattern in the desired thickness (Greeneich, 1975).
- 2) Contrast of the resist is defined in terms of rate at which a resist undergoes chain-scission as a function of dose. It gives a measure of the susceptibility of the material to a change in dose. High contrasts are desirable for obtaining better structure quality and resolution (Brewer, 1980, p. 94-97).
- 3) Dissolution rate. High dissolution rates of irradiated resists allow shorter development times and thus alleviate the effects of unwanted resist swelling and removal of resist material in non-irradiated regions in the case of positive tone resists.

The solubility of a polymer is inversely proportional to its molecular weight and thus increases with decreasing molecular weight. For the lithographic use, resist developer solutions are required to distinguish between irradiated (reduced molecular weight material, M_f) and non-irradiated (material of initial molecular weight, M_n). Consequently, a large disparity between the solubility of irradiated and non-irradiated material is beneficial and thus large ratios of M_n/M_f are desirable.

The relationship between the reduced molecular weight M_f (g/mol) due to chain-scissions induced by X-ray irradiation, the initial number average molecular weight

M_n (g/mol), and the absorbed energy density D (J/cm³) is expressed as (Greeneich, 1975).

$$M_f = \frac{M_n}{1 + \frac{gDM_n}{\rho N_a}}, \quad (4-1)$$

where ρ is the resist density (g/cm³), and N_a the Avogadro's number (1/mol). g denotes the radiation yield - the number of effective chain scissions per eV of energy absorbed. The link between the dissolution rate R in a given solvent and the reduced molecular weight is described by an empirical formula of the form (Greeneich, 1975)

$$R = R_0 + \frac{\beta}{(M_f)^\alpha}, \quad (4-2)$$

where R_0 characterizes the removal of very high molecular weight material such as the non-irradiated regions and should be kept at minimum levels. For X-ray lithography R_0 is negligible (Pantenburg et al., 1998, Achenbach et al., 2000, Liu et al., 1998, and Meyer et al., 1999). α and β are characteristic values related to resist and solvent chemistry under given conditions such as temperature (Valiev, 1992). Furthermore, α is related to the contrast of the resist (Pantenburg et al., 1998, and Brewer, 1980). Combining Eq. (4-1) and (4-2), the dissolution rate is commonly approximated by:

$$R = KD^\alpha, \quad (4-3)$$

with $K \approx \beta \frac{g}{\rho N_a}$.

For the experiments two types of PMMA sheets of 2 mm thickness were used, namely CQ and Degussa Plexiglas, both obtained from Goodfellow Corporation. Initial molecular weight distributions were acquired from Gel Permeation Chromatography (GPC) measurements in tetrahydrofuran (THF) solutions (Table 4-5). Comparing the

results for both PMMA sheets, the Degussa Plexiglas PMMA has a ten times smaller weight average molecular weight and a 15 % lower polydispersivity.

Table 4-5: Molecular weight distribution of PMMA used for the experiments. The weight distributions were obtained via Gel Permeation Chromatography (GPC) in tetrahydrofuran (THF) solution.

| Parameter | Degussa Plexiglas | CQ PMMA |
|---|-------------------|------------|
| Number Average Molecular Weight M_n [g/mol] <i>(weighs low molecular weight)</i> | 1.0797E+05 | 8.7367E+05 |
| Weight Average Molecular Weight M_w [g/mol] | 1.8893E+05 | 1.8015E+06 |
| Z Average M_z [g/mol] <i>(weighs high molecular weights)</i> | 2.8280E+05 | 2.5171E+06 |
| GPC peak molecular weight [g/mol] | 1.6817E+05 | 2.0524E+06 |
| Polydispersivity PD (M_w/M_n) <i>(indicates the range of molecular weights in the PMMA sample)</i> | 1.7498 | 2.062 |

Both types of PMMA sheets were exposed in SSLS LiMiNT beamline retrofitted with the MMES as described in section 4.4.2. PMMA sheets were fixed on top of the sample holder plate and irradiated by perpendicularly incident X-rays (see Appendix 5 describing the source spectrum).

After exposure, the irradiated PMMA sheets were developed without time delay to avoid resist relaxation effects as reported by Meyer et al. (Meyer et al., 2002). GG developer (Ghica and Glashauser, 1983, see Table 4-6) was the chosen developer solution. The developer is an established and commonly used PMMA developer solution for high resolution X-ray lithography (Achenbach, 2004, Becker et al., 1986, Meyer et al., 2002, and Zanghellini et al., 1997).

The development was done in a 3 step process cycle. In a first step, the sheets were developed 30 minute in the GG developer solution, followed by a 30 minute rinsing step in GG rinse solution and a subsequent 60 minute DI water bath. In each of the steps, the samples were dipped into the solution and occasionally (10 min interval) agitated by shaking the glass beakers by hand. Developer and rinse solutions (see Table 4-6) were mixed at least one day before usage. For most of the sample developed, the times indicated were kept constant and are stated specifically if otherwise. The temperatures of the GG developer during the development step were kept constant within ± 1 °C for each specific development experiment.

Table 4-6: GG developer and GG rinse formulation used in experiments after (Ghica and Glashauser, 1983).

| Formulation | GG developer [%] | GG rinse [%] |
|-------------------------|------------------|--------------|
| 2-2 butoxyethoxyethanol | 60 | 80 |
| morpholine | 20 | - |
| aminoethanol | 5 | - |
| DI water | 15 | 20 |

4.4.4.2 Resist-developer characterization

The MMES setup allows the study of the development rate as a function of dose with a single uninterrupted development cycle at a fixed development time. Therefore, in a first series of experiments the exposure dose is locally varied by step-wise movement of the PMMA sheets behind a 15 μm thick gold absorber (Figure 4-7). After development, the etch depth is determined with an optical profiler (Wyko 1100). In analogy to work reported earlier (Pantenburg et al., 1998, and Meyer et al., 2002) development rates, K , and α values are computed by a least square fit following Eq.

(4-3). Subsequently, the obtained data set is used to characterize the resist-developer system in respect of

- 1) exposure dose,
- 2) dose rate,
- 3) initial molecular weight, and
- 4) development temperature.

Finally, the resist-developer-system is examined in terms of surface roughness of etched micro-mirrors.

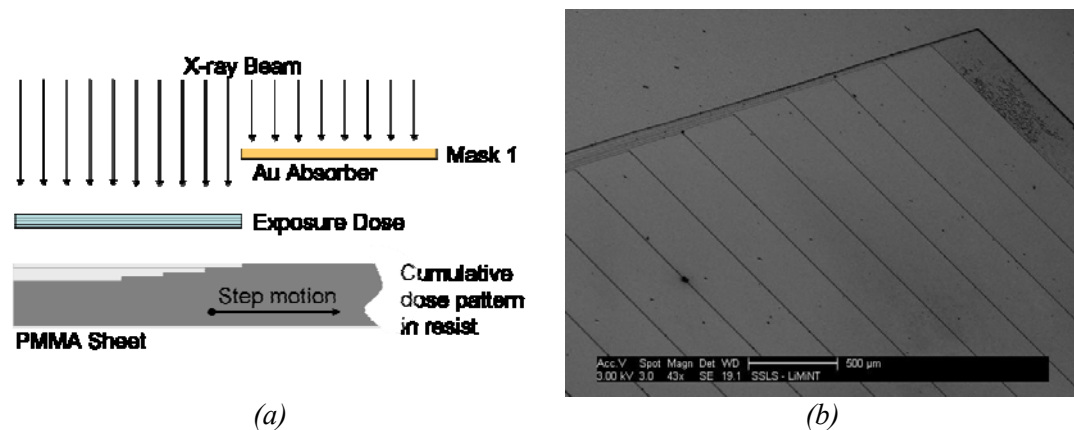


Figure 4-7: Experiment setup for step etching in PMMA. (a) Experiment schematic. Using the MMES, the PMMA sheets are moved step-wise behind a 15 μm thick absorber etch. The exposure dose increment for each step is kept constant. (b) SEM image of steps etched into PMMA. Here: Degussa Plexiglas with a stepping depth of approx 1 μm is shown. The scale bar is 500 μm.

Figure 4-8 (a) shows a general data set depicting etch-depth versus exposure dose as obtained after a standard development cycle. From this data set development rates were computed (Figure 4-8 b) by dividing the etch depth (Y-coordinate) values by the respective development times. Both figures (Figure 4-8 a, b) show a general trend found for the development of PMMA. The dependence of development rate on dose follows the power law (Eq. (4-3)) particularly for low dose regime. At higher doses the power α reduces. Thus, the development rate is split into two dose regimes:

Regime A): Development rate versus dose follows a parabolic trend for $\alpha > 1$,
and

Regime B): Development rate versus dose follows a square root trend for $\alpha < 1$.

The dose spectra corresponding to these regimes vary with development conditions and are considered separately for the data fitting. For comparison, a separation at 4 kJ/cm^3 is given for all samples.

Figure 4-8 (b) shows the agreement of experimentally determined dissolution rate and its approximation according to Eq. (4-3) for exposures from 0 – 4 kJ/cm^3 and from 4 - 8 kJ/cm^3 . Below a dose of 4 kJ/cm^3 the development rate increases parabolic with dose, and continues linearly for doses greater than 4 kJ/cm^3 .

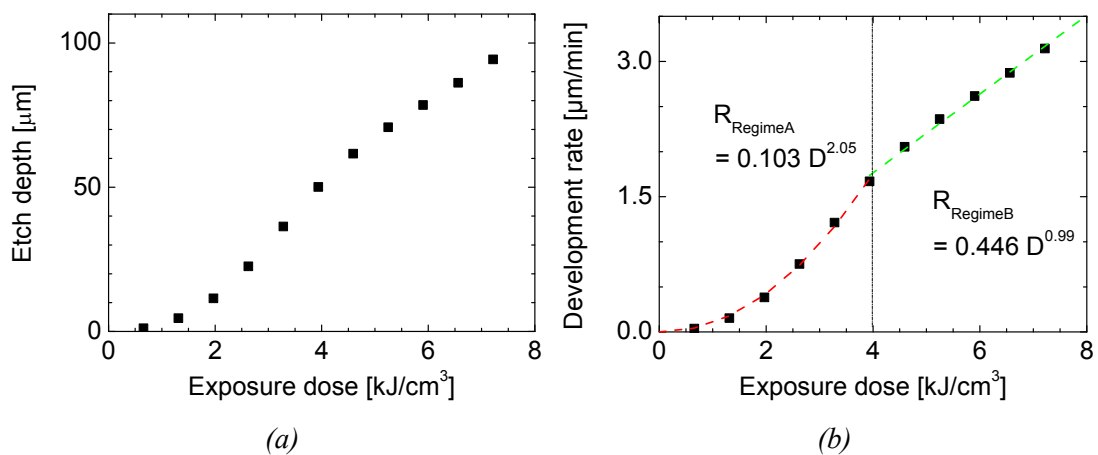


Figure 4-8: Experimental results for etching of Degussa PMMA sheet at a synchrotron beam current of 195 mA, a development cycle of 30 minutes, and a solution temperature of 30 °C.

Aside from the general and well-known dose dependence on the development rate of PMMA, the influence of the dose rate on development rate is examined. One refers to dose rate as dose delivered per unit time. For synchrotron sources, it is dependent on the storage ring current. The ring current in turn is not constant and varies during the operation of the source. Various loss processes like the emission of synchrotron radiation and the scattering off residual gas atoms/molecules cause the electron beam

current to slowly decrease with an $1/e$ lifetime of typically 17 h in the case of Helios 2 storage ring at 200 mA. To deposit a given dose during each scan of the X-ray scanner, this reduction is automatically balanced by the LiMiNT X-ray scanner speed with which the sample is scanned through the X-ray beam during the lithography process while the number of scans are maintained. For the investigation of the influence of dose rate on the development rate, exposures were conducted at three different starting beam currents, while exposure dose and development conditions were kept the same. Figure 4-9 (a) plots the examined development rates for a starting storage ring current of 195, 225, and 315 mA. The corresponding dose rates are 175, 210, and 300 mW/cm^2 , respectively. According to the figure, the development rate is dependant on the ring current and thus the dose rate. Higher dose rates result in increased development rates for a given dose. At an exposure dose of $4 \text{ kJ}/\text{cm}^3$ the development rate for 195 mA starting ring current is $1.67 \mu\text{m}/\text{min}$ and increases to 2.1 and $2.6 \mu\text{m}/\text{min}$ for 225 and 315 mA exposures, respectively. As the ring current drops during the duration of the experiment only the starting currents are mentioned here and serve as a reference value. Over the duration of the experiments, the ring current of 195 mA reduced to 175 mA, while the ring currents of the 225 mA and 315 mA dropped to 186 mA and 264 mA, respectively. Figure 4-9 (b) plots the average ring current and average dose rates for each exposure dose in the experiment. Average values are given because the exposures were performed in succession with a single gold edge covering one side of the PMMA while the un-shadowed part is irradiated multiple times until the respective area received a particular accumulated exposure dose and is moved into the shadow of the gold absorber. From the data plot, it can be seen that the dropping beam current results in a reduction of the dose rate of 4-6 % during the experiments.

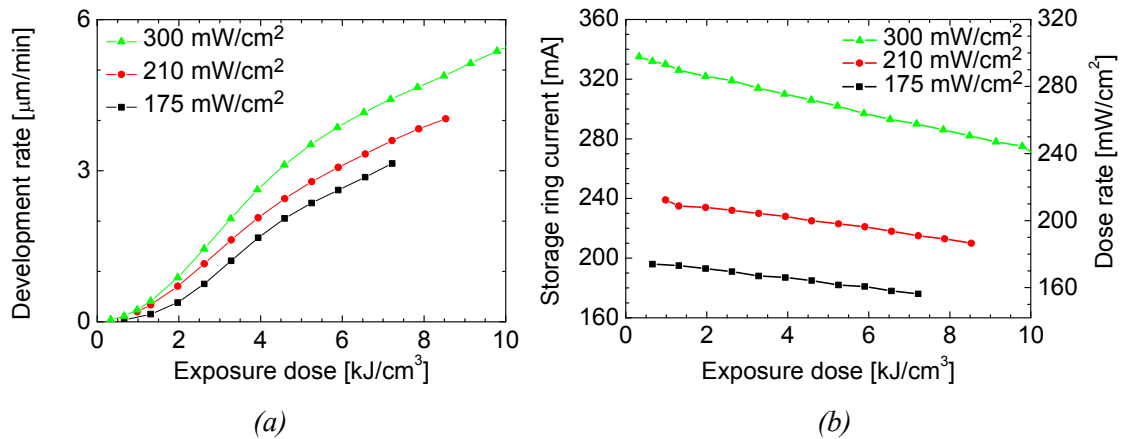


Figure 4-9: (a) Influence of dose rate on the development rate R for Degussa PMMA sheets. Samples were exposed at different ring currents whereas exposure and development conditions were kept constant. (b) Average ring currents and dose rates as a function of exposure dose. Average values are given to attribute for the accumulated exposure dose of successive exposures.

Table 4-7 lists the parameters after Eq. (4-3) for Degussa and CQ PMMA samples. The parameter α can be linked to the contrast of the resist (Brewer, 1980, Pantenburg et al., 1998, and Mappes et al., 2007). An increased value of α reduces the effect of unwanted development of PMMA in shadow regions of the mask and thus will result in better structure accuracy for the lithographic shaping. Comparing contrast and development rates of the lower molecular weight PMMA (Degussa) with the higher molecular weight CQ PMMA an obvious trend is evident: The higher molecular weight PMMA features a higher contrast, while the dissolution rate and thus the sensitivity at a given starting ring current are higher for the lower molecular weight material. This is congruent with the lower polydispersivity of the Degussa PMMA compared with CQ PMMA (Table 4-5). It is known that low polydispersivity allows higher sensitivity of the resist since fewer dosages are required to separate narrow molecular weight distributions compared to wide distributions (Brewer, 1980).

Moreover, the development temperature and the mode of agitation tremendously affect the dissolution rate. Lower bath temperatures increase the contrast of the resist-developer-system while largely reducing the development rate. In the dose regime

ranging from 0 - 4 kJ/cm³ (ring current of 315 mA), α increases by a factor of 1.9 and 1.8 by decreasing the developer temperature from 30 to 18 °C for Degussa and CQ PMMA, respectively. The development rate at an exposure dose of 4 kJ/cm² reduces from 2.6 to 0.3 $\mu\text{m}/\text{min}$ for Degussa PMMA and from 1.6 to 0.17 $\mu\text{m}/\text{min}$ for CQ PMMA (Figure 4-10) indicating a higher temperature dependence of the low molecular weight PMMA (Degussa).

Magnetically stirring the developer solution increases the development rate at the expense of contrast. For a ring current of 225 mA and an exposure dose of 4 kJ/cm³, the development rate increased by a factor of 2.18, whereas α reduces by 36 % at a development temperature of 30 °C. However, the temperature control of the system used for the experiment did not allow a precise temperature control over the period of the experiment (± 4 °C) and thus the high increase in the development rate may be due to both, the magnetic stirring and the solution temperature. Subsequently, the experiments utilizing the magnetic stirring equipment are not further examined in this work.

Mega- and ultrasonically supported development of PMMA is reported to further increase the development rates (Zanghellini et al., 1997, Malek and Yajamanyam, 2000, Meyer et al., 2002, El-Kholi et al., 1994) but were found to be counterproductive in particular for the development of CQ PMMA as it resulted in the formation of surface cracks across the entire surfaces.

Table 4-7: Development parameters after Eq. (4-3) for Degussa and CQ PMMA at different GG developer temperatures and starting ring currents. Minimum dose corresponds to an exposure dose at which etching of PMMA is observed. Parameters K and α are found by least square fit of the dissolution rate according to Eq. (4-3) for dose regime from 0 – 4 kJ/cm³ and 4 – 8 kJ/cm³.

| | Degussa PMMA | | | | | | CQ PMMA | | |
|------------------------------------|---------------|---------------|---------------|---------------|---------------|---------------|---------------|---------------|-----------------|
| Ring current [mA] | 195 | 195 | 225 | 225 | 315 | 315 | 285 | 315 | 315 |
| Dose rate [mW/cm ²] | 175 | 175 | 210 | 210 | 300 | 300 | 254 | 300 | 300 |
| Agitation | none | none | none | magn. stirrer | none | none | none | none | none |
| GG solution temp. [°C] | 20 ± 1 | 30 ± 1 | 30 ± 1 | 30 ± 4 | 30 ± 1 | 18 ± 1 | 30 ± 1 | 30 ± 1 | 18 ± 1 |
| Dose 0-4 kJ/cm ³ | | | | | | | | | |
| Minimum dose [kJ/cm ³] | > 0.45 | > 0.45 | > 0.45 | > 0.45 | > 0.45 | > 0.45 | > 0.46 | > 0.46 | > 0.46 |
| K [µm/min] | 0.002 ± 0.001 | 0.103 ± 0.010 | 0.245 ± 0.018 | 1.148 ± 0.058 | 0.292 ± 0.018 | 0.004 ± 0.002 | 0.066 ± 0.010 | 0.075 ± 0.006 | 0.0006 ± 0.0001 |
| α | 3.457 ± 0.046 | 2.046 ± 0.077 | 1.571 ± 0.061 | 1.012 ± 0.044 | 1.620 ± 0.052 | 3.067 ± 0.427 | 2.336 ± 0.122 | 2.246 ± 0.063 | 4.061 ± 0.156 |
| Dose 4-8 kJ/cm ³ | | | | | | | | | |
| K [µm/min] | 0.008 ± 0.002 | 0.445 ± 0.033 | 0.692 ± 0.036 | 1.857 ± 0.034 | 1.069 ± 0.052 | 0.040 ± 0.009 | 0.369 ± 0.040 | 0.412 ± 0.039 | 0.017 ± 0.005 |
| α | 2.395 ± 0.111 | 0.992 ± 0.041 | 0.830 ± 0.027 | 0.653 ± 0.044 | 0.711 ± 0.023 | 1.834 ± 0.112 | 1.134 ± 0.055 | 1.106 ± 0.045 | 2.113 ± 0.124 |

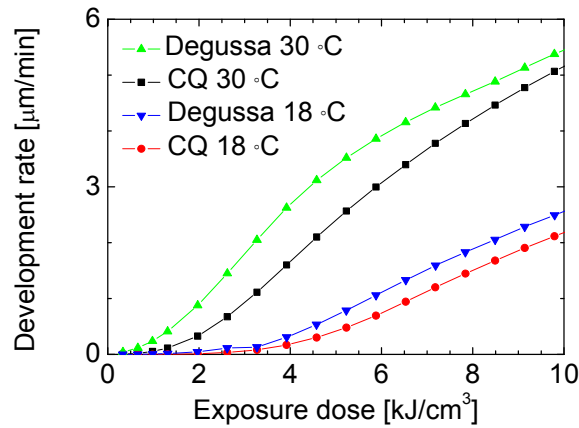


Figure 4-10: Development rate for Degussa and CQ PMMA for GG developer solutions at a temperature of 18 and 30 °C. All samples were exposed at an average dose rate of 300 mW/cm² and a starting ring current of 315 mA.

The effect of the development depth (etch depth) on the surface roughness (root-mean-square-average) for CQ and Degussa PMMA is plotted in Figure 4-11 (a). The surface roughness was measured with an optical profiler (Wyko 1100) in an area of approximately 0.5 mm² and at a sampling period of 3.31 μm. Subsequently, the roughness was acquired by high-pass data filtering, whereas the surface waviness was obtained by low-pass data filtering. Details on the surface characterization using the optical profiler and the data filtering can be found in Appendix 7. Both PMMA samples were exposed and developed under the same conditions and both samples reveal an exponentially increasing surface roughness as a function of etch depth. Comparing both, the higher development rate of Degussa PMMA results in deeper etch depths, while maintaining smoother mirror surfaces for a given etch depth. At an etch depth of 100 μm, the Degussa PMMA reveals a surface roughness of 10 nm, whereas CQ PMMA surfaces forms a surface roughness of 50 nm. Apart from the dependence of etch depth on surface roughness, the surface roughness consistently increases exponentially with the exposure dose (Figure 4-11(b)) for both types of PMMA at a given development time and temperature. Degussa and CQ PMMA reveal a similar surface waviness. Below an etching depth of 100 μm, the mirror surfaces

feature a waviness level below the 100 nm (Figure 4-11(c)), whereby the Degussa PMMA shows on average lower waviness values. Similar to the surface roughness, the waviness increases with etch depth and exposure dose, whereby the waviness data spans from 10 nm to 250 nm for Degussa PMMA and 50 to 100 nm for CQ PMMA (Figure 4-11 (c) and (d)).

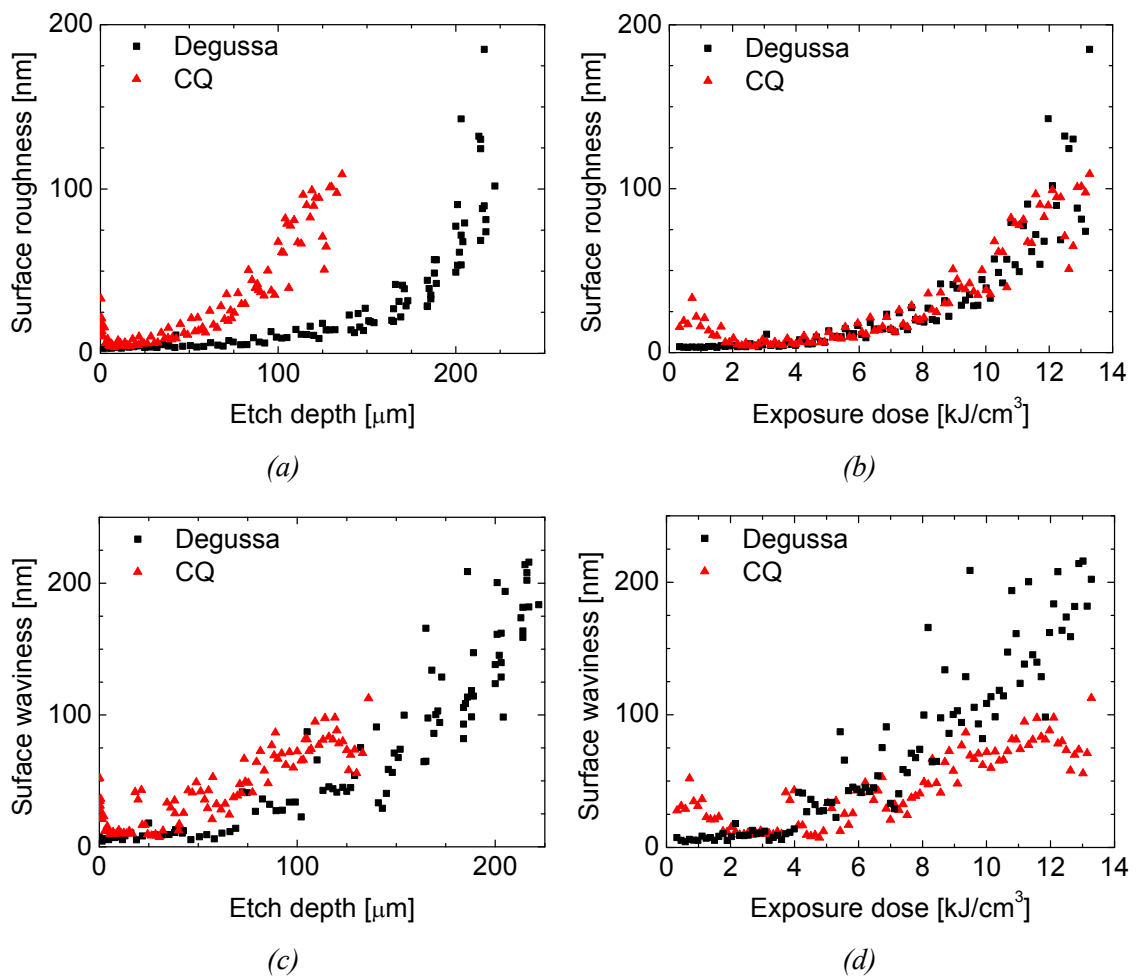


Figure 4-11: Surface roughness of etched CQ and Degussa PMMA micro-mirrors. Both samples were exposed and developed under the same conditions. (a) Surface roughness (root-mean-square-average) as a function of etch depth, and (b) as a function of exposure dose. (c) Surface waviness (root-mean-square-average) as a function of etch depth, and (d) as a function of exposure dose.

The surface roughness obtained via the optical profiler was verified via Atomic Force Microscope (AFM) measurements. Figure 4-12 shows the surface texture of etched Degussa PMMA as obtained via AFM measurement. Both techniques showed good

agreement for the obtained surface roughness. While the surface roughness obtained with the optical profiler after high-pass data filtering was 7.8 nm (rms) at an etch depth of 72.3 μm , the AFM measurement revealed a surface roughness of 6.748 nm for the same surface (Figure 4-12).

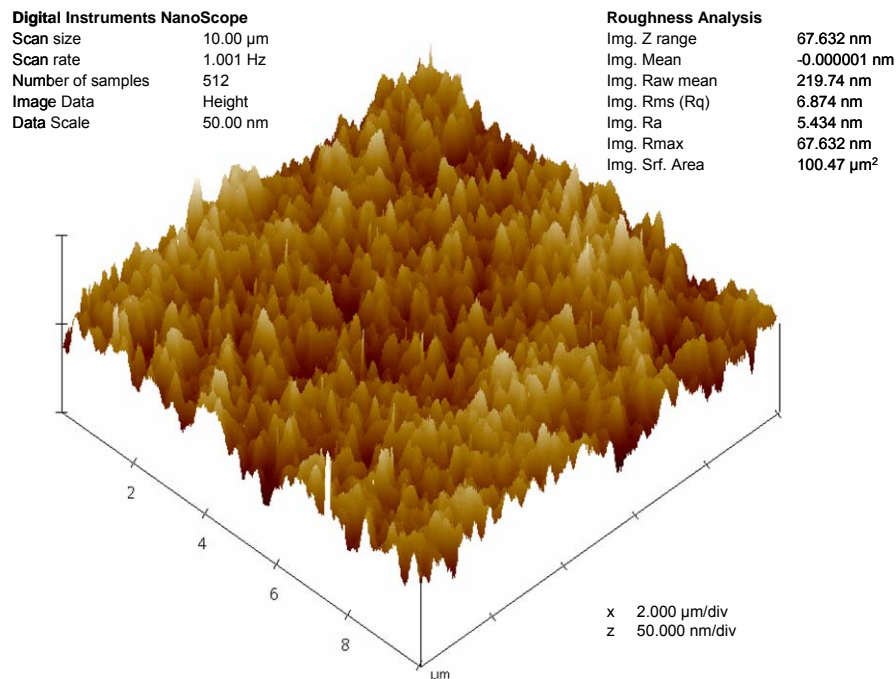


Figure 4-12: Surface structure of etched Degussa PMMA at an etch depth of 72.3 μm via Atomic Force Microscope (AFM) measurement.

The effect of developer agitation and post-exposure treatment on the surface roughness as reported in reference (Malek and Yajamanyam, 2000) was not studied. Malek and Yajamanyam showed that in an etch depth of $170 \pm 5 \mu\text{m}$, the surface roughness reduced from 51 nm to 23 nm for megasonic supported developer agitation. Moreover, the study showed a reduction in the surface roughness for a post-exposure annealing treatment at a temperature of 80 $^{\circ}\text{C}$. Both studies have to be conducted in future work.

To study the inclination of etched mirror surfaces, a MMA structure is etched according to Figure 4-1, whereby a stencil grating mask (mask 2) with a period of 160 μm (Design C, see chapter 3) is attached to the PMMA sheet surfaces and moved behind a fixed absorber (mask 1). The resulting PMMA MMA structure of 9 single cells after standard development procedure is shown in Figure 4-13. The top surfaces serve as a reference plane (red hatched surfaces in Figure 4-13 (b)) for both the interferometric use and here for the depth profiling and the determination of the mirror inclination as a function of etch depth. The mirror inclination is determined parallel (vertical) and perpendicular (horizontal) to the long side of the rectangular mirror surfaces for each of the etched cells (Figure 4-13 (a)).

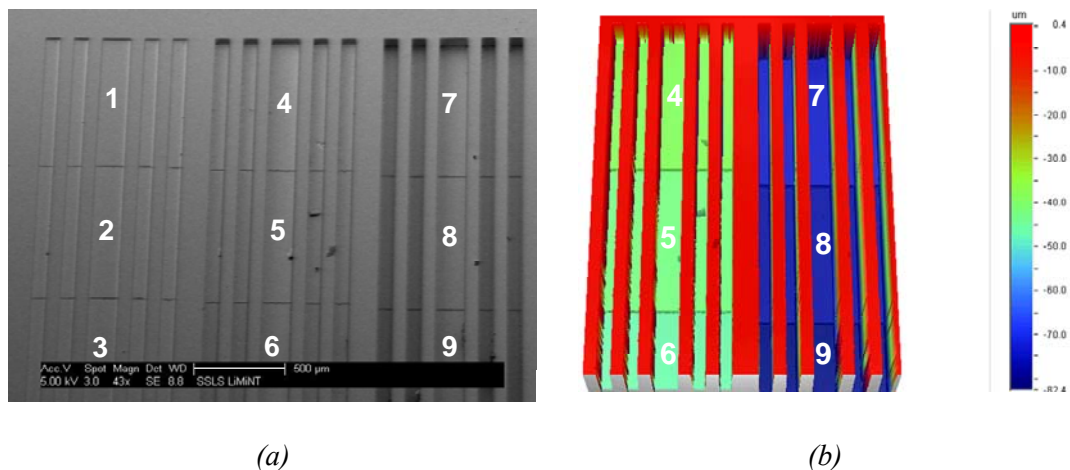


Figure 4-13: (a) SEM image of 3 x 3 3D MMA cells. Scale bar is 500 μm . In the sequence from 1 to 9 each cell is deeper than its predecessor. (b) Profiler measurement of cells 4-9 as shown in (a). Cell depths vary by 4 μm in vertical direction (4-5-6, 7-8-9) while, in horizontal direction (4-7, 5-8, 6-9) by 40 μm . From this data plot micro-mirror inclination angles were computed parallel (vertical direction in b) and perpendicular (horizontal direction in b) to the long side of the rectangular micro-mirrors.

Figure 4-14 (a) plots the obtained mirror inclination angles. The figure shows that to an etch depth of 140 μm , the inclination angle of the etched micro-mirrors concentrates in the μrad regime and stays well below 2 mrad for both PMMA materials. Furthermore, like the surface waviness, the mirror inclination increases with increasing etch depth. The corresponding surface waviness (after low-pass data

filtering) when the data is referenced to the top surfaces of micro mirrors (red hatched surfaces in Figure 4-13 (b)) is shown in Figure 4-14 (b).

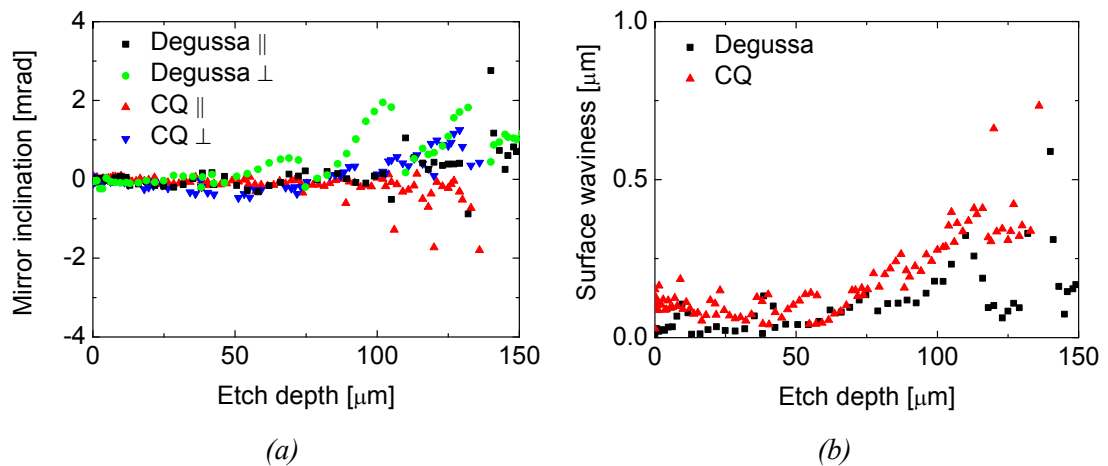


Figure 4-14: (a) Mirror inclination of etched micro-mirrors as a function of etch depth when referenced to the top mirror surface (red hatched surfaces in Figure 4-13 (b)). \parallel and \perp denote the inclination angle parallel and perpendicular to the grating grooves, respectively. (b) Corresponding average surface waviness as a function of etch depth.

Accordingly, down to an etch depth of 100 μm , the surface waviness (root-mean-square average) of all mirror surfaces is maintained below 0.25 μm and increases to 0.5 μm at 140 μm . Table 4-8 summarizes the statistics of the inclination angles independent of etch depth (etch depth < 140 μm). The standard deviation of the measured mirror inclination angles of all mirror surfaces is largest (0.626 mrad) for Degussa PMMA perpendicular to the grating grooves at a mean value of 0.401 mrad. For both directions, parallel and perpendicular to the grating grooves, CQ PMMA features a smaller standard deviation of the inclination angles implying better structure fidelity. Moreover, both types of PMMA coincidentally reveal the largest standard deviation for an inclination angle in the direction perpendicular to the grating grooves.

Table 4-8: Statistics of mirror inclination angle for Degussa and CQ PMMA down to an etch depth of 140 μm . The mirror inclination is measured with respect to the top micro-mirror surfaces as illustrated in the red hatched surfaces in Figure 4-13 (b).

| | Mean value [mrad] | Standard Deviation [mrad] |
|-----------------|-------------------|---------------------------|
| Degussa | 0.088 | 0.477 ± 0.067 |
| Degussa \perp | 0.401 | 0.626 ± 0.088 |
| CQ | -0.136 | 0.306 ± 0.031 |
| CQ \perp | 0.113 | 0.412 ± 0.050 |

Besides the study of the inclination angle of etched MMA mirror surfaces, the etch depth as a function of MMA cell number is shown in Figure 4-15 for the case of CQ PMMA. For the etching, MMA cells were exposed by a linearly increasing dose of 0.135 $\text{kJ}/\text{cm}^3/\text{cell}$. As we have described earlier, the etch depth first increases parabolic with exposure doses for doses lower than 4 kJ/cm^3 and subsequently increases linearly for exposure doses greater than 4 kJ/cm^3 (Figure 4-15 (a)). Thus, the depth of the MMA cells do not increase uniformly from cell to cell as it would be required for a uniform sampling of the interferogram (compare Eq. 3-15). This is also indicated by the changing density of the red, horizontal drop lines in Figure 4-15 (a). Figure 4-15 (b) displays the difference in the etch depth Δh from MMA cell to MMA cell. Accordingly, Δh increases parabolic until around 2 μm for the first 25 MMA cells (corresponding to an exposure dose $\leq 4 \text{ kJ}/\text{cm}^3$) and remains constant around 2 $\mu\text{m} \pm 1 \mu\text{m}$ for the rest of the cells.

The appropriate adjustment of the exposure dose, in particular for doses below 4 kJ/cm^3 may greatly reduce the variance in the difference in the etch depth Δh and thus the sampling. Additionally, a further improvement is expected by adjusting the development conditions such as development temperature or the agitation of the developer bath.

Nevertheless, these preliminary results underline a characteristic of the FPP FTS - the non-uniform sampling of the interferogram data (chapter 3.3.1.3). Although the non-

uniform sampling does not alter the spectral data, a basic requirement for the spectrometer is the knowledge of the sampling point positions and thus the requirement for an initial calibration of the device.

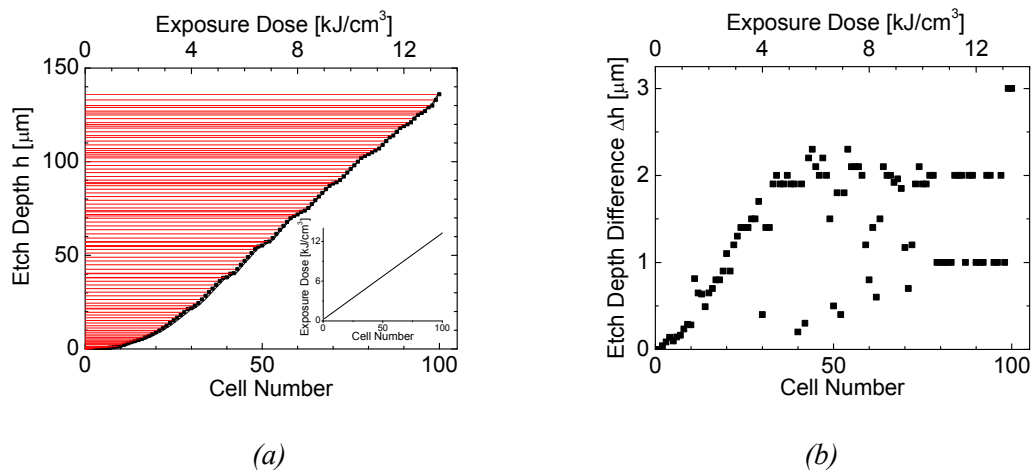


Figure 4-15: (a) Etch depth ‘ h ’ (in CQ PMMA) as a function of MMA cell number ‘ N ’ (black dotted line) for a linear increment of exposure dose (inset). The red, horizontal drop lines indicate the etch depth of each cell. The variation of the density of these lines highlights the non-uniform etch depth difference as a function of MMA cell. (b) Corresponding etch depth difference ‘ Δh ’ ($\Delta h = h_N - h_{N-1}$) as a function of MMA cell number ‘ N ’ and exposure dose.

We have shown earlier (see Table 4-7) that higher molecular weight PMMA provides higher α values which can be related to higher resist contrasts (Brewer, 1980, Pantenburg et al., 1998, and Mappes et al., 2007). To demonstrate the impact of resist contrast on the structure fidelity, we etched S-test structures of different widths but similar depths into both types of PMMA. These etch depths were $30.2 \pm 0.1 \mu\text{m}$ and $29.9 \pm 0.1 \mu\text{m}$ for Degussa (low molecular weight PMMA) and CQ PMMA (high molecular weight PMMA), respectively. Figure 4-16 shows the most prominent results. For comparison we use the two parallel sections of each S-string. In these parallel sections in the X-ray mask the S-strings is $20.4 \mu\text{m}$ wide at the top and $19.3 \mu\text{m}$ wide at the bottom string (a). The second test S-structure is $10.6 \mu\text{m}$ wide at the

top parallel section and 9.3 μm wide at the bottom parallel section (b). Comparing both PMMA etching results it is clearly evident that the higher molecular weight PMMA (c, d) provides a higher contrast whereas the development of the low molecular weight PMMA (e, f) leaks into absorber shadow of the X-ray mask. For the high molecular weight PMMA, the width of the S-structure at the top surface of the etched PMMA measures at both parallel sections 19.3 and 18.4 μm , which is about 1 μm smaller than its mask value (c). For the second structure shown (d), it is 9.9 and 9.4 μm . On the contrary, the low molecular weight PMMA clearly develops into the shadow region of the mask. For the wider S-structure (e), the low molecular weight PMMA structure broadens by 16 – 19 % and measures 24.3 μm at the top and 22.4 μm at the bottom string. The width of the finer S-string etched into the low molecular weight PMMA (f) further increases by 25 – 28 % and measures 13.2 and 11.9 μm , respectively.

The experiment clearly indicates the benefit of the high molecular weight PMMA over the low molecular weight PMMA for the lithographic patterning of microstructures. On the contrary, the low molecular weight PMMA was found advantageous to produce stepped micro mirrors of lower surface roughness.

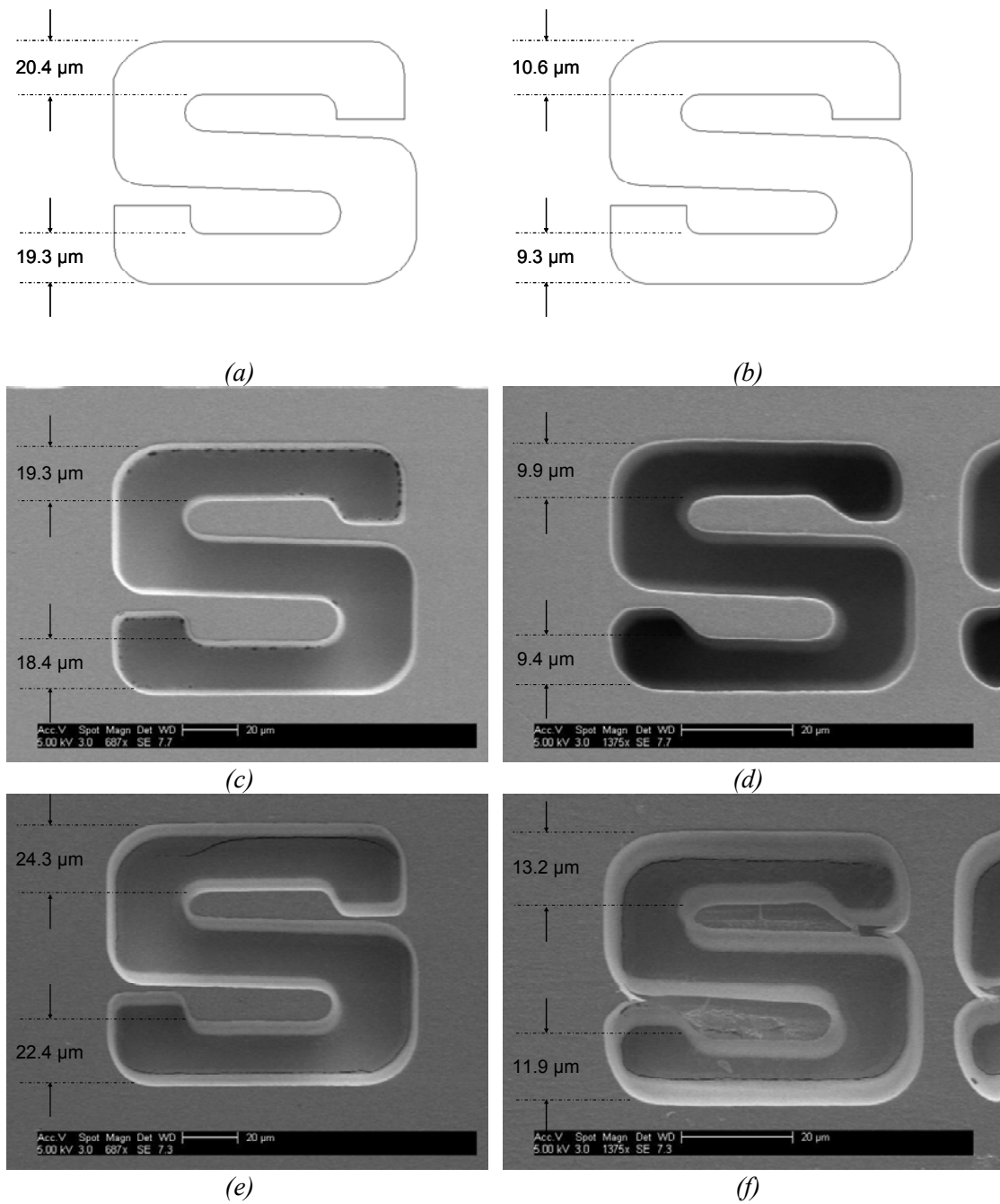


Figure 4-16: Influence of resist contrast on structure fidelity. (a, b) Reference structure and its measured structure width of the Au absorber structure. (c, d) S-test-structure etched $29.9 \pm 0.1 \mu\text{m}$ into CQ PMMA (high molecular weight). (e, f) S-test-structure etched $30.1 \pm 0.1 \mu\text{m}$ into Degussa PMMA (low molecular weight).

4.5 Reflection layer coating

As introduced in chapter 3, a gold reflection layer with a minimum thickness of roughly 40 nm is necessary for a reflectivity greater than 95 % throughout the near to mid infrared spectral band (1 - 20 μm). To verify the effect of layer thickness on the reflectivity, PMMA sheets were coated via magnetron sputter deposition with different reflection layer thicknesses and their reflectivities were compared against a standard gold mirror in a reflection measurement at SSLS Bruker IFS 66 FTIR. For all sputtered sheets, a 30 nm chromium layer serves as an intermediate adhesive layer. Figure 4-17 shows the resulting reflectivity in a spectral band from 1.3 to 16.7 μm wavelength. Accordingly, gold layer thicknesses of 8.5 and 23 nm show an increasing reflectivity for larger wavelength and remain for wavelengths larger than 8 μm at a maximum reflectivity of 90 % and 97 %, respectively. The reflectivity of a 33 nm and 122 nm thick gold reflection layers were practically indistinguishable from the reference gold mirror in the experimental setup and remained constant throughout the recorded spectrum indicating a minimum requirement of 33 nm thick gold reflection layers on top of the polymer matrix.

The respective reflection layers and their thicknesses as indicated in Figure 4-17 were investigated by high resolution x-ray specular reflectometry at grazing incidence angle in the x-ray demonstration and development (XDD) beamline at Singapore Synchrotron Light Source (SSLS) under the supervision of Dr. Yang. The diffractometer is the Huber 4-circle system 90000-0216/0, with high-precision 0.0001° step size for omega and two-theta circles. The storage ring, Helios 2, was running at 700 MeV and a typically stored electron beam current of 300 mA.

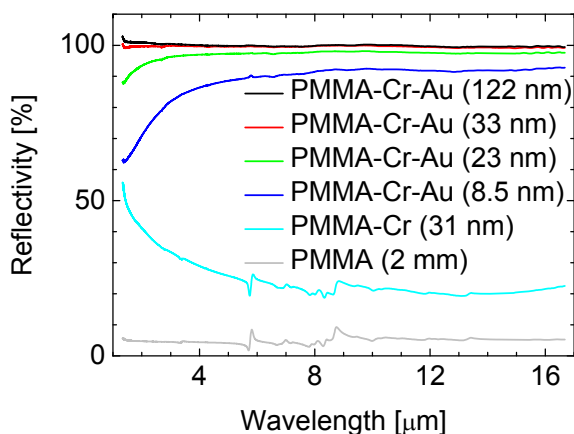


Figure 4-17: Reflectivity of sputtered Cr and Au reflection layers for various thicknesses on PMMA basis (2 mm thick Degussa PMMA sheets).

In the measurement, we selected photons of 8.048 keV energy, equivalent to $\text{CuK}\alpha_1$ radiation, with a Si (111) channel-cut monochromator (CCM) and toroidal focusing mirror. A rectangular slit system cut the beam to a 0.9 mm (vertical) and 3 mm (horizontal) footprint with a vertical divergence of about 0.01° . Another of 1.00 mm width is placed at the detector and the reflected photons are counting 5 seconds for every step and a step size of $2\text{-theta } 0.01^\circ$.

Diffuse scattering (background) of off-set scans were also measured at theta off-set angle of 0.20° in the range of above measurement. The pure reflectivity was obtained by subtracting the diffuse scattering from the raw data. The simulations were done using simulating software M805 and LEPTOS 1.07 release 2004 (Bruker). Figure 4-18 shows a typical reflectivity curve obtained high resolution x-ray specular reflectometry at grazing incidence angle and its simulated curve fit for a PMMA mirror coated with 31 ± 1 nm chromium and 8.5 ± 0.4 nm gold reflection layer. Table 4-9 summarizes all measurements.

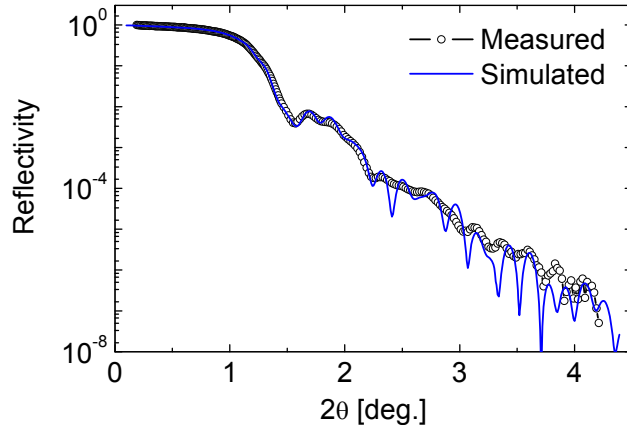


Figure 4-18: Reflectivity curve measured by high resolution x-ray specular reflectometry at grazing incidence angle versus angle 2θ and its simulated curve fit for a 2mm PMMA sheet coated with 31 ± 1 nm Cr and 8.5 ± 0.4 nm Au reflection layer.

Table 4-9: Reflection layer thickness and surface roughness obtained by high resolution x-ray specular reflectometry at grazing incidence angle at SSLS XDD beamline at X-ray energy of 8.048 keV. All layers were coated on a 2 mm Degussa PMMA sheet by magnetron sputtering (NSP 12-1 NTI) at a pressure below 5×10^{-6} bar. (Remark ^: The roughness of Cr layer varies around 1.2 nm).

| Sample (Sputter Conditions) | | Thickness (nm) | Roughness (nm) | Density (g/cm^3) |
|-----------------------------|--------------------------|----------------|------------------------|-----------------------------|
| Mirror | Au (100 W / 10 s) | 8.5 ± 0.4 | 1.1 ± 0.2 | 19.1 ± 0.7 |
| | Au (100 W / 25 s) | 23 ± 2 | 1.2 ± 0.2 | 18.9 ± 0.9 |
| | Au (100 W / 50 s) | 33.3 ± 0.3 | 1.2 ± 0.2 | 19.2 ± 0.5 |
| | Au (100 W / 150 s) | 122 ± 1 | 1.6 ± 0.1 | 18.9 ± 0.4 |
| Substrate | Cr layer (100 W / 100 s) | 31 ± 1 | $1.2 \pm 0.5^{\wedge}$ | 6.1 ± 0.4 |
| | Inter-layer | 15.0 ± 0.4 | 1.5 ± 0.3 | 2.0 ± 0.2 |
| | PMMA | - | 0.5 ± 0.2 | 1.2 (fixed) |

4.6 Summary

Chapter four discusses the fabrication of the MMA via a novel 3D X-ray lithography technique. Within this scope, a summary of the parameter developed in chapter three was presented first and three different spectrometer layouts for the visible, near- and mid- infrared were discussed. On the basis of these parameters, potential fabrication processes were reviewed and a process combining grey level exposure with X-ray lithography was developed. In contrast to earlier work, we developed a 3D X-ray lithography technique which locally varies the exposure dose by scanning multiple masks across resist surface during exposure. Its working principle and the developed exposure station were shown. A gold stencil mask for X-ray lithography was developed and tested. Aside from its throughput and through-the-mask-alignment advantage, the stencil mask proved to produce mirror surfaces of higher quality when compared to graphite masks in the PMMA etching process. Furthermore, we have shown a good thermal stability of the mask and negligible temperature rise of 1 °C when it is illuminated in the direct X-ray beam of the LiMiNT beamline. We characterized two types of PMMA resist for the 3D fabrication of the MMA according to their sensitivity, contrast, and dissolution rate. We studied influence of exposure dose, dose rate, initial molecular weight, and development temperature for the etching of stepped micro mirrors. Among the large number of studies available that addressed similar issues, critical information such as dose rate dependencies are lacking. Part of it is provided by this thesis. We demonstrated the influence of the dose rate on the development rate.

The etching of the micro mirrors was characterized by the resulting surface roughness and waviness as a function of etch depth. We have shown that the surface roughness of both types of PMMA increases with etch depth. For plane mirror surfaces, the

results suggest that low molecular weight PMMA provide smoother mirror surfaces in deeper etch depths when compared to higher molecular weight PMMA. In contrast for etching of microstructures, the higher molecular weight PMMA proved to produce micro mirrors of lower inclination angle. Moreover, the higher contrast of the high molecular weight PMMA revealed tremendously better structure fidelity. The etching of micro mirror arrays demonstrated the potential of the 3D X-ray lithography technique to produce stepped mirror surface with a stepping from the sub-micrometer to the sub-millimeter range. The variance in the stepping of the etched mirrors is expected to be improved by adjustment of the exposure and resist development conditions in particular for exposure doses below 4 kJ/cm^3 . Furthermore, the stepping variance indicated the characteristic nature of non-uniform sampling of the interferogram data for the FPP FTS based on etched PMMA MMAs.

We characterized the reflectivity of gold sputtered micro mirrors by IR measurements and characterized respective layer thicknesses by high resolution x-ray specular reflectometry at grazing incidence angle. In good agreement with the parameters developed in chapter 3, the result suggests a sufficient gold reflective layer thickness of 30 nm.

5 SPECTRAL CHARACTERIZATION

5.1 Introduction

Chapter 5 of the thesis deals with the spectral characterization of the Fast Parallel Processing Fourier Transform Spectrometer (FPP FTS). First, a test setup at the IFS 125 HR FTIR as part of the ISMI beamline of the Singapore Synchrotron Light Source (SSLS) is presented.

Preliminary test results, showing the influence of the first diffraction order on the amplitude modulation of single MMA cells are experimentally validated. On the basis of these results, prototype monolithic Diffractive Optical Elements (MMA's) fabricated via direct etching into bulk PMMA processes as introduced in chapter 4 are tested and spectra are recovered via the theories presented in chapter 2 of the thesis.

We examine noise sources and demonstrate the effect apodization and data averaging on signal-to-noise-ratios and transmission spectra. Finally, two spectrometric measurement scenarios are presented showing the inherent advantages of the FPP FTIR spectrometer. These are the measurement of single pulse radiation and time resolved spectroscopy.

5.2 Experimental setup at SSLS' IFS 125 HR spectrometer

The experimental setup to test the micro manufactured MMA's was realized in the SSLS IFS 125 HR FTIR spectrometer. The spectrometer is introduced in Appendix 8 and was chosen because of its easy accessibility of the infrared beam and its large, unobstructed, collimated beam of 10 - 20 mm diameter in the detector compartment of the spectrometer making it particular suitable for the prototype MMA measurements in the infrared. For

the optical alignment, the spectrometer was first illuminated with a NIR source producing sufficient visible light for the alignment and then operated with the globar source for the actual infrared experiments as presented thereon. Synchrotron infrared radiation produced by SSSL's storage ring source Helios 2 was not utilized up to date. All measurements and experiments were taken with the spectrometer under atmospheric conditions.

Depending on the experiment carried out, the spectrometer was operated in two optical setups:

- Setup A (Figure 5-1): standard FTIR operation used to obtain spectral information of the source, the spectral response of single MMA cells and transmission or absorption spectra of reference materials such as Teflon or polyethylene. In this optical setup, IR radiation emitted from the IR sources (A) in the source compartment is collected by a folding and spherical mirror and is directed towards the interferometer compartment. The spherical mirror is positioned two times its focal-length f (62.5 mm) from the source position casting an image of the source onto an aperture stop at $2f$ downstream the spherical mirror. The aperture stop is formed by a number of apertures of variable diameter on a rotating disk (D) limiting the source size and thus beam divergence. Parabolic and folding mirrors (E and F_1) collimate the beam and direct it through the beam splitter (G) at which one part of the beam is transmitted towards a movable corner-cube mirror (H) and the other part is reflected towards a fixed corner-cube mirror (I). Both beams recombine again after reflecting from the respective mirror at the beam splitter and are directed by mirrors (F_2 , J and F_3) to the sample compartment of the spectrometer. In the sample compartment the beam is directed through the bottom route as illustrated in the schematic. X marks the position of

samples for transmission measurements. At the opposite side of the sample compartment, a toroidal (K) and another folding mirror focus and direct the beam onto the entrance opening of the detector compartment. In the detector compartment, the beam is then collimated by a parabolic mirror (L) and directed at right angles towards a folding mirror (F_4) directing the beam to the MCT detector slot (N). Finally, a parabolic mirror (M) focuses the beam onto the detector surface.

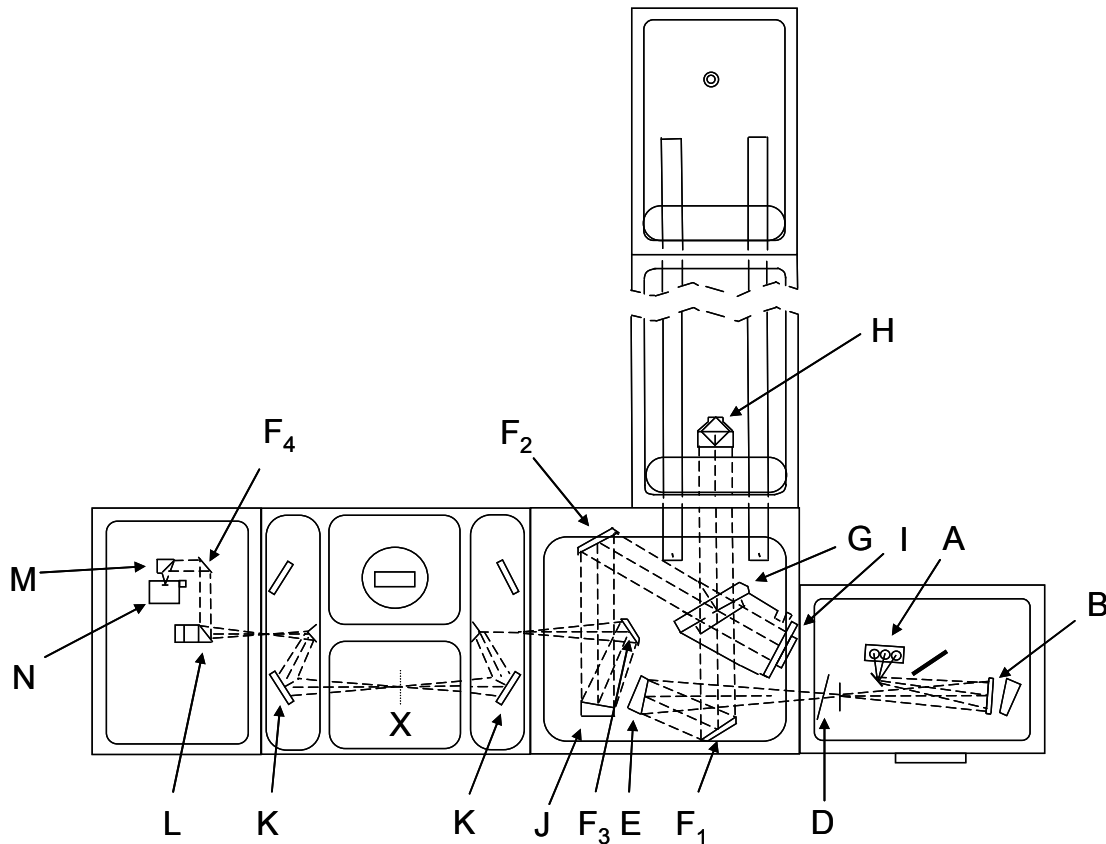


Figure 5-1: Top view IFS 125 HR in standard operation mode A. Definitions: A: Sources, B: Spherical mirror, D: Input apertures (field stop), E: Collimating parabolic mirror, F_{1-4} : Folding mirrors, G: Beam splitter, H: Scanner with movable corner-cube mirror, I: Fixed corner-cube mirror, J: Focusing parabolic mirror, K: Toroidal mirror, L: Collimating parabolic mirror, M: Focusing parabolic mirror, N: Detector position (MCT), X: Sample position for transmission measurements.

- Setup B (Figure 5-2): The modified spectrometer operation. In this setup, the spectrometer served merely as infrared source and collimator for the FPP FTS setup. The beam splitter of the interferometer is taken out and scanner optics is bypassed by flat folding mirrors (F_2 and F_3). Thus, the IR beam produced by the sources is directed from the source compartment through the spectrometer to the detector compartment without transmitting either through beam splitter or transmission windows to the detector compartment. In the detector compartment, the optics is rearranged to allow for the spatial filtering of higher diffraction orders as presented in chapter four. Thus, the radiation beam entering the detector compartment is collimated by the parabolic off-axis mirror (L) (focal length $f = 63.5$ mm). It illuminates the MMA mirrors mounted here schematically at a 45° angle (R) whereby the lamellae walls are oriented to avoid shadowing (compare chapter 3.3.1.5.1). The diameter of the collimated beam measures approximately 20 mm. Upon reflection from the MMA, a parabolic mirror (M) (focal length 19.3 mm) collects the reflected/diffracted light and focuses it onto a circular/rectangular aperture (S). Downstream of the aperture a second parabolic mirror (T) (focal length 12.3 mm) collimates the filtered beams again and directs them towards a folding mirror (F_5) which then directs the beam towards an infrared camera system consisting of a $f/0.8$ germanium lens system (U) and a micro-bolometer array detector (V) (Thermoteknix, 2009). An image of the detector compartment in setup B is shown in Figure 5-3.

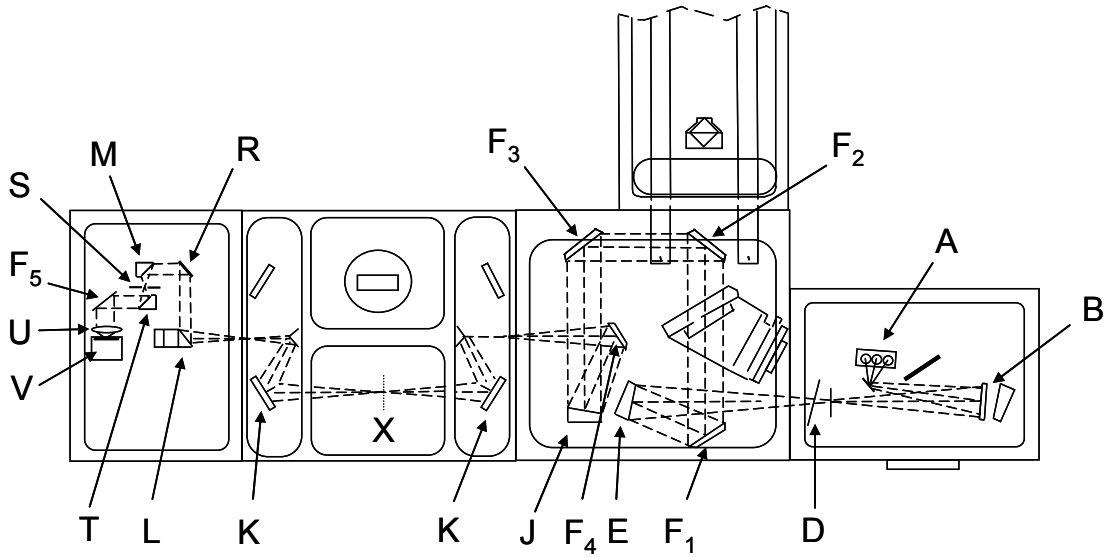


Figure 5-2: Top view IFS 125 HR spectrometer in operation mode B: Definitions: A: Sources, B: Spherical mirror, D: Input apertures (field stop), E: Collimating parabolic mirror, F₁₋₅: Folding mirrors, J: Focusing parabolic mirror, K: Toroidal mirror, L: Collimating parabolic mirror, M: Focusing parabolic mirror, R: MMA / plane mirror, S: Circular/ rectangular aperture, T: Collimating parabolic mirror, U: Germanium lens system, V: Micro-bolometer array detector, X: Sample position for transmission measurements.

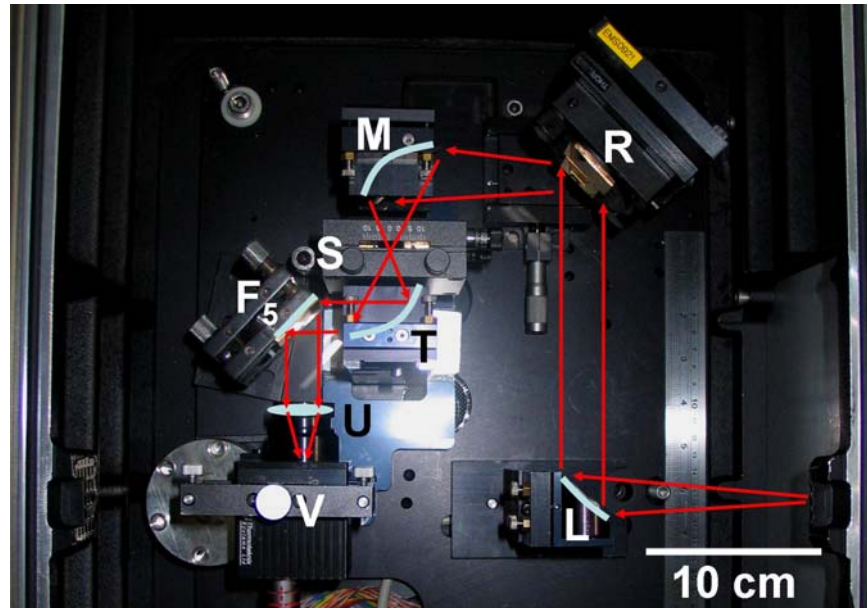


Figure 5-3: Image of the detector compartment of IFS 125 interferometer in optical setup B for the spectrometric validation of the FPP FTIR working principle. F₅: Folding mirror, L: Collimating parabolic mirror, M: Focusing parabolic mirror, R: MMA / plane mirror, S: Circular/ rectangular aperture, T: Collimating parabolic mirror, U: Germanium lens system, V: Micro-bolometer array detector.

5.3 Spectral response of single MMA cells

Prior to test multiple MMA cells, the response of single cells was examined. The emphasis was thereby put on demonstrating experimentally the influence of the first diffraction order on the modulation amplitude as introduced in chapter 3. The test structure was a 10 x 10 mm² uniform binary grating (Design A - compare chapter 3.3) manufactured according to chapter 4 and subsequently coated with a 100 nm gold reflection layer via PVD process. The grating depth and period are 8.2 μm and 200 μm, respectively. Both were confirmed with optical profiler measurements prior to the test.

The spectral response of the structure was examined with the IFS 125 HR spectrometer in setup A (see chapter 5.2) whereby the arrangement in the detector compartment was slightly modified. Folding mirror F₄ (see Figure 5-1) was replaced with the gold coated binary grating and placed with the grating lamellae walls being parallel to the normal of the incoming plane waves which are cast by the collimating parabolic mirror (L). In the focal plane of parabolic mirror (M, focal length of 19.3 mm) an adjustable circular aperture allowed the spatial filtering of higher diffraction order (compare chapter 3.3.1.4) and the transmitted radiation was focused by an elliptical mirror onto a single pyroelectric detector element (DLaTGS). After alignment of the system with the NIR source, the spectral response was recorded with the globar source, KBr beam splitter and a field stop aperture of 2.5 mm diameter in the source compartment of the spectrometer. Spectral responses were then obtained with respect to the opening diameter of the circular aperture in the focal plane of parabolic mirror M.

Figure 5-4 shows the spectral response of the single grating cell for two extreme aperture settings. It can be seen that for an aperture with a diameter of 1.0 mm, corresponding to

an acceptance angle Ψ_A of 25.9 mrad, the modulation amplitude is the highest in the spectral range from 500 - 1900 cm^{-1} and decreases with increasing wavenumbers as higher diffraction order pass the spatial filter (compare chapter 3.3.1.4).

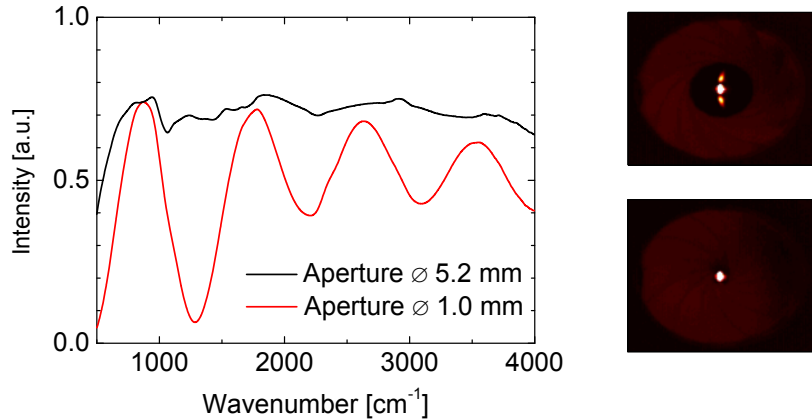


Figure 5-4: Intensity modulation of a single MMA cell at an incidence angle of 46 degrees with respect to the grating normal as a function of wavenumber for two detector aperture openings. The MMA cell (Design A) examined has a grating depth of 8.2 μm and a period of 200 μm . The inset shows the infrared images (in the spectral range of 625 – 1350 cm^{-1}) of the two cases, aperture accepting zero and higher order diffracted light (top, right) for an aperture diameter of $\varnothing = 5.2$ mm and aperture accepting zero diffraction order (in the spectral range of 625 – 1350 cm^{-1}) only (bottom, right) corresponding to an aperture diameter of $\varnothing = 1.0$ mm.

At an aperture diameter of 5.2 mm the modulation of the intensity is lost while the detector receives the highest intensity.

The insets of Figure 5-4 demonstrate the spatial filtering principle graphically. Both images were taken with the infrared camera Miricle 110K distributed by Thermoteknix Systems Ltd (Thermoteknix, 2009). In this optical setup, the camera replaced the elliptical mirror and single detector element of the previous experiment while the rest of the optical setup remained untouched. The camera, equipped with an f/0.8 germanium lens system and a nominal focal length of 15 mm, was focused to the aperture plane. The core element of the camera is the ULIS 384 x 288 LWIR uncooled amorphous silicon

micro-bolometer FPA chip (UL 03 04 1) which is sensitive in a spectral band ranging from approximately 7.5 – 15 μm wavelength (corresponding to 650 – 1350 cm^{-1}). For this spectral range and an aperture opening diameter of 5.2 mm, the corresponding infrared image (Figure 5-4, top right) shows both zeroth and first diffraction order are passing through the circular aperture. At this setting, the aperture opening allows a theoretical acceptance angle of 134 mrad and according to Eq. (3-20) first and higher order radiation for wavelength shorter than 26 μm (384.6 cm^{-1}) to pass the spatial filter. In contrast, the smallest aperture setting of 1.0 mm diameter accepts zeroth order diffracted light for wavelength smaller than 130 μm (at an estimated number of illuminated grating periods $N=50$) while the first order radiation of wavelengths longer than 5.2 μm (1923 cm^{-1}) are blocked by the spatial filter. For wavelength below 5.2 μm both, zeroth, and first diffraction order pass the spatial filter, enter the detector plane, and reduce the amplitude modulation.

The minima of the modulation (destructive interference) appear according to Eq. (5-1).

$$\lambda_{\min} = \frac{2h}{(n - \frac{1}{2})} \cos(\beta),$$

or

$$\sigma_{\min} = \frac{(n - \frac{1}{2})}{2h \cos(\beta)}. \quad (5-1)$$

From the position of these minima the actual incidence angle is according to Eq. (5-1) 46° and agrees well with the nominal angle of 45° of the optical setup.

In summary, the above experiments demonstrate the importance of filtering higher diffraction orders from entering the detector in order to maintain high modulation amplitudes and thus the interferometric information.

5.4 Spectral characterization of 10 x 10 MMA cell spectrometer

The working principle of the FPP FT spectrometer is demonstrated using a prototype micro-machined 10 x 10 cell Micro Mirror Array (MMA). The prototype MMA was positioned according to setup B and illuminated under an incident angle of $45^\circ \pm 1^\circ$ by filtered as well as unfiltered globar radiation. In this context we refer to unfiltered radiation when no additional filters, excluding the permanent filter of the detector and its optics, are inserted into the radiation path.

The tested MMA spanned a square area of $9.6 \times 9.6 \text{ mm}^2$ in which each single cell has a size of $0.96 \times 0.96 \text{ mm}^2$. Each of the single cells is of type C (compare chapter 3) with $1 \times 0.16 \text{ mm} \times 0.96 \text{ mm}$ center, and $10 \times 0.08 \text{ mm} \times 0.96 \text{ mm}$ lamellar front and back facet stripes alternating outwards. CQ PMMA was the material of choice to form the MMA structure due to its higher structure fidelity and its sufficient reflecting surface quality for mid-infrared radiation. The maximum depth and thus the maximum optical path difference at 45° were 0.136 mm and 0.192 mm , respectively. Accordingly, the nominal resolution is 26 cm^{-1} . The average increment of the optical path difference b is $1.94 \text{ }\mu\text{m}$ with a variance of $1.06 \text{ }\mu\text{m}$.

5.4.1 Data processing

The following section describes the procedure from capturing the image with the array detector to acquiring the spectral information via image data processing. The spectral analysis presented in this thesis bases on the detection of the infrared images with an amorphous silicon micro-bolometer *Miricle 110K* marketed by *Thermoteknix Systems Lt.* The camera presents a low-cost, un-cooled alternative to the high-end, state-of-the-art

Mercury Cadmium Telluride (MCT) focal plane array (FPA) detector technology used for infrared imaging. It was chosen in the frame of this work because of its comparable good performance, low-cost, and ease of access due to less stringent ex- and import licenses.

The core of the *Miricle 110K* infrared camera is the *ULIS UL 030401* amorphous silicon micro-bolometer focal plane array. Its read-out-circuitry produces a 384 x 288 pixel image every 20 ms. These images are obtained by a rolling integration and read out method - a method in which the pixel intensities of each pixel row are integrated within a 64 μ s clocking period, while the previously integrated pixel row is read out. After integration the circuit switches to the next row for integration and read out until the 288 pixel rows are read out.

The images are sequentially stored as 15-bit images in sequence files within the software platform *ThermaGram*© provided by *Thermoteknix Systems Ltd.* The software allows access to each of the images stored in the sequence files, windowing of pixel areas for detection and exporting of intensity matrices. These single image matrices are then imported into MatLab© platform for the spectral analysis.

The procedure for the spectral analysis is presented in a flowchart in Figure 5-5. The starting point is a single, 15-bit image of the MMA taken with the camera after importing into the MatLab© platform. Figure 5-6 shows an exemplary image of the 10 by 10 cell MMA illuminated with unfiltered global radiation.

The rectangular shape of MMA cells in the infrared image is a direct result of the inclined illumination and the imaging conditions. Keeping the detector and its lens perpendicular to the optical axis of the system proved to provide less image distortion.

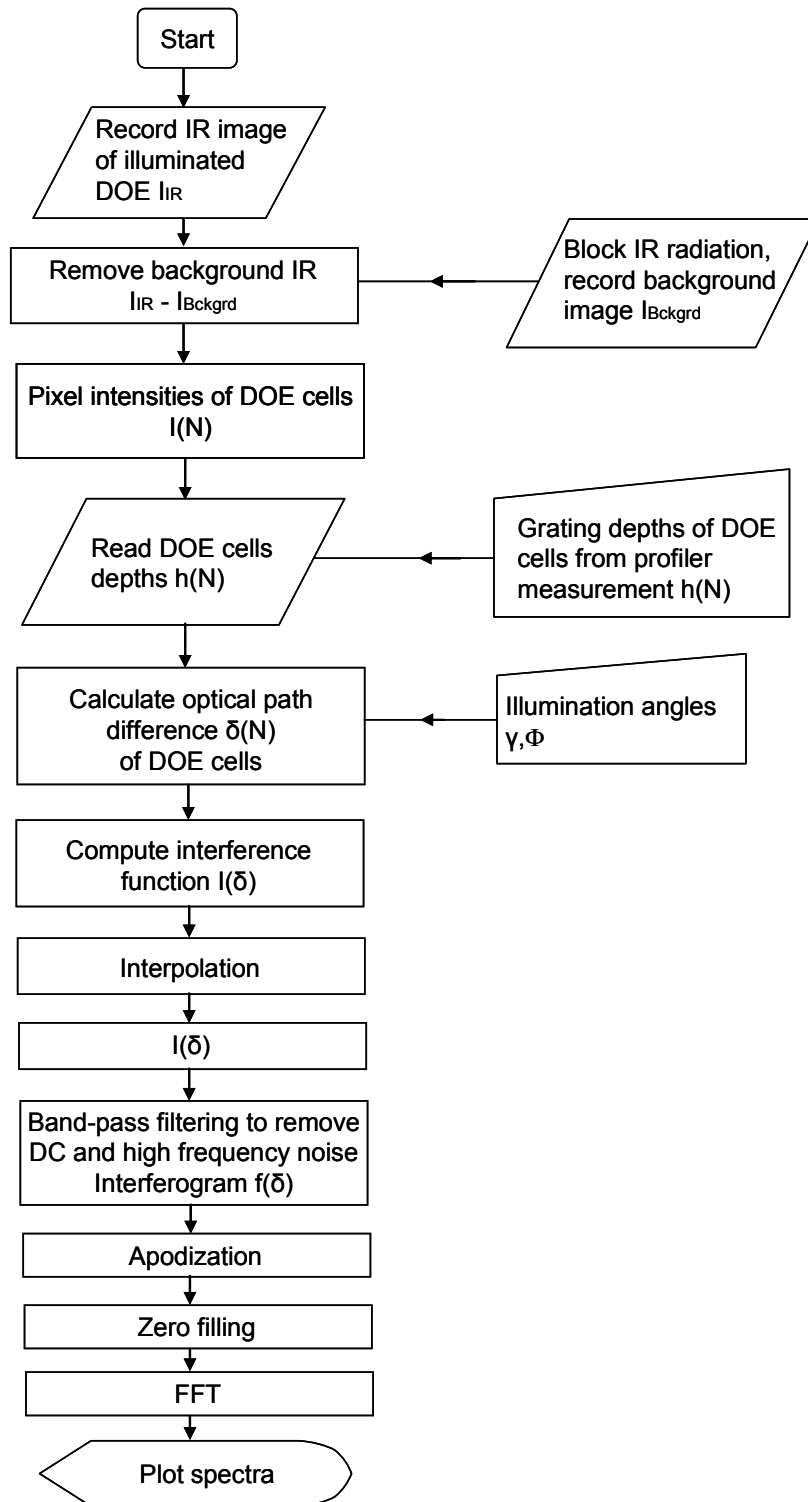


Figure 5-5: Data processing flowchart to acquire spectra

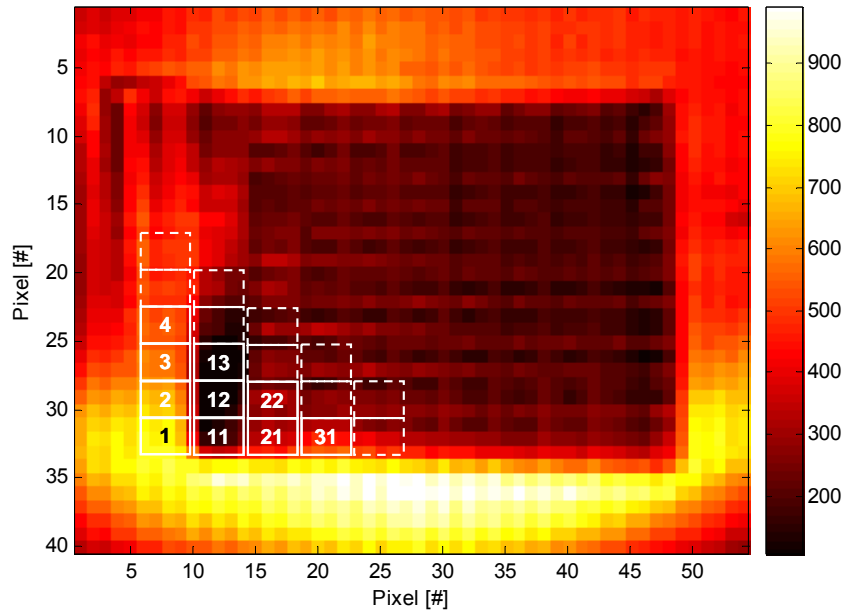


Figure 5-6: Intensity distribution and spatial interference function after reflection from the MMA (placed at position R in Figure 5-2). The white boxes indicate the imaging area of the individual MMA cells. Here each MMA cell is imaged onto 4×3 pixels.

From the position of the single MMA cell pattern in the image, the intensity of each cell is read as a function of the cell number $I(N)_r$, whereby the subscript r depicts raw data (Figure 5-7). Subsequently, the interference function (see $I(\delta)_r$ in Figure 5-8) is computed by converting the cell number into the respective optical path difference δ calculated from the cell depth for a given set of incidence and imaging angles Φ , Y , and β (see Eq. A5-1 for $\Phi = 0^\circ$, $Y = 45^\circ$, $\beta = 90^\circ$). The cell depth in turn is known from measurements using white light interferometry. Cell 1 is a plane mirror element and corresponds to zero optical path difference while the optical path difference continuously increases for higher cell numbers. Note that the variance in the spacing of the vertical drop lines in Figure 5-8 indicates the bunching of data points due to the non-uniformly spaced etching depths of the MMA grating cells. This effect can be balanced by appropriate selection of exposure

dose and development conditions in the lithography process. An experimental correction of the MMA fabrication has to be undertaken in future works.

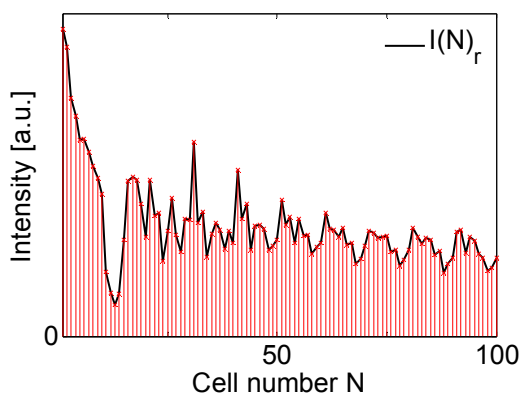


Figure 5-7: Intensity readout for a single infrared image taken with the detector.

The computation of the interferogram $f(\delta)$ from the interference function is demonstrated in Figure 5-8. The interference function $I(\delta)_r$ is first interpolated by a piecewise cubic Hermite interpolation polynomial (Fritsch and Carlson, 1980, and Kahaner et al. 1988) resulting in $I(\delta)_i$, and subsequently filtered with a fast Fourier transform (FFT) band-pass filter. Subscripts r , i , and f in the figure depict raw, interpolated, and filtered data, respectively. The pass band of the FFT filter is set by the working range of the IR camera system ($500 - 1500 \text{ cm}^{-1}$). The piecewise cubic Hermite interpolation or linear interpolation was chosen over cubic interpolation polynomials as both showed better spectral agreement with reference spectra, whereas the cubic interpolation resulted in more erroneous spectral features. After interpolation and filtering, the resulting interferogram may then be multiplied by various apodization functions followed by *zero filling*. In the *zero filling* procedure, data points of zero intensity at optical path differences greater than the physically measured data set are added to the interferogram

data allowing the computation of smoother spectra after Fourier transformation without altering the spectral information. Finally, the spectra are computed via FFT code.

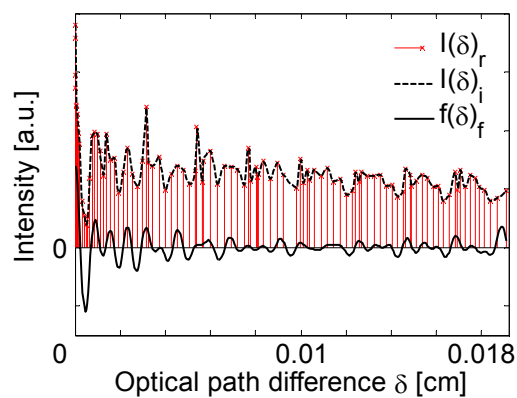


Figure 5-8: Interference function and resulting Interferogram after digital band-pass filtering.

Figure 5-9 compares the normalized spectra of the globar source taken with the IFS 125 HR spectrometer in setup A at a resolution of 4 cm^{-1} with the normalized spectra taken with the FPP FTIR spectrometer at a resolution 100 and 26 cm^{-1} , respectively.

Using the *Miracle 110K* infrared camera for the detection, the useful spectral range of the FPP FTIR is limited at low frequency at 600 cm^{-1} by the transmission characteristics of the Germanium lens and at high frequency at 1400 cm^{-1} by the filter characteristic of the microbolometer detector window.

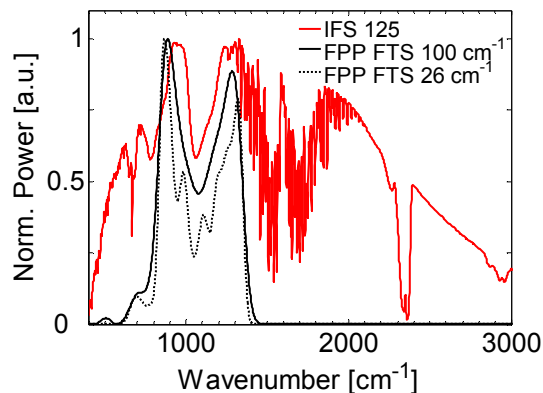


Figure 5-9: Comparison of source spectra recorded with the Bruker HR 125 spectrometer (red line) at a resolution of 4 cm^{-1} and the FPP FTS (black lines) at resolutions of 100 cm^{-1} and 26 cm^{-1} . The narrower spectral band-pass shown by the FPP FTS is due to the fact that in the current experimental set-up, the useful spectral range of the FPP FT spectrometer is limited at low frequency at 600 cm^{-1} by the transmission characteristics of the Germanium lens and at high frequency (1400 cm^{-1}) by the filter characteristics of the microbolometer detector window. All spectra were taken with triangular apodization.

5.4.2 Frequency calibration

For calibration and characterization of the FPP FTIR setup two narrow band-pass filters, centered at $10.43\text{ }\mu\text{m}$ (958 cm^{-1}) and centered at $8.01\text{ }\mu\text{m}$ (1248 cm^{-1}) wavelength respectively, were used. Both filters were first characterized with a Bruker IFS 66 FTIR at a resolution of 4 and 26 cm^{-1} (Figure 5-10). Note in Fig. 5-10 that the quantitative value of transmission level of the respective filter is determined by the spectral resolution set by the spectrometer. For spectrometer with a resolution larger than the spectral width of the band pass, the transmission spectra show lower transmission amplitudes and at the same time wider spectral transmission peaks.

In the calibration procedure, the spectrum of one transmission filter was obtained with the FPP FTS and both illumination angles Φ and Y in the calculation of the optical path difference varied until the normalized peak of the spectrum taken with the FPP FTS

coincided with the normalized peak of the reference spectrum. The second narrow band pass filter served to verify the frequency calibration.

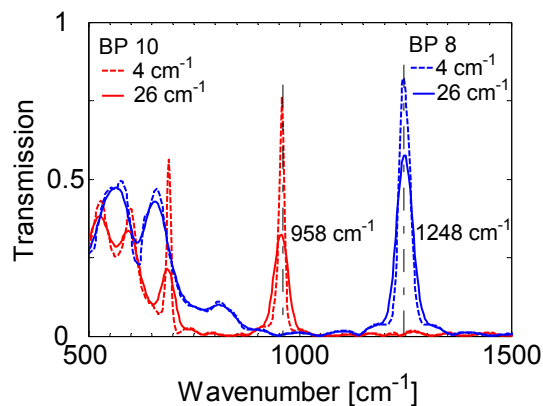


Figure 5-10: Reference transmission spectra of two narrow band-pass filters (BP10 and BP8) taken with the Bruker IFS 66 FTIR at a resolution of 4 and 26 cm^{-1} , respectively. The peak positions at a resolution of 4 cm^{-1} / 26 cm^{-1} were found at 958 cm^{-1} / 958 cm^{-1} , and at 1245 cm^{-1} / 1248 cm^{-1} for the BP10 and the BP8 transmission filter, respectively.

For the prototype setup, the procedure resulted in a peak position accuracy of smaller than 3 cm^{-1} in the spectral band from 958 cm^{-1} to 1248 cm^{-1} when compared to the reference spectra taken at a nominal resolution of 4 cm^{-1} . The illumination angle for the best fit was found to be $Y = 0^\circ$ and $\Phi = 45.3^\circ$.

Figure 5-11 demonstrates the agreement in the peak position of both filters after the calibration. The spurious peak at 1030 cm^{-1} of the BP10 filter in the spectrum taken with FPP FTS is a direct result of the truncation of the interferogram and can be removed by applying apodization functions to the interferogram.

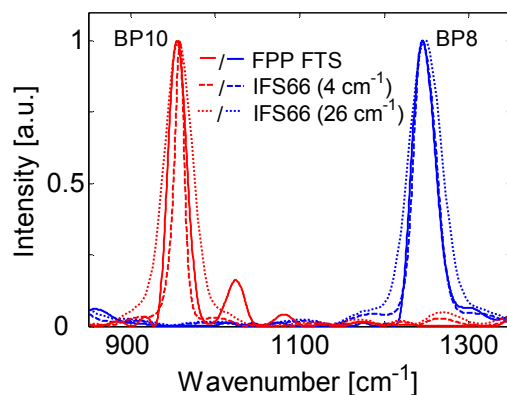


Figure 5-11: Comparison of normalized band pass filter (BP10 and BP8) spectra taken with IFS 66 at 4 cm^{-1} (dashed) and 26 cm^{-1} resolution and FPP FTS (solid) for two narrow band pass filters centered at 958 cm^{-1} (red curves) and 1046 cm^{-1} (blue curves) after frequency calibration procedure.

5.4.3 Spatial source ‘non’-uniformity and its compensation

Characteristic for stationary spectrometers such as the FPP FTIR is that the interferogram is spread in space. In the case of the FPP FTIR, the interferogram is generated by the MMA of which each of its cells produces a single interferogram point. As the cells are spread in a 2D space, the detector records a position dependent interferogram map leading inevitably to the discussion of spatial source uniformity.

To quantify the spatial source uniformity and its influence on the computed spectra, the MMA was replaced by a plane gold coated mirror in the optical setup and the source intensity distribution was recorded with the array detector with equal imaging conditions (Figure 5-12). Using the same data read out grid as presented for the MMA cells, the intensity distribution of the source is plotted as a function of the respective MMA cell position $I_0(N)$ and compared with the interference function $I(N)$ generated by the MMA (Figure 5-13). Figure 5-13 shows a significant intensity modulation of the source across the MMA surface measuring up to 30% of the input signal.

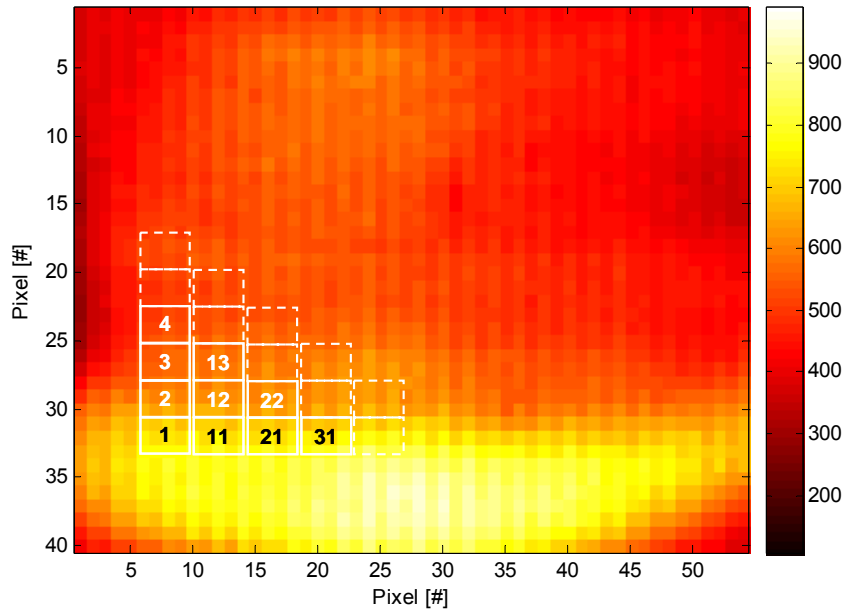


Figure 5-12: Intensity distribution of IFS 125 HR globar source obtained with plane mirror at the position of the MMA. The white boxes indicate the imaging area of the individual MMA cells. Here each MMA cell is imaged onto 4 x 3 pixels.

As the interference function $I(N)$ is modulated in the same period as $I_0(N)$, the measurement indicates an overlying intensity modulation of the interference function due to the modulation of the input radiation $I_0(N)$.

To compensate the effect, the interferogram function Eq. (2-5) is rewritten as a function of cell number to:

$$f(N) = \frac{1}{R^2} \left(I(N) - \frac{1}{2} I_0(N) w \right), \quad (5-2)$$

where the transmission T of interfering beams in Eq. (2-5) is replaced with the reflection R and the path difference δ by the cell number N . w is a weighing factor depending on the absorption of the specimen measured with the spectrometer. It is calculated from the ratio of the zero path difference intensity of specimen and the source. The weighing factor is 1 for the source and <1 for measurements of specimens.

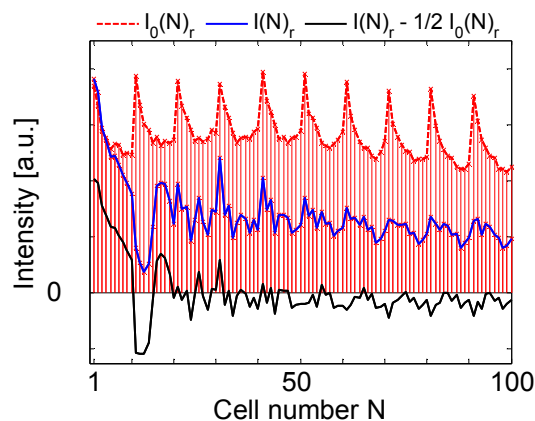


Figure 5-13: Interference function and source compensation

In the compensation procedure, each cell's signal channel is treated separately with its distinct input radiation strength I_0 . It is based on the assumption of a uniform reflection of all micro mirrors and throughout the spectrum of interest as well as uniform transmission or absorption of any specimen. The resulting interferogram function $f(N)$ is shown as a black solid line at the bottom graph of Figure 5-13.

After interpolation and subtraction of the DC components for $I_0(N)$, $I(N)$ and $f(N)$, the power spectra of each component is computed. Figure 5-14 presents these power spectra for a broad band spectral input radiation as produced by the IFS 125 globar source. The figure reveals that the intensity modulation of the source across the MMA surface generates a comparable large signature in the power spectrum ($B(\sigma)_{I_0}$), in particular at a wavenumber of 435 cm^{-1} , and more importantly, within the spectral working band (500 cm^{-1} to 1500 cm^{-1}) of the detector. It is apparent that such spectral features generate a fixed noise pattern and necessitate compensation. Nevertheless, it depends on the intensity uniformity generated by the source and may be overcome to a large extent by a better adjustment of the optics alone.

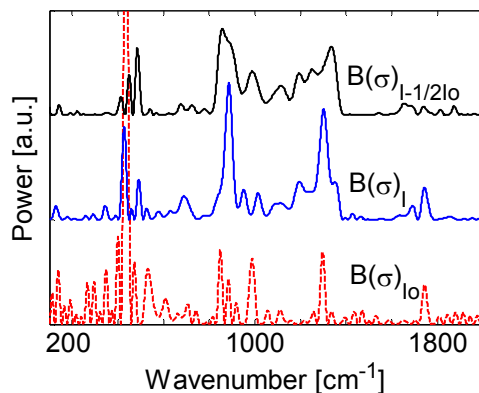


Figure 5-14: Power spectra taken with the FPP FTIR prototype. Curves are shifted with respect to each other for better viewing. $B(\sigma)_{10}$ (dashed red line), $B(\sigma)_1$ (solid blue line), and $B(\sigma)_{1-1/210}$ (solid black line) denote the power spectra arising from the source non-uniformity only, the uncompensated, and the compensated source spectra taken with the MMA, respectively.

To demonstrate the improvement in the obtained spectra after the compensation of source ‘non’-uniformity, the transmission spectra of PTFE, KBr, and both narrow band-pass filters were measured and compared to their reference transmission spectra taken with the Bruker IFS spectrometers (Figure 5-15). All transmission spectra taken with the FPP FTIR are computed from single infrared images. In contrast, all reference transmission spectra were averaged over 100 scans and apodized automatically with a 3-term Blackman-Harris function at a nominal resolution of 26 cm^{-1} .

The left column of the figure shows the spectra without apodization, whereas the right column presents the spectra after triangular apodization. Solid blue, black and red lines indicate uncompensated, compensated, and reference spectra, respectively. The top spectra compare the power spectra of the globar source. It can be seen that most of the spectral power is concentrated in the spectral band from $800 - 1400 \text{ cm}^{-1}$ and extends to 600 cm^{-1} at lower spectral powers.

The improvement of the transmission spectra after source compensation is shown most noticeably for the PTFE and the BP10 transmission spectra when no apodization function is used. For the PTFE transmission the erroneous modulation of the transmission spectra is reduced within the spectral band from 800 to 1400 cm^{-1} , whereas in the case of the BP10 transmission spectra the compensation visibly improved the transmission peak position.

Applying apodization functions to the same data set greatly reduces the noise modulations at the expense of spectral resolution. An effect which can be observed by the widening of the transmission peaks after apodization (compare BP8 transmission in Figure 5-15). Furthermore, the position of the transmission peak (see BP10) is improved. All of the presented spectra closely follow the reference in the spectral band of 800 – 1350 cm^{-1} , while at both ends of this spectral range comparably large deviations from these references are observed. This may be explained by the low spectral powers registered by the FPP FTS in the current optical setup and thus insufficient signal-to-noise ratios. Section 0 addresses this issue in greater detail.

Besides the spatial uniformity of the source, its temporal uniformity may place further restrictions on its compensation. If a source fluctuates largely, spatially as well as temporally, the described compensation procedure requires measuring both, the intensity distribution of the input radiation I_o and the interference function I for each specimen at every time instant a spectrum is taken.

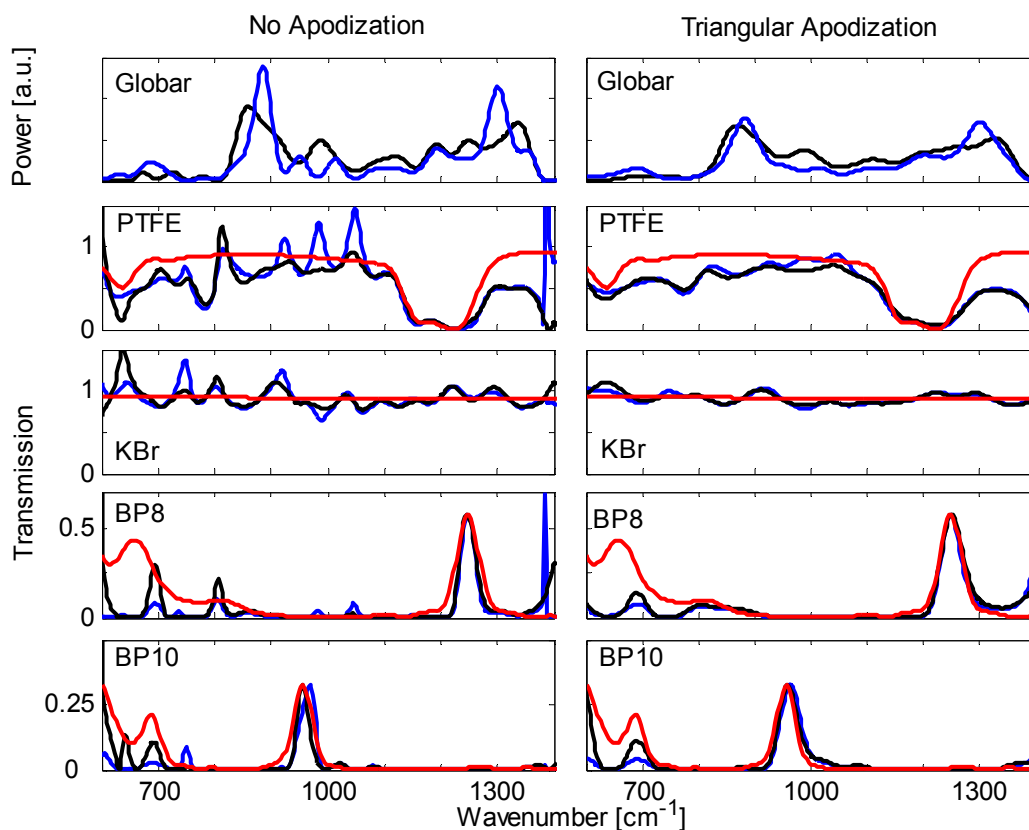


Figure 5-15: Power and transmission spectra of compensated (black) and uncompensated (blue) source uniformity taken with the FPP FTIR in comparison to the reference spectra (red) taken with the Bruker IFS spectrometers at a resolution of 26 cm^{-1} . Transmission spectra of BP8 and BP10 were normalized to the reference spectra for better comparison.

One possible way to accomplish both is to split the incoming intensity by an amplitude beam splitter, whereby either the transmitted or the reflected beam is used to measure the interference function with the MMA while the other part of the split beam is utilized to measure the source uniformity with a flat mirror reflection. Both beams are directed towards the array detector and are measured under the same imaging conditions. Its trade-off comes with the utilization of such transmission optics at the expense of the basic advantage of broad spectral working bands and high throughput provided by all reflecting optics.

The temporal fluctuation of the global source is treated in section 5.4.4.3. We show that, within the detection limit of the imaging system, the global emits temporally stable radiation and thus further compensation is not required for the prototype FPP FTS.

5.4.4 Noise

As we have shown in section 5.4.3 covering the influence of the spatial source uniformity, it is apparent that non-uniform input signals or non-uniform detection results in erroneous spectral features. These erroneous spectral features are addressed here in greater detail as noise. Sources of noise may be random or constant in nature, and are distinguished as multiplicative or additive noise, respectively (see 2.2.9.1).

In the following, we study four noise sources of the prototype FPP FTIR, namely:

- the infrared camera as a system component, including the detector and its read out circuitry,
- the background radiation of the instrument,
- the temporal source fluctuation, and
- the random noise generated in spectra.

The analysis is based on sequentially taken data at a capturing rate of 20 ms, and total time spans up to 5 seconds. The noise generated by the infrared camera is characterized for the full array of the detector, whereas the background radiation of the instrument and the temporal fluctuations of source are analyzed for the detector area of interest.

5.4.4.1 Infrared camera noise

To study the noise level generated by the infrared camera itself, we blocked the camera with a black metal piece of a temperature of 24.1 ± 0.1 °C (Figure 5-16). Under these conditions the infrared camera (*Thermoteknix Miricle 110K*) and its 15 bit (32768 grey levels) read-out circuitry produce an average output of 7913 grey levels at a uniform standard deviation below 2 grey levels for 100 consecutive images. As it can be seen in the figure, the grey level intensity at the rim of the detector array is elevated by 60 grey levels compared to the center intensity. An effect which may be attributed to thermal radiation generated by the camera itself as it is indicated by a temperature of the lens housing measured at 28.8 ± 0.1 °C. To minimize its influence for the spectrometric measurements, we utilized 54 x 40 pixels in the center of the detector array. In this pixel area the detector intensity measures 7893 ± 10 grey levels (see Figure 5-17 (a)).

The dark current of the pixels is shown in the bottom graph of Figure 5-17 (a). It was obtained by measuring a metal piece at liquid nitrogen temperature (-196 °C), beyond the nominal sensitivity range of the detector of -30 °C. At minimum, the detector delivers an average of 7162 ± 16 grey levels. This corresponds to 22 % of the total dynamic range of the camera and sets its lower limit.

The noise level of the camera in terms of standard deviation for 100 consecutive images in the center pixel area is plotted in Figure 5-17 (b) as a function of detected intensity. As seen in the figure, it remains constant in the range of 2 grey levels throughout the tested grey level intensities. This independence of noise level and signal power is characteristic for *additive Thermal noise* and effectively confirms the multiplex advantage.

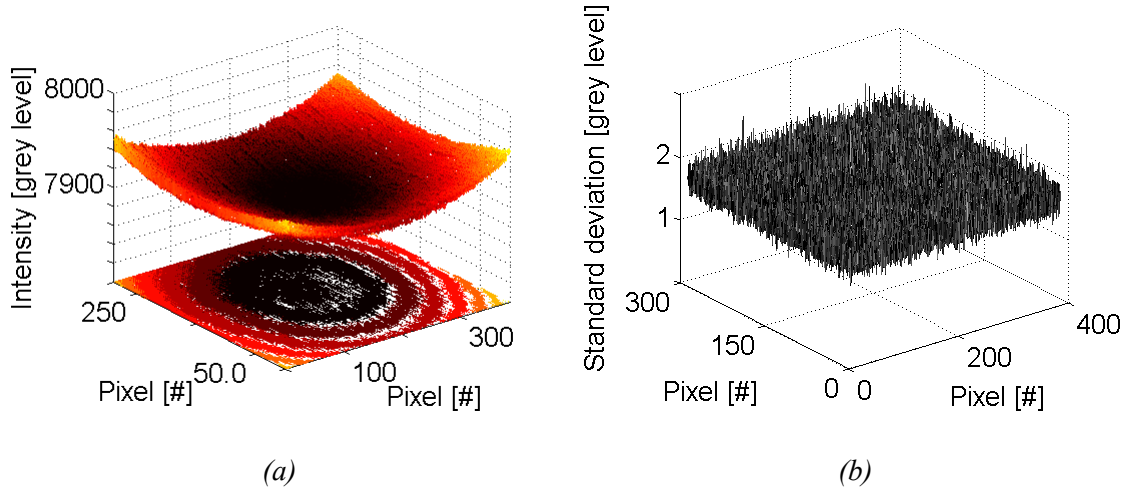


Figure 5-16: (a) Grey level intensity output of 384 x 288 pixel infrared camera (Thermoteknix Miricle 100K) at 24.1 ± 0.1 °C and (b) its standard deviation for 100 consecutive images.

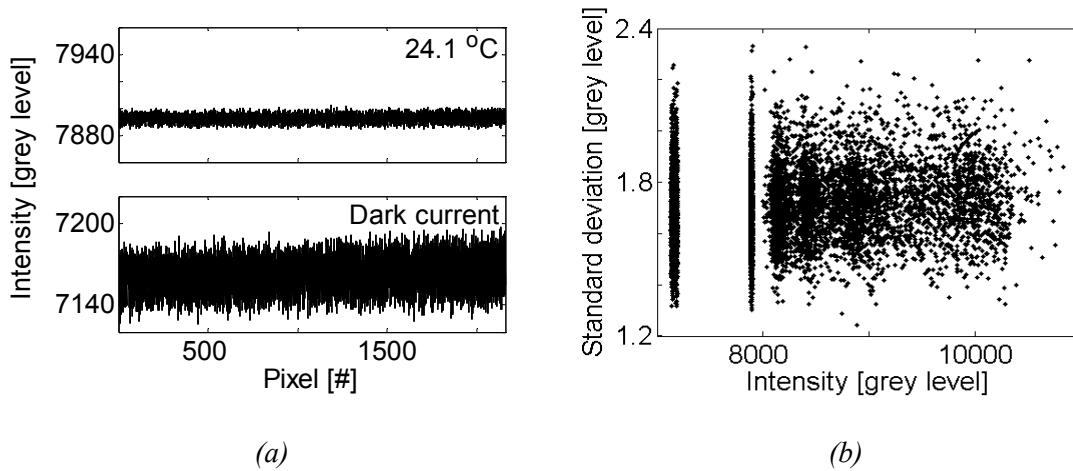


Figure 5-17: (a) Intensity of 54 x 40 pixel in the center of the array for a constant temperature of 24.1 ± 0.1 °C (top) and pixel dark current (bottom). (b) Standard deviation as a function of detected intensity as measured from the dark current (7160 grey levels), the 24.1 ± 0.1 °C background (7893 grey levels), and the globar source at various entrance aperture settings (> 8100 grey levels).

5.4.4.2 Background noise

The background of the spectrometer is obtained by blocking the source radiation from entering the detector compartment and recording the radiation emitted from the spectrometer optics. The spectrometer radiation generates a constant noise signal or fixed pattern noise. Figure 5-18 presents the mean background noise of 100 consecutive measurements in terms of detector grey levels. Accordingly, the background of the instrument radiates at an average of 7923 grey levels and a constant standard deviation of 1.4 to 2.2 grey levels.

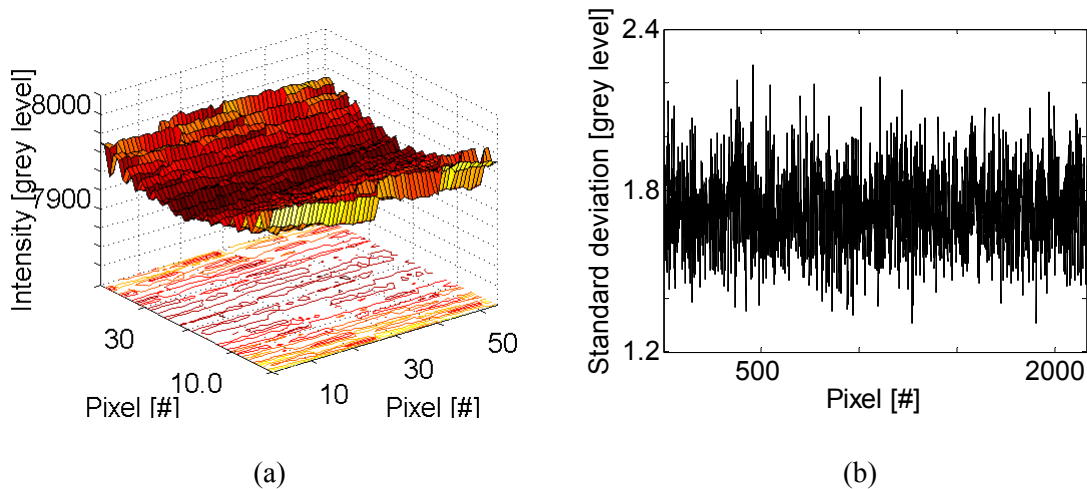


Figure 5-18: Mean background radiation of the instrument (a) and the standard deviation (b) of 100 consecutive measurements as a function of pixel number in the center of the detector array.

Its modulation produces a signature in the interference function and subsequently spectral features. Figure 5-19 presents both the interference function and the resulting spectral noise of the background radiation. In the spectral region from 600 to 1400 cm^{-1} , the integral spectral power measures 0.14 % when compared to the integral power of the global source at an entrance aperture of 2 mm. To compensate the background radiation, we subtract an averaged background image from each image taken with the spectrometer.

Additionally, active cooling parts of the spectrometer with Peltier elements or by liquid nitrogen are further viable attempts to reduce the background radiation of the instrument.

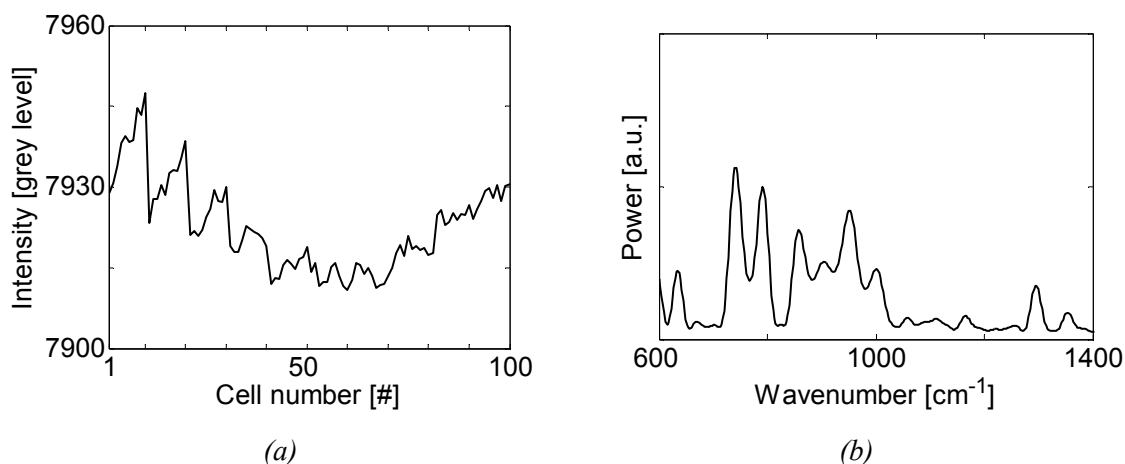


Figure 5-19: Interference function of the background as a function of cell position (a) and its resulting power spectrum (b).

5.4.4.3 Temporal source fluctuation

In section 5.4.3 of the thesis we treated the influence of the spatial source uniformity on the spectral performance of the FPP FTIR. Here, we examine the temporal source fluctuation by recording the source intensity over a time span of 5 s with the same optical setup using a plane mirror. Within this time span, the camera records 250 images. Figure 5-20 (a) illustrates the mean intensity profile of the source for a 2 mm circular entrance aperture. In this optical configuration, the IFS 125 global source produces a mean, peak, and minimum intensity of 8493, 8867, and 8241 grey levels across the center pixel area, respectively. The standard deviation of each pixel over the time span of 5 seconds is in the 2 grey level threshold of camera (Figure 5-20 (b)). This suggests that the global source radiates sufficiently uniform and possible source fluctuations are not detected by the *Thermoteknix Miricle 100K* microbolometer camera. As a result, temporal source

fluctuations are unlikely to add to the noise level and the camera system appears to be critical source of noise.

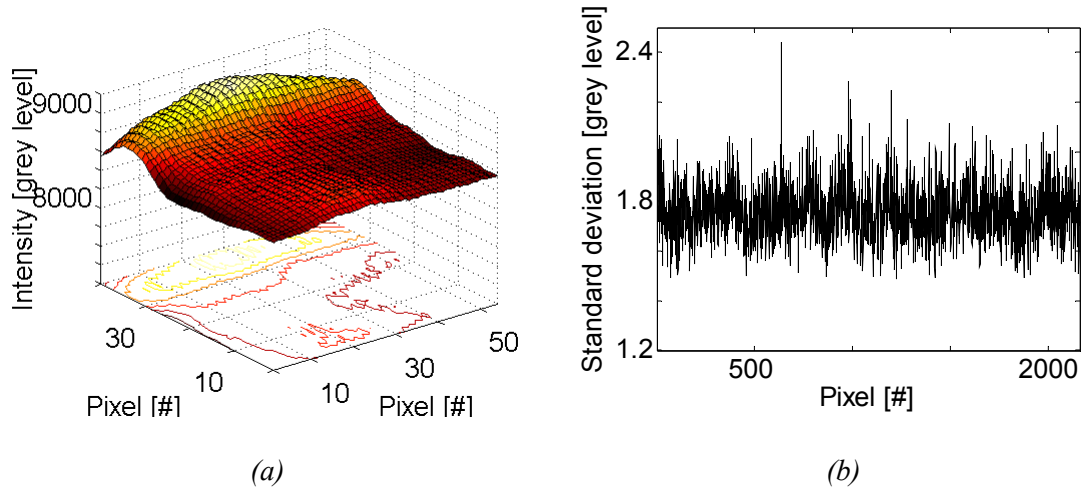


Figure 5-20: Mean source radiation of the globar at a 2 mm entrance aperture (a), and the standard deviation (b) of 250 consecutive measurements as a function of pixel number in the center of the array detector.

5.4.4.4 Noise in spectra

To estimate the random noise in spectra, we analyzed the standard deviation of 500 power spectra taken under the same conditions. We then computed signal-to-noise-ratios (SNR) from the ratio of mean of the power spectra and its standard deviation. Furthermore, we investigated the influence of various apodization functions on the power spectra, its SNR, and the effect of data averaging. The study bases on unfiltered, broad band radiation emitted from the globar at an entrance aperture of 2 mm diameter.

The influence of apodization

Figure 5-21 (a) presents the power spectra of the globar for various apodizations. As we have shown in earlier chapters, the apodization improves noisy intensity modulations at the expense of spectral resolution. The rectangular apodization in effect truncates the interferogram to a given length and does not alter the intensity modulation within its box. In our experiment, it is equivalent to no apodization as we set the truncation to the maximum optical path difference. Comparing the rectangular to all other apodizations clearly illustrates that any apodization other than the rectangular apodization reduces an overlying intensity modulation. The fact that all apodization functions reduce the abrupt end of the interferogram data by smoothly reducing the amplitude seems to have a large impact on the spectral performance. The spectral signal-to-noise-ratio (SNR) for the rectangular apodization is the lowest throughout the spectral band and remains below 40 for a single spectrum (Figure 5-21 (b)). For all apodizations, the SNR is the highest in the spectral band ranging from $800 - 1400 \text{ cm}^{-1}$, whereby the Gaussian and triangular apodization reveal the highest ratios. At wavenumbers smaller than 800 cm^{-1} , the SNR

drops from 20 to 0 at 600 cm^{-1} . On the other end of the spectrum for wavenumbers larger than 1400 cm^{-1} , the SNR falls from 10 to 0 at 1500 cm^{-1} .

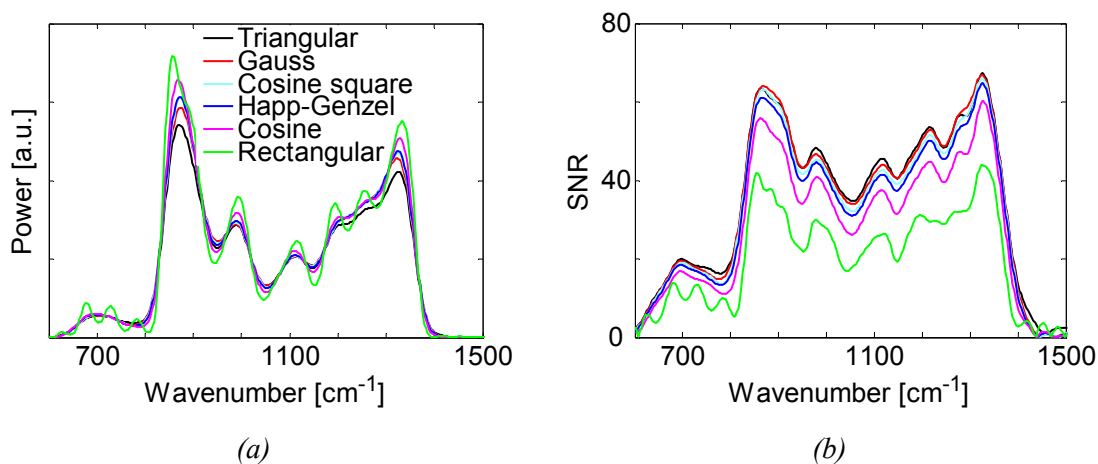


Figure 5-21 (a) Power spectra of global source for various apodization functions, and the corresponding spectral signal-to-noise-ratio (SNR) as computed from the standard deviation of 500 spectra (b). Both figures use the same color coding.

Data averaging

One way to improve the SNR is to sum up spectra. When summing spectra, its signal will grow proportional to the number of spectra, whereas the noise grows proportional to the square root of the number of spectra. As a result its SNR grows proportional to the square root of the number of added spectra. It is a common practice for weak signals buried in noise background and utilized by all infrared spectrometers. This is demonstrated in Figure 5-22 (a) by plotting the increase of the SNR as a function of added spectra. In the plot, the SNR's are computed from the integral signal and noise power in the spectral band of $600 - 1400\text{ cm}^{-1}$.

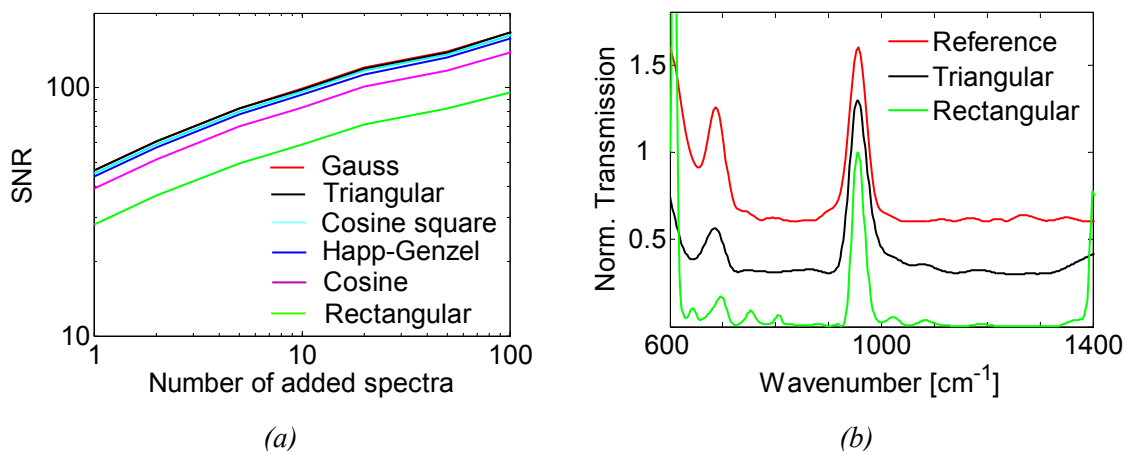


Figure 5-22: (a) Signal-to-noise-ratios (SNR) as a function of added spectra and apodization function. The apodization functions and their color coding in sequence from lowest to highest SNR performance are: Rectangular (green), cosine (magenta), Happ-Genzel (blue), cosine square (cyan), triangular (black), and Gauss (red). (b) Normalized transmission spectra of narrow band pass filter (BP10) for rectangular (green), and triangular (black) apodization function in comparison to reference spectra (red) taken with the IFS66 spectrometer. All spectra are shifted with respect to each other for better viewing.

The experimental data reveals (Figure 5-22) the general trend for the SNR. It increases according to a power law with the number of added spectra. For our experiments the SNR with an exponent lower than 0.3.

For a single spectrum the SNR for rectangular apodization is 28, while the cosine apodization improves the ratio by 39 %. For 100 added spectra the SNR increases by a factor 3.4 for the rectangular apodization. When the SNR of the apodization functions is compared to the rectangular apodization, the Gaussian and triangular apodization exhibit the largest improvement among the selected functions (Table 5-1). Of these two functions, the triangular apodization possesses the advantage of a lower increase in the FWHM value (compare Table 2-1). It appears that any function which reduces the sharp end of the interferogram data improves the SNR.

Figure 5-22 (b) presents transmission spectra of a narrow band pass filter of 250 added spectra for rectangular and triangular apodization. The graph clearly demonstrates the improvement in the spectra after apodization. Spurious spectral features for the rectangular apodization are removed and the transmission in the low SNR region for wavelength smaller than 800 cm^{-1} is significantly enhanced.

Table 5-1: Increase in signal-to-noise-ratio (SNR) for selected apodization functions.

| Apodization function | Increase in SNR [%] |
|----------------------|---------------------|
| Rectangular | reference |
| Cosine | > 39 |
| Happ-Genzel | > 55 |
| Cosine square | > 59 |
| Triangular | > 64 |
| Gauss | > 64 |

The advantage of increasing the SNR by data averaging is partially offset by the reduction of the spectrometer's time resolution. Every spectrum added, decreases the time resolution of spectrometer, and other methods to increase the signal may prove to be more feasible attempts. Such methods may include stronger light sources, detectors of higher sensitivity, reducing the number of pixels for the imaging, and retrofitting the transmission optics with reflecting optics in the infrared camera and the detector optics may further improve the signal. Another viable attempt is pixel binning.

Pixel binning

As we have presented earlier each of the MMA cells is imaged by 3 x 4 pixels. It is self-evident that the number of pixels per MMA cell used for the retrieval of the spectral data has an impact on the detected signal strength. The combining of adjacent detector pixels to form a single large pixel is commonly referred to as *pixel binning*.

Figure 5-23 demonstrates the improvement in the SNR when 4 and 12 pixels are combined together. For a single spectrum, the SNR increases from 46 to 80, and 121 for 4 and 12 pixels per cell, respectively (Figure 5-23 (a)). With the number of spectra added both follow the same power-law trend as we have shown earlier. When large numbers of spectra are summed, the improvement in the SNR for pixel binning continuously reduces. This can be seen in Figure 5-23 (b) in which we plotted the factorial increase of the SNR when 4 and 12 pixels are ‘binned’ together. The binning of 12 pixels per MMA cell increases the SNR by 2.5 for a single spectrum while the improvement continuously reduces to 1.9 at 150 added spectra. In the same token but at a lower rate, the SNR-increase of 4 ‘binned’ pixels per MMA cell gradually reduces from 1.8 to 1.6 at 150 added spectra. Nevertheless, the improvement is significant in particular for single spectra and its drop for large number of added spectra is to be expected as the SNR approaches a plateau and MMA's not increase infinitely with the number of added spectra.

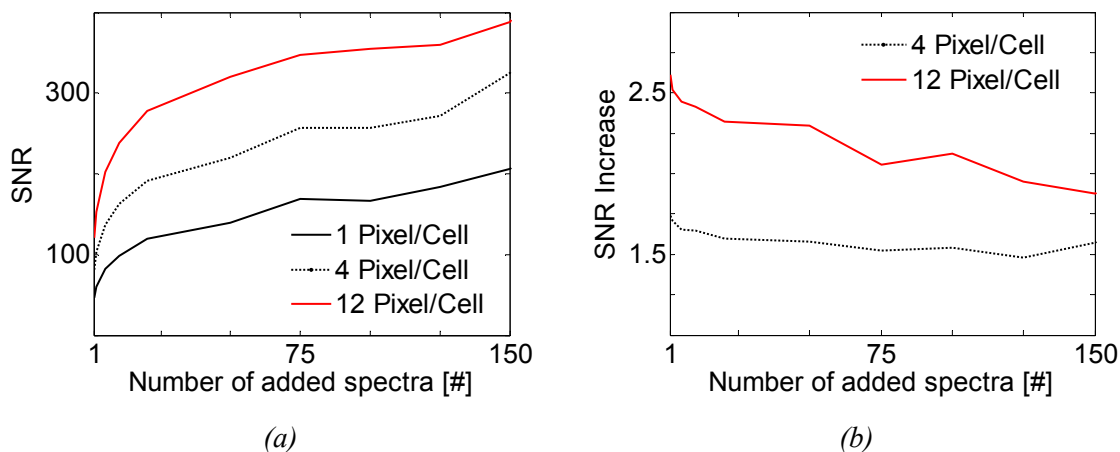


Figure 5-23: Influence of pixel binning on Signal-to-noise-ratio (SNR) for triangular apodization. (a) SNR for triangular apodization as function of added spectra and number of pixel utilized for pixel binning. (b) Factorial increase of SNR for pixel binning of 4 and 12 pixels per cell.

5.5 Single pulse spectra

One of the major advantages of the FPP FTIR spectrometer is its capability to acquire spectral data from a single pulse of light. To demonstrate this capability, we retrofitted the optical setup with a shutter taken from a single reflex camera. The shutter was placed in the focal point of a toroidal mirror, marked with 'x' in Figure 5-2. Shutter times were measured with a continuous laser beam which we directed through the shutter onto a photodiode.

The infrared array detector was the ULIS amorphous silicon micro-bolometer array we used throughout the thesis work. To integrate and read out 40 pixel rows required for the imaging of the 10 x 10 MMA, the array takes 2.6 ms total integration time at a repetition of 50 Hz, leaving an idle time of 17.4 ms until the detector rows are integrated and read out again. This long idle time, intrinsic for the rolling integration mode, necessitates accurate triggering of the radiation pulse event with the read out circuitry and constrains

the experiment. As both were not linked electronically, we repeated each pulse multiple times and chose the highest signal pulse detected for each specific shutter position. Snapshot integrating detectors which integrate each pixel of the array at the same time instant overcome this problem and will be the detector type of choice for future device developments.

Figure 5-24 (a) presents the spectra of the pulsed global radiation. All spectra were computed from interferograms after triangular apodization at a resolution of 100 cm^{-1} . Pulse length and the standard deviation (bracketed) are displayed alongside the graph. As expected, the figure illustrates the continuous decrease of spectral energy with the decreasing pulse length while the shape of the spectrum remains. When comparing the integral energy with pulse length (Figure 5-24 (b)), it can be seen that for the rolling integration mode detector used the influence of the triggering of the pulse event and the recording of the spectra cannot be neglected. In theory one expects a linear decay of the integral spectral power with the pulse length. The deviation can be seen noticeably for pulse lengths below 5 ms. For a 5 ms pulse length corresponding to 25 % of the maximum shutter time, the power is 13.6 %, nearly half of the expected value. For shorter pulses the deviation is larger. Nevertheless, the experiment demonstrates the capability of the spectrometer to recover the same spectral information from a continuously radiating source as well as from a single pulse light.

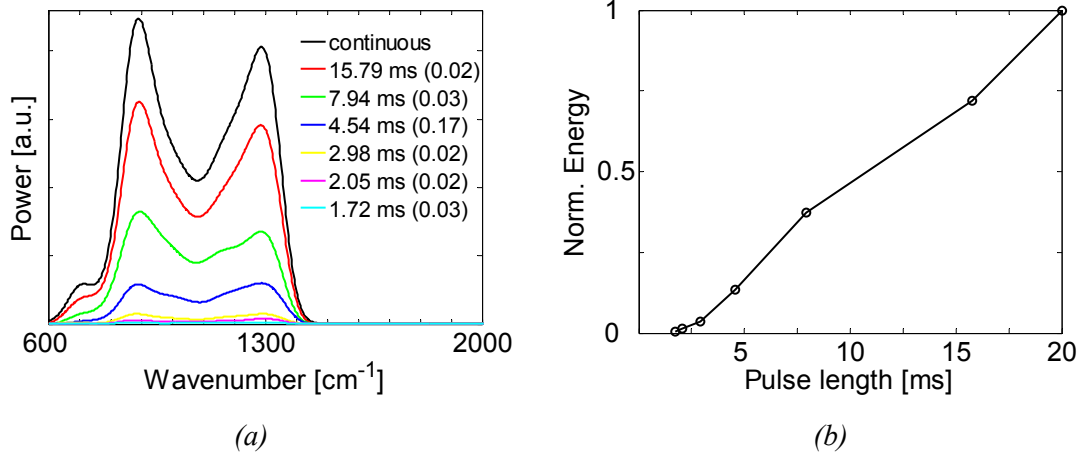


Figure 5-24: (a) Spectra of pulsed global source taken with the FPP FTS at a nominal resolution of 100 cm^{-1} . Pulse length and standard deviation (bracketed) are shown alongside the graph. (b) Normalized integral energy as a function of pulse length.

Figure 5-25 (a) shows a close-up of the single pulse-spectra below 3 ms. Spectral shape and the position of the maxima remain. Furthermore, the measurement of pulses of low spectral power provides valuable information about minimal signal-to-noise-ratios (SNR) necessary to differentiate the spectrum from the noise (Figure 5-25(b)). By sequentially comparing normalized spectra of continuous and pulsed source and the number of pixels binned together we find, that for SNR's greater than 3 the spectrum remains within a 20 % threshold. At SNR in the range of 2, spectral features are recognizable and below 2 faintly distinguishable from the background noise. This finding agrees well with Smith (Smith, 1996, p. 8) recommending a SNR of at least 3.

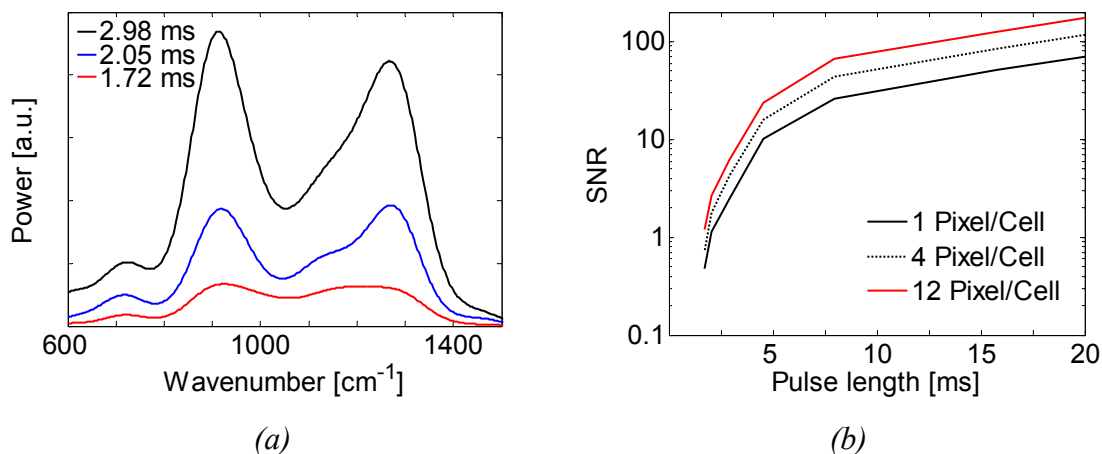


Figure 5-25: a) Close-up on pulsed global spectra taken with the FPP FTIR at a nominal resolution of 100 cm^{-1} . (b) Signal-to-noise-ratio (SNR) as a function of pulse length and number of pixels for pixel binning.

5.6 Time-resolved spectroscopy

In conjunction with the capability to analyze single pulse radiation, the FPP FTS enables in-situ spectroscopy. This is of particular interest for a vast number of applications ranging from fundamental research to process control in the chemical or pharmaceutical industries. In the scope of this thesis, we demonstrate this capability by studying *in situ* the heating process of the global source from room temperature to its working temperature at $1130\text{ }^{\circ}\text{C}$.

The optical setup for experiment is presented in Figure 5-2. Starting with switching-on the global source, we recorded spectra in a 2.4 seconds interval with the FPP FTS, while the global's temperature was monitored with a handheld digital radiation meter (Chino IR-AH) in 30 second interval. All interferograms were multiplied with the triangular apodization function at a spectral resolution of 100 cm^{-1} .

Figure 5-26 reveals the chronology of the global source heating, both spectrally (a) and its temperature development (b). Within 100 seconds, the global heats up beyond 1080

°C, 95 % of its final temperature. Spectrally the fast heating can be seen by the large gap between the spectral lines shown in a 30 seconds interval (Figure 5-26 (a)). Beyond 90 seconds from the start, the density of the spectral lines increases indicating a reduction of the spectral power rise until the spectral power reaches its maximum after 400 seconds. From there, the globar's temperature and the spectral power remains constant at 1135 ± 2 °C and 98 ± 2 %.

Beyond the scope of the trend of the globar's heating, we take a closer look at the spectral development within the first 30 seconds of the source heating. We know from the Wien's displacement law that radiation emitted from blackbodies changes its spectral peak emission with increasing temperature from low to high wavenumbers according to $\lambda_{\max} T = 2880 \mu\text{m} \cdot K$. Thus we can expect a change in the spectral emission as a function of time for the heating of the globar source.

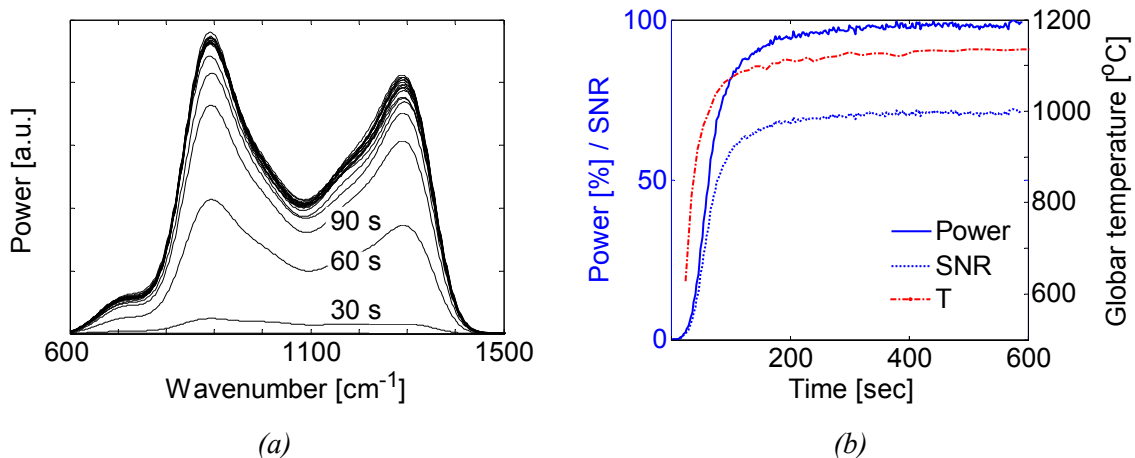


Figure 5-26: (a) In-situ spectra of globar source heating taken at a resolution of 100 cm^{-1} .
(b) Chronologic development of spectral power, SNR and globar's temperature, respectively.

Figure 5-27 reveals this first 30 seconds of the heating process. Each of the single spectra is taken at an interval of 2.4 seconds. It can be seen, that for the first 8 spectra (19.2 seconds), lower wavenumber radiation increase at a higher rate. Figure 5-27 (b) shows

the effect by comparing the increase in spectral power at 920 with 1260 cm^{-1} as a function of time. For the time between 21.6 and 24 seconds the spectral power at 1260 cm^{-1} increases at a slightly higher rate, whereas both spectral lines rise at the same rate beyond 25 seconds.

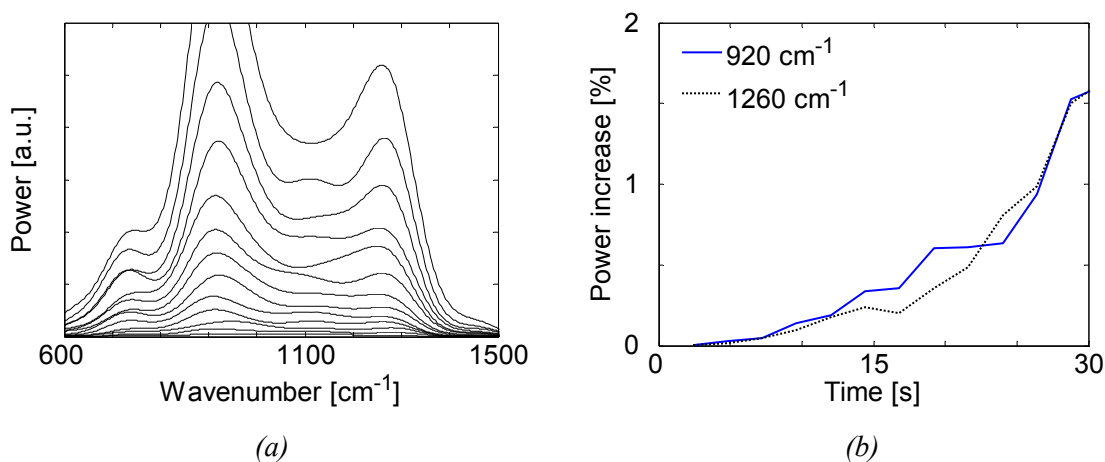


Figure 5-27: (a) In-situ spectra of first 30 seconds of globar heating taken at a time and spectral resolution of 2.4 s and 100 cm^{-1} , respectively. (b) Chronologic increase in spectral power in terms of % maximum power at 920 and 1260 cm^{-1} .

5.7 Summary

In chapter five of the thesis a prototype setup of the FPP FTIR was presented. The working principle of device was validated and a proof of concept demonstrated in a number of examples.

We have shown the influence of the first diffraction orders on the amplitude modulation and presented experimental proof for spatial filtering technique proposed in chapter three. We introduced a possible data processing flow chart and covered the influence of spatial source uniformity on the recovered spectrum. A compensation method to overcome the spatial source non uniformities was presented. Moreover, a method to compensate spatial as well as temporal source non uniformities was proposed.

We demonstrated the power of apodization functions in terms of signal to noise improvement and identified noise sources. We characterized them as additive noise sources and thus provided evidence of the multiplex advantage as expected the FTIR working in the mid-infrared. Furthermore, we showed that the current setup is detector noise limited. Data averaging methods such as time averaging and pixel binning were introduced and its influence to improve signal to noise power was demonstrated. We confirmed a minimum required SNR of 3 experimentally and showed the capability of the technique to acquire spectral data from a single pulse of light within the constraints of the current detector.

Finally, we presented an example of in-situ, time-resolved spectroscopic characterization of the heating process of a global light source.

6 SUMMARY AND CONCLUSION

This work includes the theoretical analysis, the design, construction, and experimental characterization of the Fast Parallel Processing Fourier Transform Spectrometer (FPP FTS) as invented by Moser and Moeller 15 years ago (Moser and Moeller, 1994).

We achieved the experimental proof of concept by measuring spectra in the mid-infrared and demonstrated the capability of the FPP FTS to detect spectra of single short pulses provided sufficient signal-to-noise ratios are generated by the source and the detector. We have shown that the multiplex advantage applies in the mid-infrared spectral range. Furthermore, we expect a throughput advantage as well as wider spectral working bands when compared to its competitor the grating spectrographs, since the FTS is not limited by small entrance apertures and does not require cut-off filters to reject higher diffraction orders.

The core of the spectrometer is formed by a micro mirror array (MMA). To fabricate the MMA, we developed a micro manufacturing process on the basis of X-ray lithography using the novel concept of multiple moving masks. The influence of exposure and development parameters on the inclination and surface roughness of the mirror facets were thoroughly investigated. Numerous other features of the fabrication process were also studied in detail. We have shown its capability to deliver 3D monolithic MMA's in PMMA for a prototype mid-infrared FPP FTS. The analytical treatment of the FPP FTS on the basis of Kirchhoff's diffraction theory lead to excellent agreement with experimental results.

At the time being, the full significance of the development for scientific and industrial applications cannot be fully fathomed as the infrared spectroscopy of short single pulses of radiation was hitherto not possible with FTIR.

The device may be of particular importance for the study of fast processes in chemistry or plasma physics. Industrial applications may range from monitoring gasses and mixtures to online diagnostics of combustions at the like. It may also enable a fast recognition of missiles and other heat sources in warfare. The application of the device for outer space measurements remains the dream and driving factor of the author.

Beyond the scope of this thesis, the project was recently awarded a NRF Proof-of-concept grant (NRF2009NRF-POC001-124) and work is currently ongoing to develop a portable, medium resolution FPP FTS.

Bibliography

- Achenbach S., Pantenburg F.J., Mohr J.. Optimierung der Prozessbedingungen zur Herstellung von Mikrostrukturen durch ultratiefe Roentgenlithographie (UDXRL). Wissenschaftliche Berichte FZKA 6576, 2000.
- Achenbach S.. Deep sub micron high aspect ratio polymer structures produced by hard X-ray lithography. *Microsystem Technologies* 10: 493-497, 2004.
- ANSI/ASME B46.1-1985. Surface texture (surface roughness, waviness, and lay), American National Standard, 1985.
- Ataman C., Urey H., Wolter A.. A Fourier transform spectrometer using resonant vertical comb actuators. *Journal of Micromechanics and Microengineering* 16: 2517-2523, 2006.
- Ataman C., Urey H.. Compact Fourier-transform spectrometers using FR4 platform. *Sensors and Actuators A* 151: 9-16, 2009.
- Avrutsky I., Chaganti K., Salakhutdinov I., Auner G.. Concept of a miniature optical spectrometer using integrated optical and micro-optical components. *Applied Optics*, 45(30): 7811-7817, 2006.
- Bahou M., Wen L., Ding X., Casse B.D.F., Heussler S.P., Gu P., Diao C., Moser H.O., Sim W.S., Gu J., Y.L. Mathis. Infrared Spectro/Microscopy at SSSL – edge effect source in a compact superconducting storage ring. 9th International Conference on Synchrotron Radiation Instrumentation, Daegu, Korea, AIP CP879, 603-606, 2007.
- Becker E.W., Ehrfeld W., Hagmann P., Maner A., Muenchmeyer D.. Fabrication of microstructures with high aspect ratios and great structural heights by synchrotron

- radiation lithography, galvanofforming, and plastic moulding (LIGA process).
Microelectronic Engineering 4: 35-56, 1986.
- Bell R. J.. Introductory Fourier Transform Spectroscopy. Academic Press, 1972.
- Bennett H. E.. Specular reflectance of aluminized ground glass and the height distribution of surface irregularities. Journal of Optical Society of America, 4(12): 1389-1394, 1963.
- Bennett H. E. and Bennett J. M.. Precision measurements in thin film optics. Physics of Thin Films, 4: 1-96, 1967.
- Bennett H. E. and Porteus J. O.. Relation between surface roughness and specular reflectance at normal incidence. Journal of Optical Society of America, 51(2): 123-129, 1961.
- Beutler F.J.. Sampling theorems and bases in a Hilbert space. Information and Control 4(2-3): 97-117, 1961.
- Beutler F.J.. Error-Free Recovery of Signals from Irregularly Spaced Samples. SIAM Review, 8(3): 328-335, 1966.
- Bhargava R., Levin I.W.. Spectrochemical Analysis using Infrared Multichannel Detectors. Blackwell Publishing, 2005.
- Born M., Wolf E.. Principles of Optics: Electromagnetic Theory of Propagation, Interference and Diffraction of Light, Cambridge University Press, 1997.
- Boumenir A.. Irregular Sampling and the Inverse Spectral Problem. Journal of Fourier Analysis and Applications, 5(4): 373-383, 1999.
- Brachet F., Hébert P.-J., Cansot E., Buil C., Lacan A., Roucayrol L., Coureau E., Bernard F., Casteras C., Loesel J., Pierangelo C.. Static Fourier transform spectroscopy

- breadboards for atmospheric chemistry and climate. SPIE Europe Optical Systems Design, 2 – 5 Septembre 2008, Glasgow, Royaume-Uni.
- Bracewell R.N.. The Fourier transform and its applications. WCB/ McGraw Hill, Boston, 2000.
- Brewer G.R.. Electron-beam technology in microelectronic fabrication. Academic Press, New York, 1980.
- Cabrini S., Gentili M., Di Fabrizio E., Gerardino A., Nottolla A., Leonard Q., Mastrogiacomo L.. 3D microstructures fabricated by partially opaque X-ray lithography masks. *Microelectronic Engineering* 53: 599-602, 2000.
- Cabrini S., Perennes F., Marmioli B., Olivo A., Carpentiero A., Kumar K., Candeloro P., Di Fabrizio E.. Low cost transparent SU-8 membrane mask for deep X-ray lithography. *Microsystem Technologies* 11: 370-373, 2005.
- Carlo F.D., Mancini D.C., Lai B., Song J.J.. Characterization of exposure and processing of thick PMMA for deep X-ray lithography by using hard X-rays. *Microsystem Technology* 4: 86-88, 1998.
- Chalmers J.M., Griffiths P.R.. *Handbook of Spectroscopy. Volume 1.* John Wiley and Sons, 2002.
- Chamberlain J.E.. *The principles of interferometric spectroscopy.* New York: Wiley, 1979.
- Chau F.S., Du Y., Zhou G.. A micromachined stationary lamellar grating interferometer for Fourier transform spectroscopy. *Journal of Micromechanics and Microengineering* 18: 025023 (7pp), 2008.

- Chou S. Y., Smith H.I., Antoniadis D.A.. X-ray lithography for sub-100-nm-channel-length transistors using masks fabricated with conventional photolithography, anisotropic etching, and oblique shadowing. *Journal of Vacuum Science and Technology B* 3(6): 1587-1589, 1985.
- Coane P., Friedrich C.. Fabrication of composite X-ray masks by micromilling. *SPIE* 2880: 130-140, 1996.
- Collins S.D., Smith R.L., Gonzalez C.. Fourier-transform optical microsystems. *Optics Letters*, 24(12): 844-846, 1999.
- Connes J. and P.. Near-infrared planetary spectra by Fourier spectroscopy. I. Instruments and results. *Journal of the Optical Society of America* 56(7): 896-910, 1966.
- Correia J.H., Bartek M., Wolffenbuttel R.F.. Bulk-micromachined tunable Fabry-Perot microinterferometer for the visible spectral range. *Sensors and Actuators A* 76: 191-196, 1999.
- Crocombe R.A.. Miniature Optical Spectrometers: There's Plenty of Space at the Bottom. Part 1, Background and Mid-Infrared Spectrometers. *Spectroscopy* 23(1): 38-56, January 2008.
- Crocombe R.A.. Miniature Optical Spectrometers: Part 3: Conventional and Laboratory Near-Infrared Spectrometers 23(5): 40-50, May 2008.
- Crocombe R.A.. Miniature Optical Spectrometers: The Art of the Possible Part 4: New Near-Infrared Technologies and Spectrometers 23(6): 26-27, June 2008.
- Desta Y., Loechel B., Goettert J.. X-ray masks for the LIGA process. Extended Abstract, HARMST 5-6, 2003, Monterey, CA.

- Divan R., Mancini D.C., Moldovan N., Lai B., Assoufid L., Leonard Q., Cerrina F..
Progress in the fabrication of high-aspect-ratio zone plates by soft X-ray
lithography. *SPIE 4783*: 82-91, 2002.
- Elmore D.L., Tsao M.W., Frisk S., Chase D.B., Rabolt J.F.. Design and Performance of a
Planar Array Infrared Spectrograph that Operates in the 3400 to 2000 cm^{-1} Region.
Applied Spectroscopy 56(2): 145-149, 2002.
- El-Kholi A., Mohr J., Stransky R.. Ultrasonic supported development of irradiated micro-
structures. *Microelectronic Engineering 23*: 219-222, 1994.
- Feiertag G., Schmidt M., Schmidt A.. Thermoelastic deformations of masks for deep X-
ray lithography. *Microelectronic Engineering 27*: 513-516, 1995.
- Fritsch F.N., Carlson R.E.. Monotone Piecewise Cubic Interpolation. *SIAM J. Numerical
Analysis 17*: 238-246, 1980.
- Fukuda M., Deguchi K., Suzuki M., Utsumi Y.. Three-dimensional patterning using fine
step motion in synchrotron radiation lithography. *Journal of Vacuum Sciences and
Technology B 26(6)*: 2840-2843, 2006.
- Fujimura T., Kuroki Y., Hisakado T., Ikeda A., Hattori R., Hakiai Y., Hidaka M., Choi
J.Y., Chang S.S.. Film density dependence of Polymethylmethacrylate ablation
under synchrotron radiation irradiation. *Japanese Journal of Applied Physics
40(2A)*: 916-917, 2001.
- Gao F., Yao J., Zeng Y., Xie S., Guo Y., Cui Z.. One-step lithography for fabrication of
multifunction diffractive structures with grey-tone mask. *Microelectronic
Engineering 61-61*: 165-171, 2002.

- Gibbs J.E., Gebbie H.A., Calculation of the power-spectrum from an interferogram sampled at points none of which coincides exactly with zero path-difference. *Infrared Physics* 5: 187-193, 1965.
- Ghica V., Glashauser W.. Method of stress-free development of irradiated polymethylmetacrylate. German Patent No. 3039110, 1982; US Patent No. 4393129, 1983.
- Goodman J.W.. *Introduction to Fourier Optics*. 2nd Edition, McGraw-Hill, 1996.
- Gower M.C.. Industrial applications of laser micromachining. *Optics Express* 7(2): 56-67, 2000.
- Greeneich J.S.. Developer characteristics of poly-(methylmethacrylate) electron resist. *Journal of the Electrochemical Society* 122(7): 970-976, 1975.
- Gremaux D.A. and Gallagher N.C.. Limits of scalar diffraction theory for conducting gratings. *Applied Optics*, 32(11):1948-1953, 1993.
- Gröchening K.. A Discrete Theory of Irregular Sampling. *Linear Algebra and its applications* 193: 129-150, 1993.
- Guenzler H., Gremlich H.U.. *IR Spectroscopy. An Introduction*. Wiley-VCH, 2002.
- Happ H., Genzel L. Interferenz-Modulation mit Monochromatischen Millimeter-Wellen. *Infrared Physics* 1: 39-48, 1961.
- Harvey E.C., Rumsby P.T.. Fabrication techniques and their application to produce novel micromachined structures and devices using Excimer laser projection. *Proceedings of SPIE*, 3223, 1997.
- Hébert P., Cansot E., Pierangelo C., Buil C., Bernard F., Loesel J., Tremas T., Perrin L., Courau E., Casteras C., Maussang I., Simeoni D.. Instrumental concept and

- preliminary performances of SIFTI : Static Infrared Fourier Transform Interferometer. International Conference on Space Optics 2008, October 14-17, Toulouse, France.
- Hecht E.. Optics. 4th Edition, Addison Wesley, 2002.
- Heng Q., Tao C., Tie-chuan Z.. Surface roughness analysis and improvement of microfluidic channel with Excimer laser. *Microfluid Nanofluid* 2: 357-360, 2006.
- Hertz H.R.. Ueber sehr schnelle electrische Schwingungen. *Annalen der Physik*. 267(7): 421-448, 1887.
- Heussler S.P., Moser H.O., Quan C.G., Tay C.J., Moeller K.D., Bahou M., Jian L.K.. Deep X-ray lithography in the fabrication process of a 3D diffractive optical element. *Synchrotron Radiation Instrumentation: 9th International Conference, AIP CP879*: 1503-1506, 2007.
- Hudson R.D.. Infrared system engineering. Wiley-Interscience, New York, 1969.
- IFS 125, Bruker Optik GmbH, IFS 125 HR user manual, 2006. www.brukeroptics.com
- Ivanov E.V.. Static Fourier transform spectroscopy with enhanced resolving power. *J. Opt. A: Pure Appl. Opt.* 2: 519-528, 2000.
- Jerri A.J.. The Shannon sampling theorem – its various extensions and applications: A tutorial review. *Proceedings of the IEEE* 65(11): 1565-1596, 1977.
- Jian L.K., Desta Y.M., Goettert J.. Multi-level microstructures and mold inserts fabricated with planar and oblique X-ray lithography of SU-8 negative photoresist. *Proceedings of SPIE* 4557: 69-75, 2001.

- Jian L.K., Desta Y.M., Goettert J., Bednarzik M., Loechel B., Yoonyoung J., Aigeldinger G., Singh V., Ahrens G., Gruetzner G., Ruhmann R., Degen R.. SU-8 based deep X-ray lithography/ LIGA. Proceedings of SPIE 4979: 394-401, 2003.
- Junttila M.L., Kauppinen J., Ikonen E.. Performance limits of stationary Fourier spectrometers. Journal of Optical Society of America A 8(9): 1457-1462, 1991.
- Kan J.A.v., Shao P.G., Ansari K., Bettioli A.A., Osipowicz T., Watt F.. Protron beam writing: A tool for high-aspect ratio mask production. Microsystem Technology 13: 431-434, 2007.
- Kahaner D., Moler C., Nash S.. Numerical Methods and Software. Prentice Hall, 1988.
- Kalus M., Frey M., Buchmann L.M., Reiner K., Wagner B.. Free 3D shaping with grey-tone lithography and multidose E-beam writing. Microelectronic Engineering 41/42: 461-462, 1998.
- Kato F., Fujinawa S., Tsudo M., Sugiyama S.. Fabrication of submicron three-dimensional structure by plane-pattern to the cross-section transfer method using synchrotron radiation lithography. Proceedings of SPIE 6037: 1R-1 – 1R8, 2005.
- Katoh T., Nishi N., Fukagawa M., Ueno H., Sugiyama S.. Direct writing for three-dimensional microfabrication using synchrotron radiation etching. IEEE: 556-561, 2000.
- Katoh T., Nishi N., Fukagawa M., Ueno H., Sugiyama S.. Direct writing for three-dimensional microfabrication using synchrotron radiation etching. Sensors and Actuators A 89: 10-15, 2001.
- Keller U.. Recent developments in compact ultrafast lasers. Nature 424: 831-838, 2003.

- Kim J.T., Choi C.G.. Absorber embedded X-ray mask for high aspect ratio polymeric optical components. *Journal of Micromechanics and Microengineering* 15: 615-619, 2005.
- Kruzelecky R. V., Wong B., Haddad E., Jamroz W., Zheng W., Phong L.. Advanced MEMS/Smart-Material Coding and Filtering Technologies for High-Performance Miniature Integrated IR Spectrometers. *Proceedings of the 2004 International Conference on MEMS, NANO and Smart Systems (ICMEMS'04)*, IEEE, 2004.
- Kudryashov V.A., Lee S.. A new 2D to 3D X-ray lithography technology for gray scale structures. *Microelectronic Engineering* 57-58: 819-823, 2001.
- Kung H.L., Bhalotra S.R., Mansell J.D., Miller D.A.B.. Compact transform spectrometer based on sampling standing wave. *MB2* : 19-20, IEEE, 2000.
- Y. Li. X-ray lithography mask fabricated by Excimer laser process. *Proceedings of SPIE* 5641: 316-322, 2004.
- Li D.C., Chen J.T., Chyuan S.W., Sun C.Y.. Computer simulations for mask structure heating in X-ray lithography. *Computer and Structures* 58(4): 825-834, 1996.
- Liu Z., Bouamrane F., Roulliy M., Kupka R.K., Labeque A., Megtert S.. Resist dissolution rate and inclined-wall structures in deep X-ray lithography. *Journal of Micromechanics and Microengineering* 8: 293-300, 1998.
- Malek C.K., Yajamanyam S.. Evaluation of alternative development process for high-aspect-ratio poly(methylmethacrylate) microstructures in deep X-ray lithography. *Journal of Vacuum Science and Technology B* 18(6): 3354-3359, 2000.

- Manohara H.M., Calderon G., Klopff J.M., Morris K., Vladimirsky O., Vladimirsky Y.
Temperature rise in thick PMMA resist during X-ray exposure. Proceedings of
SPIE 2880: 183-190, 1996.
- Manzardo O., Michaely R., Schaedelin F., Noell W., Overstolz T., De N. Rooij, Herzig
H.P.. Miniature lamellar grating interferometer based on silicon technology. Optics
Letters 29(13): 1437-1439, 2004.
- Marvasti F.. Nonuniform Sampling – Theory and Practice. Kluwer Academic / Plenum
Publishers, 2001.
- Mata A., Fleischmann A.J., Roy S.. Fabrication of multi-layer SU-8 microstructures.
Journal of Micromechanics and Microengineering 16: 276-284, 2006.
- Mappes T., Achenbach S., Mohr J.. Process conditions in X-ray lithography for the
fabrication of devices with sub-micron feature sizes. Microsystem Technology 13:
355-360, 2007.
- Maxwell J.C.. A dynamical theory of the electromagnetic field. Philosophical
Transactions of the Royal Society of London 155: 459-512, 1865.
- Mekaru H., Takano T., Takahashi M., Maeda R.. Fabrication of a needle array using Si
gray mask for X-ray lithography. Journal of Vacuum Science and Technology B
25(6): 2196-2201, 2007.
- Mekaru H., Takano T., Awazu K., Takahashi M., Maeda R.. Three-dimensional X-ray
lithography using silicon mask with inclined absorbers. Proceedings of SPIE 6517:
35-1 – 35-8, 2007.

- Mekaru H., Takano T., Ukita Y., Utsumi Y., Takahashi M.. A Si stencil mask for deep X-ray lithography fabricated by MEMS technology. *Microsystems Technology* 14: 1335-1342, 2008
- Meyer P., El-Kholi A., Mohr J., Cremers C., Bouamrane F., Megtert S.. Study of the developmeny behaviour of irradiated foils and microstructure. *SPIE* 3874: 312-320,1999.
- Meyer P., El-Kholi A., Schulz J.. Investigations of the development rate of irradiated PMMA microstructures in deep X-ray lithography. *Microelectronic Engineering* 63: 319-328, 2002.
- Meynart R., Sampling jitter in Fourier-transform spectrometers: Spectral broadening and noise effects. *Applied Optics*, 31(30): 6383-6388, 1992.
- Mohr J., Anderer B., Ehrfeld W., Fabrication of a planar grating spectrograph by deep-etch lithography with synchrotron radiation. *Sensors and Actuators A* 25-27: 571-575, 1991.
- Möller K.D., Wavefront dividing interferometers. *Infrared Physics*, 32: 321-331, 1991.
- Möller K.D., Wave-front-dividing array interferometers without moving parts for real-time spectroscopy from the IR to the UV. *Applied Optics*, 34(9): 1493-1501, 1995.
- Moser H.O., Möller K.D., Gitterstruktur und deren Verwendung, European patent EP0765488B1, June 18,1994.
- Neiss E., Flury M., Mager L., Rehspringer J.L., A. Fort, P. Montgomery, P. Gerard, J. Fontaine, S. Robert. Multi-level diffractive optical elements produced by Excimer laser ablation of sol-gel. *Optics Express* 16(18): 14044-14056, 2008.

- Neumann M., Pantenburg F.J., Rohde M., Sesterhenn M.. Heat transport in masks for deep X-ray lithography during the irradiation process. *Microelectronics Journal* 28: 349-355, 1997.
- Nishi N., Katoh T., Ueno H., Konishi S., Sugiyama S.. 3-dimensional micromachining of PTFE using synchrotron radiation direct photo-etching. *International Symposium on Micromechatronics and Human Science, IEEE* : 93-98, 1999.
- Nishikida K., Nishio E., and Hannah R.W.. *Selected Applications of Modern FT-IR Techniques*. Gordon and Breach, 1995.
- Nyquist H.. Certain Topics in Telegraph Transmission Theory. *Transactions of A.I.E.E.*, 617-644, 1928.
- Ogawa T., Soga T., Maruyama Y., Oizumi H., Mochiji K.. Stress-controlled X-ray mask absorber using pulse-current gold plating. *Journal of Vacuum Science and Technology B* 10(3): 1193-1196.
- Oh D.Y., Gil K., Chang S.S., Jung D.K., Park N.Y., Lee S.S.. A tetrahedral three-facet micro mirror with inclined deep X-ray process. *Sensors and Actuators A* 93: 157-161, 2001.
- Oppliger Y., Sixt P., Stauffer J.M., Mayor J.M., Regnault P., Voirin G.. One-step 3D Shaping Using a Gray-Tone Mask for Optical and Microelectronic Applications. *Microelectronic Engineering* 23: 449-454, 1994.
- Opus Version 5.5 IR spectroscopy software, © BRUKER OPTIC GmbH, 2004.
- www.brukeroptics.com/opus.html.

- Ordal M. A., Long L. L., Bell R. J., Bell S. E., Bell R. R., Alexander R. W., Jr., and Ward C. A.. Optical properties of the metals Al, Co, Cu, Au, Fe, Pb, Ni, Pd, Pt, Ag, Ti, and W in the infrared and far infrared. *Applied Optics*, 22(7):1099-1120, 1982.
- Page D.. Wyko NT1100. Operator's guide. Veeco Metrology Group. June, 2002.
- Palik E. D.. *Handbook of Optical Constants of Solids*. Academic Press, 1998
- Pantenburg F.J., Achenbach S., Mohr J.. Influence of developer temperature and resist material on the structure quality in deep X-ray lithography. *Journal of Vacuum Science and Technology B*16(6): 3457-3551, 1998.
- Peatman W.B.. *Grating, mirrors and slits: Beamline design for soft X-ray synchrotron radiation sources*. Gordon and Breach Science Publishers, Amsterdam, Netherlands, 1997.
- Pellerin C., Snively C.M., Chase D.B., Rabolt J.F.. Performance and application of a new planar array spectrograph operating in the mid-infrared (2000-975cm⁻¹) fingerprint region. *Applied Spectroscopy* 58(6): 639-646, 2004.
- Pellerin C., Frisk S., Rabolt J.F., Chase D.B.. A Faster Approach to Infrared Rheo-optics Using a Planar Array Infrared Spectrograph. *Applied Spectroscopy* 58(7): 799-803, 2004.
- Pellerin C., Pelletier I.. Planar array infrared spectroscopy: A new tool for materials characterization. *IR Spectroscopy* 10-13, October 2005.
- Pelletier I., Pellerin C., Chase D.B., Rabolt J.F.. New Developments in Planar Array Infrared Spectroscopy. *Applied Spectroscopy* 59(2): 156-163, 2005.

- Porteus J. O.. Relation between height distribution of a rough surface and the reflectance at normal incidence. *Journal of Optical Society of America*, 53(12): 1394-1402, 1963.
- Rabolt J.F., Bellar R.. The Nature of Apodization in FTS. *Applied Spectroscopy* 35(1): 132-135, 1981.
- Richards P.L.. High-resolution Fourier transform spectroscopy in the far-infrared. *Journal of the Optical Society of America*, 54(12): 1474-1484, 1964.
- Rio M.S. d., Dejus R.J.. X-ray oriented programs XOP 2.11, 2006.
- Rizvi N.H., Apte P.. Developments in laser micro-machining techniques. *Journal of Materials Processing Technology* 127: 206-210, 2002.
- Saptari V.. Fourier-transform spectroscopy instrumentation engineering. SPIE, 2004.
- Sarkissian E., and Bowman K.W.. Application of a nonuniform spectral resampling transform in Fourier-transform spectrometry. *Applied Optics*, 42(6): 1122-1131, 2003.
- Schildkraut E.R., Reyes D., Cavicchio D.J., Jensen J.O.. A MEMS based Absorption Micro-Spectrometer for Toxic Vapor Detection and Identification. Scientific Conference on Chemical and Biological Defense Research, Hunt Valley, Maryland, 15-17 November, 2004. available on Block Engineering web site:
www.blockeng.com/huntvalley.pdf
- Schmalz O., Hess M., Kosfeld R.. Structural changes in poly(methyl methacrylate) during deep-etch X-ray synchrotron radiation lithography. Part I: Degradation of the molar mass. *Die Angewandte Makromolekulare Chemie* 239: 63-77, 1996.

- Schmalz O., Hess M., Kosfeld R.. Structural changes in poly(methyl methacrylate) during deep-etch X-ray synchrotron radiation lithography. Part II: Radiation effects on PMMA. *Die Angewandte Makromolekulare Chemie* 239: 79-91, 1996.
- Schmalz O., Hess M., Kosfeld R.. Structural changes in poly(methyl methacrylate) during deep-etch X-ray synchrotron radiation lithography. Part III: Mode of action of the developer. *Die Angewandte Makromolekulare Chemie* 239: 93-106, 1996.
- Shan X.C., Maeda R., Ikehara T., Mekar H., Hattori T.. Fabricaton of X-ray masks and applications for optical switch molding. *Sensors and Actuators A* 108: 224-229, 2003.
- Shannon C.E.. Communication in the Presence of Noise. *Proceedings of the IRE*, 37(1):10-21, 1949.
- Sheats J.R., Smith B.W.. *Microlithography: Science and Technology*. CRC Press, 1998.
- Sheu J.T., Chiang M.H., Su S.. Fabrication of intermediate mask for deep X-ray lithography. *Microsystems Technologies* 4: 74-46, 1998.
- Shew B.Y., Cheng Y., Shih W.P., Lu M., Lee W.H.. High precision, low cost mask for deep X-ray lithography. *Microsystem Technologies* 4: 66-69, 1998.
- Smith B.C.. *Fundamentals of Fourier Transform Infrared Spectroscopy*. CRC Press, 1996.
- Smith G.D. and Palmer R.A.. *Fast time-resolved mid-infrared spectroscopy using an interferometer*. John Wiley and Sons Ltd, 2002.
- Smith J.P.. Spectrometers get small. *Analytical Chemistry* 72(19): 653-658, 2009.
- Stadler S., Derhalli I., Malek C. K.. Cost-effective mask fabrication on Kapton membrane for deep X-ray lithography. *SPIE* 3225: 102-108, 1997.

- Stoica P., and Sandgren N.. Spectral analysis of irregularly-sampled data: Paralleling the regularly-sampled data approaches. *Digital Signal Processing*, 16: 712-734, 2006.
- Strong J.. *Concept of Classical Optics*. W.H. Freeman & Co Ltd, 1958.
- Strong J., Vanasse G.A.. Lamellar Grating Far-Infrared Interferometer. *Journal of Optical Society of America* 50(2): 113-118, 1960.
- Stuart B.H.. *Infrared Spectroscopy: Fundamentals and applications*. John Wiley and Sons, Ltd, 2004.
- Taghizadeh M.R., Blair P., Layet B., Barton I.M., Waddie A.J., Ross N.. Design and fabrication of diffractive optical elements. *Microelectronic Engineering* 34: 219-242, 1997.
- Tan M.X., Bankert M.A., Griffiths S.K., Ting A., Boehme D., Wilson S., Balser L.M.. PMMA development studies using various synchrotron sources and exposure conditions. *SPIE* 3512: 262-270, 1998.
- Teo E.J., Breese M.B.H., Tavernier E.P., Bettiol A.A., Watt F.. Three-dimensional microfabrication in bulk silicon using high-energy protons. *Applied Physics Letters* 84(16): 3202-3204, 2004.
- Thermoteknix Systems Ltd. Product brochure Miricle 110K. <http://www.thermoteknix.com/>, 2009.
- Tian J.. Reconstruction of irregularly sampled interferograms in Fourier transform spectrometry with unknown sampling location. *Optical Engineering*, 44(4): 048201.1-048201.8, 2005.
- Tolfree D.W.L.. Microfabrication using synchrotron radiation. *Reports on Progress in Physics* 61: 313-351, 1998.

- Touloukian Y.S., Ho C.Y.. Thermophysical properties of matter. Volumes 1, 2, 4, 8, 12, 13. IFI / Plenum, New York – Washington, 1979.
- Valiev K.A.. The physics of submicron lithography. Plenum Press, New York and London, 1992.
- Veen F.v.d. and Pfeiffer F.. Coherent X-ray scattering. *Journal of Physics: Condensed Matter*, 16, 5003-5030, 2004.
- Voigt A., Heinrich M., Gruetzner G., Kuba J., Scheunemann H.U., Rudolph I.. A new UV sensitive positive resist for X-ray mask manufacture. *Microsystem Technology* 14: 1447-1450, 2008.
- Vorderburger T.V., Raja J.. Surface finish metrology tutorial. U.S. Department of Commerce, National Institute of Standards and Technology. June, 1990.
- Vorderburger T.V., Rhee H.-G., Renegar T.B., Song J.-F., Zheng A., Comparison of optical and stylus methods for measurement of surface texture. *International Journal of Advanced Manufacturing Technology* 33: 110-118, 2007.
- Wang L., Christenson T. , Desta Y.M., Fettig R.K., Goettert J.. High-resolution X-ray masks for high aspect ration microelectromechanical systems applications. *Journal of Microlithography, Microfabrication, and Microsystems* 3(3): 423-428, 2004.
- Wang S.W., Xia C., Chen X., Liu W., M. Li, Wang H., Zheng W., Zhang T.. Concept of a high-resolution miniature spectrometer using an integrated filter array. *Optics letters* 32(6): 632-634, 2007.
- Wilhelmi O., Ren K.J., Casse B.D.F., Tiam S.B., Mahmood S.B., Heussler S.P., Dasch M., Waterstradt T., Moser H.O.. Nanofabrication by X-ray lithography at SSLs. *Proceedings of Thin Films and Nanotech*, July 2004.

- Wirgin A.. Diffraction limitations of the lamellar grating interferometer in far-infrared Fourier transform spectroscopy. *Optics Communications* 7, 3, 205-210, 1973.
- Wolffenbuttel R.F.. MEMS-based optical mini- and microspectrometers for the visible and infrared spectral range. *Journal of Micromechanics and Microengineering* 15: S145-S152, 2005.
- Wollersheim O., Zumaque H., Hormes J., Kadereit D., Langen J., Haeussling L., Hoessel P., Hoffmann G.. Quantitative studies of the radiation chemical behaviour of PMMA and poly(lactides). *Nuclear Instruments and Methods in Physics Research B* 97: 273-278, 1995.
- Yao J., Su J., J. Du, Zhang Y., Gao F., Gao F., Guo Y., Cui Z.. Coding Gray-tone Mask for Refractive Microlens Fabrication. *Microelectronic Engineering* 53: 531-534, 2001.
- Yee G.M., Maluf N.I., Hing P.A., Albin M., Kovacs G.T.A.. Miniature spectrometers for biochemical analysis. *Sensors and Actuators A* 58: 61-66, 1997.
- Yin H., Wang M., Stroem M., Nordgren J.. Study of wave-front-dividing interferometer for Fourier transform spectroscopy. *Nuclear Instruments and Methods in Physics Research A* 451: 529-539, 2000.
- You H., Matsuzuka N., Yamaji T., Tabata O.. Deep X-ray exposure system with multistage for 3-D microfabrication. *International Symposium on Micromechatronics and Human Science, IEEE* : 53-57, 2000.
- Yu H., Guangya Z., Siong C.F., Feiwen L., Shouhua W., Mingsheng Z.. An electromagnetically driven lamellar grating based Fourier transform

microspectrometer. *Journal of Micromechanics and Microengineering* 18: 055016 (6pp), 2008.

Yu K., Lee D., Krsihnamoorthy U., Park N., Solgaard O.. Micromachined Fourier-transform spectrometer on silicon optical bench platform. *Sensors and Actuators A* 130-131: 523-530, 2006.

Yue W., Chiam S.Y., Ren Y., Kan J.A.v., Osipowicz T., Jian L., Moser H.O., Watt F.. The fabrication of X-ray masks using proton beam writing. *Journal of Micromechanics and Microengineering* 18: 085010 (6pp), 2008.

Zanghellini J., El-Kholi A., Mohr J.. Development behaviour of irradiated microstructures. *Microelectronic Engineering* 35: 409-412, 1997.

Zhan G.. Static Fourier-transform spectrometer with spherical reflectors. *Applied Optics* 41(3): 560-563, 2002.

Appendix 1

Cosine transforms

The cosine transformation of Eq. (2 - 8) is a result of the symmetry of the interferogram acquisition and is given:

$$F(\delta) = 2 \int_0^{\infty} B(\sigma) \cos(2\pi\sigma\delta) d\sigma \quad (2 - 8)$$

Following the complex notation of the Fourier transform integrals (Eq. 2-10)

$$F(\delta) = \int_{-\infty}^{\infty} B(\sigma) e^{i2\pi\sigma\delta} d\sigma \quad (A1 - 1)$$

If Eq. (A1 - 1) is rewritten by separating integral limits, it follows:

$$\int_{-\infty}^{\infty} B(\sigma) e^{i2\pi\sigma\delta} d\sigma = \int_0^{\infty} B(\sigma) e^{i2\pi\sigma\delta} d\sigma + \int_{-\infty}^0 B(\sigma) e^{i2\pi\sigma\delta} d\sigma \quad (A1 - 2)$$

After reversing the integral limits of the last integral term in Eq. (A1 - 2) and under the condition of a real valued interferogram function as stated in (Bell, 1972, p. 35), it follows:

$$\int_{-\infty}^0 B(\sigma) e^{i2\pi\sigma\delta} d\sigma = \int_0^{\infty} (B(\sigma) e^{i2\pi\sigma\delta})^* d\sigma \quad (A1 - 3)$$

$$\int_{-\infty}^{\infty} B(\sigma) e^{i2\pi\sigma\delta} d\sigma = \int_0^{\infty} [B(\sigma) e^{i2\pi\sigma\delta} + (B(\sigma) e^{i2\pi\sigma\delta})^*] d\sigma \quad (A1 - 4)$$

$$\int_{-\infty}^{\infty} B(\sigma) e^{i2\pi\sigma\delta} d\sigma = 2 \int_0^{\infty} \text{Re}[B(\sigma) e^{i2\pi\sigma\delta}] d\sigma \quad (A1 - 5)$$

where Re symbolizes the real part of the function. Hence, the cosine and complex Fourier transform are interrelated according to:

$$\int_{-\infty}^{\infty} B(\sigma) e^{i2\pi\sigma\delta} d\sigma = 2 \int_0^{\infty} B(\sigma) \cos(2\pi\sigma\delta) d\sigma \quad (A1 - 6)$$

Appendix 2

Effect of Truncation of the Interferogram

According to Eq. (2-7), the symmetric interferogram of a monochromatic light source is given by:

$$f(\delta) = 2B(\sigma_0)\cos(2\pi\sigma_0\delta) \quad (\text{A2 - 1})$$

And its spectrum calculated via the cosine Fourier transform is:

$$B(\sigma) = 2 \int_0^{\infty} 2B(\sigma_0)\cos(2\pi\sigma_0\delta)\cos(2\pi\sigma\delta)d\delta \quad (\text{A2 - 2})$$

If the interferogram is now taken in the limits ranging from 0 to a maximum optical path difference δ_{\max} , Eq. (A2 - 2) reduces to:

$$B(\sigma) = 4 \int_0^{\delta_{\max}} B(\sigma_0)\cos(2\pi\sigma_0\delta)\cos(2\pi\sigma\delta)d\delta \quad (\text{A2 - 3})$$

$$B(\sigma) = 2 \int_0^{\delta_{\max}} B(\sigma_0)[\cos(2\pi(\sigma_0 - \sigma)\delta) + \cos(2\pi(\sigma_0 + \sigma)\delta)]d\delta \quad (\text{A2 - 4})$$

Upon integration it follows:

$$B(\sigma) = 2\delta_{\max} B(\sigma_0) \left(\frac{\sin(2\pi(\sigma_0 - \sigma)\delta_{\max})}{2\pi(\sigma_0 - \sigma)\delta_{\max}} + \frac{\sin(2\pi(\sigma_0 + \sigma)\delta_{\max})}{2\pi(\sigma_0 + \sigma)\delta_{\max}} \right) \quad (\text{A2 - 5})$$

Thus, the calculated spectrum consists of two *sinc*-functions, one centered at $\sigma = +\sigma_0$ and the other centered at $\sigma = -\sigma_0$. Physical spectra only exist for positive wavenumbers, and with this the value of the second term is negligible compared with the first term. As a consequence, the truncation of the interferogram of a monochromatic source inevitably results in the broadening of the spectral line which is characterized by the *instrumental line shape function* according to:

$$B(\sigma) \approx 2\delta_{\max} B(\sigma_0) \frac{\sin[2\pi(\sigma_0 - \sigma)\delta_{\max}]}{2\pi(\sigma_0 - \sigma)\delta_{\max}} \quad (\text{A2 - 6})$$

Appendix 3

Fraunhofer Diffraction of identical similarly oriented apertures

Assuming spatially coherent radiation incident onto mirror surfaces of the same shape, the contribution of all single mirrors surfaces are superimposed at the image plane and Eq. (3-2) is further simplified to (Born and Wolf, 1997, p. 445):

$$U(P_i) = K \sum_{N=0}^{N-1} e^{-ik \left[\left(\frac{x_i + x_s}{s'} + \frac{y_i + y_s}{r'} \right) \xi_{NMS} + \left(\frac{y_i + y_s}{s'} + \frac{x_i + x_s}{r'} \right) \eta_{NMS} \right]} e^{-i\phi(\xi_{NMS}, \eta_{NMS})} * \iint e^{-ik \left[\left(\frac{x_i + x_s}{s'} + \frac{y_i + y_s}{r'} \right) \xi' + \left(\frac{y_i + y_s}{s'} + \frac{x_i + x_s}{r'} \right) \eta' \right]} d\xi' d\eta' \quad (A3 - 1)$$

The integral thereby expresses the effect of a single mirror element, whilst the sum represents the superposition of the coherent diffraction patterns.

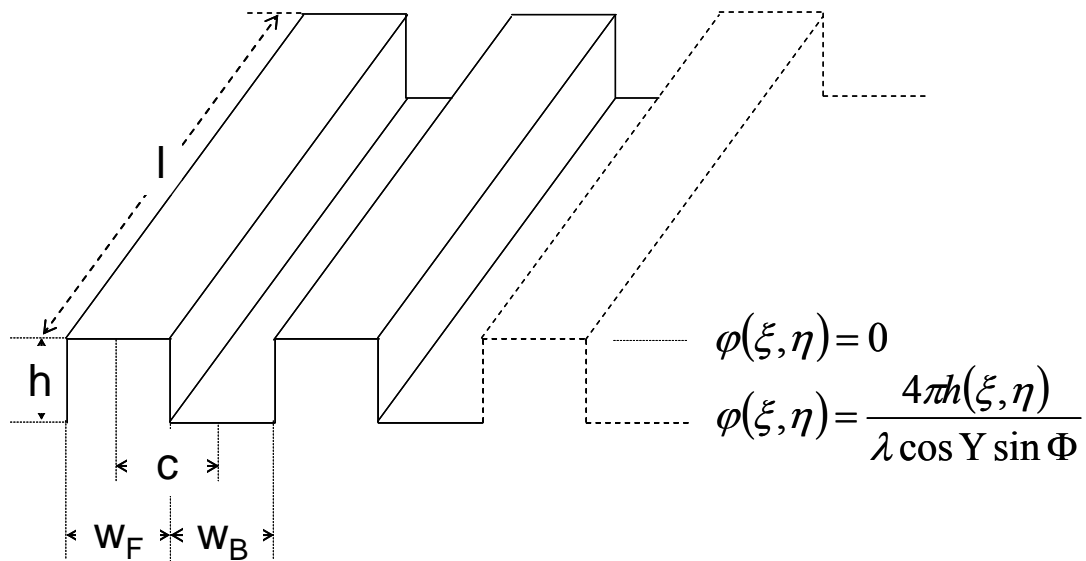


Figure A3-1: Simulation schematic for rectangular cell design of an even number of mirror surfaces. The mirror width of the front facets is denoted by w_F , the width of the back facets by w_B , the length by l , the distance between front and back facet by c , and the phase step due to the height difference h between front and back facet mirrors is ϕ .

For the mirror design of rectangular apertures with an even number of mirror surfaces N_{MS} , width w ($w = w_F = w_B$) and length l of a single mirror element and phase shifts φ (Figure A3-1), equation (A3 - 1) results in

$$U(P_i) = K \left(1 + e^{-ikc\left(\frac{x_i+x_s}{s'}+\frac{x_s}{r'}\right)} e^{-i\varphi} + e^{-ik2c\left(\frac{x_i+x_s}{s'}+\frac{x_s}{r'}\right)} + e^{-ik3c\left(\frac{x_i+x_s}{s'}+\frac{x_s}{r'}\right)} e^{-i\varphi} + \dots \right. \\ \left. \dots + e^{-ik(N_{MS}-2)c\left(\frac{x_i+x_s}{s'}+\frac{x_s}{r'}\right)} + e^{-ik(N_{MS}-1)c\left(\frac{x_i+x_s}{s'}+\frac{x_s}{r'}\right)} e^{-i\varphi} \right) \int_{-w/2}^{w/2} \int_{-l/2}^{l/2} e^{-ik\left[\left(\frac{x_i+x_s}{s'}+\frac{x_s}{r'}\right)\xi'+\left(\frac{y_i+y_s}{s'}+\frac{y_s}{r'}\right)\eta'\right]} d\xi' d\eta' \quad (A3 - 2)$$

which yields upon rearrangement of terms:

$$U(P_i) = K \left(1 + e^{-ik2c\left(\frac{x_i+x_s}{s'}+\frac{x_s}{r'}\right)} + e^{-ik4c\left(\frac{x_i+x_s}{s'}+\frac{x_s}{r'}\right)} + \dots + e^{-ik(N_{MS}-2)c\left(\frac{x_i+x_s}{s'}+\frac{x_s}{r'}\right)} \right. \\ \left. + e^{-ikc\left(\frac{x_i+x_s}{s'}+\frac{x_s}{r'}\right)} e^{-i\varphi} + e^{-ik3c\left(\frac{x_i+x_s}{s'}+\frac{x_s}{r'}\right)} e^{-i\varphi} + \dots + e^{-ik(N_{MS}-1)c\left(\frac{x_i+x_s}{s'}+\frac{x_s}{r'}\right)} e^{-i\varphi} \right) \\ * \int_{-w/2}^{w/2} \int_{-l/2}^{l/2} e^{-ik\left[\left(\frac{x_i+x_s}{s'}+\frac{x_s}{r'}\right)\xi'+\left(\frac{y_i+y_s}{s'}+\frac{y_s}{r'}\right)\eta'\right]} d\xi' d\eta' \quad (A3 - 3)$$

Rewriting the summands of equation (A3 - 3) in form of two geometric series results in:

$$U(P_i) = K \left[\frac{\sin\left(kc\frac{N_{MS}}{2}\left(\frac{x_i+x_s}{s'}+\frac{x_s}{r'}\right)\right)}{\sin\left(kc\left(\frac{x_i+x_s}{s'}+\frac{x_s}{r'}\right)\right)} e^{-ik\left(\frac{N_{MS}}{2}-1\right)c\left(\frac{x_i+x_s}{s'}+\frac{x_s}{r'}\right)} \left(1 + e^{-ik\left(\frac{x_i+x_s}{s'}+\frac{x_s}{r'}\right)} e^{-i\varphi} \right) \right] \\ * \int_{-w/2}^{w/2} \int_{-l/2}^{l/2} e^{-ik\left[\left(\frac{x_i+x_s}{s'}+\frac{x_s}{r'}\right)\xi'+\left(\frac{y_i+y_s}{s'}+\frac{y_s}{r'}\right)\eta'\right]} d\xi' d\eta' \quad (A3 - 4)$$

After integration and conversion of the exponential terms into cosine terms, the complex electric field at the image plane is calculated by:

$$\begin{aligned}
 U(P_i) = & K2wl \frac{\sin\left(k\left(\frac{x_i+x_s}{s'+r'}\right)\frac{w}{2}\right)}{k\left(\frac{x_i+x_s}{s'+r'}\right)\frac{w}{2}} \frac{\sin\left(k\left(\frac{y_i+y_s}{s'+r'}\right)\frac{l}{2}\right)}{k\left(\frac{y_i+y_s}{s'+r'}\right)\frac{l}{2}} \frac{\sin\left(kc\frac{N_{MS}}{2}\left(\frac{x_i+x_s}{s'+r'}\right)\right)}{\sin\left(kc\left(\frac{x_i+x_s}{s'+r'}\right)\right)} \\
 & * \cos\left(\frac{kc\left(\frac{x_i+x_s}{s'+r'}\right)+\varphi}{2}\right) e^{-ik\left(\frac{N_{MS}-1}{2}\right)c\left(\frac{x_i+x_s}{s'+r'}\right)} e^{-i\frac{1}{2}\left(kc\left(\frac{x_i+x_s}{s'+r'}\right)+\varphi\right)}
 \end{aligned} \tag{A3 - 5}$$

As described in section 2.1.2, the flux of energy is proportional to the square of the complex electric field, here $U(P_i)$. Thus, the complex electric field described in equation (A3 - 6) forms an energy distribution according to:

$$B(P_i) \propto U(P_i)U(P_i)^* \tag{A3 - 6}$$

$$\begin{aligned}
 B(P_i) \propto & KK^* (2wl)^2 \left(\frac{\sin\left(k\left(\frac{x_i+x_s}{s'+r'}\right)\frac{w}{2}\right)}{k\left(\frac{x_i+x_s}{s'+r'}\right)\frac{w}{2}}\right)^2 \left(\frac{\sin\left(k\left(\frac{y_i+y_s}{s'+r'}\right)\frac{l}{2}\right)}{k\left(\frac{y_i+y_s}{s'+r'}\right)\frac{l}{2}}\right)^2 \left(\frac{\sin\left(kc\frac{N_{MS}}{2}\left(\frac{x_i+x_s}{s'+r'}\right)\right)}{\sin\left(kc\left(\frac{x_i+x_s}{s'+r'}\right)\right)}\right)^2 \\
 & * \left(\cos\left(\frac{kc\left(\frac{x_i+x_s}{s'+r'}\right)+\varphi}{2}\right)\right)^2
 \end{aligned} \tag{A3 - 7}$$

Appendix 4

Optical path difference for tilted detector plane

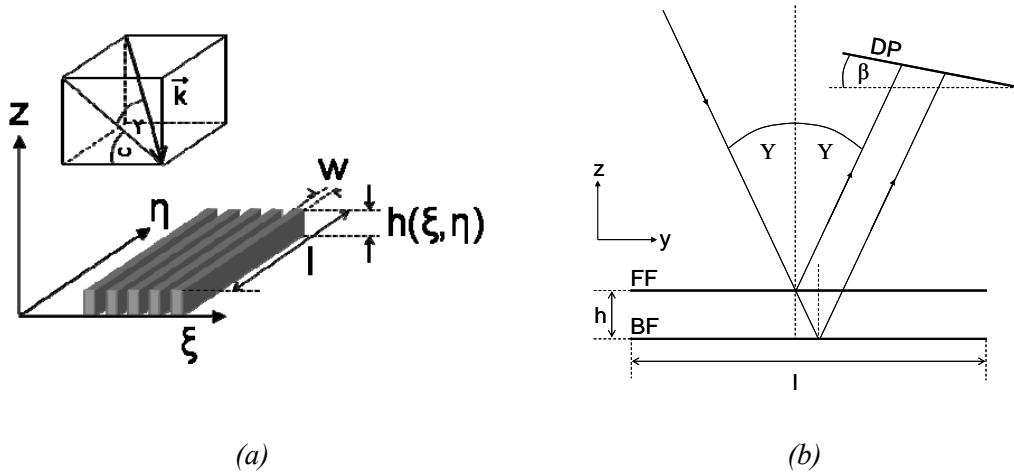


Figure A4-1: (a) Definition of grating cell orientation. The cell depth is h , lamellar width w and grating cell length l . Inset of (b): Denomination of angles: \vec{k} is the plane wave normal, Y the angle between \vec{k} and its projection in xz plane, Φ the angle between \vec{k} projection in the xz plane and the x axis. (b) Schematic (yz plane) indicating detector plane tilt β . h denotes the cell depth, DP the detector plane, Y , FF, and BF, the angle of incidence, the front and back facet reflecting surfaces, respectively.

In case of a tilt of the detector with respect to the MMA plane (as indicated in Figure A5.1

(b)), the optical path difference δ is determined by:

$$\delta = \frac{2h}{\cos(Y)\sin(\Phi)} \left[1 - \frac{\sin(Y)\sin(\beta)}{\cos(\beta - Y)} \right] \quad (\text{A4-1})$$

Accordingly, the depth of the N^{th} cell is given by:

$$h_{\text{Cell}N} = \frac{\delta_{\text{Cell}N} \cos(Y)\sin(\Phi)}{\left[1 - \frac{\sin(Y)\sin(\beta)}{\cos(\beta - Y)} \right]}, \quad (\text{A4-2})$$

The depth stepping from cell to cell Δh and the maximum cell depth h_{max} are given by Eq. (A4-3) and (A4-4), respectively.

$$\Delta h \leq \frac{\sin(\Phi)}{4\sigma_{\max} \cos(Y)}, \text{ and} \quad (\text{A4- 3})$$

$$h_{\max} = \frac{\sin(\Phi)}{4\mathfrak{R}_{LS} \cos(Y)}. \quad (\text{A4- 4})$$

Appendix 5

The LiMiNT Facility at the Singapore Synchrotron Light Source (SSLS)

The Singapore Synchrotron Light Source (SSLS) utilizes the compact storage ring Helios 2 with electron energy of 700 MeV, 4.5 T bending magnets, and a characteristic wavelength of 0.845 nm (see **Error! Reference source not found.** for specifications). The Light Source houses to-date 6 operating beamlines out of which one is dedicated for Lithography for Micro- and Nano- Technology (LiMiNT). The beamline together with its adjacent class 1000 cleanroom and equipment provides a one-stop shop for prototyping of micro- and nano- scale structures and devices. Table A5-2 lists the process infrastructure of the LiMiNT facility.

The LiMiNT Beamline

The beamline is one of the core equipments in the LiMiNT facility. Its layout is presented in Figure A5-1. Radiation emitted from the storage ring passes from the left hand side of the figure through the beamline to the scanner on the right hand side. A water cooled collimator at the beginning of the beamline determines the horizontal acceptance angle of radiation emitted from the storage ring. Power and gamma shutter open and close simultaneously and guarantee safe operation. Two Beryllium windows of 200 μm thickness each divide the beamline into 3 vacuum sections. The first window separates the high vacuum of the storage ring and the second window separates the high vacuum section of the beamline from the atmospheric pressure at the scanner side. In operation, the scanner environment is first evacuated and subsequently filled with Helium at a pressure 110 mbar. Its purpose is twofold: The Helium has lower radiation absorption and serves as a cooling gas (compare reference

(Manohara et al., 1996, and Li et al. 1996). A schematic view from above the beamline is shown in Figure A5-2. The beam port aperture at a distance of 0.952 m from the storage ring accepts a horizontal radiation fan of 60 mrad. Most of its transmitted radiation is then blocked by a 8 x 30 mm² collimating rectangular aperture. The adjacent Beryllium window (BeW1) of the same aperture size cuts the usable horizontal radiation fan to 10 mrad. A second Beryllium window (BeW2) of 8 x 110 mm² is located at 8.16 m. Its purpose is purely the division of the beamline vacuum section from the scanner environment. The exposure position is 9.352 m from the source point.

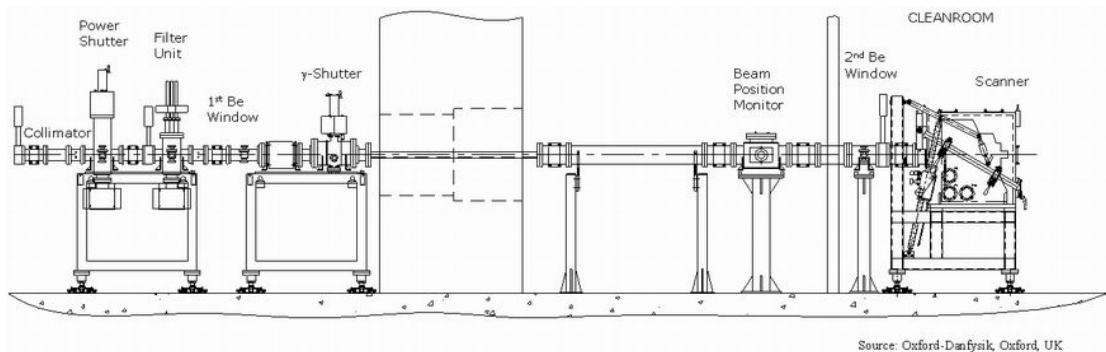


Figure A5-1: LiMiNT beamline at SSSL (Wilhelmi, 2004).

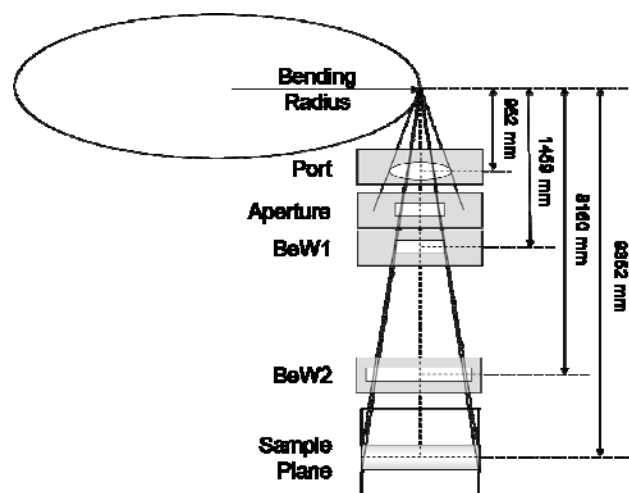


Figure A5-2: LiMiNT beamline at SSSL. Radiation emitted from the storage ring is collimated by an aperture. Two Beryllium windows (BeW1 and BeW2) divide the beamline into three vacuum sections. The size of the second aperture at the first Beryllium window determines the acceptance angle of horizontal radiation of 10 mrad.

The characteristics of the Helios 2 storage ring and the LiMiNT beamline determine the spectral power delivered to the exposure station. Table A5-1 summarizes the key parameters. On the basis of these parameters, the spectral power distribution is calculated according to reference (Peatman, 1997):

$$P\left(\frac{W}{\text{mrad}\% \text{ BW}}\right) = 5.95 \cdot 10^{-15} \left(\frac{\gamma^4 I}{\rho}\right) G_2\left(\frac{E_{cPh}}{E_{Ph}}\right), \quad (\text{A5 - 1})$$

where

$$G_2 = \left(\frac{E_{Ph}}{E_{cPh}}\right)^2 \int_{E_{Ph}/E_{cPh}}^{\infty} K_{5/3}(\eta) d\eta. \quad (\text{A5 - 2})$$

E_{cPh} is the characteristic photon energy, E_{Ph} the photon energy, γ the reduced energy given by $\gamma = 1957E$, E the energy of the electrons in the storage ring in GeV, ρ the radius of the curvature of the electron orbit in the dipole magnets in meters, and I the electron ring current in Amperes.

Figure A5-3 displays the spectral power distribution of the LiMiNT beamline for a Helios 2 current of 500 mA. The simulation was performed with XOP 2.11 software (Rio and Apte, 2006). The total power emitted from Helios 2 storage ring at a current of 500 mA into a 10 mrad horizontal radiation fan integrates to 32 W power. The transmission of the beam through the Beryllium windows reduces the transmitted power to 4.2 W and a cut-off radiation below photon energy of 2 keV. Contrary to the horizontal radiation fan of 10 mrad, the vertical divergence of the radiation fan is wavelength dependant. Harder X-rays (high energy) are concentrated near the plane of the storage ring, whereas softer X-rays diverge into large angels. Subsequently, the maximum beam size in the vertical direction is given by the photons of the smallest energy, which is in the case of the LiMiNT beamline 2 keV radiation. The maximum vertical divergence angle of the radiation fan is given by (Peatman, 1997):

$$\sigma_v (\text{mrad}) = \frac{570}{\gamma} \left(\frac{E_{cPh}}{E_{Ph}} \right)^{0.43} \quad \text{for } 0.2 < \frac{E_{cPh}}{E_{Ph}} < 100, \quad (\text{A5 - 3})$$

resulting in a vertical divergence angle of the LiMiNT beamline $\sigma_v = 0.364 \text{ mrad}$ at a wavelength of 0.62 nm (2keV). In a distance of 9.352 m from the source point (at the sample plane in the X-ray scanner) the X-ray beam size has a footprint of 92 x 8.4 mm².

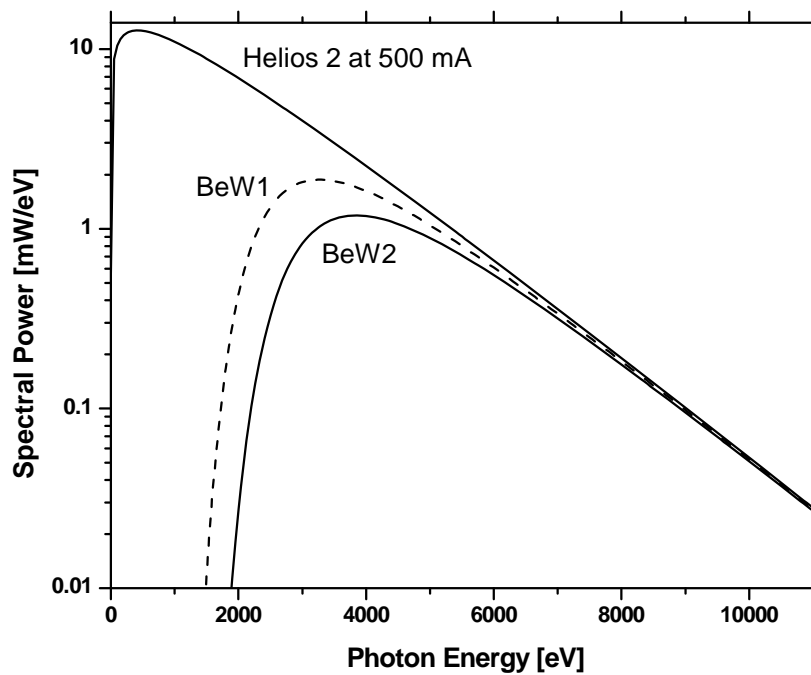


Figure A5-3: Spectral power distribution of the LiMiNT beamline for a Helios 2 current of 500 mA. Simulation was performed with XOP 2.11 software (Rio and Apte, 2006).

Table A5-1: Characteristic Helios 2 and LiMiNT beamline parameters.

| Parameter | Unit | Value |
|---|-------------------|--------------|
| Helios 2 | | |
| Electron energy | MeV | 700 |
| Magnetic field | T | 4.5 |
| Bending magnet radius | m | 0.52 |
| Characteristic photon energy | keV | 1.47 |
| Characteristic wavelength | nm | 0.845 |
| Electron current (typical) | mA | 500 |
| Circumference of electron orbit | m | 10.8 |
| Lifetime | h | 10 |
| Number of beam ports | | 21 |
| Horizontal acceptance angle | mrad | 60 |
| Spectral range | keV | 0.0001-12 |
| Integral power at port at 500 mA | W | 200 |
| LiMiNT | | |
| Port number | | 12 |
| Horizontal acceptance angle | mrad | 10 |
| Electron beam size (horizontal) | mm | 1.3 |
| Electron beam size (vertical) | mm | 0.35 |
| Electron beam divergence (horizontal) | mrad | 1.7 |
| Electron beam divergence (vertical) | mrad | 0.15 |
| Emittance (vertical) | $\mu\text{m rad}$ | 2.21 |
| Total Beryllium filter thickness in beamline | mm | 0.4 |
| Integral power after Beryllium filter at 500 mA | W | 4.2 |
| Spectral range | keV | 2-12 |
| Vertical radiation divergence | mrad | 0.364 |

Table A5-2: Process equipment LiMiNT facility / SLS









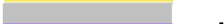



| Process Equipment | Comments |
|--|---|
| Primary pattern generation | |
| DWL 66 Heidelberg Instruments | Laser writing system, equipped with 20 and 4 mm write-heads for pattern generation. Minimum feature size < 1 μm . |
| Sirion (FEI) modified with NPGS tool (JC Nabity Lithography Systems) | Electron beam writing system for nano-pattern generation, minimum feature size below 50 nm. |
| X-ray lithography | |
| Oxford Danfysic MEMS | Lithography tool for (deep) X-ray lithography beamline and scanner |
| Wet chemistry (wet bench and fume hoods) | |
| M-O-T Micro Electroforming unit μGalv | Electro deposition of Au, Ni, and Cu. Direct (μGalv), pulse and reverse pulse current deposition are available. |
| Resist processing | Spin coater, oven, and hotplates. |
| Si, Cr, Au wet etching | |
| Plasma processes | |
| NSP 12-1 (NTI) | Magnetron sputter deposition for Cr, Au, Al thin film deposition using Ar and O ₂ process gasses. The system provides one RF and one DC sputter gun. |
| RIE 2321 (NTI) | Plasma cleaning and descum with Ar and O ₂ process gasses |
| Replication | |
| Jenoptic-Mikrotechnik HEX-01 | Hot embossing tools for replication of micro and nano-moulds. |
| Machining | |
| Engis 380-J | Lapping and polishing machine |
| Buehler Isomet 4000 | Precision saw for wafer cutting. |
| Metrology | |
| Sirion (FEI) | Scanning electron microscope (SEM) at 1-30 kV acceleration voltages. |
| Leica DML Microscope | 5 – 1000 x magnifying microscope |
| Veeco Wyko 1100 Profiler | Red and white light profiler equipped with 2.5 – 50 x magnifying lenses |
| PCIT beamline | X-ray phase contrast micro-imaging and computed tomography |
| ISMI beamline | Infrared spectroscopy and microscopy tool equipped with Bruker IFS 66 and IFS 125 HR FTIR's |
| SINS beamline | Photoemission spectroscopy, X-ray absorption fine structure spectroscopy, X-ray magnetic circular dichroism in the soft X-ray range. Electronic and magnetic properties of nanomaterials and surfaces |
| XDD beamline | Hard X-ray diffraction, anomalous scattering, X-ray reflectometry, absorption and fluorescence spectroscopy, X-ray topography. |

Appendix 6

The Gold Stencil Mask Fabrication Process

The process to fabricate gold stencil masks for X-ray lithography bases primarily on two processes, namely the electro-deposition of gold absorber membrane and the etching of the silicon base to form a free-suspended membrane. The deposition of the gold absorber membrane is thereby a crucial process step and low stress deposition is of paramount importance to impede membrane buckling. Following earlier work of Ogawa et al. (Ogawa et al, 1992), we electro-plated with pulse current at a pulse current density of 0.2 mA/ dm^2 , pulse period of 100 ms, a pulse duration of 20 ms and pulse break of 80 ms. Moreover, the silicon wafer thickness is kept throughout the process at a thickness of $500 \mu\text{m}$ and the etching of the membrane is performed in the last process steps to circumvent the breaking of the membrane and to allow easier handling. The final etching of the gold membrane bases on silicon micromachining technology. Deep reactive ion etching (DRIE) is chosen instead silicon wet etching to avoid stiction of fine gold wires. Table A6-1 illustrates the mask making process.

Table A6-1: Process flow for Au stencil mask fabrication.

| # | Schematic | Comment |
|----|---|--|
| 1 |  | The process starts from a double sided polished silicon (Si) wafer. |
| 2 |  | Deposition of 0.5 μm SiO ₂ (wafer backside) via Plasma Enhanced Chemical Vapour Deposition (PECVD). |
| 3 |  | Deposition of 30 nm Cr adhesion layer and 100 nm Au conduction layer (wafer frontside) via Physical Vapour Deposition (PVD). |
| 4 |  | Front-side structuring. Here: SU-8 2025 (MicroChem Corp). |
| 5 |  | Dip development of SU-8 photoresist |
| 6 |  | Au electro plating using Neutronex 309 (Enthone Inc.) solution. Electro plating was carried out in a beaker setup, at a 50 °C solution temperature, pH of 9.5, and under moderate agitation. Plating parameters: 1) Pulse current density 0.2 A/dm ² 2) Pulse duration 20 ms, pulse break 80 ms. |
| 7 |  | SU-8 resist stripping Immersion in N-Methyl-Pyrrolidone (NMP) (Best Chemical Company Singapore Pte Ltd) at 70 °C for 2 hours |
| 8 |  | Backside coating with AZ photoresist, pre-exposure bake and UV lithography to define the membrane area. |
| 9 |  | Development of AZ photoresist to open area for backside etching. |
| 10 |  | SiO ₂ etch |
| 11 |  | Si DRIE |
| 12 |  | Cr Au wet etch. |

Appendix 7

The characterization of surface roughness and surface waviness of etched mirror surfaces

The topic of surface roughness and surface waviness is covered in ANSI Standard B46.1.

In general, one refers to surface roughness for closely spaced peaks and valleys of a surface topography, whereas for the surface waviness wider spread irregularities are considered. For optical components the root mean square value is commonly specified to characterize the surface roughness (Vorderburger, 1990).

In principle, surface measuring techniques are classified into line profiling and area techniques. The optical profiler used for the characterization of the mirror surfaces is considered areal topography technique. This group is known to provide area properties of surfaces which are particular interesting for the characterization of etched mirror surfaces. On the one hand, the technique allows fast non-contact characterization but on the other hand, such 3D topographical techniques are also known to produce less accurate results when compared to stylus methods as discussed by Vorburger (Vorburger, 2007).

Flat stepped mirror surface were characterized with an optical profiler (WYKO 1100) in a surface area of 0.5 mm^2 at a sampling period of $3.31 \text{ }\mu\text{m}$.

The optical profiler uses a Mirau interferometer setup to analyze the surface topography of reflective samples. It allows two interferometer operations, namely, vertical scanning interferometry and phase-shifting interferometry. The vertical

scanning interferometry is characterized by a large vertical scanning distance in the range of +/- 1 mm at a resolution of approximately 3 nm for white-light illumination. Its lateral resolution depends on the objective lens used and is in general in the range of 1 μm . Phase shifting interferometry uses red light filtered light and a piezoelectric transducer shifts the reference mirror of the Mirau interferometer by a known distance and the surface roughness profile is computed. The technique is restricted to smooth surface profiles with peak-to-valley differences smaller than of $\lambda/4$, thus smaller than 150 nm.

For the characterization of the etched mirror surfaces a magnification of 2.5 times at a lateral sampling resolution of 3.31 μm was used. The vertical scanning interferometry was chosen allowing the characterization of etch depths, surface waviness and surface roughness in a single measurement. Given the large number of samples characterized the method proved to give valuable and fast results. More information on the profiler can be found in reference (Page, 2002).

After the data acquisition, the raw data is filtered by digital filters such as window filters. In window filtering, a weighted window of a chosen size (number of pixel) is scanned across the selected area in the image and a new filtered image is calculated. To study the surface waviness of the mirrors, a low pass window filter is applied. For a window filter of 3x3 pixels, an average value of the center pixel (Z_{Cnew}) is calculated while the window filter scans through the selected image area (here e.g. pixel 1-9 in a X-Y coordinate system, whereby C denotes the center pixel of the window and Z_1 - Z_9 the height value of respective pixels surrounding it). Equation (A7-1) shows the calculation schematically.

$$\begin{array}{c} Z_1 Z_2 Z_3 \\ Z_4 Z_C Z_6 \\ Z_7 Z_8 Z_9 \end{array}$$

$$Z_{C_{new}} = \frac{Z_1 + Z_2 + Z_3 + Z_4 + Z_C + Z_6 + Z_7 + Z_8 + Z_9}{9} \quad (\text{A7-1})$$

As a result, higher frequency surface textures are filtered out and do not contribute to the surface profile. Surface waviness W is then obtained from the filtered data set via:

$$W = \sqrt{\frac{1}{N} \sum (Z_{inew})^2}, \quad (\text{A7-2})$$

where N is the number of pixels in the selected image area.

To study the surface roughness, a high pass window filter is applied. Equation (A7-3) shows the mathematics.

$$\begin{array}{c} Z_1 Z_2 Z_3 \\ Z_4 Z_C Z_6 \\ Z_7 Z_8 Z_9 \end{array}$$

$$Z_{C_{new}} = Z_C - \frac{Z_1 + Z_2 + Z_3 + Z_4 + Z_6 + Z_7 + Z_8 + Z_9}{8} \quad (\text{A7-3})$$

As for the waviness W , the root mean square value of the surface roughness R_q is calculated according to Eq. (A7-4).

$$R_q = \sqrt{\frac{1}{N} \sum (Z_{inew})^2}, \quad (\text{A7-4})$$

The window filtering technique proved to provide quick and reliable estimates for the surface quality.

Appendix 8

The Bruker IFS 125 HR FTIR at SSSL ISMI beamline

The IFS 125 HR FTIR is a stand-alone, high resolution ($\mathfrak{R} < 0.005 \text{ cm}^{-1}$), Michelson-type Fourier transform infrared spectrometer marketed by Bruker Optics. It can be operated with various IR sources such as NIR (Tungsten lamp), MIR (Globar), FIR (Hg lamp), and, via an input port in the source compartment of the spectrometer, the Helios 2 storage ring. The spectrometer is an integral part of SSSL beamline for Infrared Spectro-Microscopy (ISMI) which extracts IR flux produced at the edge of dipole D1 of storage ring Helios 2, and thus the available IR flux for the spectrometer covers a spectral range from 10000 to 10 cm^{-1} enabling high resolution IR experiments of extremely small samples (Bahou et al., 2007). Fig. A7-1 shows the frontview of the ISMI beamline and its attached IFS 125 HR spectrometer as installed at SSSL. Depending on the spectral working range, the spectrometer allows a number of amplitude beam splitters and detectors which are installed in the interferometer and detector compartment of the spectrometer, respectively. The spectrometer rests on vibration damping posts and occupies a space of approximately $220 \times 60 \times 25 \text{ mm}^3$ and $115 \times 40 \times 25 \text{ mm}^3$ for the optics and the scanner compartments, respectively.

The schematic of the spectrometer is illustrated in Fig. A7-2. In standard FTIR operation, radiation emitted from the sources (A) in the source compartment is collected by a spherical mirror (B). In case Helios 2 is the chosen light source, the radiation enters via input port (C). In both cases, the radiation beam is directed towards the interferometer compartment. Near the focal point of the spherical mirror,

selectable field stop apertures on a rotating disk (D) limit the beam divergence depending on the aperture size chosen.

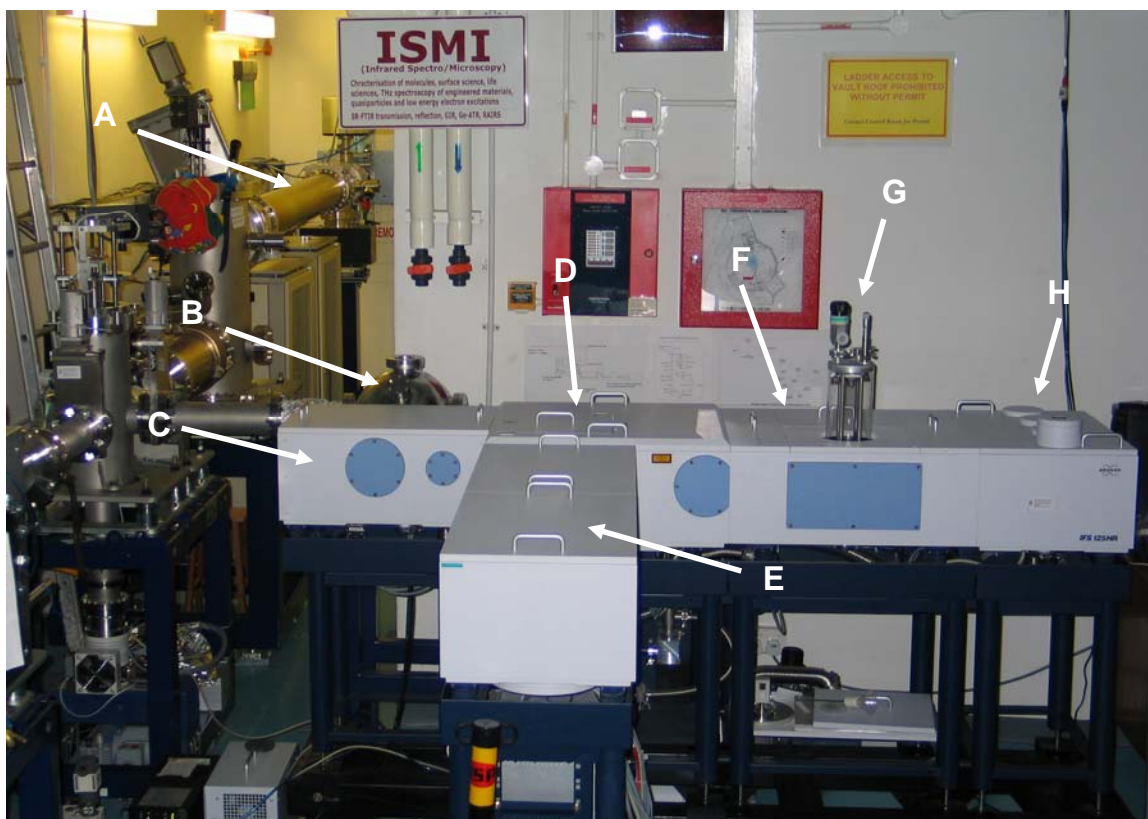


Figure A8-1: View of IFS 125 HR FTIR as installed at ISMI beamline of SSSL. Definitions: A: ISMI beamline pipes, B: Input port for IR produced by Helios 2, C: Source compartment, D: Interferometer compartment, E: Scanner compartment, F: Sub-chambers for beam switching and sample compartment, G: Gas cell, H: Detector compartment.

Downstream the field stop, a parabolic mirror (E) collimates the beam and directs it towards a flat folding mirror (F_1) in the interferometer compartment of the spectrometer. Upon reflection from the folding mirror the beam is directed through the beam splitter cell. The beam splitter is positioned in a 30 degrees angle with respect to the incoming beam and the beam diameter at the beam splitter surface measures approximately 62 mm. At the beam splitter (G), one half of the beam is transmitted through the beam splitter towards the scanner compartment in which a movable corner-cube mirror (H) reflects the beam backwards. Its movement during the scanning operation is continuously monitored by a HeNe Laser LED. The other

half of the beam is reflected by the beam splitter towards a fixed corner-cube mirror (I). Both beams recombine again at the beam splitter and reflect towards a flat folding mirror (F_2). A focusing parabolic mirror (J) and another folding mirror (F_3) direct the beam subsequently through the sample compartment. In the sample compartment the beam can be switched to follow two optional routes either through the gas cell mounted in on the top route or through the bottom route as illustrates in the schematic. At the opposite side of the sample compartment, toroidal (K) and folding mirrors focus and direct the beam onto the entrance opening of the detector compartment. The beam is then collimated by a parabolic mirror (L) and directed at right angles towards a switchable folding mirror (F_4) directing the beam either to the bolometer (P) or MCT (N) detector position. Depending on the respective detector slot chosen, the beam is then focused onto the detector surface by parabolic mirrors (O, M).

The signal received by the detectors is amplified by a pre- and main- amplifier system and subsequently converted via a 24 bit A/D converter. The spectrometer is fully automated via the operation system OPUS® (Opus, 2004). Table A7-1 lists the main specifications of SSSL's IFS 125 HR spectrometer.

When switched on, the system requires a 25 minutes waiting time prior to measurements to allow the LED reference laser and its electronics to stabilize.

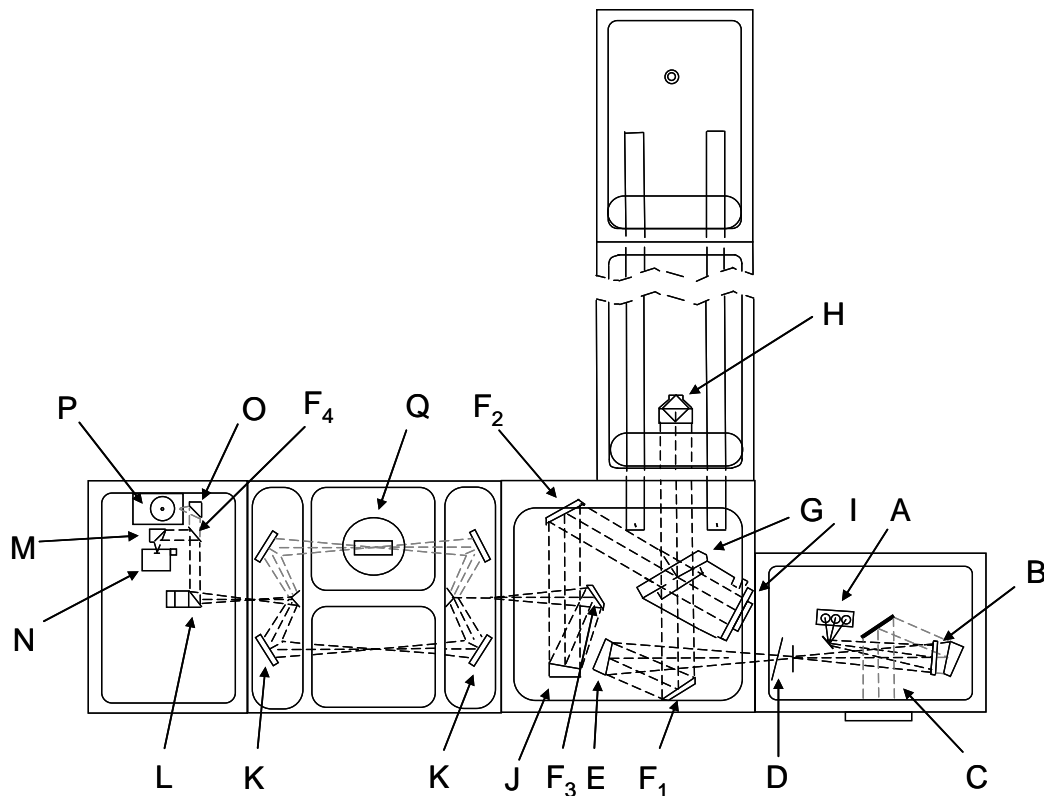
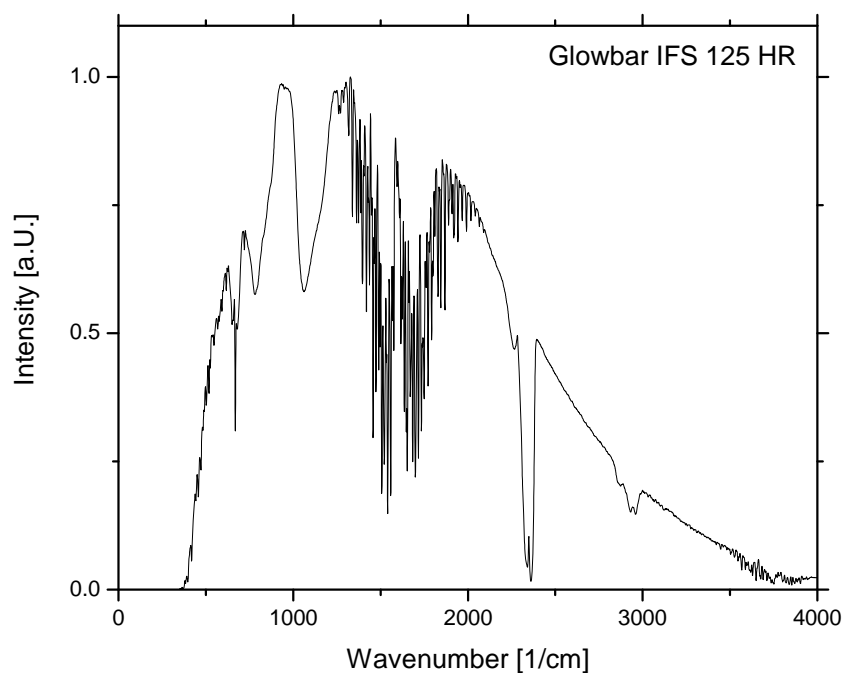


Figure A8-2: IFS 125 HR in standard operation mode A. Definitions: A: Sources, B: Spherical mirror, C: ISMI beamline input port, D: Input apertures (field stop), E: Collimating parabolic mirror, F_{1-4} : Folding mirrors, G: Beam splitter, H: Scanner with movable retroreflecting mirror, I: Fixed retroreflecting mirror, J: Focusing parabolic mirror, K: Toroidal mirror, L: Collimating parabolic mirror, M: Focusing parabolic mirror, N: Detector position (MCT), O: Focusing parabolic mirror, P: Detector position (Bolometer).

All measurements and experiments presented in the thesis were taken with the spectrometer under atmospheric conditions and a MIR globar source. Figure A7-3 shows the typical blackbody spectrum of the glow-bar source in ambient air taken with the IFS 125 HR at a resolution of 4 cm^{-1} . The sharp lines in the spectral band ranging from $1300 - 1800\text{ cm}^{-1}$ indicate the H_2O absorption of the ambient air.

Table A8-1: Specifications of SSLS' IFS 125 HR spectrometer (IFS125, 2006).

| Parameter | Unit | Specification |
|------------------------|------------------|---|
| Spectral range | cm ⁻¹ | 10 – 10000 |
| Resolution | cm ⁻¹ | < 0.005 |
| Resolving power | - | > 10 ⁶ |
| Wavenumber accuracy | cm ⁻¹ | < 5 x 10 ⁻⁷ |
| Vacuum system | hPa (mBar) | ≤ 2 x 10 ⁻² (0.02) |
| Sources | - | Helios 2, globar, tungsten lamp |
| Beam splitter | - | CaF ₂ , KBr, Mylar® film |
| Scanner | - | 6 mirror velocities 0.16 – 2.5 cm/sec mechanical displacement, max mirror displacement (currently) ~ 1 m |
| Field stop | mm | 16 positions 0.5 – 12.5 |
| Sample compartment | | Dual channel |
| Detector | - | DigiTect™ detector systems, D201 / D301 (DTGS with PE/ KBr window), D211 (Si bolometer), D315 / D316 (MCT- wide/ mid band), D413 (InSb) |
| Amplifier | - | Pre-amplifier with 4 gain levels, main amplifier with 5 gain levels |
| A/D converter | bit (kHz) | 24 (96) Delta-Sigma ADC |
| Spectroscopic software | - | Analytical software package OPUS [Opus04] |

**Figure A8-3:** Normalized spectrum of globar source as taken with IFS 125 HR FTIR at a resolution of 4 cm⁻¹. The spectrum was recorded in ambient atmosphere with KBr beam splitter and MCT detector.